ÇUKUROVA UNIVERSITY

INSTITUTE OF NATURAL AND APPLIED SCIENCES

MSc THESIS

Ramazan AKAR

COMBUSTION CHAMBER DESIGN WITH COMPUTATIONAL FLUID DYNAMIC

DEPARTMENT OF MECHANICAL ENGINEERING

ADANA, 2005

ABSTRACT

MSc THESIS

COMBUSTION CHAMBER DESIGN WITH COMPUTATIONAL FLUID DYNAMIC

Ramazan AKAR

DEPARTMENT OF MECHANICAL ENGINEERING
INSTITUTE OF NATURAL AND APPLIED SCIENCES
UNIVERSITY OF ÇUKUROVA

Supervisor : Prof. Dr. Kadir AYDIN
Year: 2005, Pages: 158
Jury : Prof. Dr. Kadir AYDIN
Assoc. Prof. Dr. Hüseyin AKILLI
Assoc. Prof. Dr. Recep YURTAL

In this study, flow characteristics of some engine models in two dimension, three dimension and dynamic model were investigated numerically by means of FLUENT CFD solver. FLUENT program uses finite volume method in order to model the flow inside of engine. Experimental results obtained by Yasar were used for one engine model to validate numerical result and to have solution methods for other engine models. Numerical methods were carried out at various valve gaps for all models.

The results of numerical studies show that flow structure is highly affected by the valve position and cylinder length. The result obtained by dynamic grid model is thought to have a great importance in engine design period. It is seen that burned gas level in combustion chamber from previous cycle is influenced by valve timing. Results obtained from one intake port model shows good agreement with experimental results.

Keywords: Intake Flow, Combustion, Fluent, Computational Fluid Dynamics (CFD), Finite Volume Method.

ÖZ

YÜKSEK LİSANS TEZİ

MOTORLARDA YANMA ODALARININ HESAPLAMALI AKIŞKANLAR DİNAMİĞİ İLE TASARLANMASI

Ramazan AKAR

ÇUKUROVA ÜNİVERSİTESİ
FEN BİLİMLERİ ENSTİTÜSÜ
MAKİNA MÜHENDİSLİĞİ ANABİLİM DALI

Danışman : Prof. Dr. Kadir AYDIN
Yıl: 2005, Sayfa: 158
Jüri : Prof. Dr. Kadir AYDIN
Doç. Dr. Hüseyin AKILLI
Doç. Dr. Recep YURTAL

Bu çalışmada, iki boyutlu, üç boyutlu ve dinamik modeller olmak üzere farklı motor modelindeki akış karakteristikleri nümerik olarak FLUENT programı kullanılarak incelenmiştir. FLUENT programı motorlar içerisindeki akış karakteristiklerini modellemek için sonlu hacimler metodunu kullanmaktadır. Daha önceden yapılmış olan deneysel sonuçlar nümerik sonuçların doğruluğunu kanıtlamak ve kullanılacak diğer motor modelleri için bir temel oluşturması amacı ile tezde bulunmakta olan bir modelle karşılaştırılmıştır. Nümerik metotlar çeşitli valf açıklıkları için tüm modellerde uygulanmıştır.

Nümerik çalışmanın sonucunda valf açıklığının ve silindir uzunluğunun akış yapısı üzerinde büyük bir etkisi olduğu görülmüştür. Dinamik metot yöntemi çalışmalarından bulunan sonuçların motor tasarımı üzerinde büyük öneme sahip olacağı düşünülmektedir. Bu çalışmalardan; bir önceki çevrimden yanma odasında kalmış olan yanmış gazların miktarının valf zamanlamasından etkilendiği görülmüştür. Tek emme supaplı motor modelinden bulunan sonuçların deneysel sonuçlarla uyum içerisinde oldukları görülmüştür.

Anahtar Kelimeler: Supaplar etrafından akış, Yanma, FLUENT, Hesaplamalı Akışkanlar Dinamiği (CFD), Sonlu Elemanlar Metodu.

ACKNOWLEDGEMENT

Initially, I would like to present my appreciations to my supervisor, Prof. Dr. Kadir AYDIN. His supports and guidance for this study is unforgettable for me. I hope, we can work together for big innovations in automotive sector near future.

I have a lot of thanks to Prof. Dr. Beşir Şahin, Head of Department of Mechanical Engineering. He is a kind of person working a lot no matter which day it is, so that, it was probably possible to see him when I went his room even it was Saturday or Sunday. His supports and interests to my study encouraged me a lot.

When I am thinking another important supporter to me, I have to express my special thanks to Assoc. Prof. Dr. Hüseyin AKILLI. His friendly dialog and CFD knowledge helped me a lot.

During my studies, I did not have any anxieties and troubles to be successful, although some difficulties were in my topic. I was always happy and believed to be successful at the end, since I studied with professional lecturer.

In addition to my words, I would really like to emphasize my thanks to all of the members of Department of Mechanical Engineering of Çukurova University and especially, research Assist. Durmuş Ali BİRCAN, Kerim Can ÇELEBİ, Adnan ÖZTÜRK, Azize AKKOCA, N. Adil ÖZTÜRK.

Finally, I am very thankful to my family for their support and helps. Although my stressful times and my mood during thesis studies were bored them a lot, they always showed big patience to me. Besides my family, some of my friend, Fırat Fırat and Melih Dikeç deserve special thanks for their supports during my low spirited time.

CONTENTS **Page**

ABSTRACT…… I

ÖZ…… II

ACKNOWLEDGEMENT……... III

CONTENTS…… IV

LIST OF TABLES…….. VI

LIST OF FIGURES……. VII

NOMENCLATURE……..... XIV

1. INTRODUCTION……... 1
2. PREVIOUS STUDIES ……..... 4
   - 2.1 Outline of Present Study……... 33
   - 2.2 Outline of Dissertation…….. 34
3. MATERIAL AND METHODS……... 36
   - 3.1 Cylinder Geometries and Combustion Chambers……. 36
   - 3.2 Components of a Numerical Solution…… 48
   - 3.3 Mathematical Model…….. 49
     - 3.3.1 Governing Equations…….. 49
     - 3.3.2 The Mass Conservation Equation……... 50
     - 3.3.3 Momentum Conservation Equation…… 50
     - 3.3.4 Energy Conservation Equation……... 51
   - 3.4 Discretization Method……... 52
   - 3.5 Numerical Grid…….. 56
     - 3.5.1 The Choice of Grid……. 61
     - 3.5.2 Grid Generation…….. 63
     - 3.5.3 Grid Quality…… 66
     - 3.5.4 Grid Independency…….. 68
   - 3.6 Finite Approximations……... 70
   - 3.7 Solution Method……. 71
     - 3.7.1 Linearization…… 74
   - 3.8 Convergence Criteria…….. 75

3.9 Turbulence Model…….. 75
3.10 Boundary Conditions…… 81
3.11 Dynamic Grid Model…… 83
4. RESULTS AND DISCUSSIONS…… 88
4.1 Two Dimensional Calculations……. 91
4.2 Three Dimensional Calculations…… 114
4.3 Dynamic Grid Calculations……... 139
5. CONCLUSIONS…….. 152
REFERENCES……. 155
CURRICULUM VITAE……... 158

LIST OF TABLES **Page**

Table 3.1 Quality measurement based on skewness…….. 67

Table 3.2 Dynamic grid parameters for 2d model……... 85

LIST OF FIGURES **Page**

Figure 1.1	A four stroke engine and its members……..	2
Figure 2.1	The Swirl and Tumble motion of flow in combustion chamber..	7
Figure 2.2	Effect of squish area location on tumble flow formation…….	8
Figure 2.3	Valve lift profiles of inlet and exhaust valves……..	10
Figure 2.4	Evolution of tumble flow motions during intake stroke in symmetry axial plane. Engine speed N = 1500 rpm. Velocity data are ensemble-averaged from 100 instantaneous measurements…….	11
Figure 2.5	Dynamic grid system just before valve is opened……	13
Figure 2.6	Computational grid of DISC engine……..	14
Figure 2.7	Velocity vector and temperature at -30° after TDC……...	15
Figure 2.8	Four valve DOHC computational model……...	16
Figure 2.9	Valve lift history……	16
Figure 2.10	Velocity vector at CA = 60°, 120°, 180, and 600°…….	17
Figure 2.11	GDI engine model and its computational grid……	18
Figure 2.12	Computed velocity fields……...	19
Figure 2.13	Computed velocity fields on the xz cutting plane at y=0 mm…..	20
Figure 2.14	Geometry of combustion chambers……	21
Figure 2.15	Computational domain……	22
Figure 2.16	Sketch of the cylinder head with the location of the measurement points……	22
Figure 2.17	Velocity fields in axial mid-section at 35 CA after TDC…..	23
Figure 2.18	Velocity field in cross section located at 10 mm from cylinder head at 35 CA after TDC…….	24
Figure 2.19	Velocity field at 115 CA after TDC……..	24
Figure 2.20	Velocity field at 165 CA after TDC……..	25
Figure 2.21	2d cylinder model with valves and piston positions corresponding to two different crank angles…….	26

Figure 2.22 Close-up of the grid in the valve region……. 26
Figure 2.23 Views of grid deformation during the intake-compression Strokes…….. 27
Figure 2.24 Views of velocity magnitude contours in the intake valve plane during the intake-compression strokes…….. 27
Figure 2.25 Views of velocity magnitude contours in the exhaust valve plane during the exhaust stroke…….. 28
Figure 2.26 Schematic of geometry section…….. 29
Figure 2.27 Fuel flow through the inlet valve at different valve openings.. 29
Figure 2.28 Fuel distribution below the inlet valve at different valve Openings……. 30
Figure 2.29 Air flow through the inlet valve at different valve openings…. 31
Figure 2.30 Vertical (y-direction) velocity contours of air flow within the chamber…… 32
Figure 2.31 (a) Fuel distribution showing the flow patterns on the side walls (z= 15 mm). (b) Velocity contours 1mm from the side walls (z=14mm)…… 33
Figure 3.1 Basic cylinder geometry section used in 2d……. 37
Figure 3.2 Basic cylinder geometry with valve used in 3d…… 38
Figure 3.3 3d Valve geometry used in 3d studies…….. 41
Figure 3.4 2d valve geometry used in 2d studies……... 41
Figure 3.5 2d cylinder geometry sharing same center with intake Manifold……... 42
Figure 3.6 2d cylinder geometry in different axis than cylinder axis…… 43
Figure 3.7 2d cylinder geometry having an intake manifold with radius….. 43
Figure 3.8 Pent-roof cylinder geometry……. 44
Figure 3.9 Parametric studies in CFD calculations…… 46
Figure 3.10 An example of parametric design table…… 47
Figure 3.11 3d cylinder model and its drawing with one intake port…….. 47
Figure 3.12 3d cylinder model and its drawing with two intake port…….. 48
Figure 3.13 Control volume used to illustrate discretization of a scalar

transport equation……. 55
Figure 3.14 Grid components…….. 57
Figure 3.15 Discrete grid points…… 58
Figure 3.16 An example of unstructured grid……... 59
Figure 3.17 An example of hybrid mesh……... 60
Figure 3.18 Cell types…….. 62
Figure 3.19 An illustration of sizing function capability near the valve region…….. 65
Figure 3.20 A view of 2d model before adaptation…….. 69
Figure 3.21 Marking of adaptation places……. 69
Figure 3.22 A view of 2d model after adaptation……. 70
Figure 3.23 Overview of the Segregated Solution Method……... 73
Figure 3.24 2d unsteady model……... 85
Figure 3.25 The intake and exhaust valve profiles……. 86
Figure 4.1 A sample of residuals history…….. 89
Figure 4.2 A sample of mass flow history on outlet boundary……. 89
Figure 4.3 Measurement points for 3d calculation…… 90
Figure 4.4 Velocity vectors colored by velocity magnitude a) 3 mm valve lift standard turbulence method, b) 3 mm valve lift RNG turbulence method…… 94
Figure 4.5 Velocity vectors colored by velocity magnitude a) 5 mm valve lift standard turbulence method, b) 5 mm valve lift RNG turbulence method…… 95
Figure 4.6 Velocity vectors colored by velocity magnitude a) 7 mm valve lift standard turbulence method, b) 7 mm valve lift RNG turbulence method…… 96
Figure 4.7 Velocity vectors colored by velocity magnitude a) 9 mm valve lift standard turbulence method, b) 9 mm valve lift RNG turbulence method…… 97
Figure 4.8 Velocity vectors colored by velocity magnitude a) 3 mm valve lift standard turbulence method, b) 3 mm valve lift RNG

turbulence method…… 98
Figure 4.9 Velocity vectors colored by velocity magnitude a) 5 mm valve lift standard turbulence method, b) 5 mm valve lift RNG turbulence method…… 99
Figure 4.10 Velocity vectors colored by velocity magnitude a) 7 mm valve lift standard turbulence method, b) 7 mm valve lift RNG turbulence method…… 100
Figure 4.11 Velocity vectors colored by velocity magnitude a) 9 mm valve lift standard turbulence method, b) 9 mm valve lift RNG turbulence method…… 101
Figure 4.12 Velocity vectors colored by velocity magnitude a) 3 mm valve lift standard turbulence method, b) 3 mm valve lift RNG turbulence method…… 102
Figure 4.13 Velocity vectors colored by velocity magnitude a) 5 mm valve lift standard turbulence method, b) 5 mm valve lift RNG turbulence method…… 103
Figure 4.14 Velocity vectors colored by velocity magnitude a) 7 mm valve lift standard turbulence method, b) 7 mm valve lift RNG turbulence method…… 104
Figure 4.15 Velocity vectors colored by velocity magnitude a) 9 mm valve lift standard turbulence method, b) 9 mm valve lift RNG turbulence method…… 105
Figure 4.16 Velocity vectors colored by velocity magnitude a) 3 mm valve lift standard turbulence method, b) 3 mm valve lift RNG turbulence method…… 106
Figure 4.17 Velocity vectors colored by velocity magnitude a) 5 mm valve lift standard turbulence method, b) 5 mm valve lift RNG turbulence method…… 107
Figure 4.18 Velocity vectors colored by velocity magnitude a) 7 mm valve lift standard turbulence method, b) 7 mm valve lift RNG turbulence method…… 108

Figure 4.19 Velocity vectors colored by velocity magnitude a) 9 mm valve lift standard turbulence method, b) 9 mm valve lift RNG turbulence method…… 109
Figure 4.20 Velocity vectors colored by velocity magnitude near valve region for 3mm valve gap a) first model b) second model c) third model d) fourth model……. 110
Figure 4.21 Velocity vectors colored by velocity magnitude near valve region for 5mm valve gap a) first model b) second model c) third model d) fourth model……. 111
Figure 4.22 Velocity vectors colored by velocity magnitude near valve region for 7mm valve gap a) first model b) second model c) third model d) fourth model……. 112
Figure 4.23 Velocity vectors colored by velocity magnitude near valve region for 9mm valve gap a) first model b) second model c) third model d) fourth model……. 113
Figure 4.24 An example of grid independency study……. 115
Figure 4.25 a) Contours of velocity magnitude (m/s) b) contours of turbulence intensity (%) for 3 mm valve gap…….. 118
Figure 4.26 a) Contours of velocity magnitude (m/s) b) contours of turbulence intensity (%) for 5 mm valve gap……... 119
Figure 4.27 a) Contours of velocity magnitude (m/s) b) contours of turbulence intensity (%) for 7 mm valve gap……... 120
Figure 4.28 a) Contours of velocity magnitude (m/s) b) contours of turbulence intensity (%) for 9 mm valve gap……... 121
Figure 4.29 Velocity vectors colored by velocity magnitude (m/s) for measurement points a) 3 mm valve gap b) 5 mm valve gap…… 122
Figure 4.30 Velocity vectors colored by velocity magnitude (m/s) for measurement points a) 7 mm valve gap b) 9 mm valve gap…… 123
Figure 4.31 Velocity magnitude comparison between experimental results and turbulence models for 3 mm valve gap a) z = 27.5 mm b) z = 58 mm c) z = 88.5 mm……..... 125

Figure 4.32 Velocity magnitude comparison between experimental result and turbulence models for 5 mm valve gap a) z = 27.5 mm b) z = 58 mm c) z = 88.5 mm…….. 126
Figure 4.33 Velocity magnitude comparison between experimental result and turbulence models for 7 mm valve gap a) z = 27.5 mm b) z = 58 mm c) z = 88.5 mm…….. 128
Figure 4.34 Velocity magnitude comparison between experimental result 129 and turbulence models for 9 mm valve gap a) z = 27.5 mm b) z = 58 mm c) z = 88.5 mm…….. 129
Figure 4.35 Visualization planes…… 130
Figure 4.36 An example of 3d model with two intake pipes……. 132
Figure 4.37 A view from plane 1 for a) RNG $k-\varepsilon$ turbulence model b) realizable $k-\varepsilon$ turbulence model (valve gap = 5 mm)……. 133
Figure 4.38 A view from plane 2 for a) RNG $k-\varepsilon$ turbulence model b) realizable $k-\varepsilon$ turbulence model (valve gap = 5 mm)……. 134
Figure 4.39 A view from plane 1 for a) RNG $k-\varepsilon$ turbulence model b) realizable $k-\varepsilon$ turbulence model (valve gap = 7 mm)…….. 135
Figure 4.40 A view from plane 2 for a) RNG $k-\varepsilon$ turbulence model b) realizable $k-\varepsilon$ turbulence model (valve gap = 7 mm)…….. 136
Figure 4.41 A view from plane 1 for a) RNG $k-\varepsilon$ turbulence model b) realizable $k-\varepsilon$ turbulence model (valve gap = 9 mm)…….. 137
Figure 4.42 A view from plane 2 for a) RNG $k-\varepsilon$ turbulence model b) realizable $k-\varepsilon$ turbulence model (valve gap = 9 mm)…….. 138
Figure 4.43 Velocity vectors in different CA a) 390° b) 502° c) 570° d) 705° e) 907° f) 930° g) 1020° h) 1080°…… 145
Figure 4.44 a) Contours of Static pressure (Pa) b) Contours of temperature (K) near the TDC position…… 146
Figure 4.45 Convergence history of mass fraction of burned gases on combustion chamber……. 147
Figure 4.46 Convergence history of static pressure on combustion chamber without combustion…….. 147

Figure 4.47 Contours of mass fraction of burned gasses in different CA
a) 367° b) 390° c) 412° d) 457° e) 930° f) 975°g)1042°……. 151

NOMENCLATURE

a	Acceleration (m/s^2)
t	Time (s)
V	Volume (m^3)
u, v, w	Velocity magnitudes in direction x,y,z (m/s)
p	Pressure (Pa)
f	Body force (N)
F	Force vector (N)
e	Internal energy per unit mass (J)
k	Thermal conductivity (W/mK)
q	Heat flux (W/m^2)
T	Temperature (K)

Greek Symbols

α	Thermal diffusivity (m^2 / s)
ρ	Fluid density (kg/m^3)
ϕ	Equivalence ratio (dimensionless)
τ	Stress tensor (Pa)
ε	Turbulent dissipation rate (m^2 / s^3)
μ	Dynamic viscosity (Pa – s)
υ	Kinematic viscosity (m^2 / s)

Abbreviations

2d, 3d	Two, three dimensional
BDC	Bottom Dead Center
CA	Crank Angle
CAD	Computer Aided Drawing
CFD	Computational Fluid Dynamics

CPU	Central Processing Unit
CV	Control Volume
FD	Finite Difference
FE	Finite Element
FV	Finite Volume
GDI	Gasoline direct injection
IC	Internal Combustion
LDA	Laser Doppler Anemometry
LDV	Laser Doppler Velocimetry
LES	Large Eddy Simulation
NSE	Navier-Stokes Equation
PIV	Particle Image Velocimetry
RSM	Reynolds Stress Model
TDC	Top Dead Center

1. INTRODUCTION

The reciprocating internal combustion engine must be by far the most common form of engine or prime mover. As with most engines, the usual aim is to achieve a high work output with a high efficiency; the means to these ends are developed by investigating flow characteristics throughout this thesis.

There are two types of internal combustion engine; one is spark ignition (SI) engines, where the fuel is ignited by a spark, the other is compression ignition (CI) engines, where the rise in temperature and pressure during compression is sufficient to cause spontaneous ignition of the fuel. The spark ignition engine is also referred to as the petrol, gasoline or gas engine from its typical fuels, and the Otto engine, after the inventor. The compression ignition engine is also referred to as the Diesel or oil engine; the fuel is also named after the inventor. During each crankshaft revolution there are two strokes of the piston, and both types of engine can be designed to operate in either four strokes, as it is investigated in this thesis, or two strokes of the piston. The explanation of the four stroke operating cycle is set up in order as follows:

- The induction stroke. The inlet valve is open, and the piston travels down the cylinder, drawing in a charge of air. In the case of a spark ignition engine the fuel is usually pre-mixed with the air.
- The compression stroke. Both valves are closed, and the piston travels up the cylinder. As the piston approaches top dead centre (TDC) ignition occurs. In the case of compression ignition engines, the fuel is injected towards the end of the compression stroke.
- The expansion, power or working stroke. Combustion propagates throughout the charge, raising the pressure and temperature, and forcing the piston down. At the end of the power stroke the exhaust valve opens, and the irreversible expansion of the exhaust gases is termed ‘blow-down’.
- The exhaust stroke. The exhaust valve remains open, and as the piston travels up the cylinder, the remaining gases are expelled. At the end of the exhaust

stroke, when the exhaust valve closes some exhaust gas residuals will be left, these will dilute the next charge.

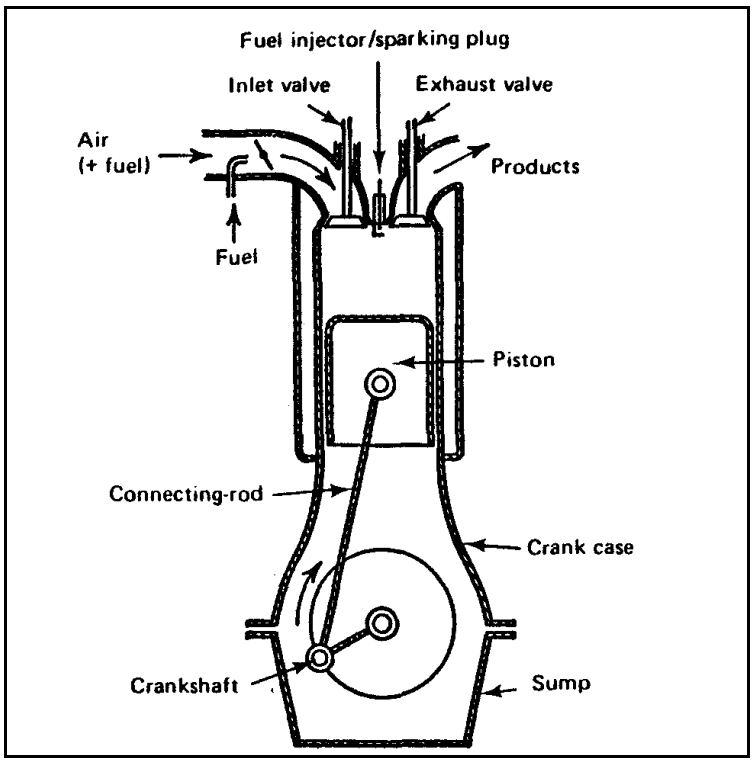


Figure 1.1 A four stroke engine and its members

The four stroke cycle is sometimes summarized as ‘suck, squeeze, bang and blow’. Since the cycle is completed only once every two revolutions the valve gear (and fuel injection equipment) have to be driven by mechanisms operating at half engine speed. Some of the power from the expansion stroke is stored in a flywheel, to provide the energy for the other three strokes.

An analysis of an internal combustion (IC) engine presents some of the most challenging problems faced by engineers in the automotive industry, because simulations need to address the moving parts in an appropriate manner. In this way, computational fluid dynamic (CFD) tools have become essential in aiding in the engine development. They allow the understanding of basic combustion phenomena, flow characteristics and help to optimize various parameters of a pre-existing

combustion system or to design a combustion chamber from scratch. Automotive engines become more and more complex in order to address the conflicting demands based on more stringent emission standards and customer desire for “fun-to-drive” vehicles, such as higher torque and power output. Therefore combustion and flow characteristics are constantly evolving in order to keep CFD in pace with engine innovations.

In this study, a commercial CFD program FLUENT is used. In order to envisage flow domain more in engine model, FLUENT’s moving and deforming grid feature is used. A cold flow analysis is performed for this purpose. Cold flow simulations for IC engines can provide valuable design information to engineers. These simulations allow for the effect on volume efficiency, swirl and tumble characteristics to be predicted based on changes in port and combustion chamber design, valve lift timing, or other parameters.

Flow in engine cylinder produces a complex three-dimensional phenomenon involving turbulence, unsteadiness, etc. Moreover, the geometry is complex and asymmetric due to the cylinder head. Both experimental and numerical approaches have been reported and have contributed to the understanding of the highly complex flow interactions that occur in an engine.

CFD techniques are very useful tools for design and analysis of complex engine geometries. Although most of the current CFD research activities are on steady flows, there is an increasing interest in unsteady flow computations. The equations of fluid dynamics can be solved numerically with the aid of modern computers. The set of techniques and procedures to achieve this has lead to the development of what is known as CFD. Although it is not possible to leave out real experiments, numerical study using CFD allow the determination of certain trends and give an insight into the physics of complex problems that would be impractical to study experimentally.

The present study tries to validate CFD prediction in selected engine geometries. The study has demonstrated that the experimental results obtained by Yasar do not exactly produce good agreement with numerical results in some points. But their reason will be explained in detail in Conclusion section.

2. PREVIOUS STUDIES

It is well known that the reciprocating engines exhibit many complex features and phenomena, perhaps more complex than any other mechanical device.

Although the Internal Combustion Engine has gone through over a century of very ambitious development, the margin for improvement can still be considered as relatively wide. Regulations, economy and emissions target, new technologies, development time and costs reduction and marketing constrains require engineers to develop and propose increasingly sophisticated solutions in order to improve performance even further. To cope with the demands, control over combustion is a key objective, but one that is difficult to attain due to the complexity of the processes involved. Basically, these processes include the flow of air and the fuel into the combustion chamber, mixing of air and fuel, ignition, combustion and thus, formation of exhaust gases. Reduction of engine emissions and fuel consumption can be reached by an improved control over the degree of homogeneity of the air-fuel mixture, cycle-to-cycle variation, and turbulence intensity as well as large-scale motion (Zellat, 2002).

Spark ignition (SI) engine cycles consist of four consecutive processes: intake, compression, combustion (including expansion) and exhaust. Of these processes, the combustion process is the most important process because the chemical energy of the fuel is converted into sensible internal energy of the charge during this process. Furthermore, the details of the flame propagation process influence the efficiency of energy conversion and engine performance, as well as pollutant formation. Because of the above mentioned reasons, a significant part of the research studies conducted on spark ignition engines has been devoted to simulating the combustion process. In the combustion modeling studies, the main purpose is to specify the mass fraction of burned gases at any time during the combustion process (Bayraktar and Durgun, 2004).

As Chiavola (2002) indicated in his study, Experimental and computational techniques have been developed aimed at providing a better understanding of the complex phenomena occurring inside intake and exhaust systems in order to

analyze and compare various configurations and operating points. A variety of modeling procedures has been proposed in the literature and is currently applied to predict the propagation of fluid flow along intake and exhaust systems.

As a computational technique in engine design field, Computational Fluid Dynamics (CFD) is an indispensable tool for engine development nowadays. For more application of CFD in the development, a reduction of simulation time and more detailed simulation method for unsteady turbulence flow analysis are required. In computational methods, Fast mesh generation is an effective method for reduction of simulation time because mesh generation currently takes a long time (Sukegawa et al., 2003).

Hong et al. (1998) studied computational analysis of turbulence and it was found that the evolution of the detailed process has to be carefully studied in order to enhance the controllability of the flow field. The in-cylinder fluid motion is so complex that it is of non-stationary turbulence and is subject to flow re-circulation as well as boundary layer separation. Both modern techniques of numerical simulation and laser diagnostics can be employed to investigate the in-cylinder flow field. However, poor computational fluid dynamics (CFD) predictions may be resulted due to lack of suitable in-cylinder turbulence models. From the viewpoint of the fundamental turbulence physics, the major two parameters which are required to represent the turbulent flow characteristics are the turbulence kinetic energy, k, and its dissipation rate, ε. The former is related to the turbulence intensity, which is a measure of the characteristic speed of the turbulent flow over a characteristic distance. The turbulence dissipation rate is related to the turbulence kinetic energy and the turbulence length scale. The length scale is a quantitative measure of the distance characteristic of the flow structure.

As Heywood (1998) mentioned in his book, turbulence at the end of the compression stroke has to be enhanced by the breakdown of large scale structures retained through the induction and compression strokes, or by the squish motion occurring near TDC of compression in certain combustion chamber geometries. However, in four-valve engines squish is very weak and its effect as a turbulence promoter is limited as well as localized around the squish lip.

For piston engine flows, the valves trajectories are prescribed and the velocity on these trajectories is a function of the piston position. All these mechanical displacements control the flow characteristics at the combustion ignition and have crucial effects on the engine performances (Mantel, 1992).

Since CFD calculation has a big key factor while designing flow motion in engines, another important key must be its visualization. No matter which type of CFD solver is used, the crucial thing is whether solver has a good visualization tool to find out how flow acts in engine cylinders.

As it is mentioned by Laramee et al. (2004), Visualization is an important part of exploring, analyzing, and presenting the results of a CFD simulation. As the size of CFD simulation data sets increases, the utility of scientific visualization for gaining insight into the data sets also increases. Visualization offers one way to manage such large collections of simulation data since it brings the data to a higher level of abstraction. Simply reading the raw data does not meet all of the demands set forth by the user and may not even be feasible. Furthermore, no single visualization solution can span the range of each engineer's needs. Hence a range of solutions must be at the user's disposal.

For many of the automotive components that undergo evaluation, there is an ideal pattern of flow engineers try to create. Figure 2.1, left illustrates the swirl motion of fluid flow in a combustion chamber from a diesel engine. In order to generate swirl motion, fluid enters the combustion chamber from the intake ports. Later on in the engine cycle, the kinetic energy associated with this swirl motion is used to generate turbulence for mixing of fresh oxygen into the fluid. The more turbulence generated, the better the mixture of air and diesel fuel, and thus the better the combustion itself. Ideally, enough turbulent mixing is generated such that 100% of the fuel is burned.

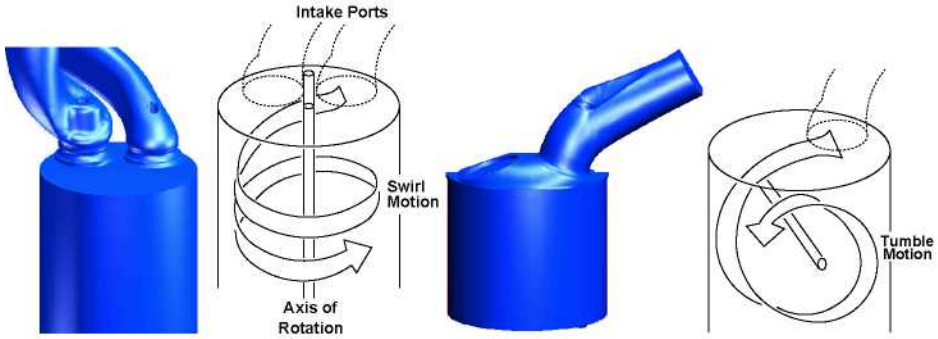


Figure 2.1 The Swirl and Tumble motion of flow in combustion chamber

In the flow within a cylinder, it can be distinguished between two types of motion: swirl flow commonly found in diesel engines and tumble flow commonly found in gas engines. In both cases, rotational motion occurs about an axis, though the position of the respective axis is different. In the case of swirl flow, the axis is more or less coincident with the cylinder axis, as shown in Figure 2.1, left. In the case of tumble (Figure 2.1, right), the rotation axis is perpendicular to the cylinder axis and more complex, thus making tumble flow more difficult to control than swirl flow. The swirl or tumble motion should be maximized to maximize turbulence. From the point of view of the mechanical engineers designing the intake ports, the ideal flow pattern leads to beneficial conditions.

Some authors investigated effect of combustion chamber shape on tumble flow and squish generated flow. Fujimoto et al. (2002) clarified the tumble and squish-generated flow velocity distributions in the case with the squish area located at the intake valve and the exhaust valve side by using PIV method. They used four-valve spark ignition engine with a pent roof type combustion chamber in their experiment.

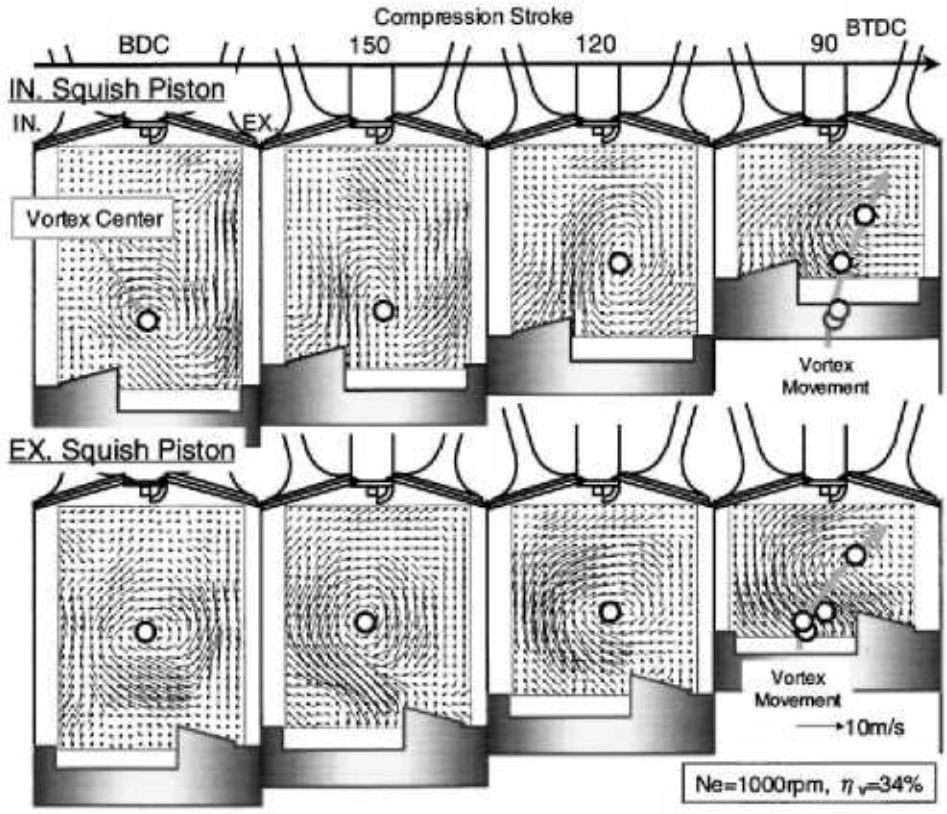


Figure 2.2 Effect of squish area location on tumble flow formation (Fujimoto, 2002).

Figure 2.2 shows the velocity vector maps of in-cylinder tumble flow formation for the intake squish piston and the exhaust squish piston by Fujimoto et al. (2002). When the case on the intake squish piston is seen, it is understood that the main intake flow was impinged in the edge part of the squish area at BDC, and was raised toward the cylinder head. As a result, the tumble flow was formed compactly outside the squish area as the piston compression advanced. When the case of the exhaust squish piston is seen, the main intake flow rose along with the squish area toward the cylinder head of the intake valve side, and circulated to the squish area again. Thus, the tumble flow was formed. As the piston compression advanced, the tumble flow, which has circulated through the pent roof, was not able to keep a vortex shape since the squish area moves to the upper side of the cylinder.

In study of Chan and Turner (2000), a three-component LDA system has been employed to investigate the structure of the flow inside the cylinder of a motored internal combustion engine. The engine was equipped with overhead valve gear and optical access was provided in the top and side walls of the cylinder. A principal objective was to study the influence of the inlet port design on the flow within the cylinder during the induction and compression strokes of the engine. Experimental data presented for an inclined inlet port configuration reveal the complex three-dimensional nature of the flow inside the model engine cylinder. Not surprisingly, the results also show that the inclined inlet port created flow conditions more favorable to mixing in the cylinder. Specifically, the inclined inlet flow was found to generate a region with a relatively high shear and strong recirculation zones in the cylinder. Inclining the inlet port also produced a more nearly homogeneous flow structure at top dead centre during the compression stroke.

In a similar study, Huang et al. (2005) diagnosed the evolution processes of the in-cylinder flows in the axial and diametric planes of a motored two-valve, single-cylinder, and four-stroke engine during the intake and compression strokes by using PIV method. In this study, a device, which is called the “inlet deflection-valve”, being capable of deflecting the inlet flow is installed upstream of the inlet port. The engine cylinder, piston, and accessories are modified to meet the requirements of laser-light sheet shooting and camera viewing when the PIV is applied. Figure 2.3 shows valve lift profiles that was used for this study.

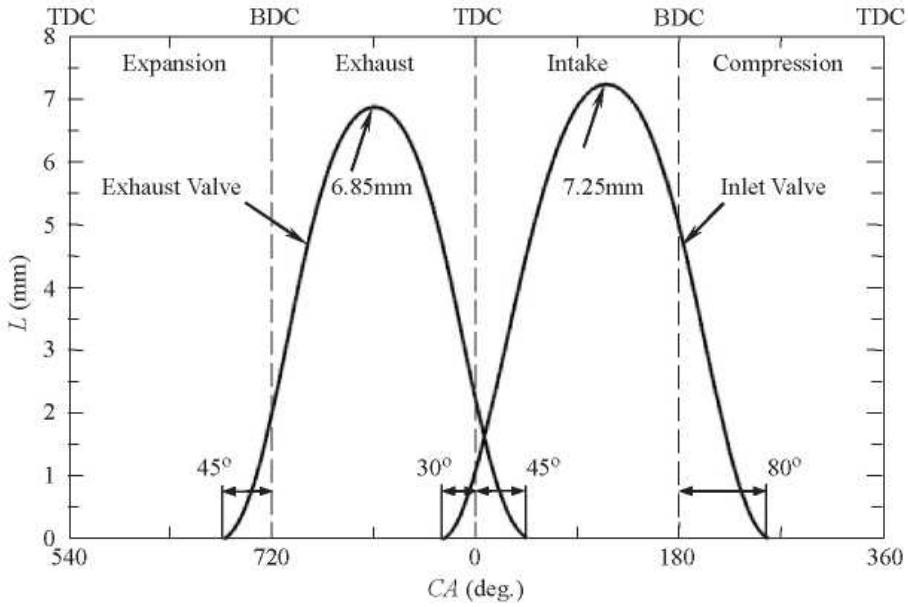


Figure 2.3 Valve lift profiles of inlet and exhaust valves (Huang et al., 2005).

As a result of this study, Huang et al. (2005) found velocity values from their experiment as it is shown in Figure 2.4.

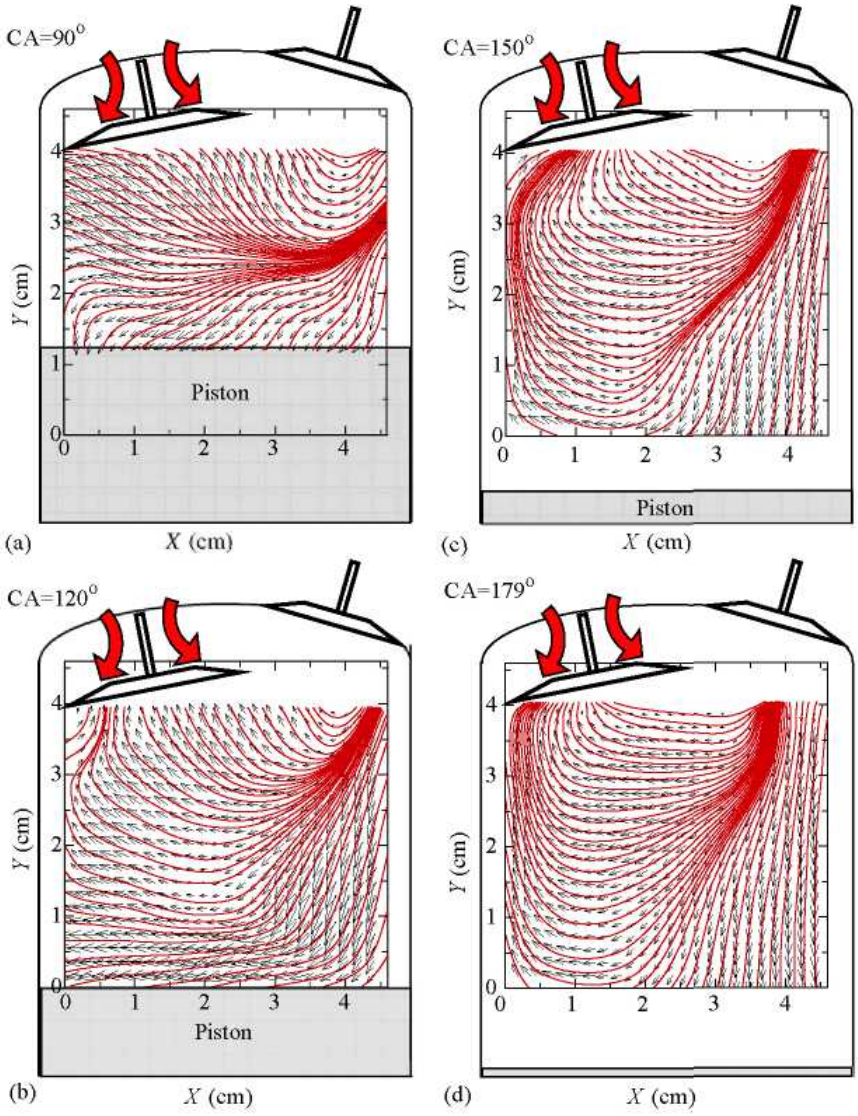


Figure 2.4 Evolution of tumble flow motions during intake stroke in symmetry axial plane. Engine speed N = 1500 rpm. Velocity data are ensemble-averaged from 100 instantaneous measurements (Huang et al., 2005).

There have been some experimental studies for cycle-resolved 2d flow measurement and flow visualization within spark ignition engine cylinders. Reeves et al. (1999) was one of them. In this study, authors describe a turnkey, high-speed digital imaging system that provides combined real-time flow visualization and rapidly processed PIV data in an industrial optical research engine facility. The system is based on commercially available, high-speed imaging and laser technology and conventional digital cross-correlation processing to provide cycle-

resolved PIV data and flow visualization within timescales appropriate for engine development. As a result of this study the PIV vector maps show that the flow is not a simple solid body rotation. Large spatial variations in the in-plane velocity indicate either a significant deviation from whole-body rotation or a significant out-of-plane velocity structure.

Kang and Baek (1998) investigated turbulence characteristics of the tumble flow in a four-valve engine by using LDV method and analyzed by means of turbulence intensity, integral time and length scales, and energy spectrum. The integral time scales obtained by three kinds of different definitions and their characteristics were compared. The results show that tumble causes turbulence intensity to increase considerably during the compression stroke and its distribution to be homogeneous. The effect of tumble on integral time scale is negligible, while the integral length scale increases by tumble.

Besides some experimental studies that have been mentioned so far, there have been numerous computational studies about in-cylinder flow. Since CFD is a most challenging area in computational studies, too many commercial programs, such as KIVA, FLUENT, have been used to approach real situation in models considered. In order to visualize real engine situation, there have been some computational models have been used, for instance k-ε, LES; RSM are most popular turbulence models to have accurate results in engine simulations. After presenting some experimental studies, following paragraphs will be mostly interested in computational studies.

Moureau and Angelberger (2004) used LES method and 3d CFD code AVBP to predict cyclic variability in IC engines. In a first step, the implementation of an arbitrary Lagrangian Eulerian (ALE) method into AVBP is described, allowing moving solid boundaries. Then the principles and implementation of the Conditioned Temporal Interpolation (CTI) mesh management technique is described, and some specific adaptations for LES simulations are discussed. The turbulent LES models of AVBP are a classical Smagorinsky, a filtered Smagorinsky and a Wall Adapting Linear Eddy (WALE) model. The Smagorinsky model has been heavily tested and used in LES simulations. It is known to correctly

predict the global turbulent quantities but also to over-dissipate when used for transient flows. The filtered Smagorinsky model is similar to the Smagorinsky model but the velocity field is explicitly filtered with a higher-filter width before the evaluation of the turbulent viscosity. It has been developed to better represent the local phenomena of the flow. Finally, the WALE model, also based on the Smagorinsky model, is used for wall-bounded flows attempting to recover the scaling laws of the wall.

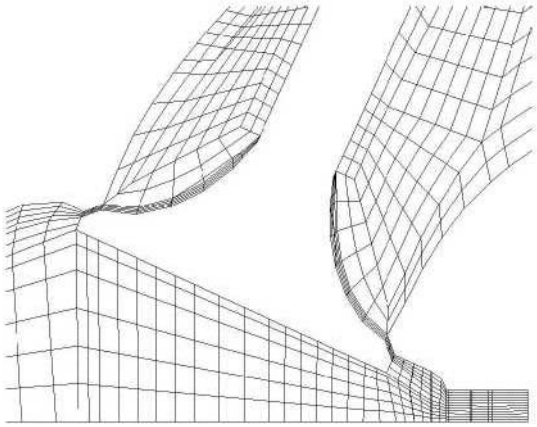


Figure 2.5 Dynamic grid system just before valve is opened (Moureau and Angelberger, 2004).

Another LES application is presented by Wu and Perng (2002). They investigated the turbulent flow field and wall heat transfer during the compression-expansion strokes in two types of engine configuration under realistic engine conditions. In this study, the SIMPLE-C method and LES are employed in investigating the fluid flow and wall heat transfer in internal combustion engines. Second-order backward Euler (SBE) method is implemented for discretizing the transient term to remove stability restrictions and extended linear upwind differencing (ELUD) method (third-order scheme) for discretizing the convection terms to avoid severe oscillations. As the initial conditions, the calculations are started at a crank angle of 260° (100° BTDC (before top dead center)) in the compression stroke and terminated at 420° (60° ATDC (after top

dead center)) in the expansion stroke for the engine speed of 1500 rpm. Predictions were compared with experimental measurements (including the local heat flux and swirl velocity), and with those calculated from the conventional *k*-ε model. The results of the Van Driest wall damping model for LES were found to be in the best agreement with experimental data.

Zheng et al. (2005) studied combustion process and fluid flow in a compression ignition natural gas engine with separated chamber by coupling Multi-dimensional CFD code FIRE with detailed chemical kinetic mechanism. The calculated data are first validated by experimental data. Subsequently, multidimensional simulations at a baseline condition are carried out to investigate combustion process, fluid flow, mixture formation and NO emission distribution in the chamber. As computational grid, 60,888 grids at BDC and 42,753 grids at TDC are used. The calculations are carried out on a HP XW6000 workstation and cost about 170 h of CPU time on average for each case. At the end of the study, the results show that calculated data are in good agreement with the experimental data.

Yang et al. (2005) presented a study on the use of the RSM and KIVA CFD code for engine flow simulation. They investigated a simplified direct injection stratified charged (DISC) IC engine and a four-valve double overhead camshaft (DOHC) IC engine. The DISC engine chamber and its grid structure are shown in Figure 2.6.

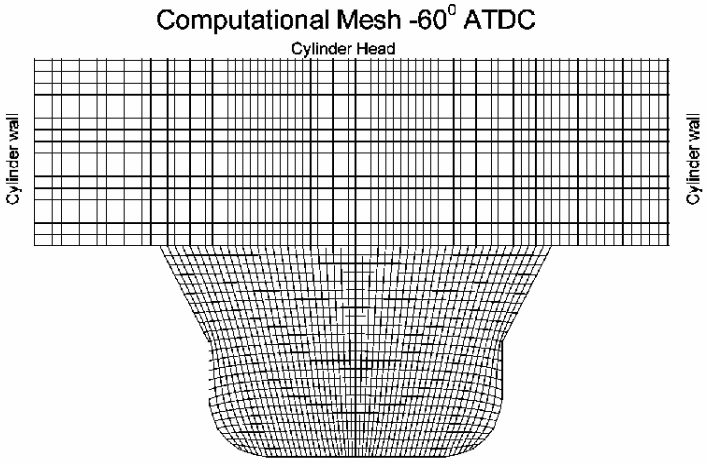


Figure 2.6 Computational grid of DISC engine (Yang et al., 2005)

There are drastic differences between RSM and k-ε model results can be observed from the Figure 2.7. Moreover, the magnitude of the eddy viscosity is over predicted by the k-ε model, which is expected since the model typically over predicts μ_t. Figure 2.7 shows the k-ε and RSM flow and temperature field results at —30° ATDC, shortly before ignition.

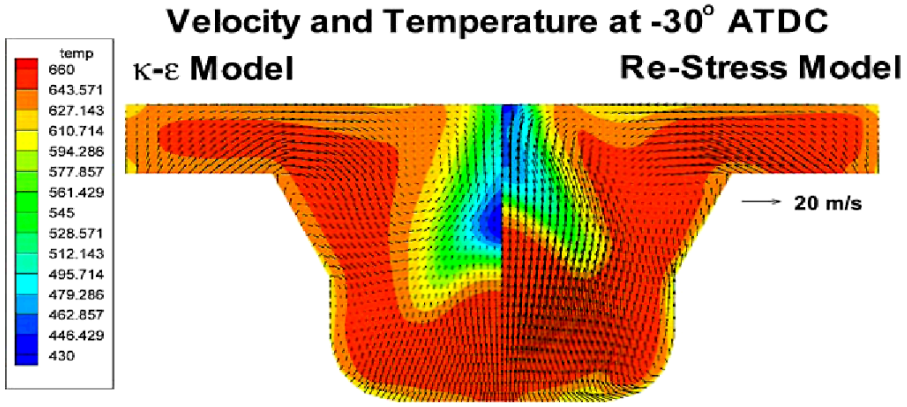


Figure 2.7 Velocity vector and temperature at -30° after TDC (Yang et al., 2005)

As it is mentioned, second study of Yang et al. (2005) is a four-valve double overhead camshaft (DOHC) IC engine. In this study, standard k-ε model and RSM without the wall-reflection term are used to obtain how velocity vectors act inside of cylinders by using KIVA code. The engine under consideration is 1200 c.c. with four cylinders and group port injection. Each cylinder has two intake and two exhaust valves and are canted at ±10°. The engine has a compression ratio of 9.5, a 7.45 cm cylinder diameter, 6.87 cm stroke, 11.27 cm connecting rod length, and operates at 1500 rpm. Figure 2.8 shows the geometry and computational mesh of the DOHC engine. The valve lift history is given in Figure 2.9.

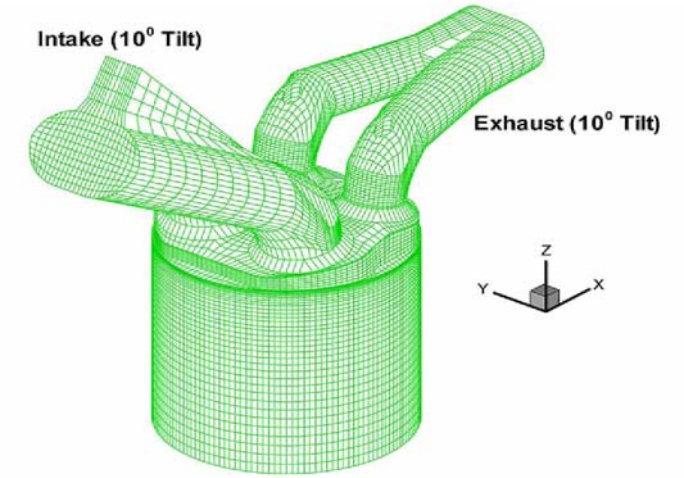


Figure 2.8 Four valve DOHC computational model (Yang et al., 2005)

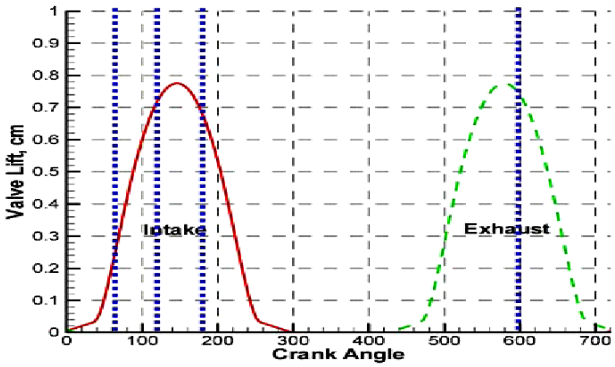


Figure 2.9 Valve lift history (Yang et al., 2005)

Figure 2.10 shows the velocity vectors at different crank angles during intake and exhaust strokes. At the beginning of the intake, high-velocity air is drawn in through the intake valve and produces vortices below it, Figure 2.10 a. Both models show similar flow patterns at this crank angle. At CA = 120°, just past the maximum lift (see Figure 2.9), visible flow differences can be seen in Figure 2.10 b. Two vortices, one underneath the intake valve and the other near the bottom of the piston surface, are clearly shown in the RSM model prediction. Toward the end of the intake process, at CA = 180° (Figure 2.10 c), the vortex structures predicted by these two models are quite different, although the general flow patterns are somewhat similar.

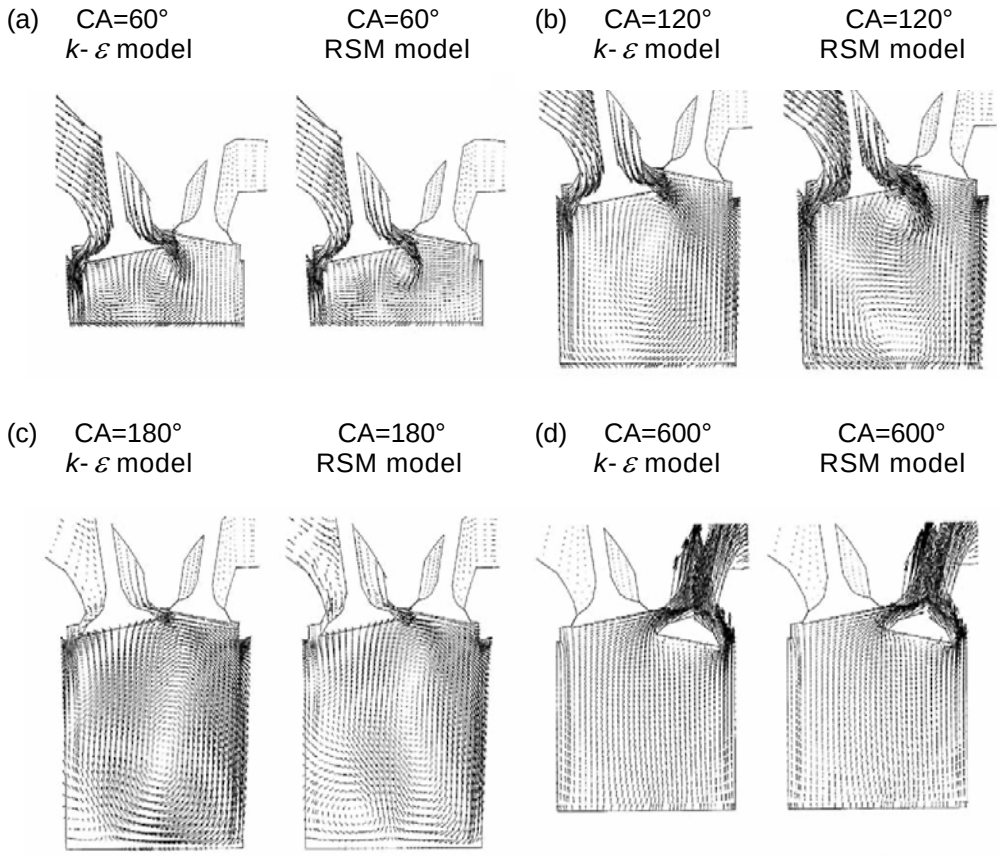


Figure 2.10 Velocity vector at CA = 60°, 120°, 180, and 600° (Yang et al., 2005)

Another numerical model was performed by Kim et al. (1999). In their study, detailed in-cylinder air motion during the induction and compression strokes was simulated to understand the interaction of air motion with high-pressure fuel spray injected directly into the cylinder using KIVA-3V code. In order to study the effects of in-cylinder air motion two aspects were analyzed in details; the full computations from induction to compression were done for both a flat piston and a bowled piston. A solid-body swirl flow assumption was also analyzed by solving only the compression stroke. A single cylinder GDI engine based on a 4-valve pent-roof type combustion chamber was used in this study. Figure 2.11 shows this engine model.

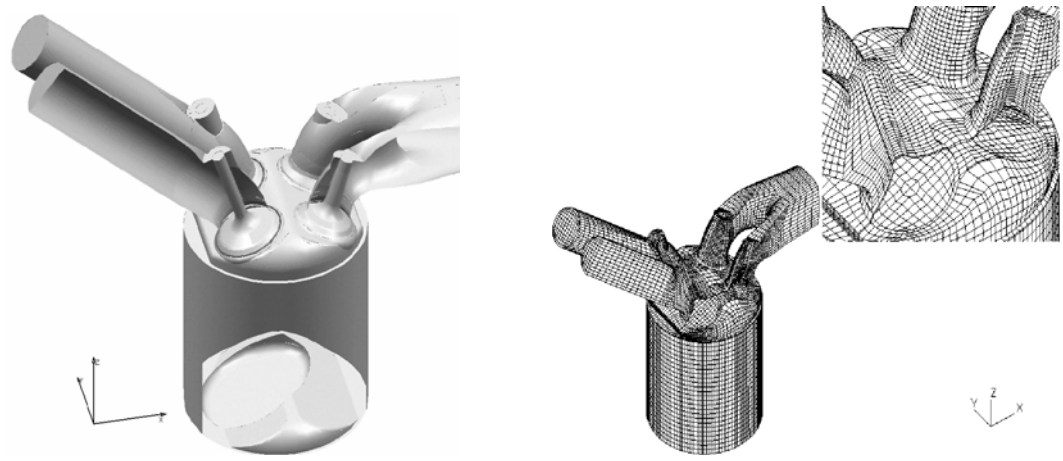


Figure 2.11 GDI engine model and its computational grid (Kim et al., 1999)

A grid generation program, ICEM CFD-HEXA was used to generate a block structured hexahedron grid and to set up boundary conditions for moving valves. Total number of computational cells was about 67,000 with a typical cell size of 2.2x2.2x3.0 mm^3. Typical CPU time taken for the simulation of complete induction and compression strokes was about 37 hours on an IBM RS 6000/590 workstation.

In-cylinder air motion before fuel injection has a decisive role over an appropriate formation of air-fuel mixture, which finally affects on combustion in a GDI engine. In the following some details of in-cylinder air motion without fuel injection are described for a swirl flow driven stratification.

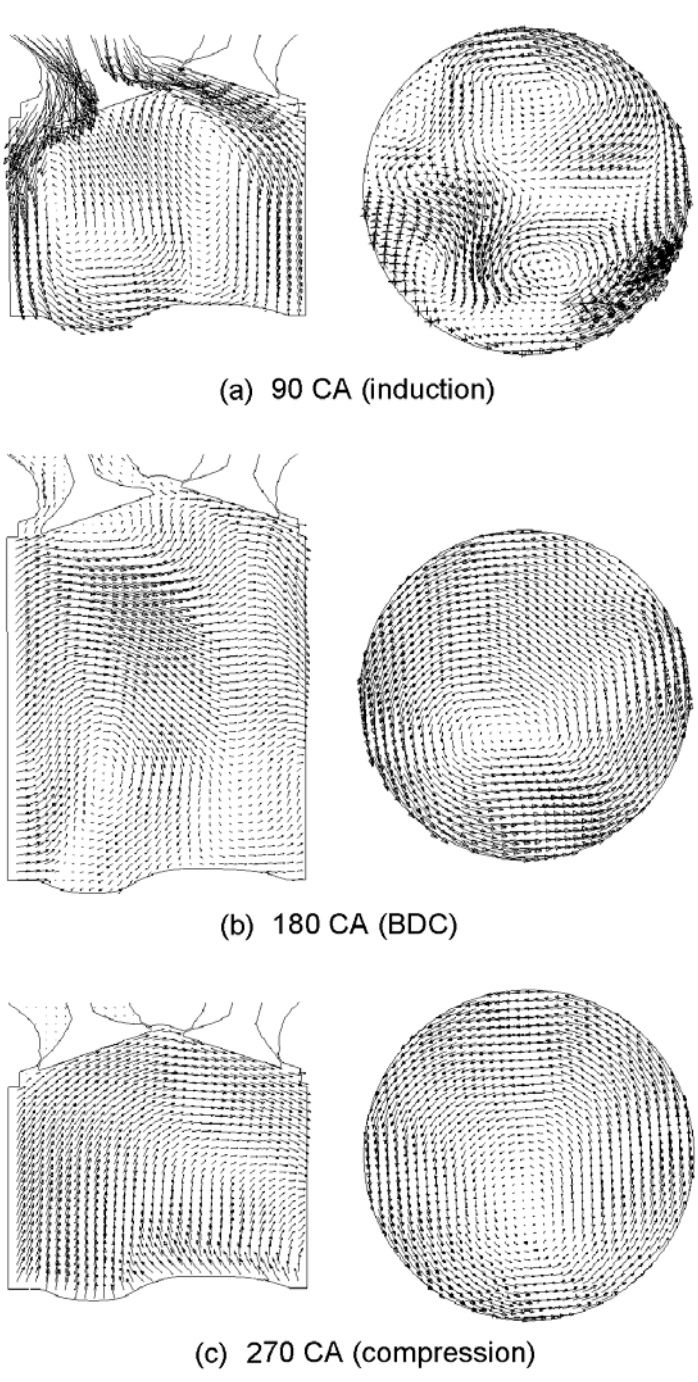


Figure 2.12 Computed velocity fields (Kim et al., 1999)

Figure 2.12 shows the velocity fields at three CA's through the induction and compression strokes. As shown in the induction stroke there is a strong annular jet

flow through the valve curtain area as flow velocity in this crank angle reaches near the maximum value. And this strong flow makes a counter-clockwise swirl which is shown in the lower part of xy plane of Figure 2.12 (a). As the piston moves down to the BDC, the in-cylinder air motion is developing into a large-scale inclined tumble motion while the swirl ratio reaches its maximum value and maintains the level thereafter. From Figure 2.12 (c) it is shown that the swirl center and the swirl strength are not changed much from the BDC, and the normal tumble motion also shows well defined. It was also studied to show comparison of flow structures between the flat piston and the bowled piston. Figure 2.13 shows this comparison:

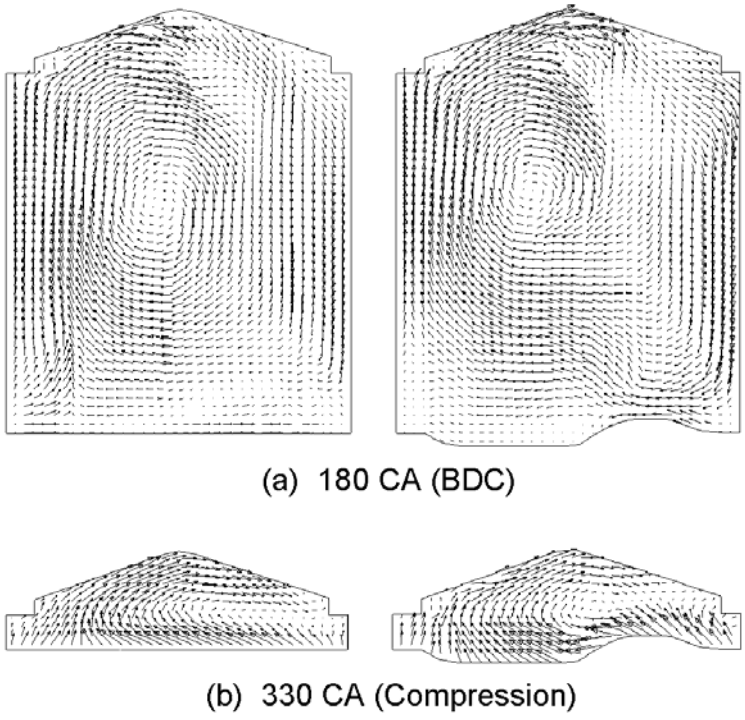


Figure 2.13 Computed velocity fields on the xz cutting plane at y=0 mm (Kim et al., 1999)

Another three-dimensional flow calculation of the intake and compression stroke of a four-valve direct-injection Diesel engine has been carried out with different combustion chambers by Payri et al. (2004). The calculated flow field in three different combustion chambers (shown in Figure 2.14) was compared

with laser Doppler velocimetry measurements; the comparison shows that the three-dimensional model is reasonably accurate for crank-angles around TDC.

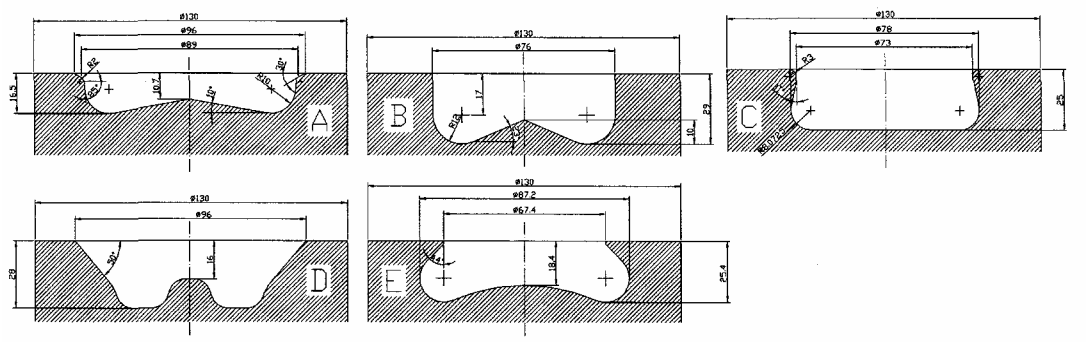


Figure 2.14 Geometry of combustion chambers (Payri et al., 2004)

A finite volume commercial flow program has been used to solve the discretized Navier-Stokes equations in this study. The standard k-ε turbulence model for high Reynolds numbers with wall function is used for closure. The program is based on the pressure-correction method and uses the PISO algorithm. The first order upwind differencing scheme is used for the momentum, energy and turbulence equations. The temporal discretization is implicit, with variable time step depending on the stage of the cycle. At the beginning and at the end of the intake stroke, when the valve lift is small, there are high local velocities in the discharge zone. Hence, the time step must be small enough (0.1 crank angle degree per iteration) to comply with the stability criterion. During the middle phase of the intake stroke and during the compression stroke, before the piston arrives at TDC, the time step may be doubled since there are no high local velocities and the effect of the squish during compression is not important yet. Finally, near TDC, the time step must be reduced again because of the effect of squish and the small clearance between the piston and the cylinder head. Computational grid structure and the location of measurement points are shown in Figure 2.15 and 2.16 respectively.

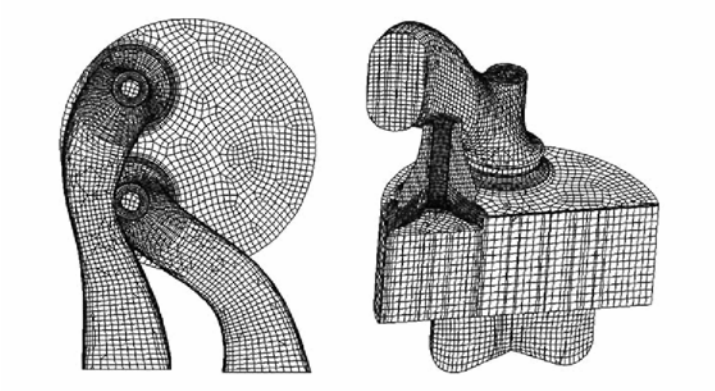


Figure 2.15 Computational domain (Payri et al., 2004)

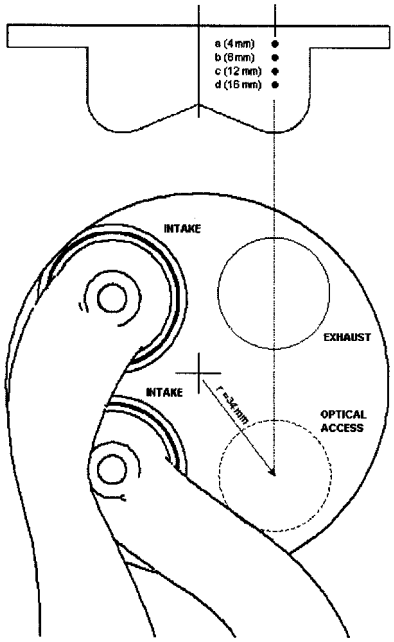


Figure 2.16 Sketch of the cylinder head with the location of the measurement points (Payri et al., 2004)

In order to confirm that the solution was grid-independent, the number of cells in the combustion chamber was doubled in each direction. In addition, a structured grid topology was also tried, in both cases, the calculations yielded very similar results to those observed with the initial mesh.

In conclusion, it has been experimentally verified that the turbulence assumption of the standard k-ε model is reasonably accurate for calculations of the in-cylinder flow, particularly in quiescent combustion chambers where there is no strong interaction between swirl and squish and, more generally, in zones of the cylinder where the radial flow does not dominate the flow pattern (Payri et al., 2004).

Some computed velocity fields results can be seen following figures.

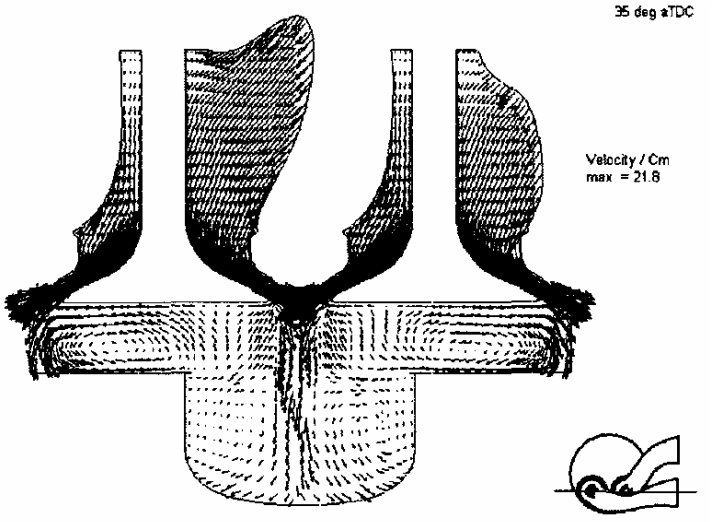


Figure 2.17 Velocity fields in axial mid-section at 35 CA after TDC (Payri et al., 2004)

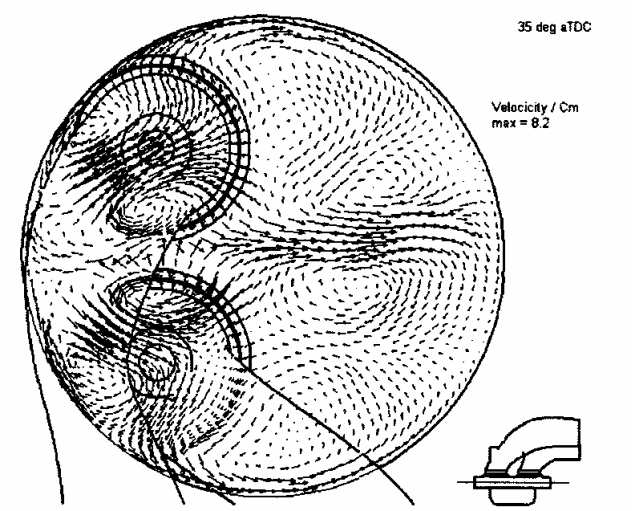


Figure 2.18 Velocity field in cross section located at 10 mm from cylinder head at 35 CA after TDC (Payri et al., 2004)

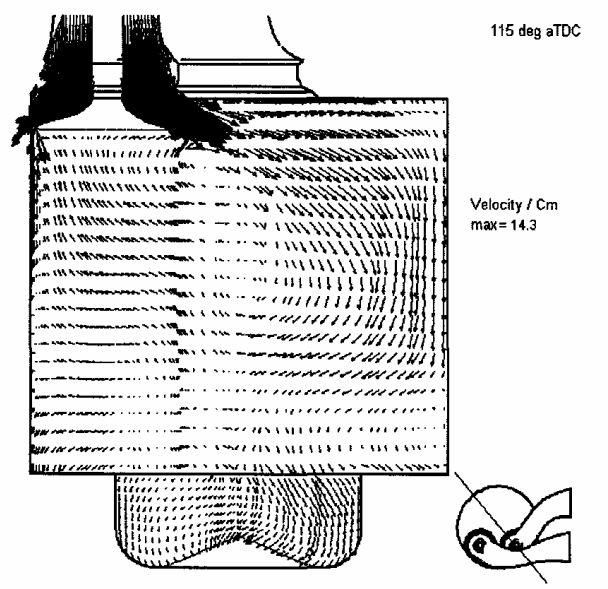


Figure 2.19 Velocity field at 115 CA after TDC (Payri et al., 2004)

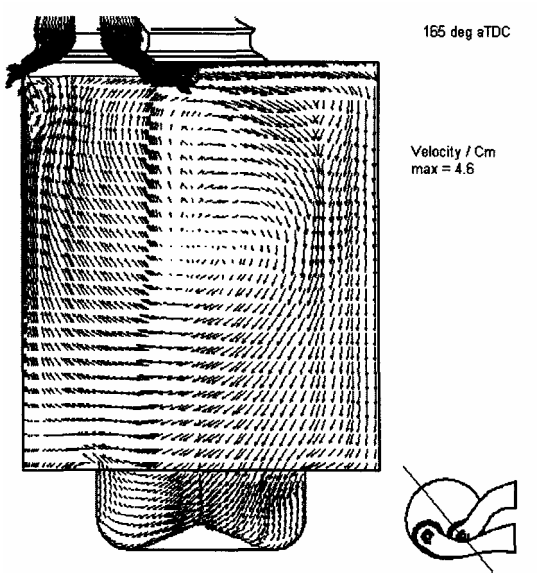


Figure 2.20 Velocity field at 165 CA after TDC (Payri et al., 2004)

The results confirmed that the piston geometry had little influence on the in-cylinder flow during the intake stroke and the first part of the compression stroke. However, the bowl shape plays a significant role near TDC and in the early stage of the expansion stroke by controlling both the ensemble-averaged mean and the turbulence velocity fields.

Johan et al. (2001) presented a numerical strategy based on the finite element method for solving unsteady flows without combustion inside an operating engine cylinder. A compressible flow solver that can withstand highly distorted elements is presented. A robust mesh deformation procedure capable of handling the large valve and piston motions and deforming the unstructured mesh accordingly is then described. Turbulence is added through a one-equation model. The proposed strategy is applied to a three-dimensional realistic problem. Results are presented for the exhaust, intake and compression strokes of the cylinder operation. The following figures represent some of the dynamic grid structures which were made in this study:

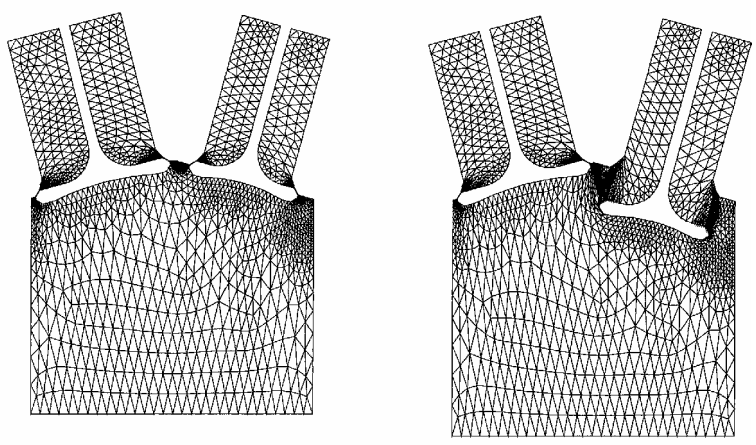


Figure 2.21 2d cylinder model with valves and piston positions corresponding to two different crank angles (Johan et al., 2001)

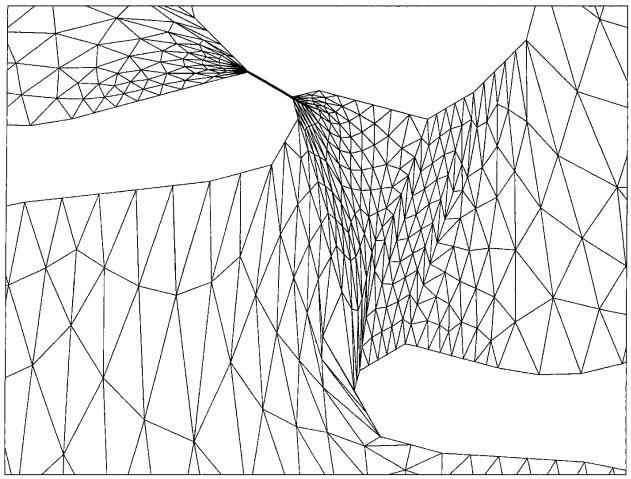


Figure 2.22 Close-up of the grid in the valve region (Johan et al., 2001)

The computation is performed using an implicit time-marching procedure. At each time step, several solves are done. Firstly, it is solved the grid deformation problem based on the displacements of the grid boundaries and update the node coordinates and velocities. Secondly, it is solved the fluid flow problem using the grid velocities computed at previous step and using the turbulent quantities obtained at previous time step and finally, it is solved the turbulence equations using the grid and flow quantities obtained previous steps.

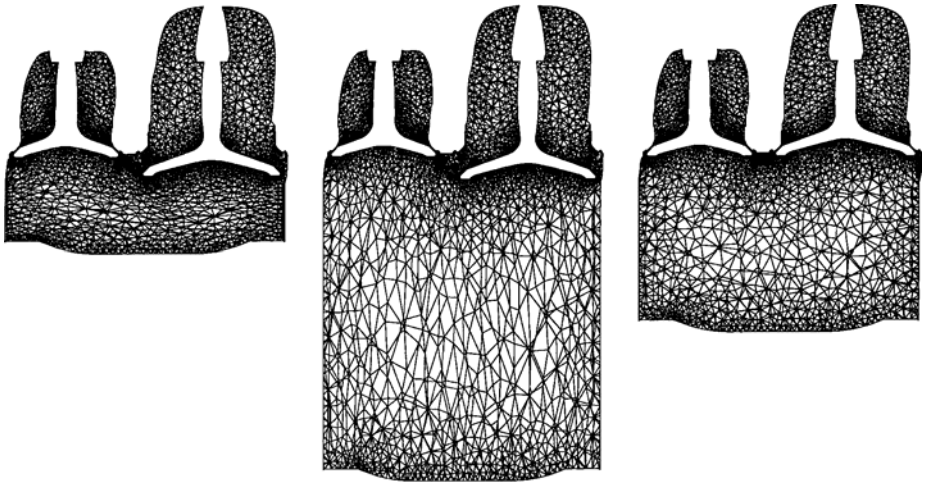


Figure 2.23 Views of grid deformation during the intake-compression strokes (Johan et al., 2001)

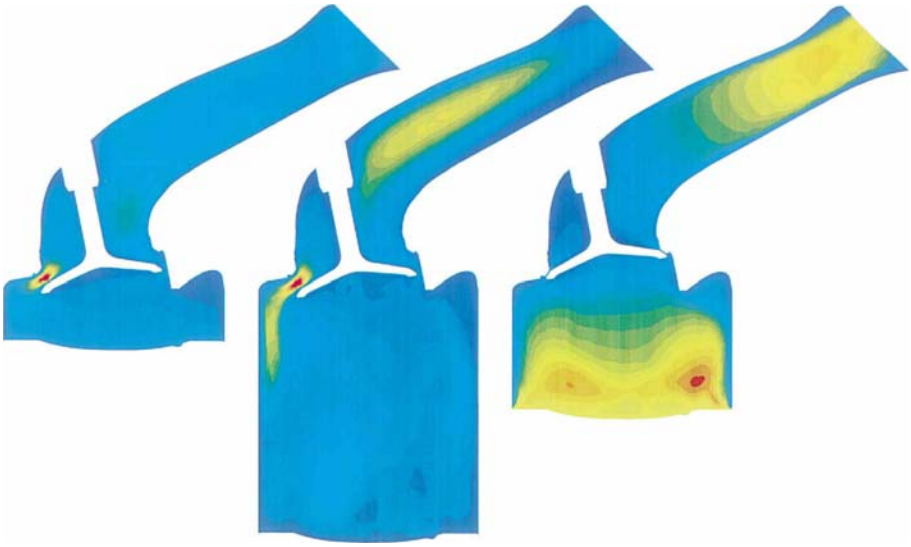


Figure 2.24 Views of velocity magnitude contours in the intake valve plane during the intake-compression strokes (Johan et al., 2001)



Figure 2.25 Views of velocity magnitude contours in the exhaust valve plane during the exhaust stroke (Johan et al., 2001)

Fang and Majdalani (2003) investigated the numerical simulation of an innovative, cold-wall bidirectional vortex combustion chamber. They used FLUENT CFD software program in their study. As turbulence scheme, k-ε and RSM model were used. It was seen that on average, the RSM requires 50-to-60% more CPU time per iteration and 15-to-20% more memory when compared to the k-ε turbulence model.

Another FLUENT application was performed by Milton et al. (2001). They studied the two-phase fuel/air flow through an internal combustion engine inlet valve experimentally first and then they compared results with numerical results for only air flow. As it is known the mixing of the fuel and air in spark ignition engines is a critical factor in obtaining good performance together with low emission levels. In this study, the flows are two-phase, separated, multi-component, unsteady and turbulent. Hence, they are highly complex.

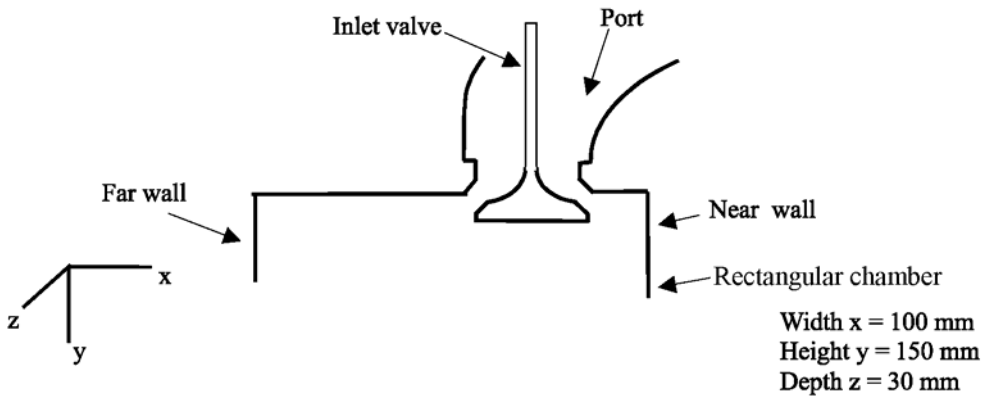
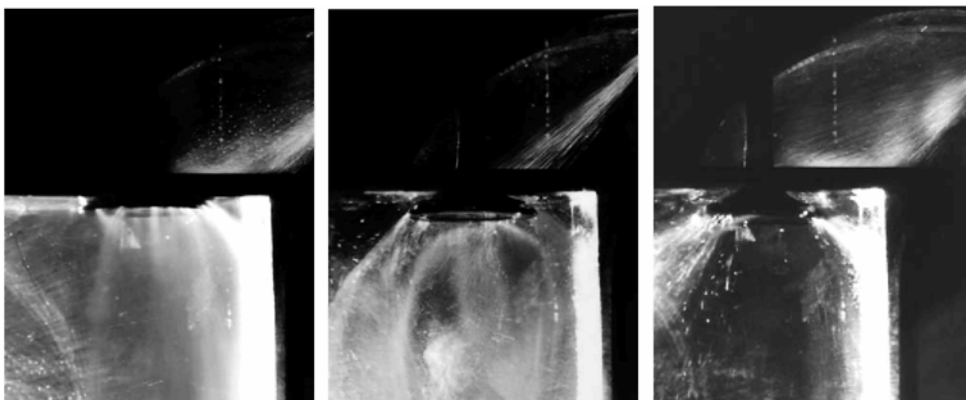


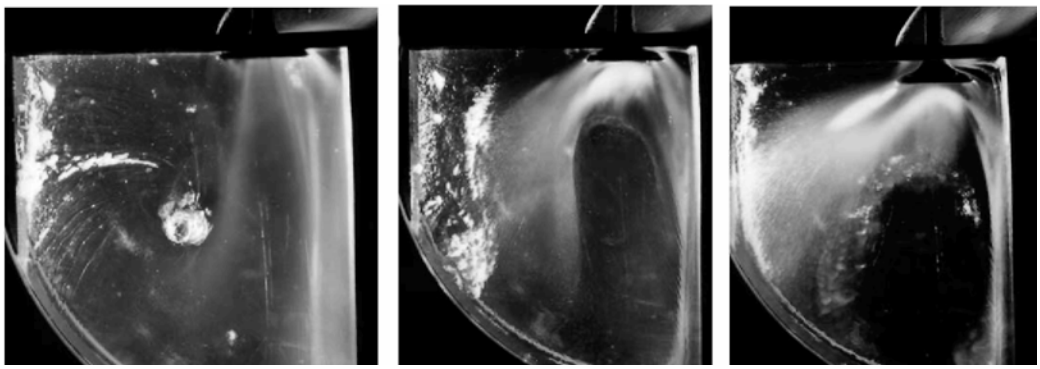
Figure 2.26 Schematic of geometry section (Milton et al., 2001)

Some of the experimental results can be seen as follows:



a) **b)** **c)**

Figure 2.27 Fuel flow through the inlet valve at different valve openings: (a) valve lift = 1 mm, $V_{man.\ air}$ = 10.5 m/s, $V_{valve\ air}$ = 120 m/s; (b) valve lift = 2.5 mm, $V_{man.\ air}$ = 17.5 m/s, $V_{valve\ air}$ = 80 m/s; (c) valve lift = 4 mm, $V_{man.\ air}$ = 18.5 m/s, $V_{valve\ air}$ = 53 m/s. (Milton et al., 2001)



a) **b)** **c)**

Figure 2.28 Fuel distribution below the inlet valve at different valve openings: (a) valve lift = 1 mm, $V_{man.\ air}$ = 10.5 m/s, $V_{valve\ air}$ = 120 m/s; (b) valve lift = 2.5 mm, $V_{man.\ air}$ = 17.5 m/s, $V_{valve\ air}$ = 80 m/s; (c) valve lift = 4 mm, $V_{man.\ air}$ = 18.5 m/s, $V_{valve\ air}$ = 53 m/s. (Milton et al., 2001)

In numerical part, only the base airflow has been considered. Typical simulation results are shown in Figure 2.29. The simulation depicts a flow that is well in accordance with the experimental results. Figure 2.29 shows the velocity contours (total velocity magnitude) for the flow around the valve. At a small valve opening of 1.75 mm (Figure 2.29 (a)) where the manifold velocity is 10 m/s, the jet reaches a high local (maximum) velocity of around 111 m/s through the valve gap. At a larger valve opening of 4 mm (Figure 2.29 (b)), the manifold velocity is higher at 19 m/s but the maximum local value within the valve gap reduces to 91 m/s.

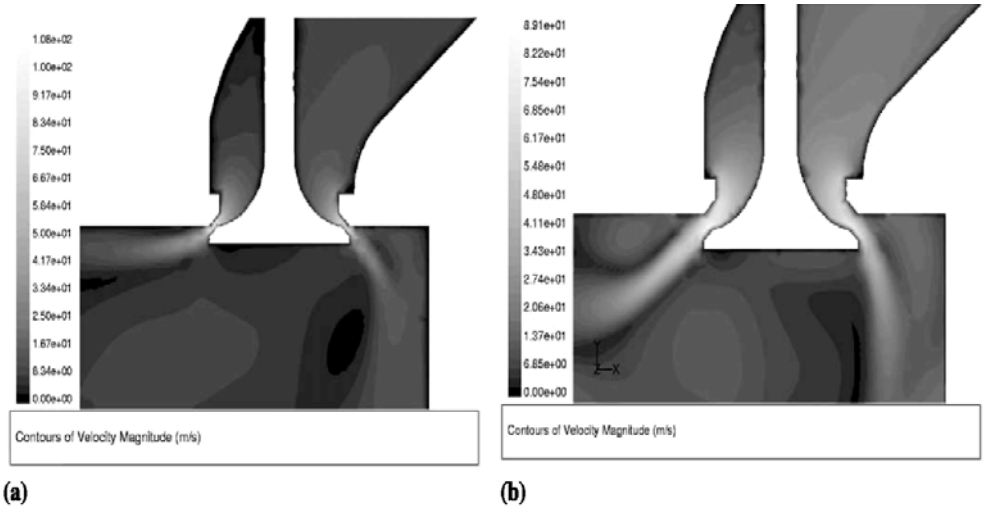
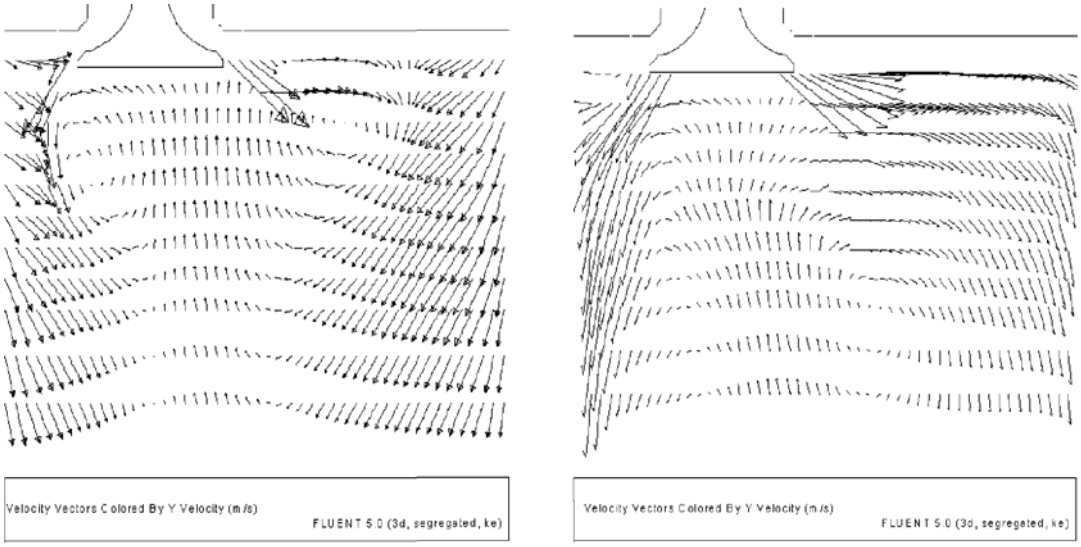


Figure 2.29 Air flow through the inlet valve at different valve openings: (a) valve lift = 1.75 mm, $V_{man.\ air}$ = 10.0 m/s, $V_{valve\ air}$ = 111 m/s; (b) valve lift = 4 mm, $V_{man.\ air}$ = 18.9 m/s, $V_{valve\ air}$ = 91 m/s. (Milton et al., 2001)

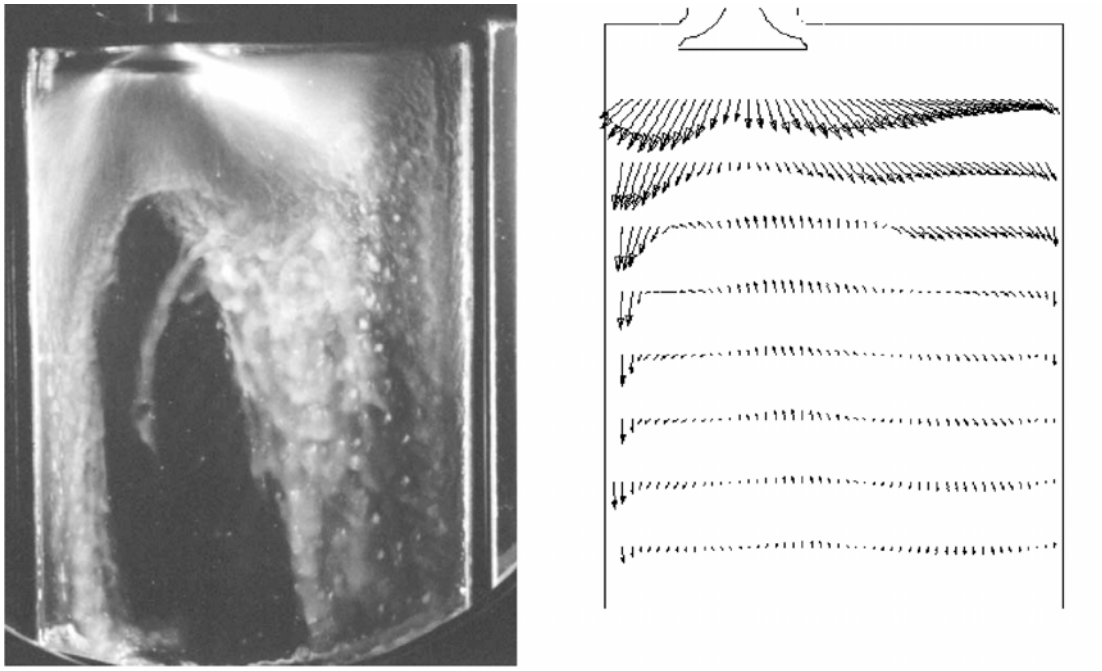
There are two main re-circulation zones, these being anticlockwise below and to the left, and also clockwise to the right, of the valve. The re-circulation to the right of the valve is positioned high in the chamber compared to the experiments. However, this is a two-dimensional plot of a very complex three-dimensional flow, the figure being plotted from data at the plane of symmetry (z = 0). Away from the symmetry plane, both re-circulation zones become lower as can be seen by comparing Figure 2.30 (a) and (b), the latter being taken in a plane 10 mm from the centerline (z = 10 mm).



(a) **(b)**

Figure 2.30 Vertical (y-direction) velocity contours of air flow within the chamber in the (a) centreline, z = 0 plane, (b) z=10 mm plane: valve lift = 4 mm; $V_{man.\ air}$ = 15.0 m/s; $V_{valve\ air}$ = 81.7 m/s. (Milton et al., 2001)

From Figure 2.31 (a) and (b), it can be seen that the velocities calculated from the FLUENT simulation give a distribution that compares reasonably well with the liquid spray trajectories.



(a) **(b)**

Figure 2.31 (a) Fuel distribution showing the flow patterns on the side walls (z= 15 mm). (b) Velocity contours 1mm from the side walls (z=14mm) (Milton et al., 2001)

2.1 Outline of Present Study

In this study, FLUENT computational solver was used to illustrate flow domain inside of a selected internal combustion engine cylinder. FLUENT relies on a science branch that is named as CFD standing for Computational Fluid Dynamics. CFD is the science of predicting fluid flow, heat transfer, mass transfer, chemical reactions, and related phenomena by solving mathematical equations that represent physical laws, using a numerical process. FLUENT program has been widely used in the field of internal combustion engine design. In this package program, the mass conservation and momentum equations were solved numerically using a FV-based algorithm. The internal flow inside of the engine cylinder in different valve lift and dynamic model were analyzed by solving the fully NSEs coupled with k-ε turbulence model.

Many scientists frequently use PIV and LDV methods in order to explore manifold and in-cylinder flow. There will also be some experimental studies in Previous Studies part of this thesis that were performed by some scientists. For validation of this study, calculated numerical results are compared with experimental results that were obtained by Yasar (2002) in different valve gaps. Moreover, there will be some turbulence models comparisons in Results and Discussion part in order to navigate future studies.

The purpose of the present study is to show a numerical study in IC engines using a commercial CFD program and clarify how flow acts inside of combustion chamber and near valve region. In order to accomplish this, different valve gaps 3, 5, 7, 9 mm were taken into account for all 2d and 3d models. As it is mentioned previous paragraph, three type turbulence models were compared for all valve gaps and all models. But 2d dynamic grid model feature is a little bit different from other calculation because of its inherent behavior. The present study shows and makes a sense during IC engine production for all manufacturers. Because it does not only show how flow acts inside of whole intake cycle and engine cycle, but it also clarify some places in which designer should consider some geometrical innovations. This last sentence can be more understandable as soon as Material Methods section of this thesis is read. The ultimate aim of this study does not intend to use exact engine geometries. In other words, the geometric values used in this study does not exactly reflect real geometries that those of used in real life engines. By the point of this view, parametric study and feedback mechanism increase their importance. Consequently, the aim must have been in a way that the designers should have turned back their design again after completing computational part and they should have changed their geometric design repeatedly in order to obtain optimum design point and it is thought to be accomplished in this study.

2.2 Outline of Dissertation

In this thesis, introduction part presents general information on the flow structure in IC engines and importance of CFD science. In previous studies section are

mostly about numerical and experimental studies which were performed by other scientists. Material and method part discuss model creation processes, calculation methods and their selections. Experimental and some numerical results are compared in results and discussion part. All numerical results are also shown in this section by using different visualization techniques.

Finally, conclusion part summarize the main purpose of present work and provide suggestions for further investigations and future works.

3. MATERIAL AND METHODS

Computer simulation of the inlet port and combustion chamber are helping to provide improved fuel economy and emissions in most of the engine design nowadays. The flow coefficient and tumble ratio - the ratio describing the angular motion of the incoming air - of the inlet port are critical factors in determining how lean the engine can be run while maintain good combustion stability. In the past, it took at least a month to prototype a single inlet port configuration and run a test that provided no information on internal flow patterns. But today, it is possible to analyze a new port design within a week and provide complete information on flow velocity and pressure throughout the model by means of CFD solvers. As a result, engineers have been able to improve the efficiency of inlet ports and combustion chamber designs.

The purpose of the present study is to show numerical studies carried out in some engine models. By doing this, the effect of flow inside of intake ports and cylinder can be seen and as a result, their designs can be improved. This aim has been done with the commercial software package FLUENT. This program uses the FVM and solves 3D NSEs with unstructured grid; include dynamic conditions and unsteady calculations.

3.1 Cylinder Geometries and Combustion Chambers

Cylinders can be in a wide variety of configurations and they are used for many applications, especially in internal combustion engines and compressors. It is possible to see them in different shape and different engine construction. They are generally characterized by defining their bore diameter and their volume in engines. Cylinder bore diameter has a big importance during the production of power in engines. It is theoretically true that the more diameter in cylinder the more power. But it is not practically efficient increasing this value because of more space problem and more fuel consumption. And as it is known that there is a relation between bore

diameter and cylinder volume. Rising of diameter increases cylinder volume defined as a volume which is swept out by engine piston.

There are some other important parts in engine geometries. These are piston and cylinder roof. Pistons can be numerous shapes depending on whether they have flat surface, curvature surface or bowled surface. In this study, during the 2d and 3d calculation, a piston that has flat surface is used. Most of bowled pistons are used for producing more swirl and tumble effect inside of cylinder.

The basic cylinder geometries which are used in 2d studies and 3d studies are shown in Figure 3.1 and Figure 3.2 respectively. Some detailed figures will be shown later. As indicated in Figure 3.1, cylinder geometry, namely combustion chamber consists of main four lines like a rectangular shape. The vertical lines indicate lateral faces of cylinder and the bottom horizontal line piston, upper line cylinder head.

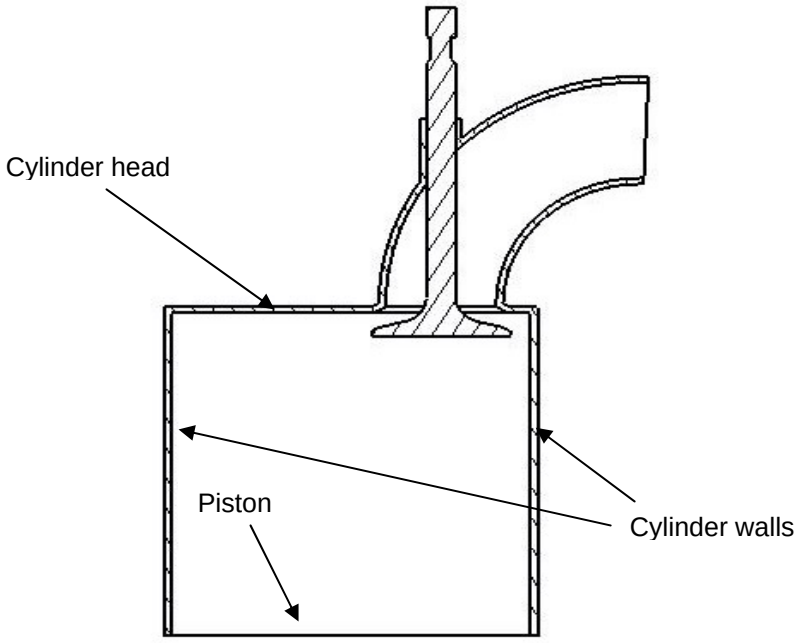


Figure 3.1 Basic cylinder geometry section used in 2d

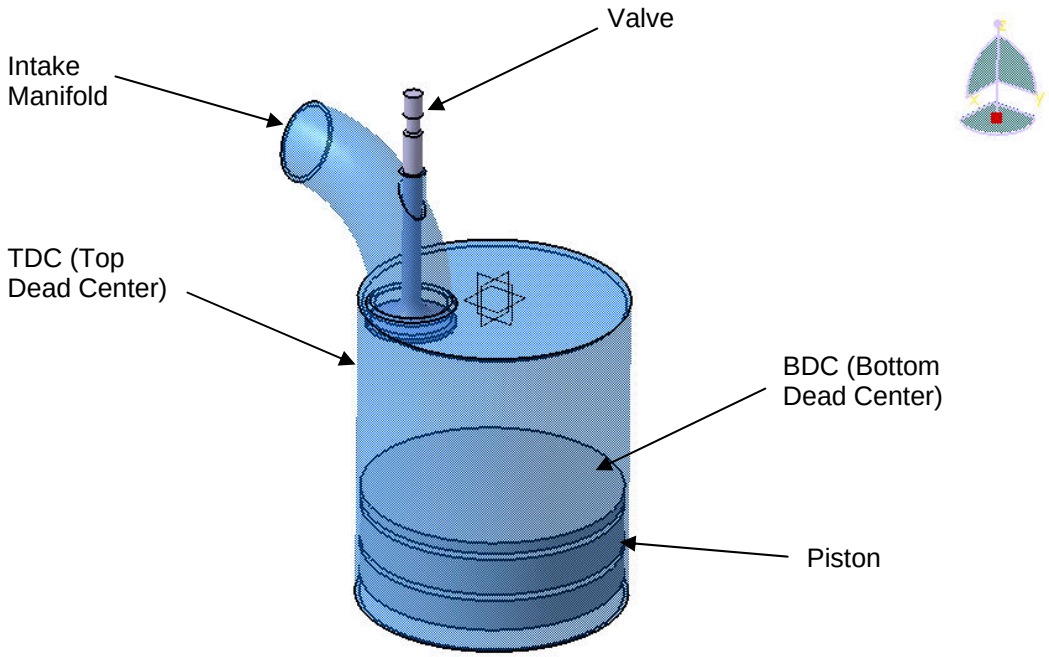


Figure 3.2 Basic cylinder geometry with valve used in 3d

As it is seen in figures, when piston comes its TDC position during the compression stroke, there is a small volume where combustion process happens between piston surface and cylinder head. This small volume has a great importance for combustion. This volume is sometimes named squish area because of the compression. If too large a squish area is used the combustion becomes too rapid and noisy. This design also reduces the susceptibility to knock, since the gas furthest from the sparking plug is in the squish area. The end gas in the squish area is less prone to knock since it will be cooler because of the close proximity of the cylinder head and piston. Excessive turbulence also causes excessive heat transfer to the combustion chamber walls, and should be avoided for this reason also (Stone, 1992).

The main considerations in combustion chamber design are:

- The distance traveled by the flame front should be minimized
- The exhaust valve(s) and spark plug(s) should be close together
- There should be sufficient turbulence
- The end gas should be in a cool part of the combustion chamber.

By minimizing the distance between the spark plug and the end gas, combustion will be as rapid as possible. This has two effects. Firstly, it produces high engine speeds and thus higher power output. Secondly, the rapid combustion reduces the time in which the chain reactions that lead to knock can occur. This implies that, for geometrically similar engines, those with the smallest diameter cylinders will be able to use the highest compression ratios.

The exhaust valve should be as close as possible to the sparking plug. The exhaust valve is very hot so it should be as far from the end gas as possible to avoid inducing knock or pre-ignition.

There should be sufficient turbulence to promote rapid combustion. However, too much turbulence leads to excessive heat transfer from the chamber contents and also to too rapid combustion, which is noisy. The turbulence can be generated by squish areas or shrouded inlet valves.

The small clearance between the cylinder head and piston in the squish area forms a cool region. Since the inlet valve is cooled during the induction stroke, this too can be positioned in the end gas region.

For good fuel economy all the fuel should be burnt and the quench areas where the flame is extinguished should be minimized. The combustion chamber should have a low surface-to-volume ratio to minimize heat transfer. The optimum swept volume consistent with satisfactory operating speeds is about 500 cm^3 per cylinder. For high-performance engines, smaller cylinders will enable more rapid combustion, so permitting higher operating speeds and consequently greater power output. For a given geometry, reducing the swept volume per cylinder from 500 cm^3 to 200 cm^3 might increase the maximum engine speed from about 6000 rpm to 8000 rpm (Stone, 1992).

The ratio of cylinder diameter to piston stroke is also very important. When the stroke is larger than diameter, the engine is said to be ‘under-square’. Over-square engines are defined as reverse idea of under-square engines. In other word, their engines have diameter which is larger than the piston stroke, and this permits larger valves for a given swept volume. This improves the induction and exhaust processes, particularly at high engine speeds. In addition the short stroke reduces the

maximum piston speed at a given engine speed, so permitting higher engine speeds. The disadvantage with over-square engines is that the combustion chamber has a poor surface-to-volume ratio, so leading to increased heat transfer. There has been a return to under-square engines, as these have combustion chambers with a better surface-to-volume ratio, and so lead to better fuel economy.

In four-stroke engines the induction and exhaust processes are controlled by valves. A valve is a mechanical device that regulates the flow of fluids by opening, closing, or partially obstructing various passageways. Two-stroke engines do not need separate valves in the combustion chamber, since the flow can be controlled by the piston moving past ports in the cylinder.

The most commonly used valve is the mushroom-shaped poppet valve. Poppet valves are commonly used in internal combustion engines to regulate the fuel mixture intake and exhaust. It has the advantage of being cheap, with good flow properties, good seating, easy lubrication and good heat transfer to the cylinder head. Rotary and disc valves are still sometimes used, but are subject to heat transfer, lubrication and clearance problems (Heywood, 1998).

In this study, mushroom-shaped poppet valve is used to model flow inside of the cylinder in 2d and 3d applications. The valve shape which was drawn in Catia program is shown in Figure 3.3. In Figure 3.4, front view of this model is illustrated. This model is used in 2d calculations as well. It is clear to see geometric dimensions in Figure 3.4. As indicated in Figure 3.4, valve seat angle is 30 degree and valve radius is 8 mm.

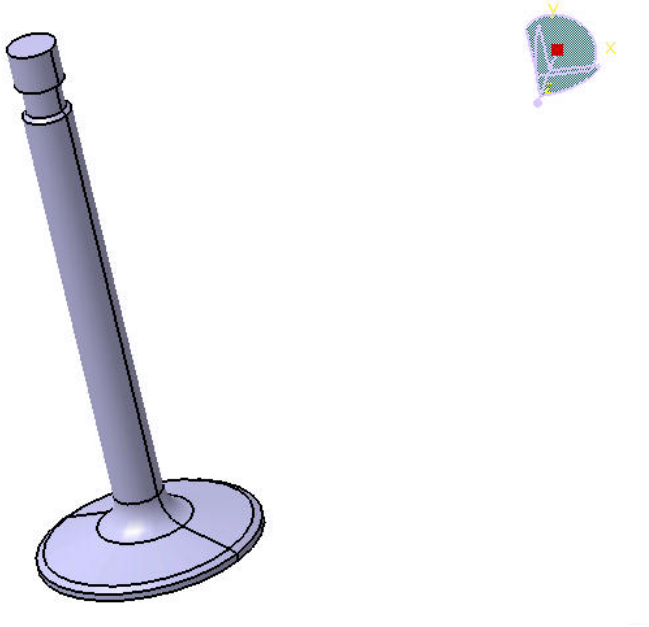


Figure 3.3 3d Valve geometry used in 3d studies

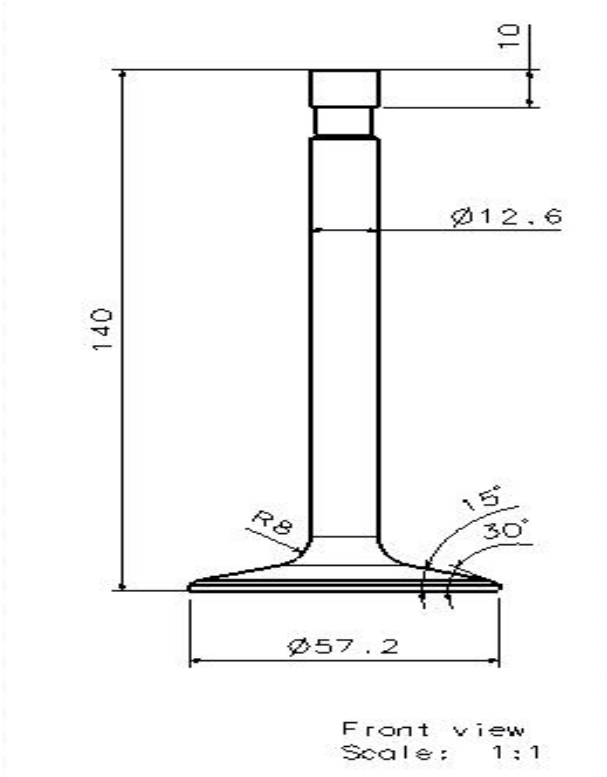


Figure 3.4 2d valve geometry used in 2d studies.

As it was mentioned before, the Figure 3.1 and Figure 3.2 are basic illustrations of cylinder geometries. The real geometries which are used in 2d studies are shown with their geometric values in following figures.

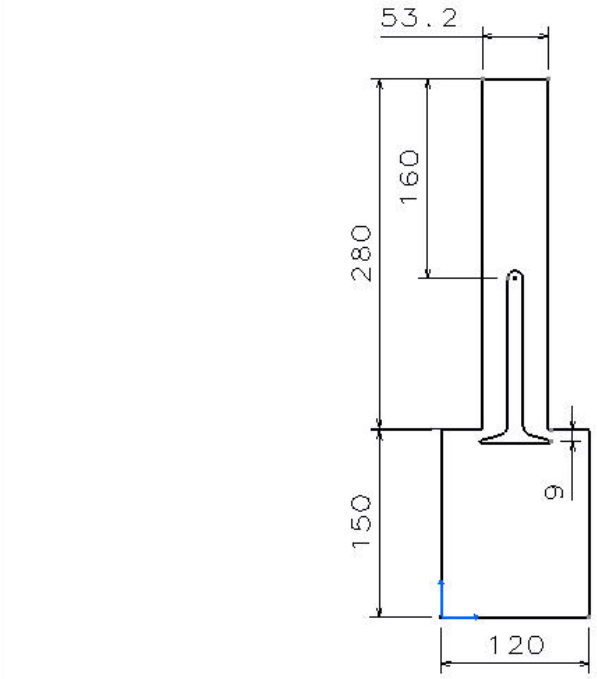


Figure 3.5 2d cylinder geometry sharing same center with intake manifold

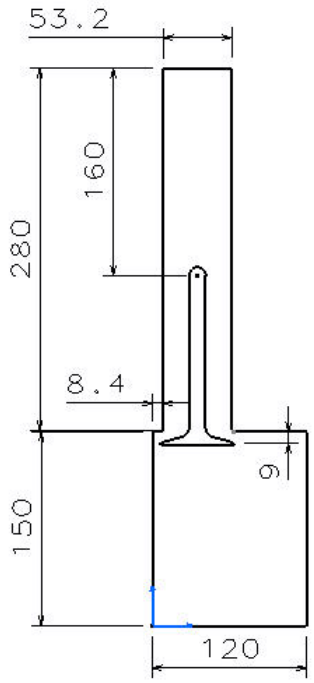


Figure 3.6 2d cylinder geometry in different axis than cylinder axis

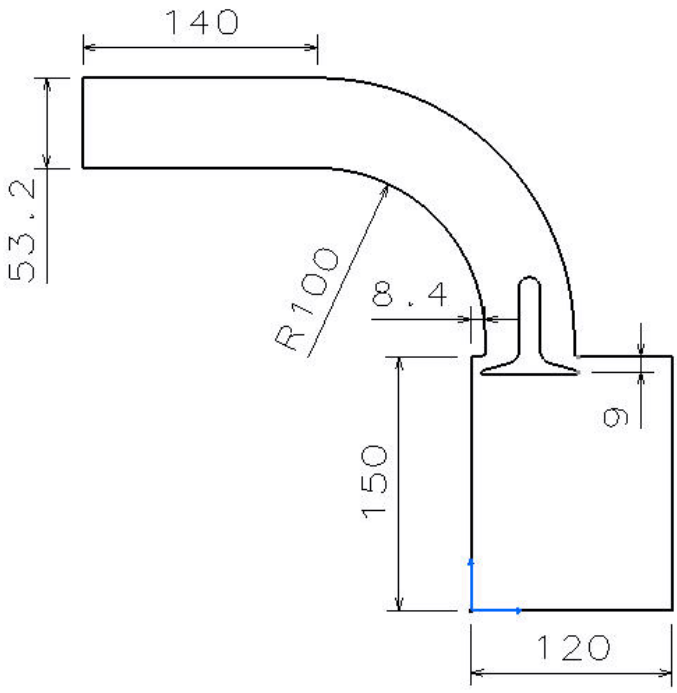


Figure 3.7 2d cylinder geometry having an intake manifold with radius

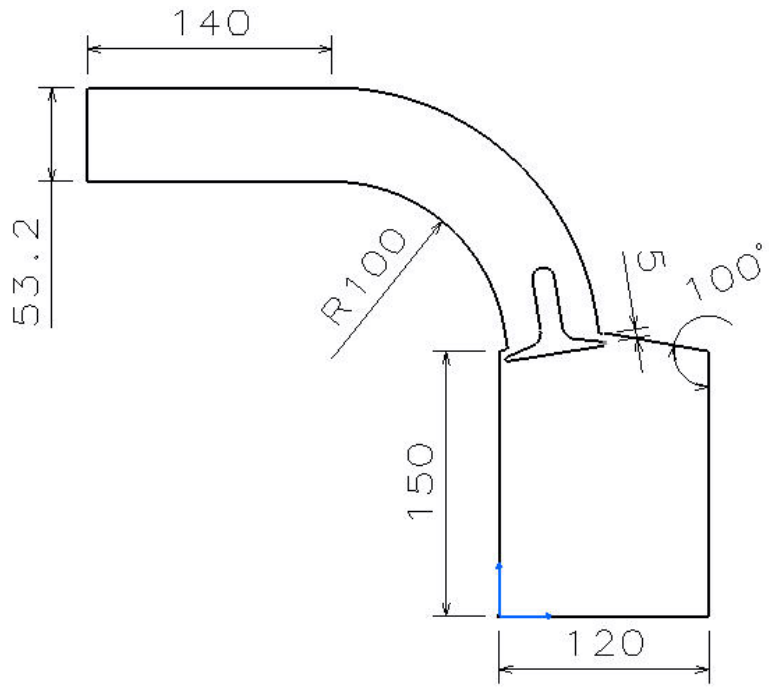


Figure 3.8 Pent-roof cylinder geometry

As it is seen in figures, all of the cylinder models are classified as valve-in-head engine type. In other word, all of the intake manifolds of the models are directly connected to the cylinder head. This concept has a compact combustion chamber with short flame paths. This improves resistance to auto-ignition and increases efficiency by reducing combustion duration (Benson and Whitehouse, 1979).

All of the above figures include different valve geometry that was shown as valve geometry before in this study. As known, valve pivot has to go out from the intake pipe and connect to camshaft. But it is not the case in these figures because of geometrical constraints. Should the valve pivot divides intake pipe, there will be no flow area and FLUENT program recognizes it like two different flow domains. As a result, calculation fails. Because of this reason, valve geometry is designed not to divide intake pipe. Except this configuration, there are no differences in the valve geometry that is shown before.

In Figure 3.5 shows a basic cylinder model. As it is seen in this figure, intake manifold has same axis with cylinder axis. This is a simple chamber that produces good results and it is easy to install valve drive train mechanism. But this shape has

some undesirable swirl effects near the valve region and especially near the lateral-up faces of cylinder wall that can be seen in results and discussion section. Moreover, it is difficult to fix more than 1 valve to this shape since it is assumed that valve axis shares same axis with cylinder axis in Figure 3.5. In Figure 3.6 there is no concentricity between valve axis and cylinder axis. Hence, it is possible to fix another valve near this valve. And also it is possible to fix 4 valves to the cylinder head if it is thought 3d. In Figure 3.7, the intake manifold does not connect to cylinder head with straight pipe. An elbow is used instead. Finally, in the last figure, angular cylinder head which is named as pent-roof is used. The advantages and disadvantages of these shapes will be shown in results and discussions part.

As 3d models, two types of cylinder model were used. Both of them were modeled by using Catia part model designer and they were designed as principle of changeable geometric features and parametric study. Before showing 3d models, it had better to explain meaning of changeable geometric features and parametric study first:

In order to optimize the performance of engine with the models established in this study, a set of parametric studies are performed to explore the effect of flow. Parametric study is mostly interested in geometric dimension, geometric constraints and relations between these values. In 2d studies, all of the geometric dimensions can be changed by the user in the solid model program. This capability gives users more elastic model design. In other words, if there are undesirable results at the end of the CFD calculations because of the geometrical properties that models have, it is easy to be chanced this dimensions in the solid model environment. But in this case, calculation has to turn to beginning namely, creation of model. Figure 3.9 explains this process clearly.

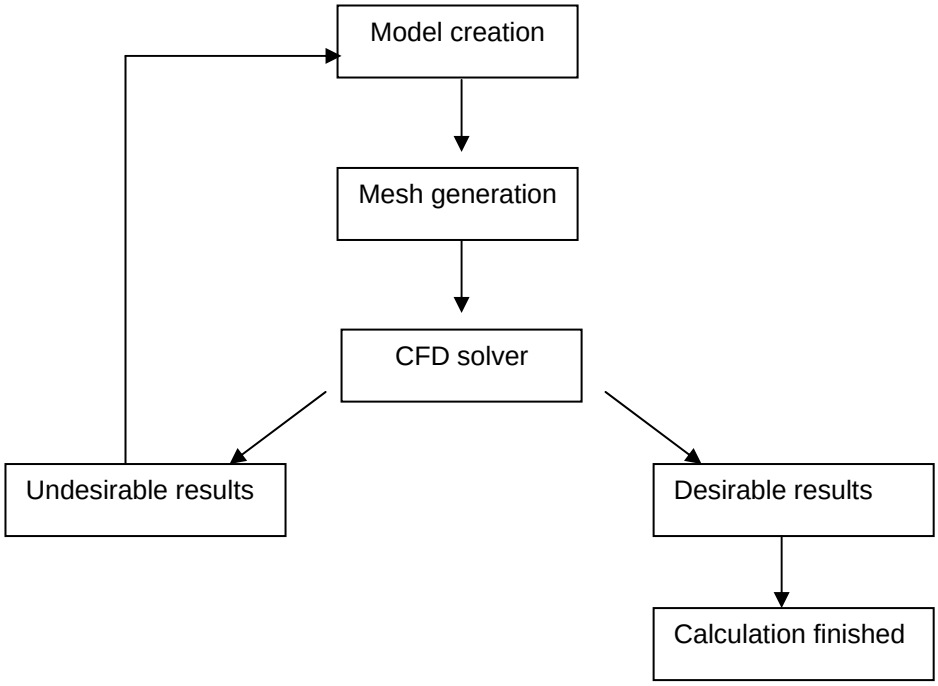


Figure 3.9 Parametric studies in CFD calculations.

In 3d studies, apart from studies which are fulfilled in 2d, there is a table that is created in office Excel program for 3d model dimensions. The dimensions in the model can be changed easily by means of this table. This table contains all of or some of the critical dimension values of the model and there is a link between this table and solid model. If user changes, for instance diameter of engine cylinder value in table, it is changed immediately in solid model environment. Moreover, relationship between these values can be created with controlling this table. For instance, there is a dependency between piston stroke and valve lift level. These two mechanic part connect each other with a mechanism in real life. But this is meaningless case in solid model world. Therefore, relation between these two parts can be created by using parametric approach in 3d solid model program. Example of parametric design table is illustrated in Figure 3.10.

	A	B	C	D
1	valve_lift	5		
2	dcylinder	120		
3	dintake_valve	57.2		
4	dintake_port	53.2		
5	stroke	150		
6	chamfer	2		
7	valve_radius	8		
8				
9				
10				
11				
12				
13				

Figure 3.10 An example of parametric design table

After parametric study explanation, 3d models can be seen as follows:

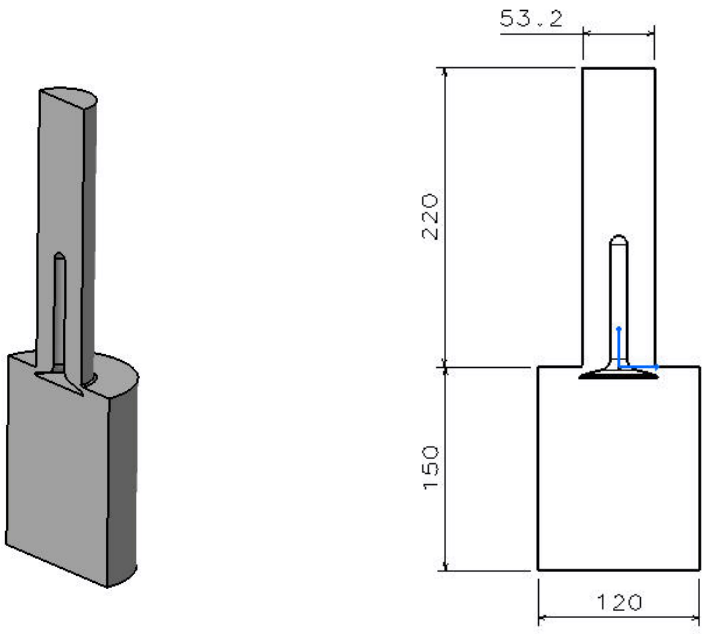


Figure 3.11 3d cylinder model and its drawing with one intake port

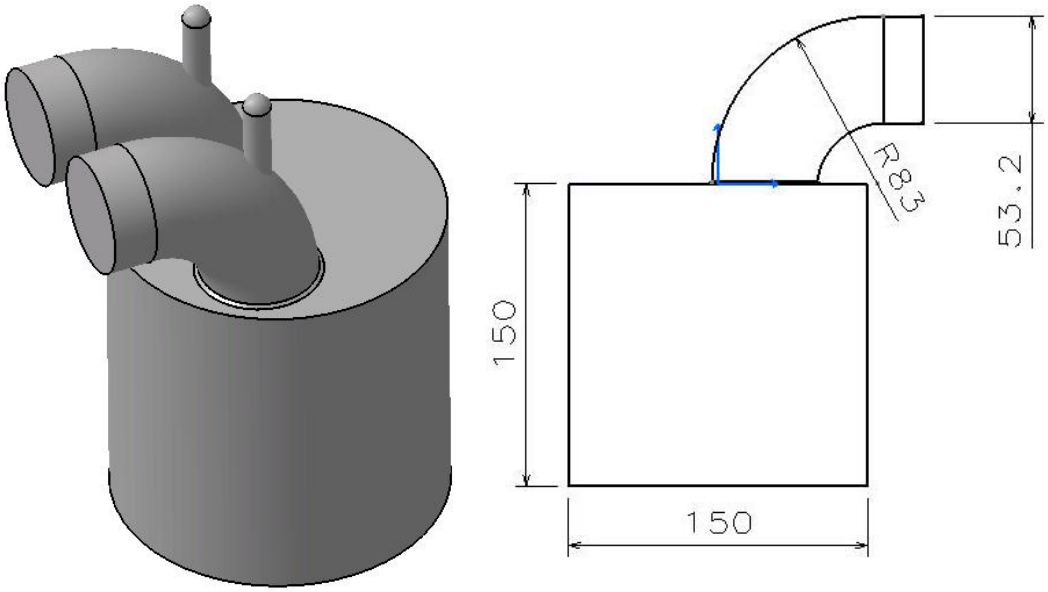


Figure 3.12 3d cylinder model and its drawing with two intake port

As it is seen from Figure 3.11, it is illustrated for only half of the model. Since model has totally symmetric condition, it was cut from symmetry plane. By doing this, computational effort and time were reduced too much than those of doing without cut. But this modification does not work very well in Figure 3.12 as it is clarified in Boundary Conditions section of this thesis. Therefore this model was used without making any operation in geometry.

After exporting these 3d models to GAMBIT program, valves geometries are subtracted from whole body. As a result, flow domains are created and the models are ready to be generated grid structure.

3.2 Components of a Numerical Solution

CFD simulation often requires a number of repeating steps. There is no every time exact solution for a given problem. It is not always possible to reach reasonable solution in every problem. The procedure includes tuning the mesh system, adjusting

boundary conditions, selecting correct numerical parameters, finding the right physical model, monitoring iteration and finally, viewing the results. This shows how much experience CFD users should have. Some crucial numerical solution algorithms are explained briefly next, to understand what CFD solvers use to predict flow domain.

3.3 Mathematical Model

The starting point of any numerical method is the mathematical model, i.e. the set of partial differential or integral equations and boundary conditions. In CFD applications, some sets of equations used for flow prediction and one of them chooses an appropriate model for the target application (incompressible, inviscid, turbulent; two or three-dimensional, etc.). A solution method is usually designed for a particular set of equations. Trying to produce a general purpose solution method, i.e. one which is applicable to all flows, is impractical, if not impossible and, as with most general purpose tools, they are usually not optimum for any one application (Ferziger and Peric, 2002).

3.3.1 Governing Equations

All of CFD, in one form or another, is based on the fundamental governing equations of fluid dynamics—the continuity, momentum, and energy equations. These equations speak physics. They are the mathematical statements of three fundamental physical principles upon which all of fluid dynamics is based:

- Mass is conserved.
- Newton's second law, F=ma.
- Energy is conserved.

The governing equations can be obtained in various different forms. For most aerodynamic theory, the particular form of the equations makes little difference. However, for a given algorithm in CFD, the use of the equations in one form may

lead to success, whereas the use of an alternate form may result in oscillations (wiggles) in the numerical results, incorrect results, or even instability. Therefore, in the world of CFD, the various forms of the equations are of vital interest. In turn, it is important to derive these equations in order to point out their differences and similarities, and to reflect on possible implications in their application to CFD (Anderson, 1995).

Conservation laws can be derived by considering a given quantity of matter or control mass and its extensive properties, such as mass, momentum and energy. This approach is used to study the dynamics of solid bodies, where the control mass (sometimes called the system) is easily identified. In fluid flows, however, it is difficult to follow a parcel of matter. It is more convenient to deal with the flow within a certain spatial region that is called a control volume (CV), rather than in a parcel of matter which quickly passes through the region of interest. This method of analysis is called the control volume approach that is also used in FLUENT solver.

3.3.2 The Mass Conservation Equation

The mass conservation equation can be written as follows:

$$\frac{\partial \rho}{\partial t} + \nabla.(\rho V) = 0 \qquad (3.1)$$

Equation 3.1 is the general form of mass conservation equation which is generally called as continuity equation. This equation is used throughout all cells in 2d and 3d models during the calculation in order to satisfy mass conservation.

3.3.3 Momentum Conservation Equation

Momentum conservation equation can be written in three directions as follows:

$$\rho \frac{Du}{Dt} = -\frac{\partial p}{\partial x} + \frac{\partial \tau_{xx}}{\partial x} + \frac{\partial \tau_{yx}}{\partial y} + \frac{\partial \tau_{zx}}{\partial z} + \rho f_x \qquad (3.2)$$

which is the x component of the momentum equation for a viscous flow. In a similar fashion, the y and z components can be obtained as:

$$\rho \frac{Dv}{Dt} = -\frac{\partial p}{\partial y} + \frac{\partial \tau_{xy}}{\partial x} + \frac{\partial \tau_{yy}}{\partial y} + \frac{\partial \tau_{zy}}{\partial z} + \rho f_y \qquad (3.3)$$

$$\rho \frac{Dw}{Dt} = -\frac{\partial p}{\partial z} + \frac{\partial \tau_{xz}}{\partial x} + \frac{\partial \tau_{yz}}{\partial y} + \frac{\partial \tau_{zz}}{\partial z} + \rho f_z \qquad (3.4)$$

3.3.4 Energy Conservation Equation

Energy conservation equation can be written as follows:

$$\frac{\partial}{\partial t}\left[\rho\left(e+\frac{V^2}{2}\right)\right] + \nabla.\left[\rho\left(e+\frac{V^2}{2}\right)V\right] = \rho\dot{q} + \frac{\partial}{\partial x}\left(k\frac{\partial T}{\partial x}\right) + \frac{\partial}{\partial y}\left(k\frac{\partial T}{\partial y}\right) + \frac{\partial}{\partial z}\left(k\frac{\partial T}{\partial z}\right)$$

$$-\frac{\partial(up)}{\partial x} - \frac{\partial(vp)}{\partial y} - \frac{\partial(wp)}{\partial z} + \frac{\partial(u\tau_{xx})}{\partial x} + \frac{\partial(u\tau_{yx})}{\partial y} + \frac{\partial(u\tau_{zx})}{\partial z} + \frac{\partial(v\tau_{xy})}{\partial x} + \frac{\partial(v\tau_{yy})}{\partial y}$$

$$+\frac{\partial(v\tau_{zy})}{\partial z} + \frac{\partial(w\tau_{xz})}{\partial x} + \frac{\partial(w\tau_{yz})}{\partial y} + \frac{\partial(w\tau_{zz})}{\partial z} + \rho f.V \qquad (3.5)$$

This energy equation was not activated during the most calculation. Since flow characteristic was investigated most of the model, usage of energy equation in the solver required more CPU time and computational expense. Because of this reason, it was used only dynamic grid studies.

3.4 Discretization Method

After selecting the mathematical model, one has to choose a suitable discretization method, i.e. a method of approximating the differential equations by a system of algebraic equations for the variables at some set of discrete locations in space and time. There are many approaches, but the most important of which are finite differences (FD), finite volumes (FV) and finite elements (FE) methods. Other methods, like spectral schemes, boundary element methods, and cellular automata are used in CFD but their use is limited to special classes of problems. Each type of method yields the same solution if the grid is very fine. However, some methods are more suitable to some classes of problems than others.

FD, is the oldest method for numerical solution. It is believed to have been introduced by Euler in the 18th century. It is also the easiest method to use for simple geometries. The starting point in this method is the conservation equation in differential form. The solution domain is covered by a grid. At each grid point, the differential equation is approximated by replacing the partial derivatives by approximations in terms of the nodal values of the functions. The result is one algebraic equation per grid node, in which the variable value at that and a certain number of neighbor nodes appear as unknowns.

The FE method is similar to the FV method in many ways. The domain is broken into a set of discrete volumes or finite elements that are generally unstructured; in 2D, they are usually triangles or quadrilaterals, while in 3D tetrahedral or hexahedral are most often used. The distinguishing feature of FE methods is that the equations are multiplied by a weight function before they are integrated over the entire domain. In the simplest FE methods, the solution is approximated by a linear shape function within each element in a way that guarantees continuity of the solution across element boundaries. Such a function can be constructed from its values at the corners of the elements. The weight function is usually of the same form. This approximation is then substituted into the weighted integral of the conservation law and the equations to be solved are derived by requiring the derivative of the integral with respect to each nodal value to be zero; this corresponds to selecting the best solution

within the set of allowed functions (the one with minimum residual). The result is a set of non-linear algebraic equations.

The FV method uses the integral form of the conservation equations as its starting point. The solution domain is subdivided into a finite number of contiguous CVs, and the conservation equations are applied to each CV. At the centroid of each CV lies a computational node at which the variable values are to be calculated. Interpolation is used to express variable values at the CV surface in terms of the nodal (CV-center) values. Surface and volume integrals are approximated using suitable quadrature formula. As a result, one obtains an algebraic equation for each CV, in which a number of neighbor nodal values appear.

The FV method can accommodate any type of grid, so it, is suitable for complex geometries. The grid defines only the control volume boundaries and need not be related to a coordinate system. The method is conservative by construction, so long as surface integrals (which represent convective and diffusive fluxes) are the same for the CVs sharing the boundary.

The disadvantage of FV methods compared to FD schemes is that methods of order higher than second are more difficult to develop in 3D. This is due to the fact that the FV approach requires three levels of approximation: interpolation, differentiation, and integration (Ferziger and Peric, 2002).

The discretization procedure consists of the integration of the conservation equations over each control volume assuming uniform values of the variables over the cell. This results in a set of algebraic equations, which relate the values of the variables at discrete points (assumed to be the centers of the cells) and at the faces of the cell, the fluxes across the faces of the cell and the dimensions of the cell. It is this set of algebraic equations which is actually solved by the code. The values of the variables at the centers of the cells become the unknowns. The values of the variables at the faces of the cells need to be interpolated between the values at the centers of two adjacent cells. This interpolation procedure is an important part of the solution scheme.

FLUENT uses a control-volume-based technique to convert the governing equations to algebraic equations that can be solved numerically. This control

volume technique consists of integrating the governing equations about each control volume, yielding discrete equations that conserve each quantity on a control-volume basis.

Discretization of the governing equations can be illustrated most easily by considering the steady-state conservation equation for transport of a scalar quantity. This is demonstrated by the following equation written in integral form for an arbitrary control volume V as follows:

$$\oint \rho\phi \vec{v}.d\vec{A} = \oint \Gamma_\phi \nabla\phi.d\vec{A} + \int_V S_\phi dV \tag{3.6}$$

where ρ = density, $\vec{v}$ = velocity vector, $\vec{A}$ = surface area vector, Γ_ϕ = diffusion coefficient for ϕ, ∇_ϕ = gradient of ϕ, S_ϕ = source of ϕ per unit volume.

Equation 3.6 is applied to each control volume, or cell, in the computational domain. The 2d triangular cell shown in Figure 3.13 is an example of such a control volume. Discretization of equation (3.6) on a given cell yields,

$$\sum_f^{N_{faces}} \rho_f \vec{v}_f \vec{\phi}_f . \vec{A}_f = \sum_f^{N_{faces}} \Gamma_\phi (\nabla\phi)_n . \vec{A}_f + \vec{S}_\phi V \tag{3.7}$$

Where N_{faces} = number of faces enclosing cell, ϕ_f = value of ϕ convected through face f, $\rho_f \vec{v}_f . \vec{A}_f$ = mass flux through the face, $\vec{A}_f$ = area of face f, $(\nabla\phi)_n$ = magnitude of $\nabla\phi$ normal to face f, V = cell volume.

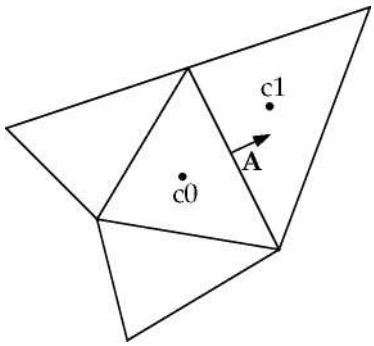


Figure 3.13 Control volume used to illustrate discretization of a scalar transport equation.

The equations solved by FLUENT take the same general form as the one given above and apply readily to multi-dimensional, unstructured meshes composed of arbitrary polyhedra.

By default, FLUENT stores discrete values of the scalar ϕ at the cell centers (c0 and c1 in Figure 3.13). However, face values ϕ_f are required for the convection terms in equation 3.7 and must be interpolated from the cell center values. This is accomplished using an upwind scheme. Upwinding means that the face value ϕ_f is derived from quantities in the cell upstream, or "upwind", relative to the direction of the normal velocity v_n in equation 3.7. FLUENT allows choosing from several upwind schemes: first-order upwind, second-order upwind, power law, and QUICK. When first-order accuracy is desired, quantities at cell faces are determined by assuming that the cell-center values of any field variable represent a cell-average value and hold throughout the entire cell; the face quantities are identical to the cell quantities. On the other hand, when second-order accuracy is desired, quantities at cell faces are computed using a multidimensional linear reconstruction approach. In this approach, higher-order accuracy is achieved at cell faces through a Taylor series expansion of the cell-centered solution about the cell centroid (FLUENT User's Guide, 2002)

In this study, first-order upwind discretization method is used first. Should the results do not satisfy, or in case of reaching divergence result, second

order upwind discretization method is used to provide high accuracy. As residual criteria, it is taken 1.0 e^{-6} for RMS (root-mean-square) for both of the discretization methods. It is forced to reach the above value in each run. Computations are continued until the values of residuals were progressively reducing to desirable result, although some cases this is not achieved. The monitoring the representative flow variables through iterations may show that the residual have stagnated and do not change with further iterations. This could also be considered that problem has convergence. Another method in convergence criteria is that surface monitoring could be used apart from residual monitoring to find converged results. Pressure inlet and pressure outlet boundary condition has been selected for surface monitoring in this study. It is assumed that the solution is converged in case there is no fluctuation in the surface monitoring panel. Two surface monitors are used; one for static pressure the other one is mass flow rate on the inlet and outlet boundary sections. An example of surface monitor and residual monitor are shown in results and discussions section.

3.5 Numerical Grid

Most of the CFD calculation needs to have physical space which must be subdivided into a number of cells by means of a structured or unstructured grid. The aim of this subdivision is to have calculation points in order to perform the discretization of the governing equations. The grid can be constructed using a rectangular, a cylindrical or a body fitted coordinate system. In the first two cases, the grid lines are aligned with the coordinate axes (either cartesian or cylindrical) while in the latter the grid lines conform to the geometry. The node points, i.e. the points where the grid lines intersect, define the cells. It is possible to enumerate the grid nodes, so that instead of working with the physical coordinates of the nodes, the integer numbers of the enumerated nodes are used. The space where the integer numbers are used is called the computational domain, and it is said to be mapped to the physical domain once a one-to-one relation has been established. The mapping

process essentially performs a transformation between the integer indices and the physical coordinates of the nodes and additionally gives weighting factors to each of the faces of the cells in order to compute correctly the fluxes and gradients. A mesh is broken up into control volumes, or cells. Each cell is defined by a set of grid points (or nodes), a cell center, and the faces that bound the cell. This convenience is shown in Figure 3.14 (Versteeg and Malalasekera, 1995 and Anderson, 1995).

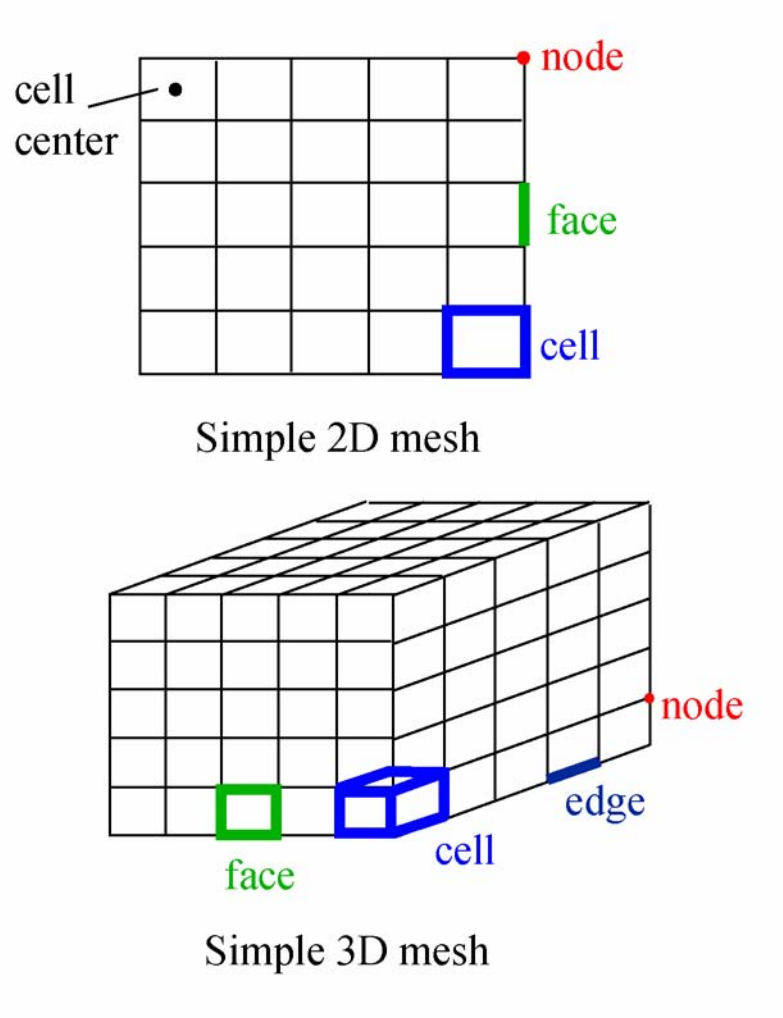


Figure 3.14 Grid components

Analytical solutions of partial differential equations involve closed-form expressions which give the variation of the dependent variables continuously

throughout the domain. In contrast, numerical solutions can give answers at only discrete points in the domain, called grid points. For example, Figure 3.15 shows a section of a discrete grid in the xy plane. As it is seen in figure, Δx indicates spacing of the grid points in the x direction and Δy in the y direction. Δx and Δy can be different value or they can be equal. However, the majority of CFD applications involve numerical solutions on a grid which contains uniform spacing in each direction, because this greatly simplifies the programming of the solution, saves storage space, and usually results in greater accuracy. As a result of this view, structured grids are defined as the grid points which are placed in a geometrical regularity ($\Delta x = \Delta y$). In contrast, unstructured grid points are placed in the flow field in a very irregular fashion. Figure 3.15 is an example of a structured grid (Anderson, 1995).

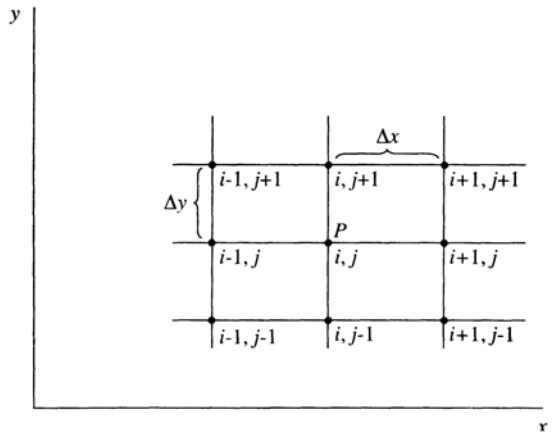


Figure 3.15 Discrete grid points.

In this study unstructured grids are used both of the 2d and 3d studies. GAMBİT preprocessor has a capability of generating structured and unstructured grid. But it is necessary to produce compress grid structure (unstructured grid) such a place that changing of the derivatives can be easily computed by the solver. Therefore unstructured capability is used all of the 2d and 3d models. Unstructured grid which is generated for one of the 2d study is shown in Figure 3.16. As it is seen in figure, grid structure is compressed near the valve region.

Since velocity value is so high near this region, it is predicted that changing of derivative of velocity is also big when comparing rest of the region. This compressed grid capability is also used in 3d study.

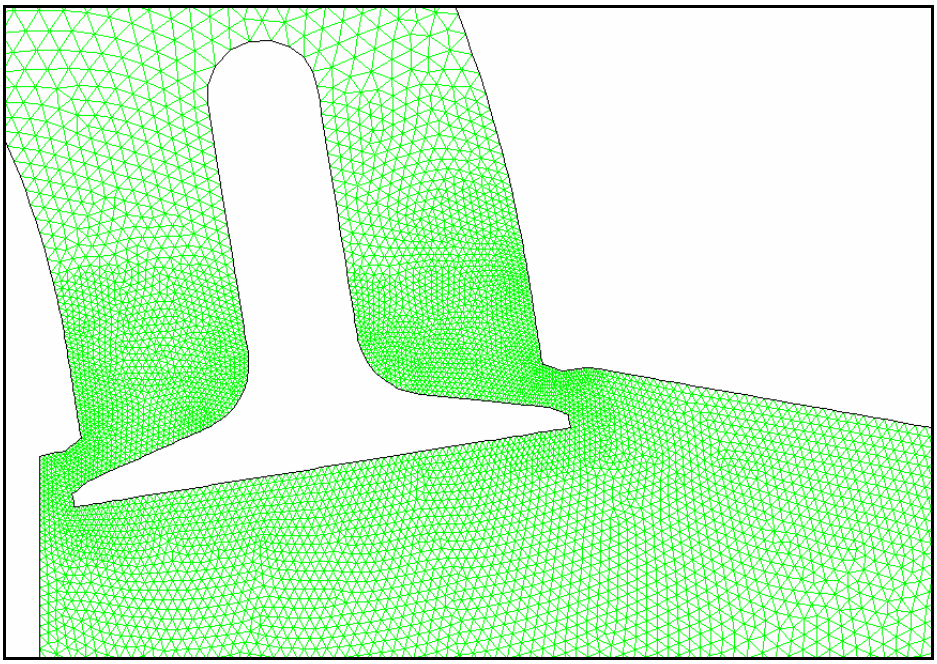


Figure 3.16 An example of unstructured grid

The process of structured grid generation involves breaking the domain in to smaller blocks in which structured grids is generated. An unstructured grid generation has two basic steps, point creation and point connection. The choice of location of point creation and point connection gives the flexibility that makes this type of grid a favored choice for complicated computational domains, while a structured grid may also give a good quality of domain discretization but the process is very time consuming as the grid may need to manually broken into several blocks depending on the nature of the geometry. The flexibility and the convenience make unstructured grid a favorable choice, but a cost, as the solution accuracy may be relatively poor due to presence of skewed elements in sensitive regions like boundary layers. Although structured grid may be more desirable attribute in terms of the solution accuracy, an unstructured grid may be an easier

way out for complicated geometries. Due to the accuracy and efficiency concerns with an unstructured grid as it may take a large number of elements to fill a region with this type of grid, a compromise is made in the form of hybrid grid which uses the desirable features of both of the above mentioned generic grid types. In a hybrid grid, the viscous region can be filled with prismatic or hexahedral cells while the rest of the zone can be filled with tetrahedral cells. This type of grid structure is also used in this study. Especially drawn 2d models, having an intake pipe with radius, have hybrid grid. Quadrilateral grid structure is generated in region of straight section of intake pipe. On the other hand, triangular elements are used in elbow section of intake pipe. This type of grid is shown in Figure 3.17. In order to connect these two regions each other, interface boundary condition is selected. It has been observed that a hybrid grid in viscous regions creates much lesser number of elements than completely unstructured grid with similar resolution. This idea has been generalized further to give rise to what is called generalized grid. Since generalized grids have no restriction on the number of edges or faces on a cell, it makes this type of grid extremely flexible for topological adaptivity. (FLUENT User's Guide, 2002)

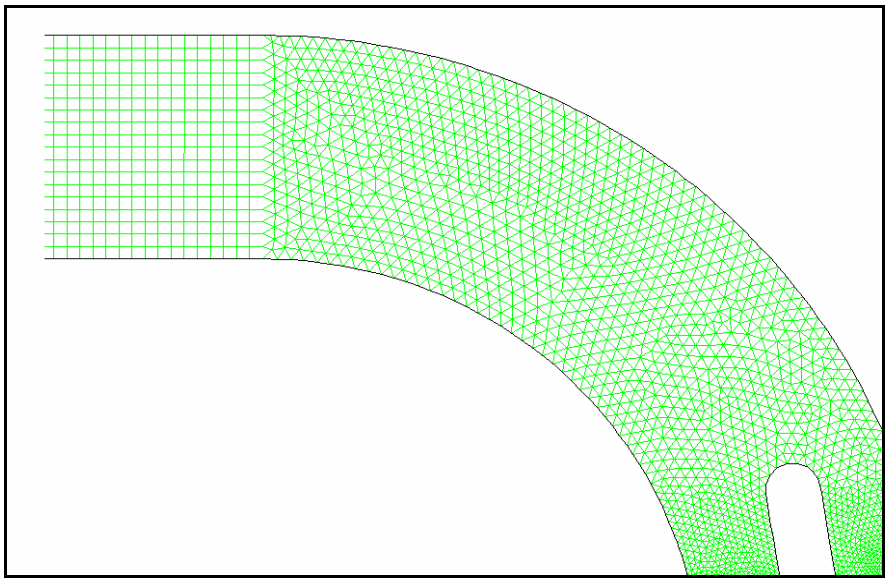


Figure 3.17 An example of hybrid mesh

3.5.1 The Choice of Grid

Most flows in engineering practice involve complex geometries which are not readily fit with Cartesian grids. Although the principles of discretization and solution methods for algebraic systems described earlier may be used, many modifications are required. The properties of the solution algorithm depend on the choices of the grid and of the vector and tensor components, and the arrangement of variables on the grid. When the geometry is regular (e.g. rectangular or circular), choosing the grid is simple: the grid lines usually follow the coordinate directions. In complicated geometries, the choice is not at all trivial. The grid is subject to constraints imposed by the discretization method. If the algorithm is designed for curvilinear orthogonal grids, non-orthogonal grids cannot be used; if the CVs are required to be quadrilaterals or hexahedra, grids consisting of triangles and tetrahedra cannot be used, etc. When the geometry is complex and the constraints cannot be fulfilled, compromises have to be made. The topological information to be verified begins with the number of faces and nodes per cell. A triangular cell (2d) has 3 faces and 3 nodes, a tetrahedral cell (3d) has 4 faces and 4 nodes, a quadrilateral cell (2d) has 4 faces and 4 nodes, and a hexahedral cell (3d) has 6 faces and 8 nodes. In order to understand more, Figure 3.18 shows this cell types clearly. (Anderson, 1995)

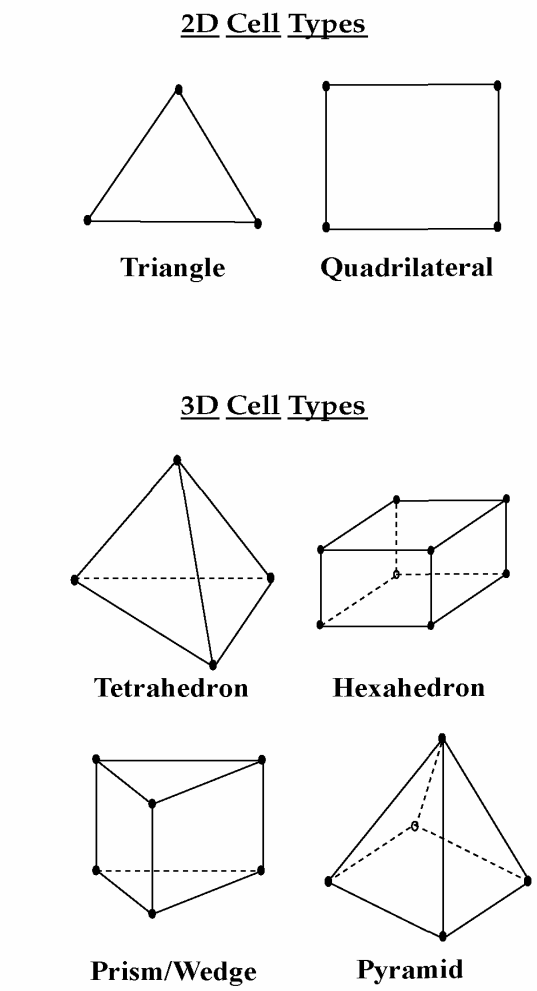


Figure 3.18 Cell types

The flexibility and the convenience make irregular (unstructured) grid a favorable choice, but solution accuracy may be relatively poor due to presence of skewed elements in sensitive regions like boundary layers. Although there are some regularity most of the 2d and 3d models which are used in this study, the region near the valve area requires to be made grid unstructured. Because of above reasons unstructured triangular and tetrahedron grids are used in 2d and 3d studies

respectively. As it is mentioned in Figure 3.17, quadrilateral grid tissue is used to create hybrid mesh in regular geometry sections.

3.5.2 Grid Generation

CFD obtains solutions of the governing NSEs and, depending upon the particular application, solves additional equations involving multiphase, turbulence, heat transfer and other relevant processes. The partial differential NSEs and associated equations are converted into algebraic form (solvable by computer) on a grid that defines the geometry and flow domain of interest. Appropriate boundary and initial conditions are applied on the grid, and the distributions of quantities such as velocity, pressure, turbulence, temperature and concentration are determined iteratively at every point in space and time within the domain.

A grid generation program, GAMBIT and TGrid were used to generate appropriate grid blocks and to set up boundary conditions for inlet and outlet ports. Since model and grid generation processes have complex behavior, it had better to explain them in sequence: Firstly, All of the 2d and 3d models are created by using Catia solid model program. After completing these models, they were exported to GAMBIT program. As it is mentioned at the beginning of the paragraph, only this program has ability of generating grid. In case of unsatisfying condition after mesh generation, this generated mesh is exported to Tgrid program which is another mesh arrangement program, not generation program. This undesirable condition sometimes happen some 3d models. But GAMBIT is sufficient to create most of the 2d grid structures. After providing all of the quality sufficiency, the grid is ready to be exported to solver program namely, FLUENT. No matter which type of grid is generated in Gambit, FLUENT provides complete mesh flexibility with structured and unstructured grids. Moreover, it supports grid types including 2d triangular and quadrilateral, 3d tetrahedral, hexahedral, pyramid and wedge. These all grid (cell) types are shown in Figure 3.18. FLUENT also allows refining or coarsening grid based on the flow solution. It is understood from this point that grid generation is not

restrictive with the GAMBIT and TGrid programs. It can be carried out inside of FLUENT solver.

Grid generation has a big impact over the all numerical methods that are used in FE, FD and FV methods. The important concept in grid generation is that there must have bounded and unbounded flow domains. These domains define real geometry of problem. In order to discrete the flow equation in these domains, GAMBİT processor uses two methods: (*i*) it forces to map the flow domain to a rectangular or parallel piped domain where a simple equispaced Cartesian grid is used. This is the simple method that employs only simple geometries. (*ii*) It covers the entire domain with unstructured grid. The choice of which method is suitable depends on geometry complexity and flow movement. If there is too much complexity, unstructured grid option should be used. Anyway, GAMBIT processor does not want to map grid tissue if this is the case. If the user wants to have excellent accuracy and visualization, the map or sub-map schemes must be used. These methods require geometry decomposition in complex models. It is not possible to use map and sub-map schemes, since there is too much complexity near the valve region in this study. Therefore, unstructured triangular (2d) and unstructured tetrahedral (3d) grid capability of GAMBIT is used instead.

Many flow problems solved in engineering practice involve complex geometries. These problems are also extremely time-consuming. When geometries are complex or the range of length scales of the flow is large, a triangular/tetrahedral mesh can often be created with far fewer cells than the equivalent mesh consisting of quadrilateral/hexahedral elements. This is because a triangular/tetrahedral mesh allows cells to be clustered in selected regions of the flow domain, whereas structured quadrilateral/hexahedral meshes will generally force cells to be placed in regions where they are not needed. Unstructured quadrilateral / hexahedral meshes offer many of the advantages of triangular / tetrahedral meshes for moderately complex geometries. One characteristic of quadrilateral / hexahedral elements that might make them more economical in some situations is that they permit a much larger aspect ratio than triangular / tetrahedral cells. A large aspect ratio in a triangular / tetrahedral cell will invariably affect the skewness of the cell,

which is undesirable as it may impede accuracy and convergence. Therefore, if there is a relatively simple geometry in which the flow conforms well to the shape of the geometry, such as a long thin duct, it had better to use a mesh of high aspect-ratio quadrilateral/hexahedral cells. The mesh is likely to have far fewer cells than using triangular/tetrahedral cells (FLUENT User's Guide, 2002).

Another crucial process during grid generation is to use sizing function properties of GAMBIT processor. Sizing function controls mesh distribution in a region of space (edges, faces, and volumes) in a manner analogous to the way grading controls mesh distribution on edges. There are three sizing function type in GAMBIT. These are: Fixed, Curvature and Proximity. Fixed type sizing function is used in this study. The target of using this capability is to provide good grid resolution near the valve region of engine cylinder. As it is known, valve regions have highly curvature structure and there are too much gradient differences especially, in velocity value. In order to compensate these features, mesh density was increased near this region. In other words, sizing function property was used. This is shown in an example of 3d model in Figure 3.19.

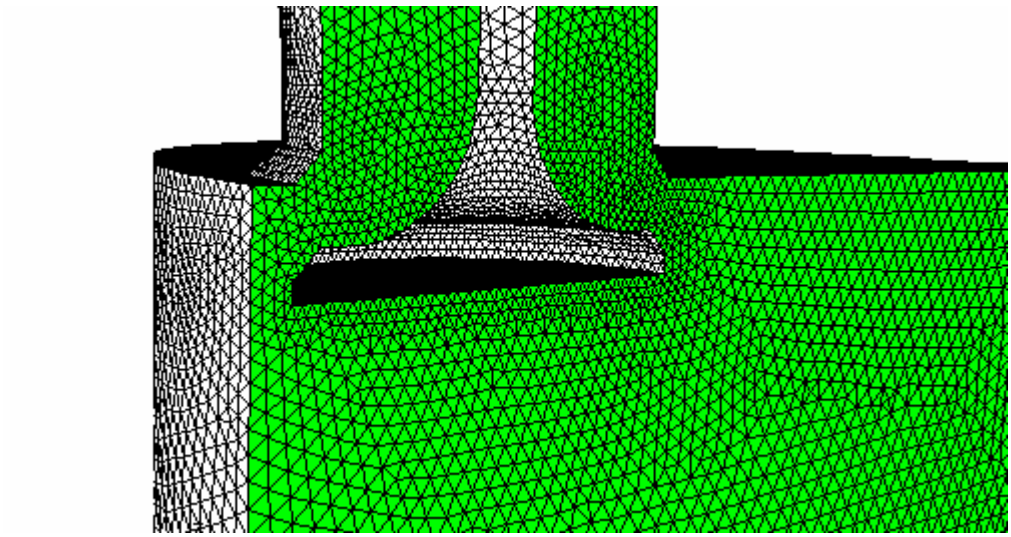


Figure 3.19 An illustration of sizing function capability near the valve region

It is clear to see in Figure 3.19 that grid elements near the valve region are smaller than other elements in the rest of the domain. If small elements are used entire domain, there are many unnecessary elements and this causes too much calculation time. On the other hand, big elements cause not to predict gradient changes well near the valve region.

As it was mentioned before, Tgrid program was used to refine mesh quality more in some 3d models. After using refinement tools of GAMBIT, there can be some highly skewed elements and negative volumes. Since FLUENT solver can not begin a calculation, these skewed elements and negative volumes must be removed by Tgrid. Not only does Tgrid help to remove these undesirable conditions but it also help to refine grid structure and to increase grid quality. In this study, all of the 3d models were exported to Tgrid and grid refinement was made for all of them. This process was not needed for 2d studies since GAMBIT processor was sufficient to generate good quality grid for 2d models.

3.5.3 Grid Quality

The quality of the grid plays a significant role in the accuracy and stability of the numerical computation. The attributes associated with grid quality are node point distribution, smoothness, and skewness.

Since there is discretely defining a continuous domain, the degree to which the salient features of the flow (such as shear layers, separated regions, shock waves, boundary layers, and mixing zones) are resolved depends on the density and distribution of nodes in the grid. In many cases, poor resolution in critical regions can dramatically alter the flow characteristics. For example, the prediction of separation due to an adverse pressure gradient depends heavily on the resolution of the boundary layer upstream of the point of separation.

Proper resolution of the grid for turbulent flows is also very important. Due to the strong interaction of the mean flow and turbulence, the numerical results for turbulent flows tend to be more susceptible to grid dependency than

those for laminar flows. In the near-wall region, different mesh resolutions are required depending on the near-wall model being used.

Rapid changes in cell volume between adjacent cells translate into larger truncation errors. Truncation error is the difference between the partial derivatives in the governing equations and their discrete approximations. FLUENT solver provides the capability to improve the smoothness by refining the mesh based on the change in cell volume or the gradient of cell volume.

The shape of the cell (including its skewness and aspect ratio) also has a significant impact on the accuracy of the numerical solution. Skewness can be defined as the difference between the cell's shape and the shape of an equilateral cell of equivalent volume. Highly skewed cells can decrease accuracy and destabilize the solution. For example, optimal quadrilateral meshes will have vertex angles close to 90 degrees, while triangular meshes should preferably have angles of close to 60 degrees and have all angles less than 90 degrees.

Defining of the quality was also a major problem in this study. Especially, it was difficult to increase the quality criteria to exact value in 3d studies. Complex valve geometry and cylinder head geometry tend to generate highly skewed grid structure. In order to generate good grid quality, skewness quality criteria, which is default quality measurement tool in GAMBIT, is used. There were also some grid refinement and smoothness procedure that were made in GAMBIT and TGrid in order to reduce coarse grid level, and to have desirable quality. In order to obtain good grid quality in computational domain, value of skewness should be at least acceptable level as it is shown in Table 3.1.

Table 3.1 Quality measurement based on skewness (FLUENT User's Guide, 2002)

Value of Skewness	**Excellent**	**Good**	**Acceptable**	**Poor**	**Sliver**	**Degenerate**
Cell Quality	0-0.25	0.25-0.50	0.50-0.80	0.80-0.95	0.95-0.99	0.99-1.00

As it is mentioned before, since grid quality criteria for 2d studies are sufficient in most of the models, there is no necessity to use grid refinement tools in any other program. 2d models used in this study have excellent or good cell quality range. But this is not always the case for some 3d models that can reach sometimes 0.7 and 0.8 level. Nevertheless they are still in acceptable range of cell quality. But refinement tools in TGrid were always carried out regardless of their situation and 0.7 and 0.8 level were tried to reduce below 0.5 or 0.6 levels in order to obtain better accuracy and fast convergence.

3.5.4 Grid Independency

It should be tested whether the converged results obtained so far are independent of the grid resolution. In order to do this, it should be either uniformly doubled the total cell count, or used the grid adaptation feature of the FLUENT solver to achieve the objective more efficiently.

Grid independence is attained when further mesh refinement yields only small and insignificant changes in the solution fields. It can be used many possible criteria to adapt the mesh. Velocity gradient adaptation procedure was used in this study to calculate velocity value more accurate. Figure 3.20 shows one of the 2d models before any adaptation process is made.

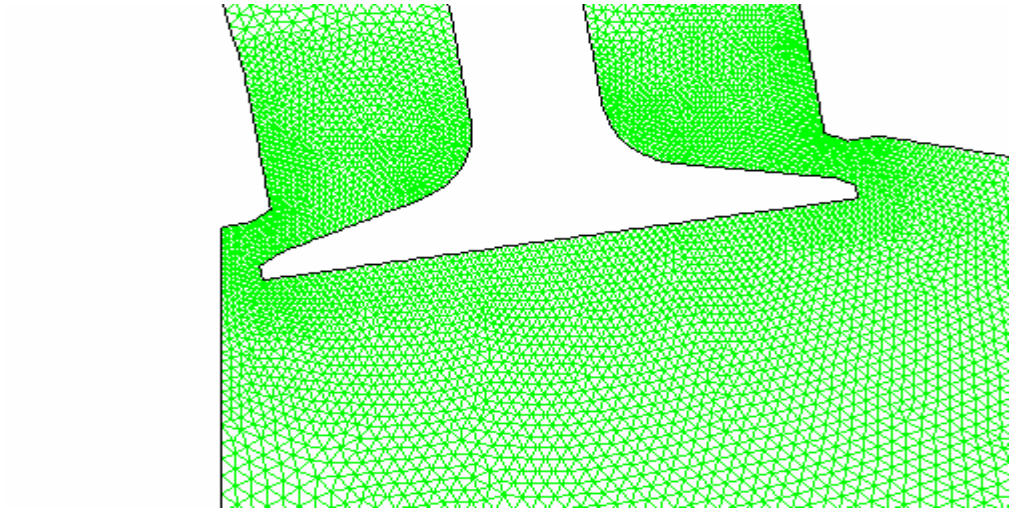


Figure 3.20 A view of 2d model before adaptation

After using adaptation process, FLUENT define which place needs adaptation as it is shown in Figure 3.21. As it is noted in figure, these regions are such places that velocity gradient changes a lot. Once this grid transformation finishes, FLUENT changes grid structure (Figure 3.22) so that entire domain needs calculation again.



Figure 3.21 Marking of adaptation places.

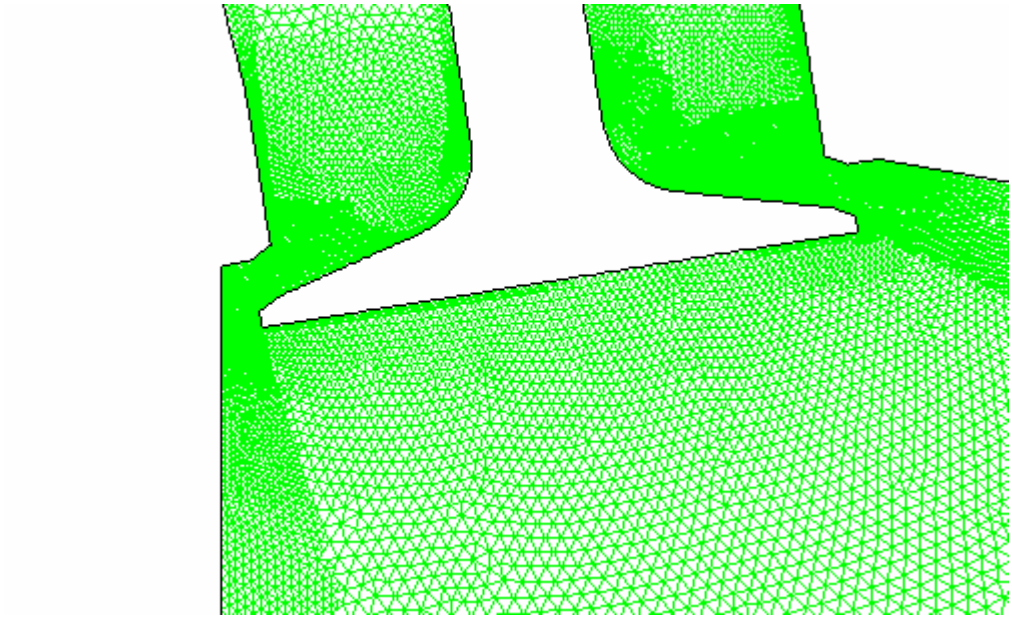


Figure 3.22 A view of 2d model after adaptation.

Once whole adaptation process finishes, calculation can be started. Then two results (before and after adaptation) might be compared. Should there are not significant differences; it means that problem is a grid independent anymore. This adaptation capability was used most of the 2d and 3d models if there is convergence problem and differences between adapted grid and normal grid results.

3.6 Finite Approximations

After the choice of grid type, one has to select the approximations to be used in the discretization process. In a finite difference method, approximations for the derivatives at the grid points have to be selected. In a finite volume method, one has to select the methods of approximating surface and volume integrals. In a finite element method, one has to choose the shape functions (elements) and weighting functions.

There are many possibilities to choose which method is suitable. The choice influences the accuracy of the approximation. It also affects the difficulty of developing solution method, coding it, debugging it, and the speed of the code. More accurate

approximations involve more nodes and give fuller coefficient matrices. The increased memory necessity may require using coarser grids, partially offsetting the advantage of higher accuracy. A compromise between simplicity, ease of implementation, accuracy and computational efficiency has to be made.

3.7 Solution Method

Discretization yields a large system of non-linear algebraic equations. The method of solution depends on the problem. For unsteady flows, methods based on those used for initial value problems for ordinary differential equations (marching in time) are used. At each time step an elliptic problem has to be solved. Steady flow problems are usually solved by pseudo-time marching or an equivalent iteration scheme. Since the equations are non-linear, an iteration scheme is used to solve them. These methods use successive linearization of the equations and the resulting linear systems are always solved by iterative techniques. The choice of solver depends on the grid type and the number of nodes involved in each algebraic equation (Ferziger, 2002).

FLUENT allows choosing either of two numerical methods:

- Segregated solver
- Coupled solver

Using either method, FLUENT will solve the governing integral equations for the conservation of mass and momentum, and (when appropriate) for energy and other scalars such as turbulence and chemical species. In both cases a control-volume-based technique is used that consists of:

1. Division of the domain into discrete control volumes using a computational grid.

2. Integration of the governing equations on the individual control volumes to construct algebraic equations for the discrete dependent variables (“unknowns”) such as velocities, pressure, temperature, and conserved scalars.

3. Linearization of the discretized equations and solution of the resultant linear equation system to yield updated values of the dependent variables.

All solvers formulations will provide accurate results for a broad range of flows, but one formulation may sometimes have better results than the others. The two numerical methods employ a similar discretization process (finite-volume), but the approach used to linearize and solve the discretized equations is different.

The segregated and coupled approaches differ in the way that the continuity, momentum, and (where appropriate) energy and species equations are solved. In case of using the segregated approach, the governing equations are solved sequentially (i.e., segregated from one another). Because the governing equations are non-linear (and coupled), several iterations of the solution loop must be performed before a converged solution is obtained. Each iteration consists of the steps illustrated in Figure 3.23 and outlined below:

1. Fluid properties are updated, based on the current solution. (if the calculation has just begun, the fluid properties will be updated based on the initialized solution.)

2. The *u, v,* and *w* momentum equations are each solved in turn using current values for pressure and face mass fluxes, in order to update the velocity field.

3. Since the velocities obtained in step 2 may not satisfy the continuity equation locally, a "Poisson-type" equation for the pressure correction is derived from the continuity equation and the linearized momentum equations. This pressure correction equation is then solved to obtain the necessary corrections to the pressure and velocity fields and the face mass fluxes such that continuity is satisfied.

4. Where appropriate, equations for scalars such as turbulence, energy, species, and radiation are solved using the previously updated values of the other variables.

5. When interphase coupling is to be included, the source terms in the appropriate continuous phase equations may be updated with a discrete phase trajectory calculation.

6. A check for convergence of the equation set is made.

These steps are continued until the convergence criteria are found.

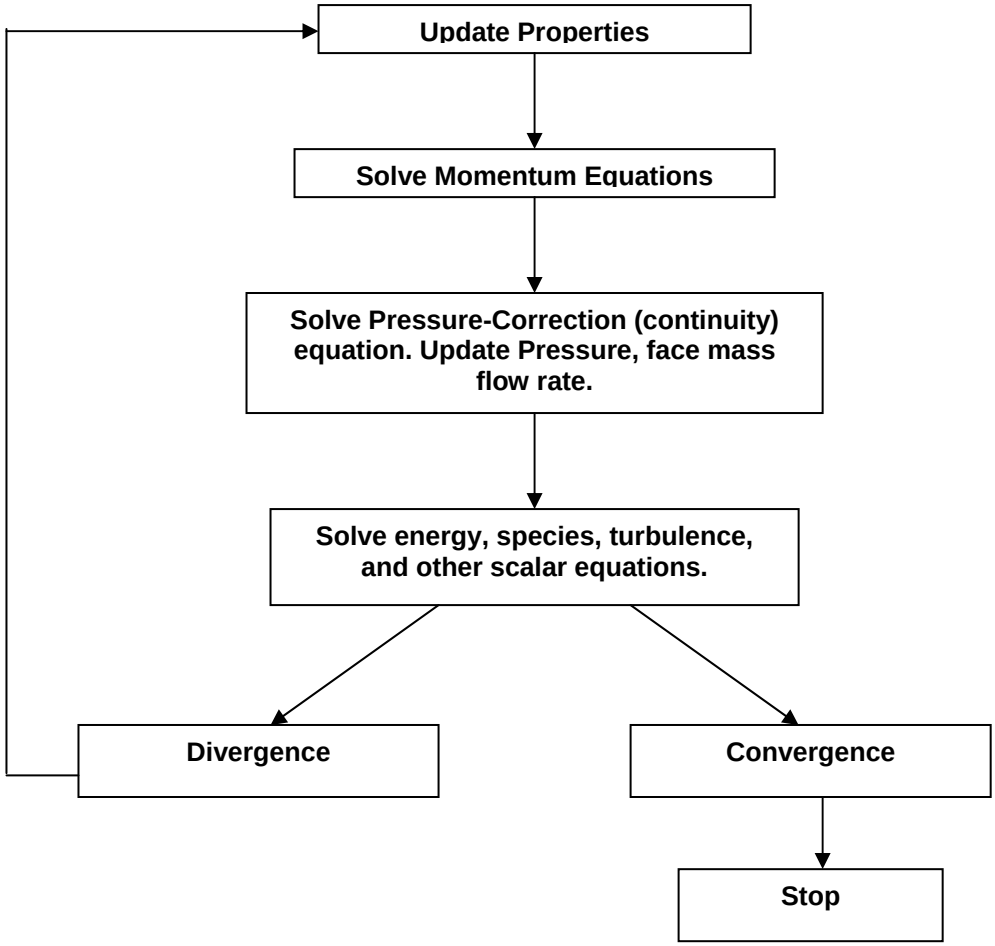


Figure 3.23 Overview of the Segregated Solution Method

The coupled solver solves the governing equations of continuity, momentum, and (where appropriate) energy and species transport simultaneously (i.e., coupled together). Governing equations for additional scalars will be solved sequentially (i.e., segregated from one another and from the coupled set) using the procedure described for the segregated solver above. Because the governing equations are non-linear (and coupled), several iterations of the solution loop must be performed before a converged solution is obtained. Each iteration consists of the steps outlined below:

1. Fluid properties are updated, based on the current solution. (If the calculation has just begun, the fluid properties will be updated based on the initialized solution.).

2. The continuity, momentum and (where appropriate) energy and species equations are solved simultaneously.

3. Where appropriate, equations for scalars such as turbulence and radiation are solved using the previously updated values of the other variables.

4. When interphase coupling is to be included, the source term in the appropriate continuous phase equations may be updated with a discrete phase trajectory calculation.

5. A check for convergence of the equation set is made.

These steps are continued until the convergence criteria are met.

In this study, segregated scheme was used in order to find flow domain results. Since the flow velocity is low in the intake port (approximately 1.954 m/s), using of segregated solution method is recommended by the solver settings. Coupled scheme is used for compressible and high velocity flows (FLUENT User's Guide, 2002).

3.7.1 Linearization

In both the segregated and coupled solution methods the discrete, non-linear governing equations are linearized to produce a system of equations for the dependent variables in every computational cell. The resultant linear system is then solved to yield an updated flow-field solution.

The manner in which the governing equations are linearized may take an "implicit" or "explicit" form with respect to the dependent variable (or set of variables) of interest. By implicit, it is meant that for a given variable, the unknown value in each cell is computed using a relation that includes both existing and unknown values from neighboring cells. Therefore each unknown will appear in more than one equation in the system, and these equations must be solved simultaneously to give the unknown quantities. On the other hand, for a

given variable, the unknown value in each cell is computed using a relation that includes only existing values in explicit method. Therefore each unknown will appear in only one equation in the system and the equations for the unknown value in each cell can be solved one at a time to give the unknown quantities (FLUENT User's Guide, 2002).

3.8 Convergence Criteria

When using iterative solvers, it is important to know when to quit. The most common procedure is based on the difference between two successive iterates; the procedure is stopped when this difference, measured by some norm, is less than a pre-selected value. Usually, there are two levels of iterations: inner iterations, within which the linear equation are solved, and outer iterations, that deal with the non-linearity and coupling of the equations. Deciding when to stop the iterative process on each level is important, from both the accuracy and efficiency points of view.

As convergence criteria, each run were set to be values between 1.0 e^{-5} and 1.0 e^{-6} for RMS (root-mean-square) residuals of equations. Some equations sometimes reached 1.0 e^{-8} value. But in order to have fully converged results, all of the equations have to be converged to a predefined value.

3.9 Turbulence Model

Turbulence modeling is one of three key elements in Computational Fluid Dynamics (CFD). Very precise mathematical theories have evolved for the other two key elements, grid generation and algorithm development. By its nature, in creating a mathematical model that approximates the physical behavior of turbulent flows - far less precision has been achieved in turbulence modeling. Aside from any physical considerations, turbulence is inherently three dimensional and time dependent. Thus, an enormous amount of information is required to completely describe a turbulent flow.

For "small enough" scales and "low enough" velocities, in the sense that the Reynolds number is not too large, the equations of motion for a viscous fluid have well-behaved, steady solutions. Such flows are controlled by viscous diffusion of vorticity and momentum. The motion is termed laminar and can be observed experimentally and in nature. At larger Reynolds numbers, the viscous stresses are overcome by the fluid's inertia, and the laminar motion becomes unstable. Rapid velocity and pressure fluctuations appear and the motion becomes inherently three dimensional and unsteady. When this occurs, it is described the motion as being turbulent. In the cases of fully-developed Couette flow and pipe flow, for example, laminar flow is assured only if the Reynolds number based on maximum velocity and channel height or pipe radius is less than 1500 and 2300, respectively.(Wilcox, 2000)

Virtually all flows of practical engineering interest are turbulent. Flow past vehicles such as rockets, airplanes, ships and automobiles, is always turbulent. 2d and 3d cylinder models that are used in this study have also turbulent characteristic. Even though there is low velocity that is chosen for inlet port, velocity value reaches turbulent level in some sections especially, near valve region.

As it is noted above, Turbulent flows are characterized by fluctuating velocity fields. These fluctuations mix transported quantities such as momentum, energy, and species concentration, and cause the transported quantities to fluctuate as well. Since these fluctuations can be of small scale and high frequency, they are too computationally expensive to simulate directly in practical engineering calculations. Instead, the instantaneous (exact) governing equations can be time-averaged, ensemble-averaged, or otherwise manipulated to remove the small scales, resulting in a modified set of equations that are computationally less expensive to solve. However, the modified equations contain additional unknown variables, and turbulence models are needed to determine these variables in terms of known quantities.

In turbulent flow calculation, grid generation and selected turbulence model have vital importance. First of all, due to the strong interaction of the mean flow and turbulence, the numerical results for turbulent flows tend to be

more susceptible to grid dependency than those for laminar flows. Therefore fine grid structure is recommended in the regions where the mean flow changes rapidly. Turbulence model selection is also important action during calculation. It is an unfortunate fact that no single turbulence model is universally accepted as being superior for all classes of problems. The choice of turbulence model will depend on considerations such as the physics encompassed in the flow, the established practice for a specific class of problem, the level of accuracy required, the available computational resources, and the amount of time available for the simulation. In order to make the most appropriate choice of model, it is needed to understand the capabilities and limitations of the various options. In order to find out which turbulence method is suitable in this study, several example was solved.

CFD solver program that is used in this study is talent of solving some turbulence models such as, Spalart-Allmaras, k-ε, k-ω, Reynolds Stress, LES model etc. k-ε turbulence model was chosen from all of them because of having some advantage. First of all, it has been used in numerous studies up to now especially, in combustion chamber models and engine models. Secondly its usage requires less computational cost per iteration than usage of other models that are mentioned above.

The simplest "complete models" of turbulence are two-equation models in which the solution of two separate transport equations allows the turbulent velocity and length scales to be independently determined. The standard k-ε model in FLUENT falls within this class of turbulence model and has become the workhorse of practical engineering flow calculations in the time since it was proposed. Robustness, economy, and reasonable accuracy for a wide range of turbulent flows explain its popularity in industrial flow and heat transfer simulations. It is a semi-empirical model, and the derivation of the model equations relies on phenomenological considerations and empiricism (Launder and Spalding, 1972).

As the strengths and weaknesses of the standard k-ε model have become known, improvements have been made to the model to improve its performance.

There are two strong *k-ε* models exist in FLUENT solver: RNG *k-ε* model and realizable *k-ε* model.

The RNG *k-ε* model was derived using a rigorous statistical technique (called renormalization group theory). It is similar in form to the standard *k-ε* model, but includes the following refinements:

- The RNG model has an additional term in its *ε* equation that significantly improves the accuracy for rapidly strained flows.
- The effect of swirl on turbulence is included in the RNG model, enhancing accuracy for swirling flows.
- The RNG theory provides an analytical formula for turbulent Prandtl numbers, while the standard *k-ε* model uses user-specified, constant values.
- While the standard *k-ε* model is a high-Reynolds-number model, the RNG theory provides an analytically derived differential formula for effective viscosity that accounts for low-Reynolds-number effects. Effective use of this feature does, however, depend on an appropriate treatment of the near-wall region.

These features make the RNG *k-ε* model more accurate and reliable for a wider class of flows than the standard *k-ε* model.

The RNG-based *k-ε* turbulence model is derived from the instantaneous Navier-Stokes equations, using a mathematical technique called "renormalization group" (RNG) methods. The analytical derivation results in a model with constants different from those in the standard *k-ε* model, and additional terms and functions in the transport equations for *k* and *ε*. (FLUENT User's Guide, 2002).

$$\frac{\partial}{\partial t}(\rho k) + \frac{\partial}{\partial x_i}(\rho k u_i) = \frac{\partial}{\partial x_j}(\alpha k \mu_{eff} \frac{\partial k}{\partial x_j}) + G_k + G_b - \rho\varepsilon - Y_M + S_k \qquad (3.8)$$

and

$$\frac{\partial}{\partial t}(\rho\varepsilon)+\frac{\partial}{\partial x_i}(\rho\varepsilon u_i)=\frac{\partial}{\partial x_j}(\alpha_\varepsilon\mu_{eff}\frac{\partial\varepsilon}{\partial x_j})+C_{1\varepsilon}\frac{\varepsilon}{k}+(G_k+C_{3\varepsilon}G_b)-C_{2\varepsilon}\rho\frac{\varepsilon^2}{k}-R_\varepsilon-S_\varepsilon$$

(3.9)

In these equations, G_k represents the generation of turbulence kinetic energy due to the mean velocity gradients, G_b is the generation of turbulence kinetic energy due to buoyancy. Y_M represents the contribution of the fluctuating dilatation in compressible turbulence to the overall dissipation rate. The quantities α_k and α_ε are the inverse effective Prandtl numbers for k and ε, respectively. S_k and S_ε are user defined source terms.

In this study, default values of $C_{1\varepsilon}$ and $C_{2\varepsilon}$ constants in solver were used. They are $C_{1\varepsilon}$ = 1.42 and $C_{2\varepsilon}$ = 1.68 respectively.

Another *k*-ε turbulence model is realizable *k*-ε turbulence model that was used for comparing with standard *k*-ε and RNG *k*-ε turbulence model in this study. The realizable *k*-ε model is a relatively recent development and differs from the standard *k*-ε model in two important ways:

- The realizable *k*-ε model contains a new formulation for the turbulent viscosity.
- A new transport equation for the dissipation rate, ε, has been derived from an exact equation for the transport of the mean-square vorticity fluctuation.

The term "realizable" means that the model satisfies certain mathematical constraints on the Reynolds stresses, consistent with the physics of turbulent flows. Neither the standard *k*-ε model nor the RNG *k*-ε model is realizable.

An immediate benefit of the realizable *k*-ε model is that it more accurately predicts the spreading rate of both planar and round jets. It is also likely to provide superior performance for flows involving rotation, boundary layers under strong adverse pressure gradients, separation, and recirculation.

Both the realizable and RNG k-ε models have shown substantial improvements over the standard k-ε model where the flow features include strong streamline curvature, vortices, and rotation. Since the model is still relatively new, it is not clear in exactly which instances the realizable k-ε model consistently outperforms the RNG model. However, initial studies have shown that the realizable model provides the best performance of all the k-ε model versions for several validations of separated flows and flows with complex secondary flow features.

The modeled transport equations for k and ε in the realizable k-ε model are

$$\frac{\partial}{\partial t}(\rho k)+\frac{\partial}{\partial x_i}(\rho k u_j)=\frac{\partial}{\partial x_i}\left[\left(\mu+\frac{\mu_t}{\sigma_k}\right)\frac{\partial k}{\partial x_j}\right]+G_k+G_b-\rho\varepsilon-Y_M+S_k \tag{3.10}$$

$$\frac{\partial}{\partial t}(\rho \varepsilon)+\frac{\partial}{\partial x_j}(\rho \varepsilon u_j)=\frac{\partial}{\partial x_j}\left[\left(\mu+\frac{\mu_t}{\sigma_\varepsilon}\right)\frac{\partial \varepsilon}{\partial x_j}\right]+\rho C_1 S_\varepsilon-\rho C_2\frac{\varepsilon^2}{k+\sqrt{\nu\varepsilon}}+C_{1\varepsilon}\frac{\varepsilon}{k}C_{3\varepsilon}G_b+S_\varepsilon \tag{3.11}$$

where

$$C_1=\max\left[0.43,\frac{\eta}{\eta+5}\right],\quad \eta=S\frac{k}{\varepsilon}$$

In these equations, G_k represents the generation of turbulence kinetic energy due to the mean velocity gradients, G_b is the generation of turbulence kinetic energy due to buoyancy, Y_M represents the contribution of the fluctuating dilatation in compressible turbulence to the overall dissipation rate, and C_2 and $C_{1\varepsilon}$ are constants. σ_k and σ_ε are the turbulent Prandtl numbers for k and ε, respectively. S_k and S_ε are user-defined source terms and model constants that were used in this study are: $C_{1\varepsilon}$ = 1.44, C_2 = 1.9, σ_k=1.0 and finally σ_ε = 1.2.

All models in 2d and some 3d problems were solved with standard, RNG and realizable k-ε turbulence models in this study. After some implementation, it was decided not to use of standard k-ε turbulence models all 3d models especially, after proving its weak side over other two k-ε model. This was decided after terminating straight intake pipe model calculation in 3d studies. But all of the turbulence models were used in 2d studies (FLUENT User's Guide, 2002).

3.10 Boundary Conditions

Once the problem has been specified, an appropriate set of boundary conditions must be selected. Boundary types which may be encountered include solid walls, inflow and outflow boundaries, periodic boundaries, symmetry boundaries, etc. The boundary conditions which must be defined depend upon the model and its real life situation. Boundary conditions specify the flow and thermal variables on the boundaries of the physical model. They are therefore, a critical component of CFD simulations and it is important that they are specified appropriately.

As boundary condition, there are several boundary conditions available in FLUENT. They are classified as follows:

- Flow inlet and exit boundaries: pressure inlet, velocity inlet, mass flow inlet, inlet vent, intake fan, pressure outlet, pressure far-field, outflow, outlet vent, exhaust fan.
- Wall, repeating, and pole boundaries: wall, symmetry, periodic, axis.
- Internal cell zones: fluid, solid.
- Internal face boundaries: fan, radiator, porous jump, wall, interior.

In this study, velocity inlet, pressure inlet, pressure outlet, wall and symmetry boundary conditions were used. As internal cell zone, fluid zone was used. Before explaining why these types of boundary conditions were chosen, it had better to give brief information about these boundary conditions first and then their reasons in each paragraph below:

Velocity inlet boundary conditions are used to define the flow velocity, along with all relevant scalar properties of the flow, at flow inlets. The total (or stagnation) properties of the flow are not fixed, so they will rise to whatever value is necessary to provide the prescribed velocity distribution. This boundary condition is intended for incompressible flows, and its use in compressible flows will lead to a nonphysical result. Since velocity value is low in inlet port except dynamic model (V=1.974 m/s) it is assumed to be incompressible. Therefore velocity inlet boundary condition was selected for inlet. Not only this reason has been over weighted for selection but velocity value for same model by Yasar, (2002) was also available.

Pressure outlet boundary conditions define flow exits from computational domain. They require the specification of a static (gauge) pressure at the outlet boundary. The value of static pressure specified is used only while the flow is subsonic. Should the flow become locally supersonic, the specified pressure is no longer used; pressure will be extrapolated from the flow in the interior. All other flow quantities are extrapolated from the interior. A set of “backflow” conditions is also specified to be used if the flow reverses direction at the pressure outlet boundary during the solution process. Convergence difficulties will be minimized if it is specified realistic values for the backflow quantities. The reason why this type of boundary condition was used in this study is that the use of a pressure outlet boundary condition instead of an outflow condition often results in a better rate of convergence when backflow occurs during iteration.

Wall boundary conditions are used to bound fluid and solid regions. In viscous flows, the no-slip boundary condition is enforced at walls by default, but it can be specified a tangential velocity component in terms of the translational or rotational motion of the wall boundary, or model a “slip” wall by specifying shear. Wall boundaries can be either stationary or moving. The stationary boundary condition specifies a fixed wall, whereas the moving boundary condition can be used to specify the translational or rotational velocity of the wall, or the velocity components. Since there is no rotation or translation on the

walls, moving boundary condition was not used in this study. But all of the walls in the models were defined as stationary wall.

Symmetry boundary conditions are used when the physical geometry of interest, and the expected pattern of the flow, have mirror symmetry. They can also be used to model zero-shear slip walls in viscous flows. By using this type of boundary condition, it is possible to reduce the extent of to a symmetric subsection of the overall physical system. Symmetry boundary conditions were used only 3d straight intake pipe model. Since this model can be assumed totally symmetric and there is no normal velocity vector to the symmetric plane, that is most important key factor while using this boundary condition, symmetric condition was selected. Not only this is the main reason why this boundary was used, but the total element number effecting calculation time was also reduced by using this capability. This boundary condition can be seen in 3d straight intake pipe model in geometry creation section clearly.

A fluid zone is a group of cells for which all active equations are solved. The only required input for a fluid zone is the type of fluid material. It must be indicated which material the fluid zone contains so that the appropriate material properties will be used. As a fluid material, air was used to simulate real conditions in this study. Since only fluid motion was investigated, energy equation was not activated during calculation except dynamic grid study. Therefore some values such as temperature and C_p for air was neglected while defining air condition.

3.11 Dynamic Grid Model

The dynamic grid model in FLUENT can be used to model flows where the shape of the domain is changing with time due to motion on the domain boundaries. The motion can be either a prescribed motion (e.g., it can be specified the linear and angular velocities about the center of gravity of a solid body with time) or an unprescribed motion where the subsequent motion is determined based on the solution at the current time (e.g., the linear and

angular velocities are calculated from the force balance on a solid body). The update of the volume mesh is handled automatically by FLUENT at each time step based on the new positions of the boundaries. In order to use the dynamic mesh model, it is necessary to provide a starting volume mesh and the description of the motion of any moving zones in the model. FLUENT allows describing the motion using either boundary profiles or user-defined functions (UDFs).

FLUENT expects the description of the motion to be specified on either face or cell zones. If the model contains moving and non-moving regions, it is necessary to identify these regions by grouping them (faces or cells) into their respective face or cell zones in the starting volume mesh that is generated. Furthermore, regions that are deforming due to motion on their adjacent regions must also be grouped into separate zones in the starting volume mesh. The boundary between the various regions need not be conformal. It can be used the non-conformal or sliding interface capability in FLUENT to connect the various zones in the final model (FLUENT User's Guide, 2002).

In this study, 2d pent-roof cylinder model has been selected to demonstrate how much dynamic grid capability is important. It could have been better if one of the 3d models had been selected. But as it is known, dynamic grid feature needs more CPU time and more calculation effort than other methods. For example basic steady 3d problem with approximately 500.000 elements can require 8 days in order to complete entire calculation by using 3.2 Ghz micro processor and 1 GB RAM. When it is assumed to be unsteady calculation, time requirements can be clearer. 2d model used in this study is shown in Figure 3.24. It has same specifications like 2d steady pent-roof model namely, same geometric features. It was created by author inspiring an engine model that was seen some books.

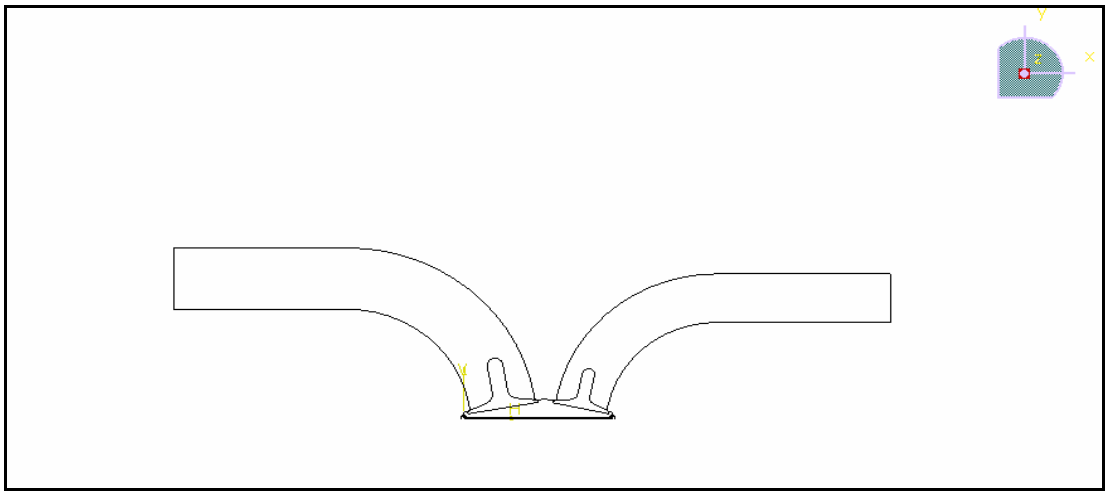


Figure 3.24 2d unsteady model.

As it is seen from figure, piston is in its TDC position and valves are totally close indicating as if combustion process happens. Calculation is not started from this position. This position was created for only grid generation. Calculation starts 345 CA just before inlet valve opens. Table 3.2 shows some initial and necessary parameters about calculation process.

Table 3.2 Dynamic grid parameters for 2d model

Crank shaft speed (rpm)	1500
Starting crank angle (deg)	345
Crank period (deg)	720
Crank angle step size (deg)	0.25
Piston stroke (mm)	120
Connection rod length (mm)	170
Piston stroke cut off (mm)	10
Maximum valve lift (mm)	0.4

FLUENT provides a built-in function to calculate the piston location as a function of crank angle. If the piston motion is specified using this function, it is needed to specify the piston stroke and connection rod length. The piston stroke cut-off and minimum valve lift values are used to control the actual values of the valve lift and piston stroke.

Piston motion and other parameters can be specified as they are mentioned in Table 3.2. But the motion of valves has to be defined in different way. In order to define the motion of the valves, it is necessary to use profiles that describe the variation of valve lift with crank angle. The actual valve lift profiles that are used in this dynamic grid model are shown in Figure 3.25.

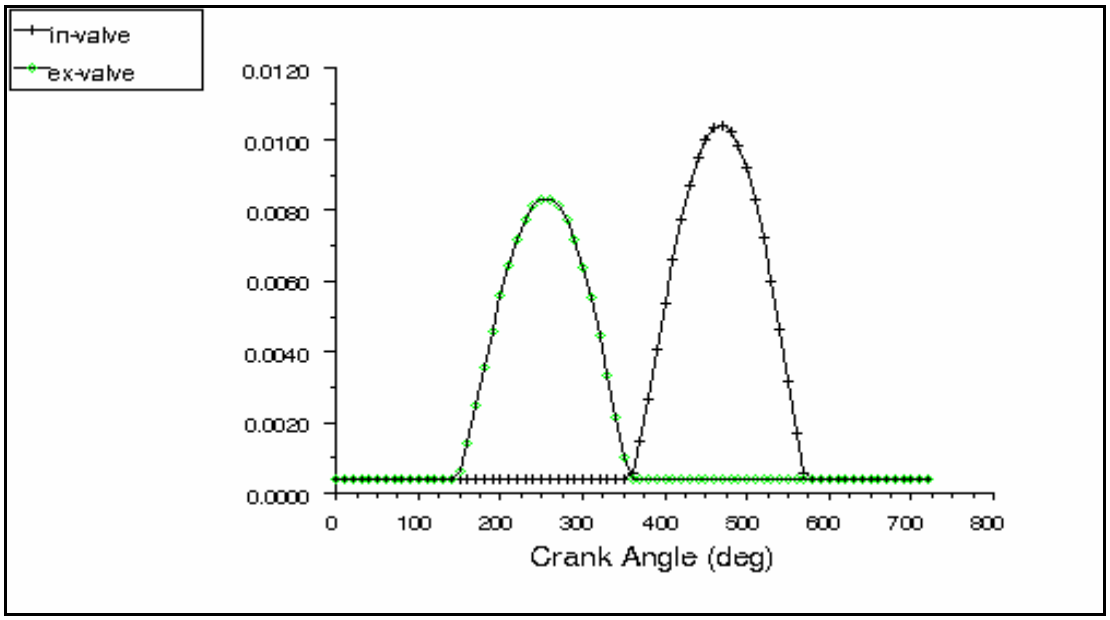


Figure 3.25 The intake and exhaust valve profiles.

Since FLUENT uses SI unit system, lift profiles are accepted as meter. Therefore, y-axis shows lift value as meter in Figure 3.25.

Choosing of calculation and discretization method is similar like 2d steady calculations that were explained before. RNG $k-\varepsilon$ turbulence method and second order discretization methods were also used in this dynamic grid model. In addition

to these similarities, two types of fluid material and species transport model was used as different method. The first and default fluid element is air and second fluid was defined as burned fluid. This fluid material does not contain exactly the burned gasses after combustion process happens. It has same features like air. But it makes a big sense during the calculation in a way how much air can mix with burned gasses and where mixture will move inside of cylinder. This mixture process was modeled using species transport model of FLUENT. Combustion process can be also modeled by using this model. Detailed figures and graphics about mixture process will be shown in Results and Discussion section of this thesis.

4. RESULTS AND DISCUSSION

In this study, the experimental results obtained by Yasar were compared with CFD results and then most convenient methods were carried out all of the models. In order to have same condition with experimental results, cylinder and valve geometries were chosen same condition with real geometries. At the beginning of the calculations on the FLUENT solver, flow domains were characterized by using 2d models. The all solver provider in CFD world suggests the users to begin their calculation in most primitive shape reflecting real geometry. In other words, 2d models are recommended at the beginning of the calculation instead of 3d real geometry. One reason is that 2d models require less memory and hardware necessity and the other is that 2d models need less time for calculation and also have good capability predicting swirl effects and flow characteristics which are created by geometry. This explains why 2d models were created and chosen at the beginning of this study. But 2d models that were calculated for this study do not reflect correct results that were found by Yasar. Because solver program extrapolates one unit entire 2d plane in normal direction in order to calculate mass balance between inlet and outlet and as a results of this action 2d results are not the same with 3d results. Therefore, results from Yasar were used for only comparison of 3d straight intake pipe model.

Convergence was monitored by checking the information from computed residuals of all equations and also by keeping track of surface monitors. In this study both of them were monitored. The convergence criteria for each run were set to be values between 1.0 e^{-5} and 1.0 e^{-6} for RMS (root-mean-square) residuals of mass-momentum equations and $k - \varepsilon$ equations (Figure 4.1). It sometimes reached 1.0 e^{-8} in some residual values but sometimes it oscillated between 1.0 e^{-5} and 1.0 e^{-6} as it is assumed to be converged value. The target of these residual of equations is to have all of equations converged in mentioned value by user.

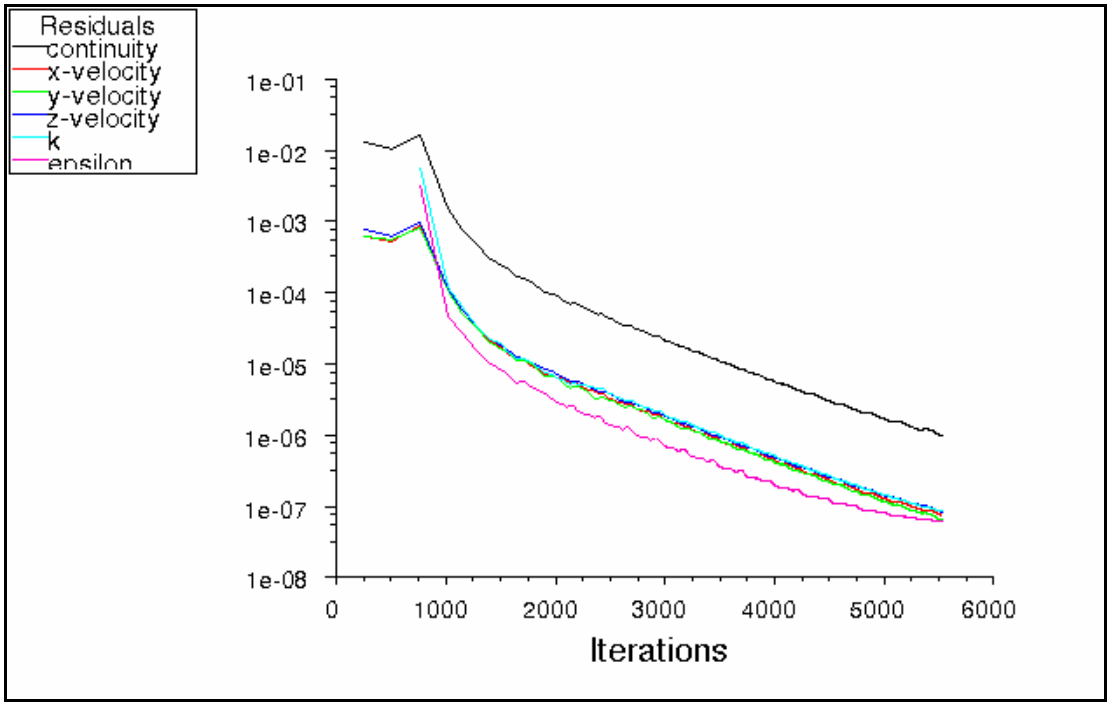


Figure 4.1 A sample of residuals history

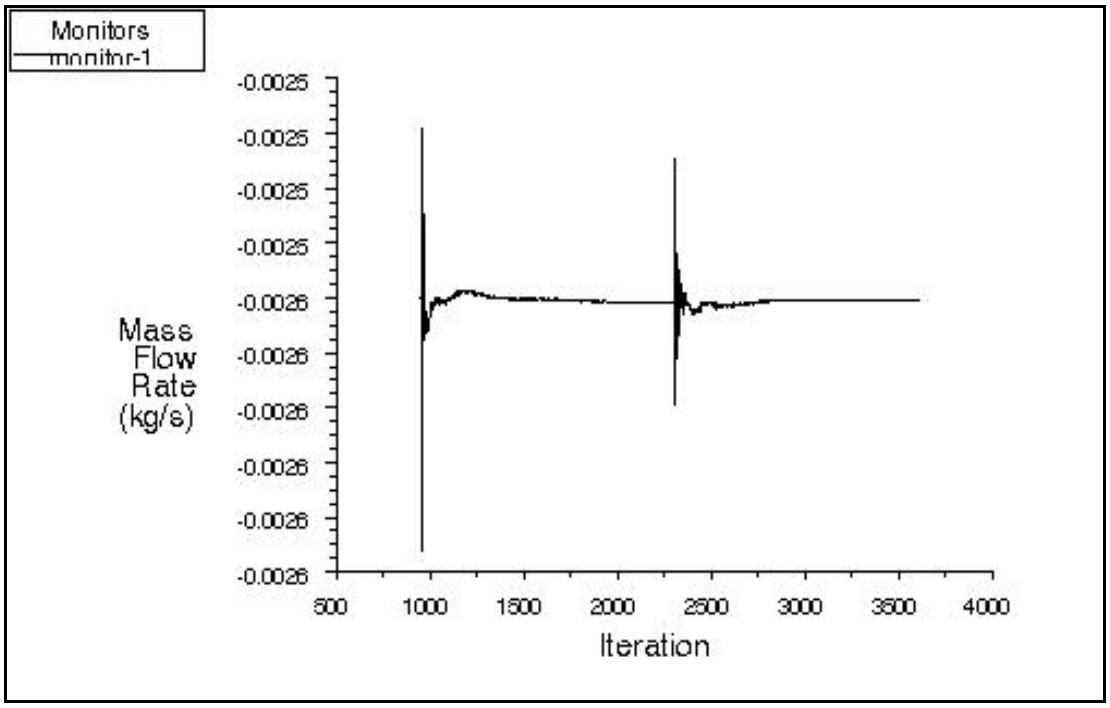


Figure 4.2 A sample of mass flow history on outlet boundary

Convergence criteria were not only performed for all equations but it also monitored on inlet and outlet boundaries. Figure 4.2 shows a sample of mass flow rate on one of the outlet of models. As it is seen from figure, there is a large fluctuation in some periods. Initialization of problem or changing of discretization methods causes this type of fluctuations. This unstable period warns the users that converged solution could not be reached. But after some iteration, it can be seen that solution becomes stable and mass flow on inlet does not change anymore.

Numerical results were performed for 3, 5, 7 and 9 mm valve gap in 2d and 3d models. Measurement points for velocity values were selected 27.5, 58 and 88.5 mm from cylinder head (Figure 4.3).

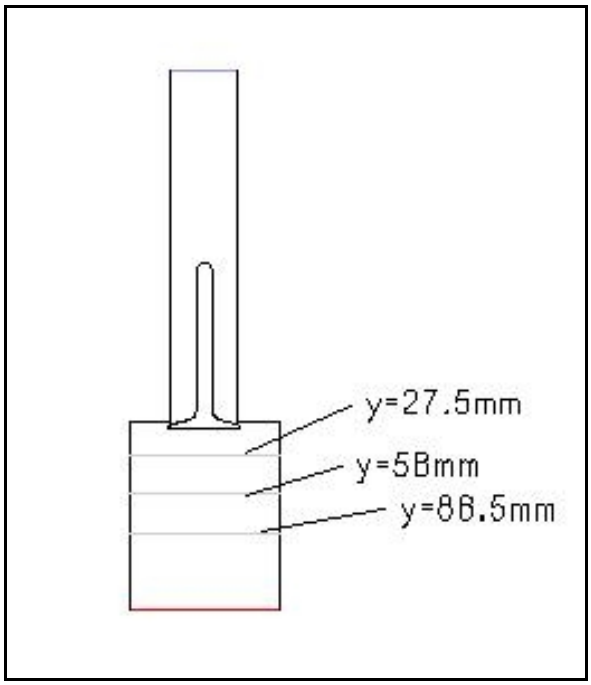


Figure 4.3 Measurement points for 3d calculation.

Before comparing experimental results with numerical results, it had better to characterize flow domains as 2d models.

4.1 Two-Dimensional Calculations

In this section, four cylinder models are considered, details of the model and dimensional properties were explained in Chapter 3. It is easy to see how flow acts inside of cylinder for all 2d models by looking at following figures. 2d models reflect the flow pattern by changing the inlet port and combustion chamber geometry as well as the inlet valve gaps. Moreover, they exactly reflect all undesirable flow effects inside of engine cylinders. In this section, velocity vectors in entire cylinder domain and detailed near valve region velocity vectors will be shown following figures for 3, 5, 7 and 9 mm valve gaps. Standard and RNG $k-\varepsilon$ turbulence models were carried out for all 2d models. As a result of comparing this two turbulence models, it is obtained that RNG $k-\varepsilon$ turbulence model finds more realistic results than standard $k-\varepsilon$ turbulence model. This result is also parallel with recommendations of solver user's guide. Moreover, it will be seen that standard $k-\varepsilon$ model can not predict flow domain well even though it shares same convergence criteria with RNG $k-\varepsilon$ model. These reasons explain why RNG $k-\varepsilon$ model is reliable for this type of applications. As discretization method, first and second order upwind methods are performed all of the calculation respectively. Calculation results will begin with most basic model than others in order to see advantage and disadvantage of model. Therefore first model will be 2d cylinder geometry sharing same center with intake manifold as it is shown in Figure 4.4.

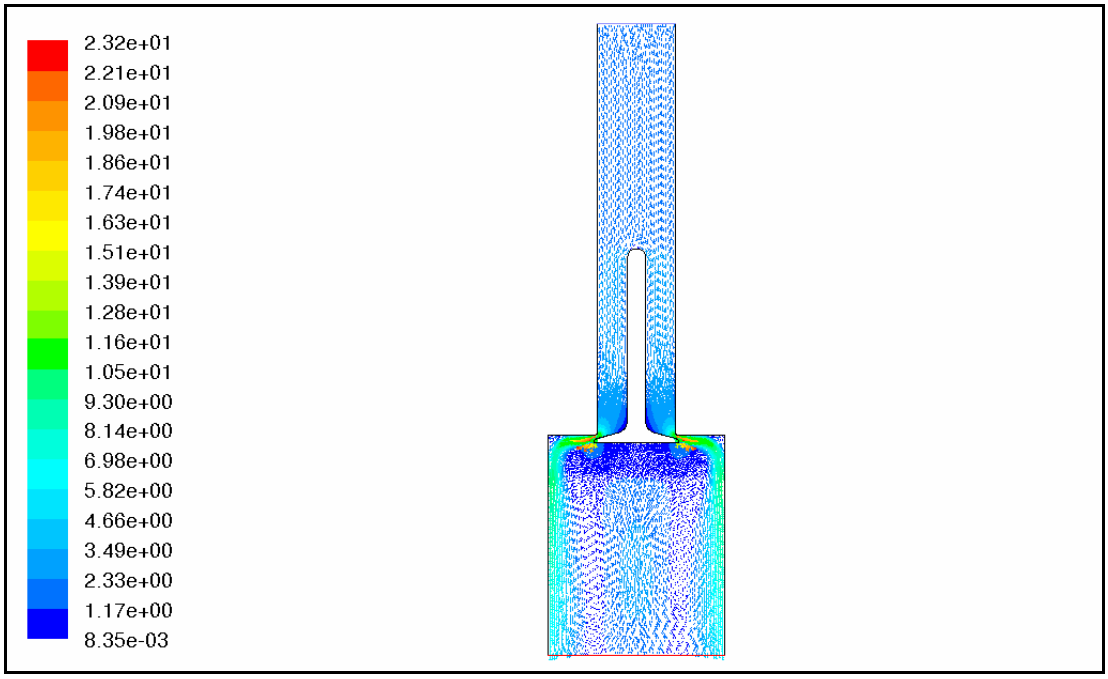
There is a comparison between standard and RNG $k-\varepsilon$ model in all of the 2d models from Figure 4.4 through Figure 4.19. Models are fixed, so that it is also easy to see differences in flow pattern between models. In Figure 4.4 RNG $k-\varepsilon$ model predicts flow domain better than standard model. As it is seen from figure, the jet effect which is created by RNG $k-\varepsilon$ model produces two small jets in head of the cylinder. But standard model has a flow path peeling off cylinder head. The jet effect is created near the valve gap region both of and all of the models because this area is the narrowest flow region in engines. Maximum velocity predictions in both models are nearly the same. It is clear once more time to see weakness of the standard turbulence model in Figure 4.5. In this figure standard model does not

predict flow domain as it is expected. There should have been two jets originated from valve gap. But it was not created. These two cylinder model explain that standard turbulence model does not predict jet flow very well. This result clarifies why an advancing turbulence models should be chosen if there is highly jet effect in model. But jet effect decreases as valve is getting down (Figure 4.6). In this case, both of the turbulence models are in good agreement. As it is seen from Figure 4.6, maximum velocity value is so close in jet area and both of the models have similar back flow characteristic in outlet. In Figure 4.7, jet effect is getting to calm down but flow structure has still same characteristic like other models. In this valve gap (9 mm), the results of two turbulence models are still nearly same. After Figure 4.7 and so on, different cylinder model is considered. The weakness of standard turbulence model still dominates over this model as it is seen from Figure 4.8 to Figure 4.10. Standard turbulence models can not predict places where swirl effect should be created and how much magnitude it should have. But this is not the case for Figure 4.11 since jet effect calms down and results for both turbulence models are almost similar. From Figure 4.12 through Figure 4.15 shows a different cylinder geometry having an intake pipe with radius. It is still easy to see differences between two turbulence models from these figures. But another important thing is that flow generates stronger jet effect in right valve gap area than left area since inlet pipe radius causes this difference. Finally, pent-roof cylinder model results can be seen from Figure 4.16 to Figure 4.19. There are not too many differences between turbulence models except Figure 4.19 that predicts generation of anticlockwise swirl effect near right cylinder head. As it is noticed, pent-roof cylinder model sweep out inside of cylinder better than other models. Despite all of the other models in different valve gaps generate undesirable swirl effects near cylinder head, pent-roof structure does not create swirl until 9 mm valve gap as seen in Figure 4.19.

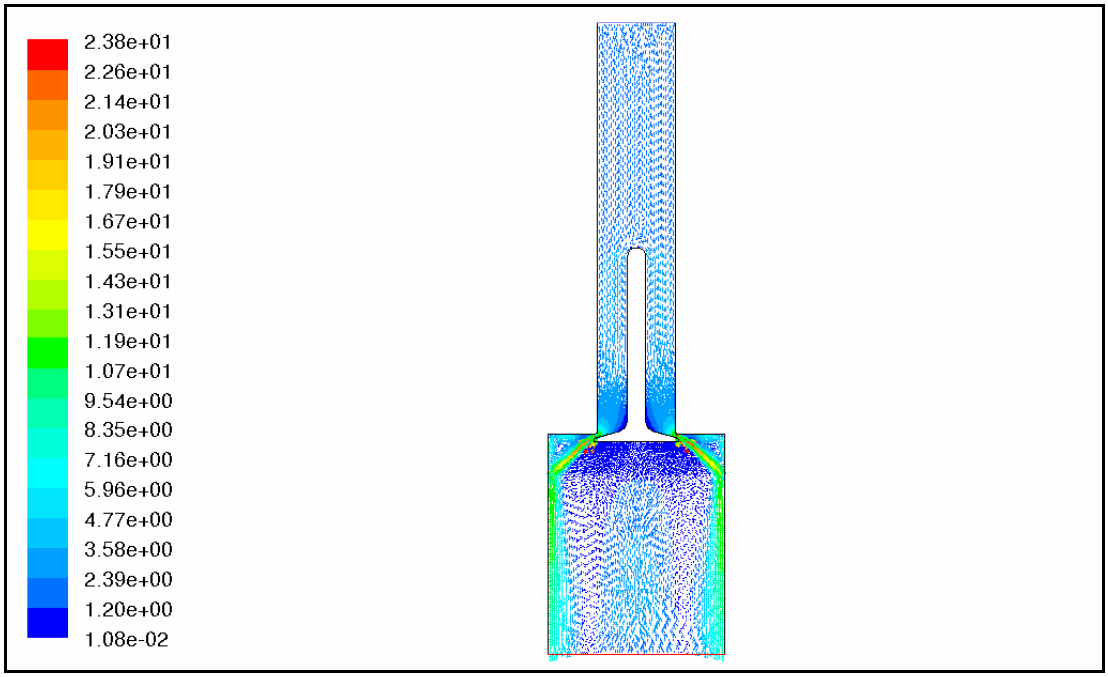
Detailed valve gap regions are illustrated from Figure 4.20 through Figure 4.23. These figures clarify swirl generation and valve jet effect more clearly. These models make some senses in mind of manufacturer in a way of reducing undesirable swirl effects and controlling velocity magnitude in predefined regions. For example,

after being investigated these figures, manufacturer will most probably decide to use pent-roof type cylinder head.

To sum up 2d model calculation, it can be felt that, 2d models can be used for flow visualization, it is difficult to obtain exact numeric results from 2d models as it was mentioned in Chapter 3. In other words, they can be defined as pre-design process before investigating real 3d models. These results and models than can be transferred to complex 3d environment comfortably.

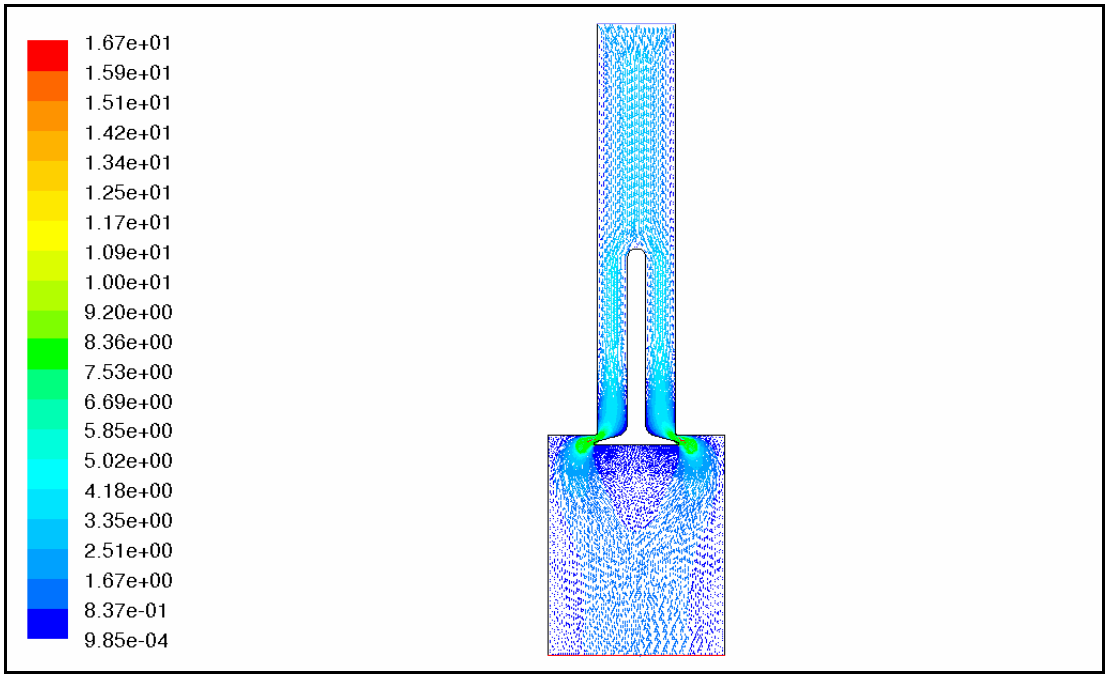


a)

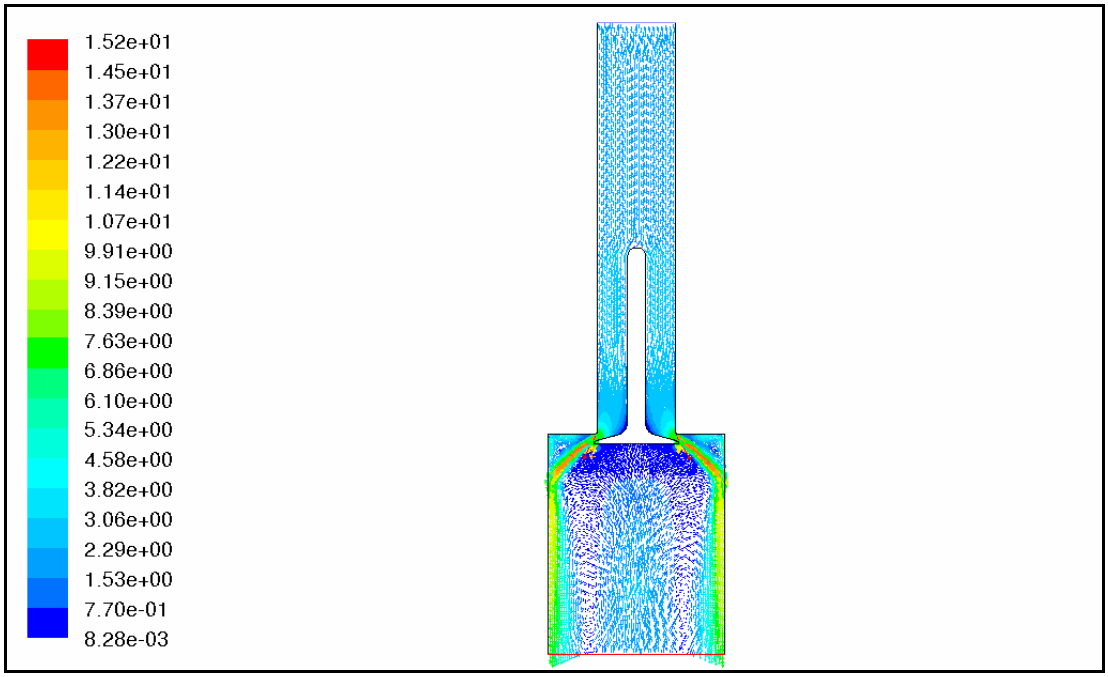


b)

Figure 4.4 Velocity vectors colored by velocity magnitude a) 3 mm valve lift standard turbulence method, b) 3 mm valve lift RNG turbulence method

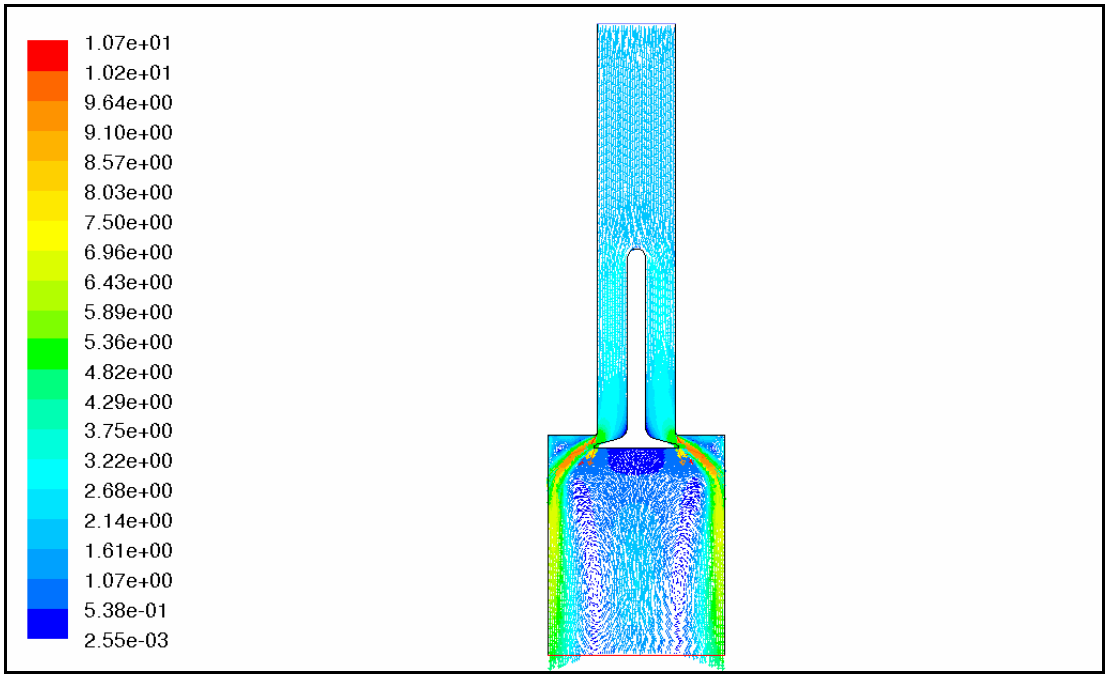


a)

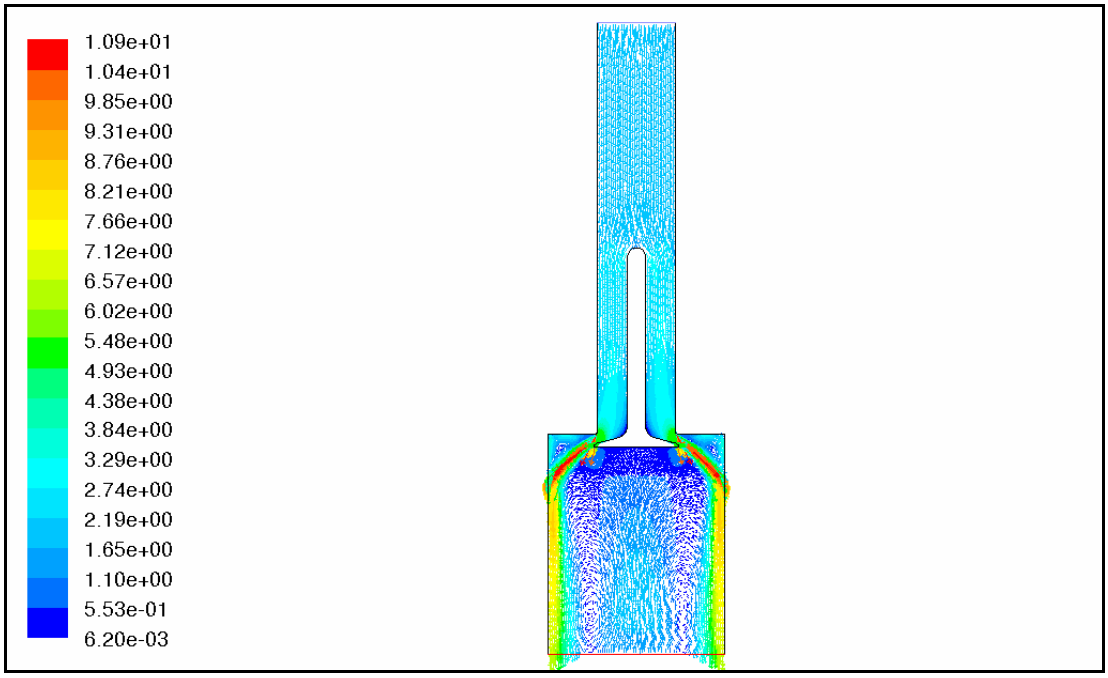


b)

Figure 4.5 Velocity vectors colored by velocity magnitude a) 5 mm valve lift standard turbulence method, b) 5 mm valve lift RNG turbulence method

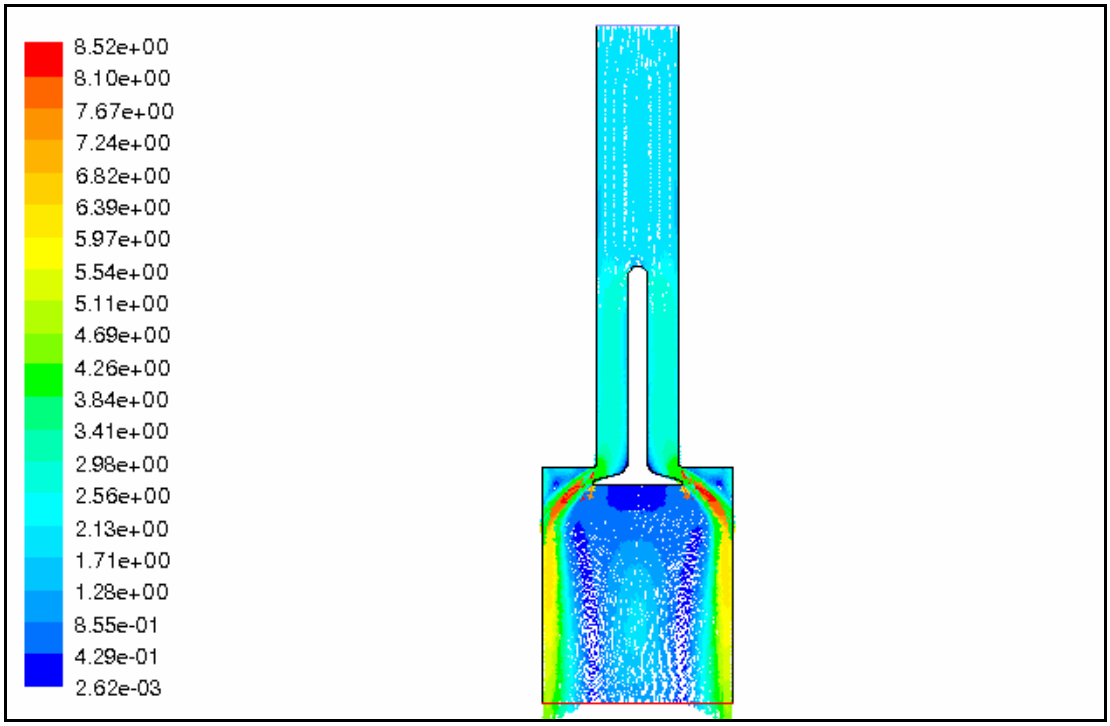


a)

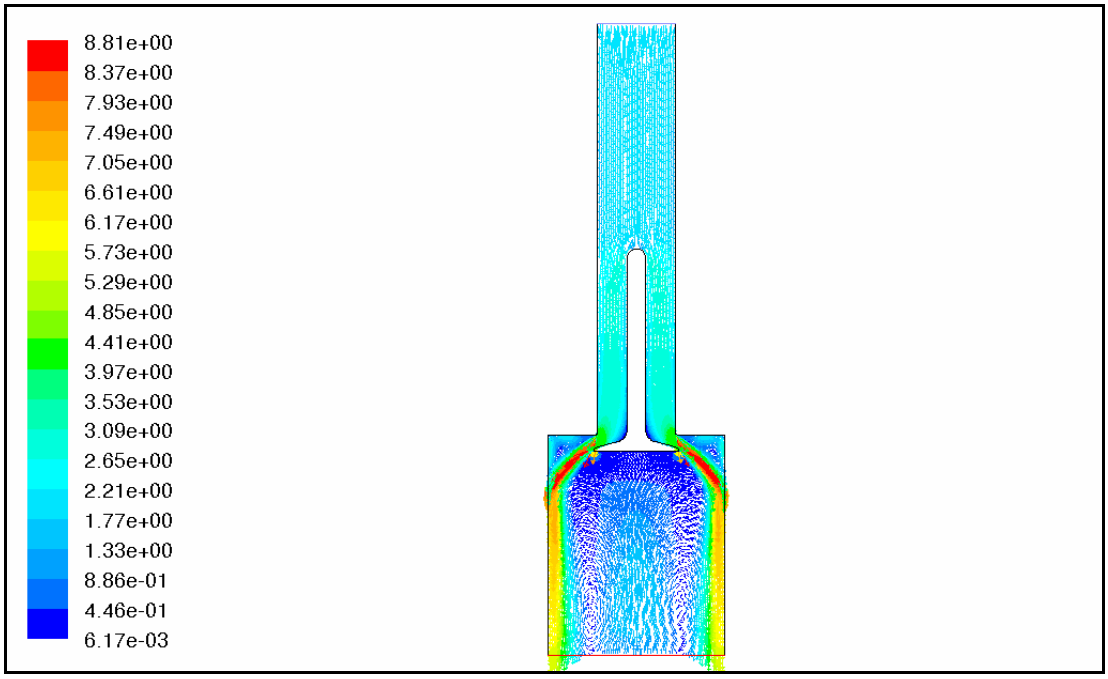


b)

Figure 4.6 Velocity vectors colored by velocity magnitude a) 7 mm valve lift standard turbulence method, b) 7 mm valve lift RNG turbulence method

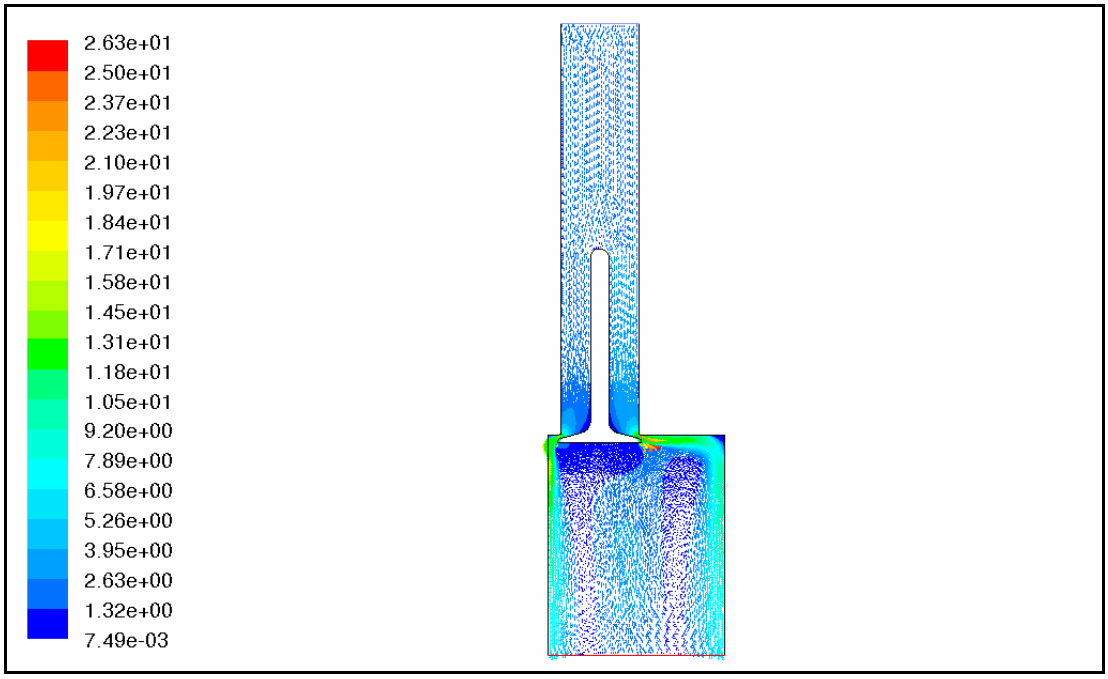


a)

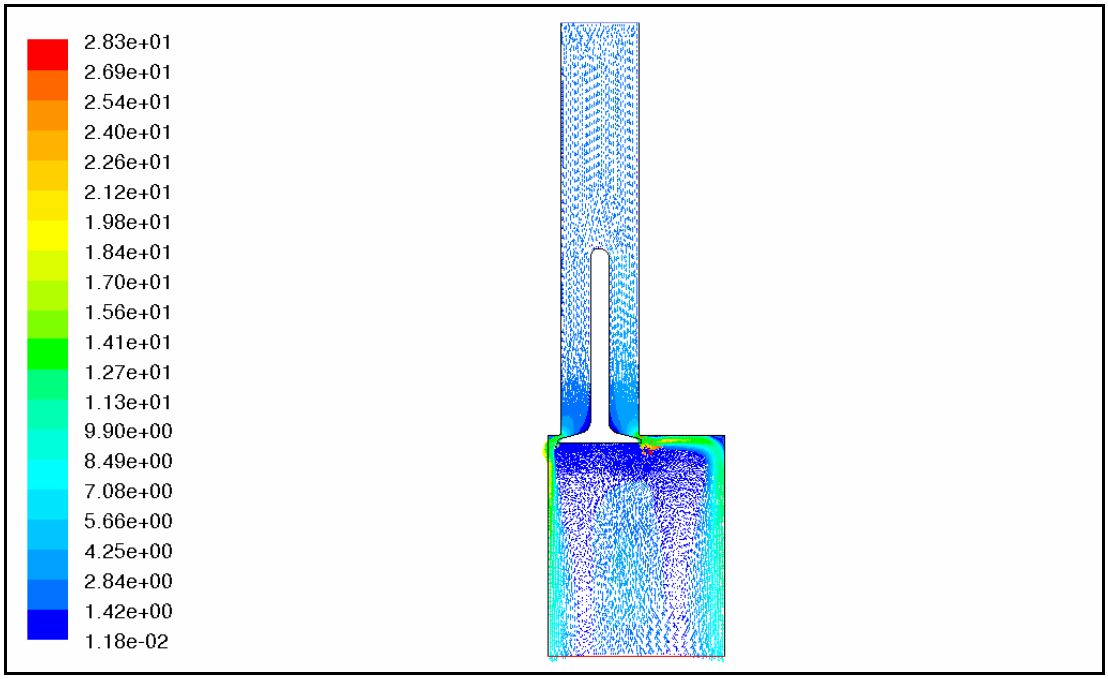


b)

Figure 4.7 Velocity vectors colored by velocity magnitude a) 9 mm valve lift standard turbulence method, b) 9 mm valve lift RNG turbulence method

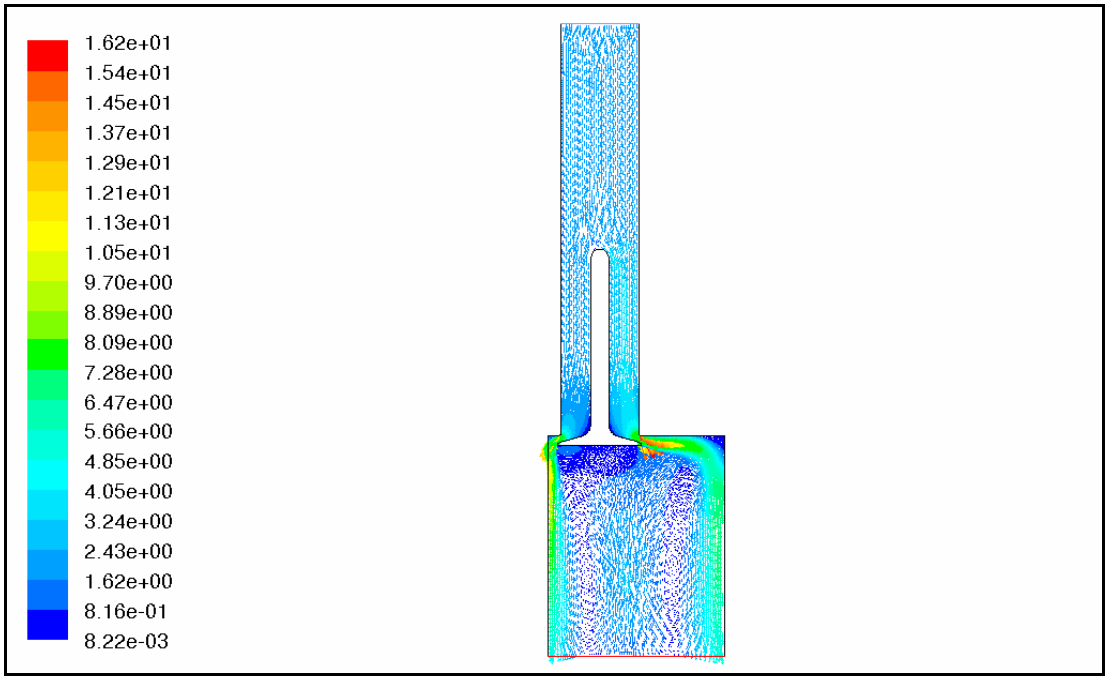


a)

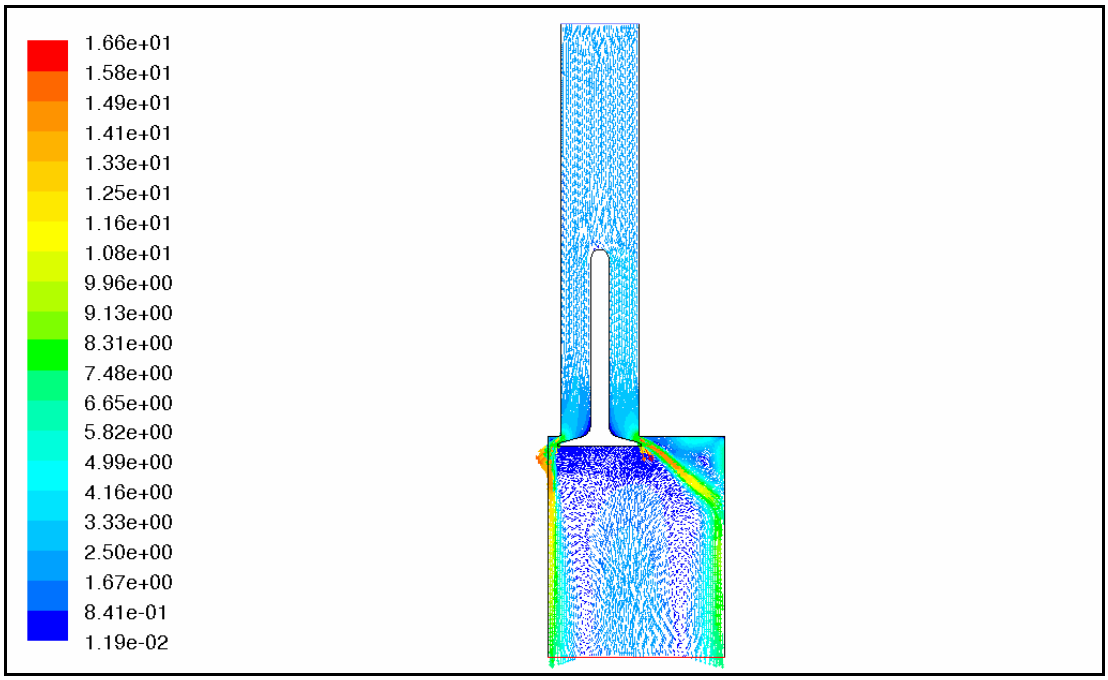


b)

Figure 4.8 Velocity vectors colored by velocity magnitude a) 3 mm valve lift standard turbulence method, b) 3 mm valve lift RNG turbulence method

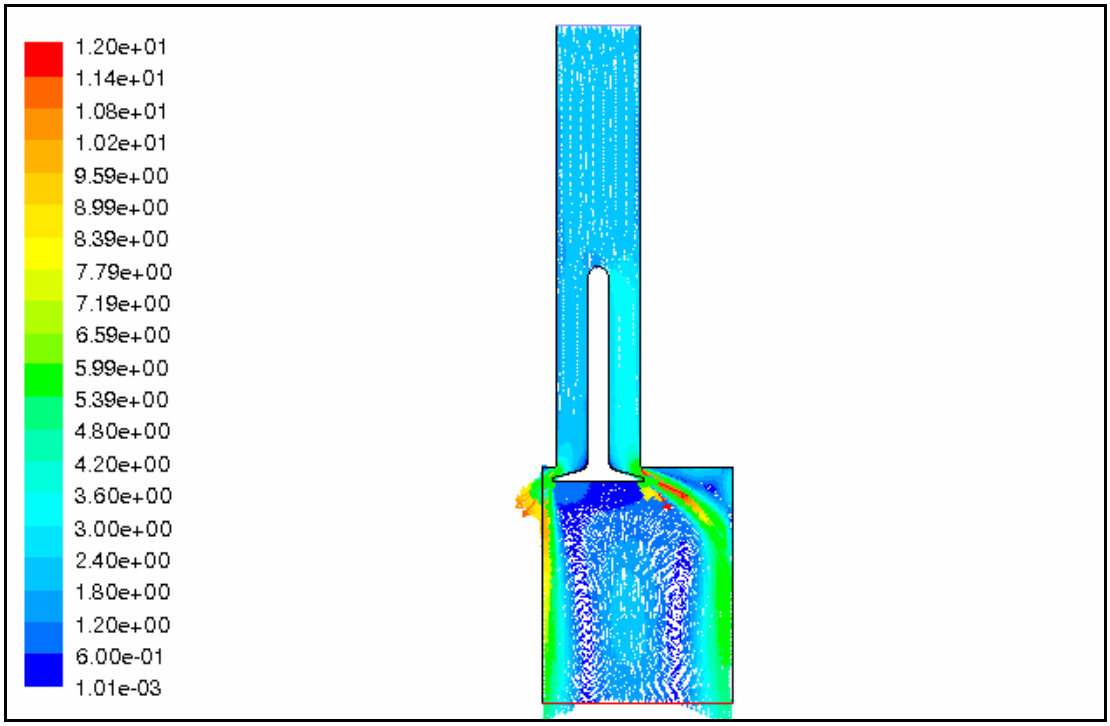


a)

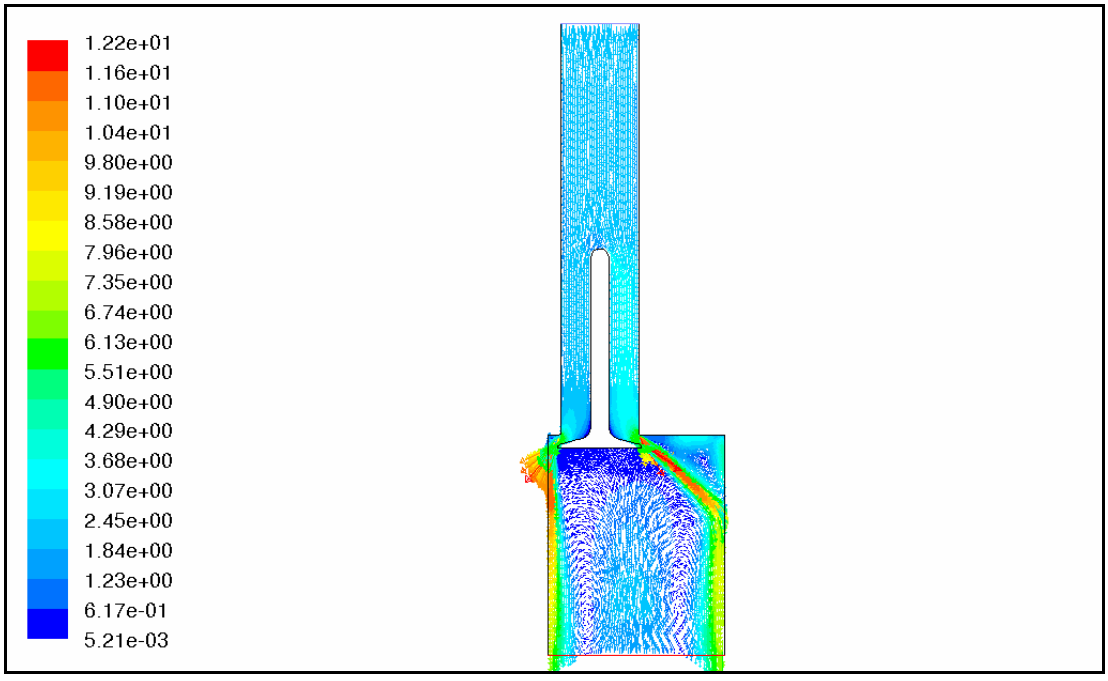


b)

Figure 4.9 Velocity vectors colored by velocity magnitude a) 5 mm valve lift standard turbulence method, b) 5 mm valve lift RNG turbulence method

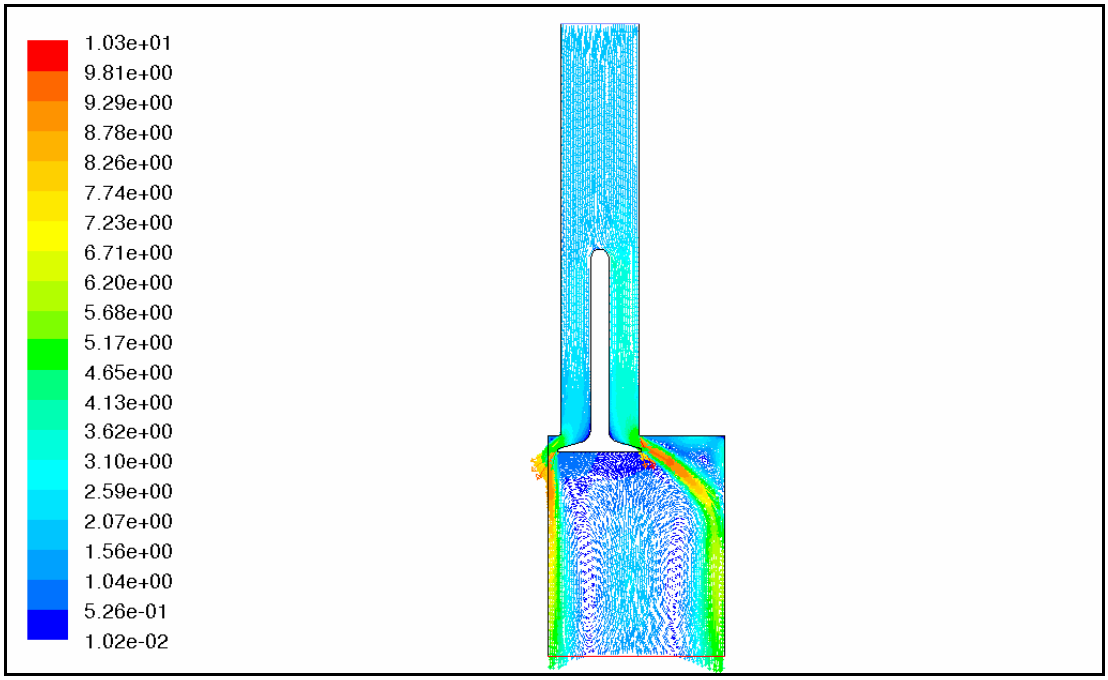


a)

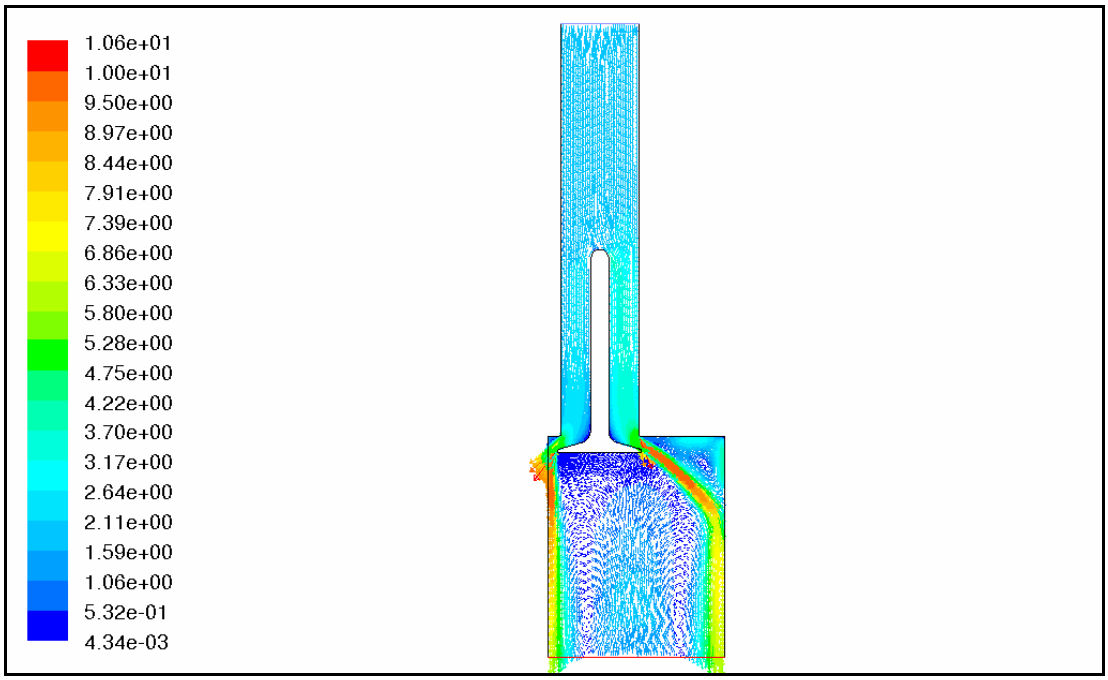


b)

Figure 4.10 Velocity vectors colored by velocity magnitude a) 7 mm valve lift standard turbulence method, b) 7 mm valve lift RNG turbulence method

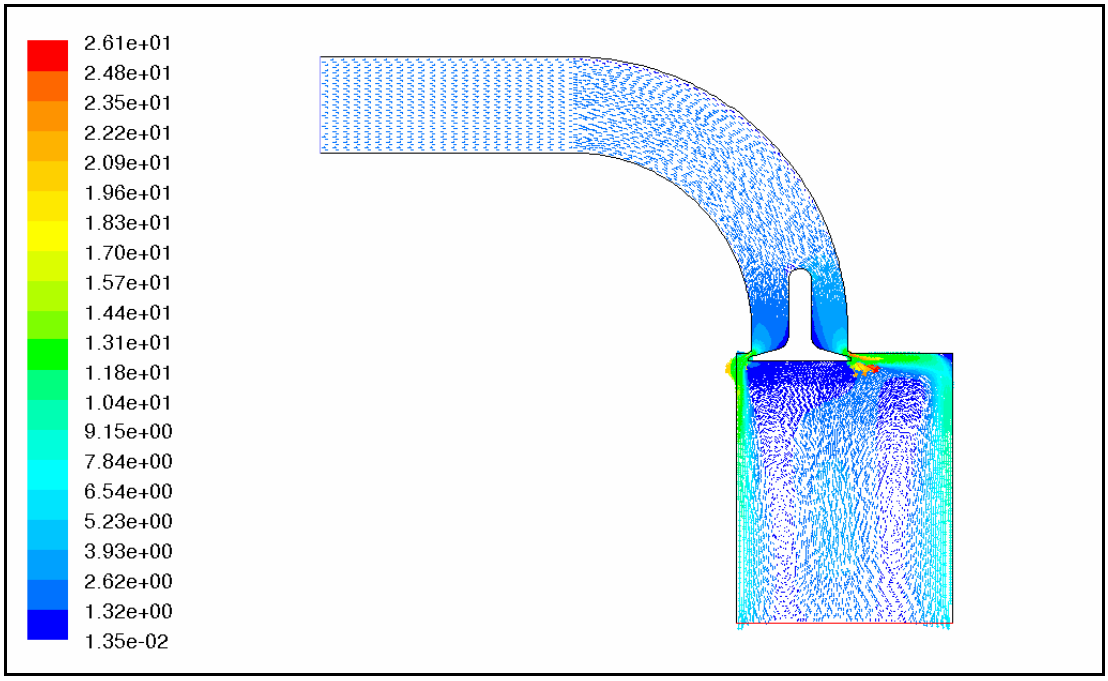


a)

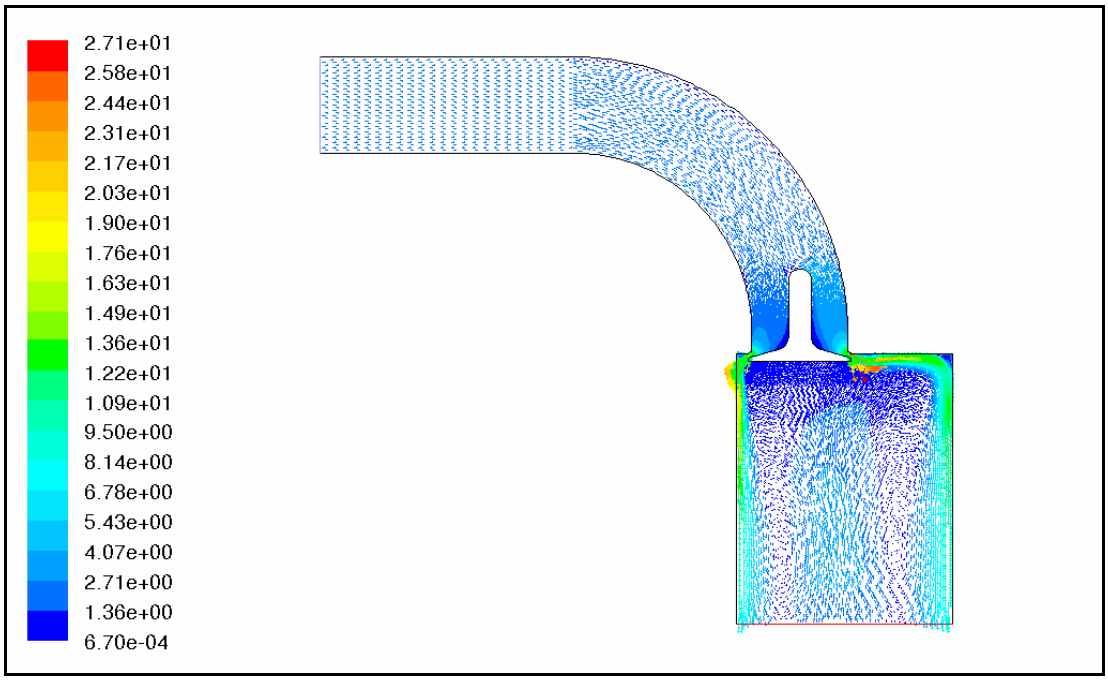


b)

Figure 4.11 Velocity vectors colored by velocity magnitude a) 9 mm valve lift standard turbulence method, b) 9 mm valve lift RNG turbulence method

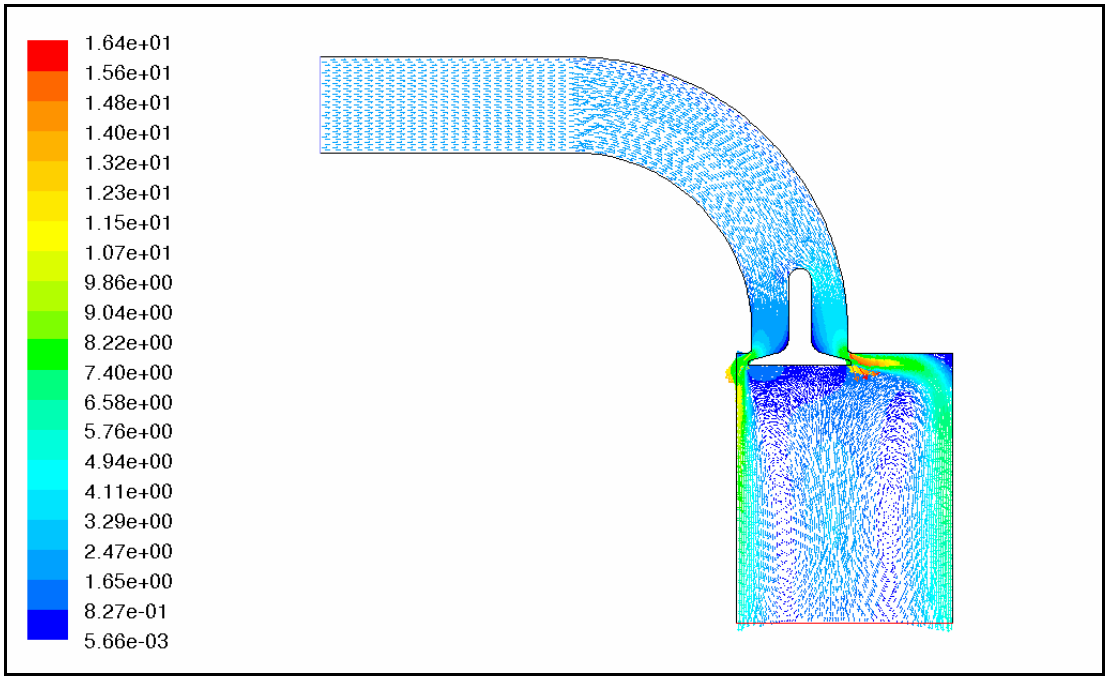


a)

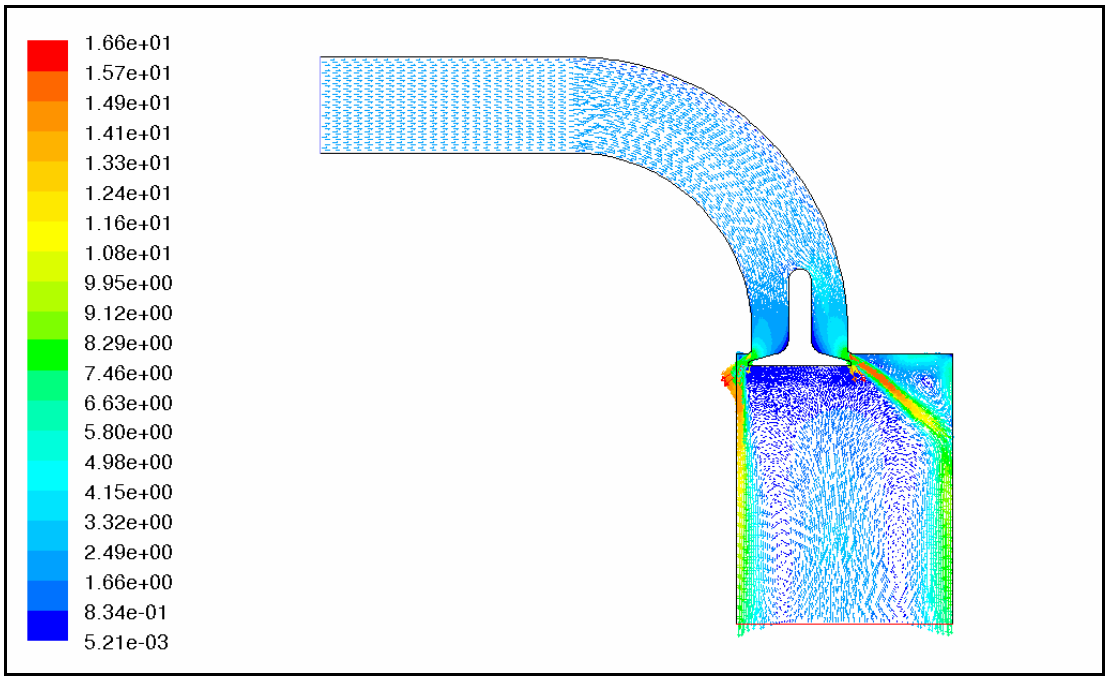


b)

Figure 4.12 Velocity vectors colored by velocity magnitude a) 3 mm valve lift standard turbulence method, b) 3 mm valve lift RNG turbulence method

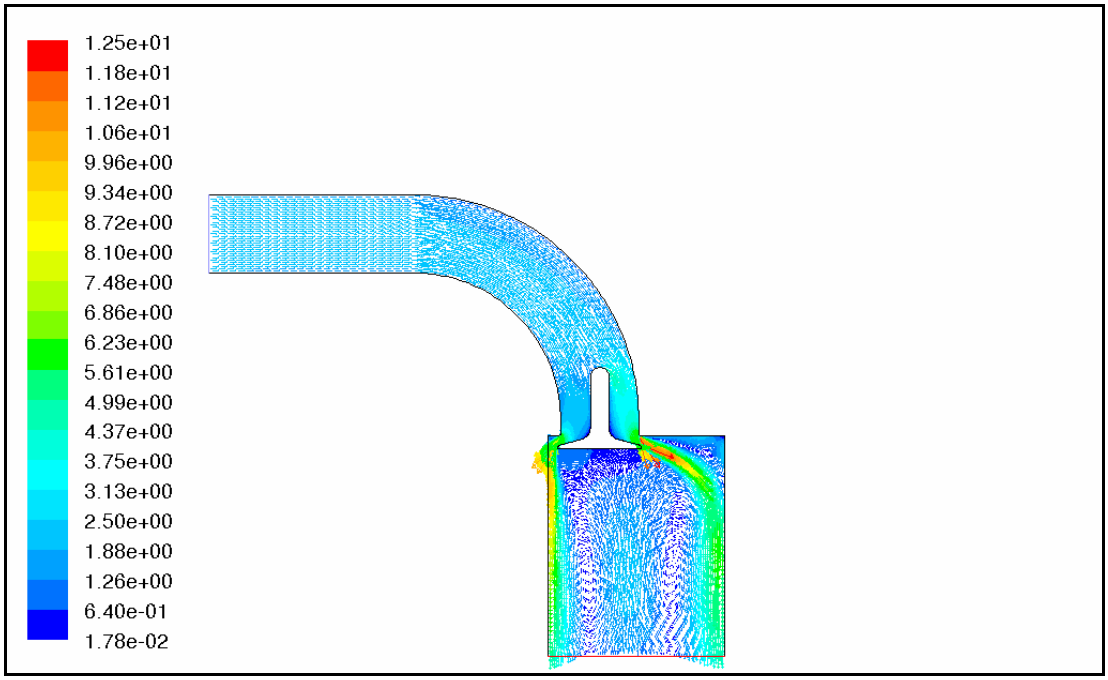


a)

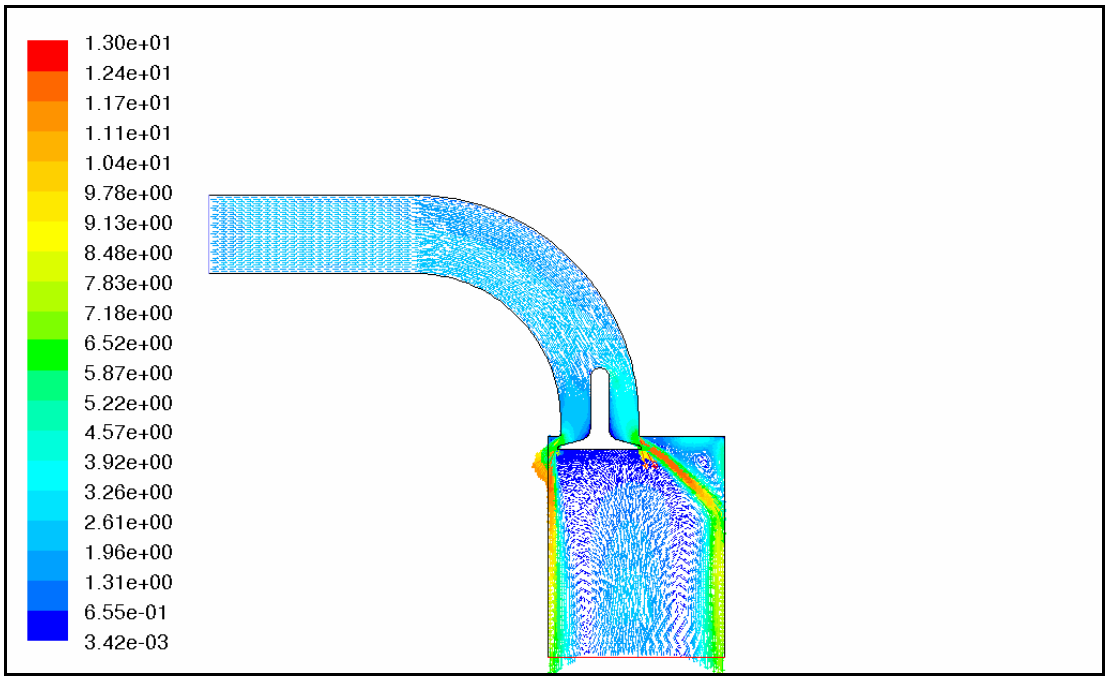


b)

Figure 4.13 Velocity vectors colored by velocity magnitude a) 5 mm valve lift standard turbulence method, b) 5 mm valve lift RNG turbulence method

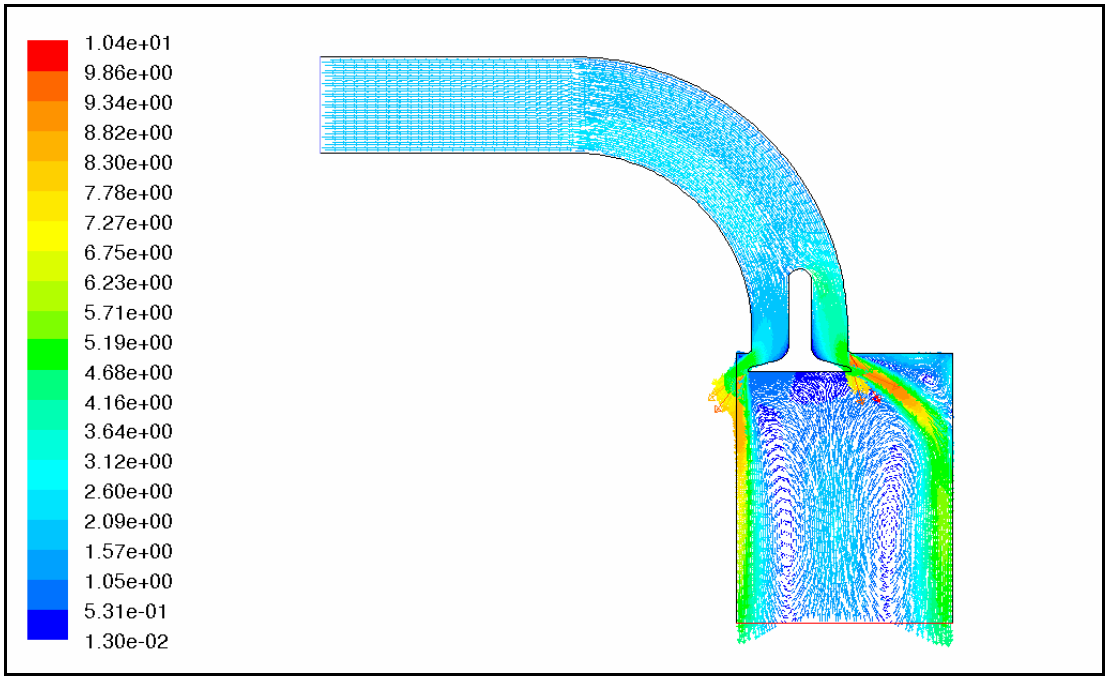


a)

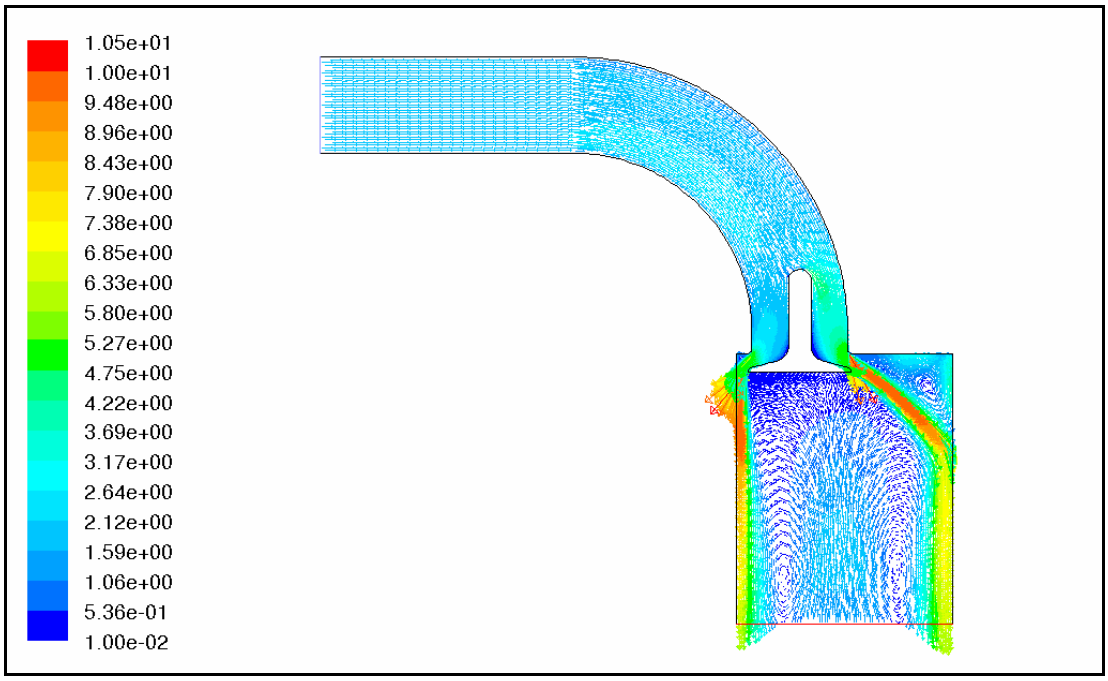


b)

Figure 4.14 Velocity vectors colored by velocity magnitude a) 7 mm valve lift standard turbulence method, b) 7 mm valve lift RNG turbulence method

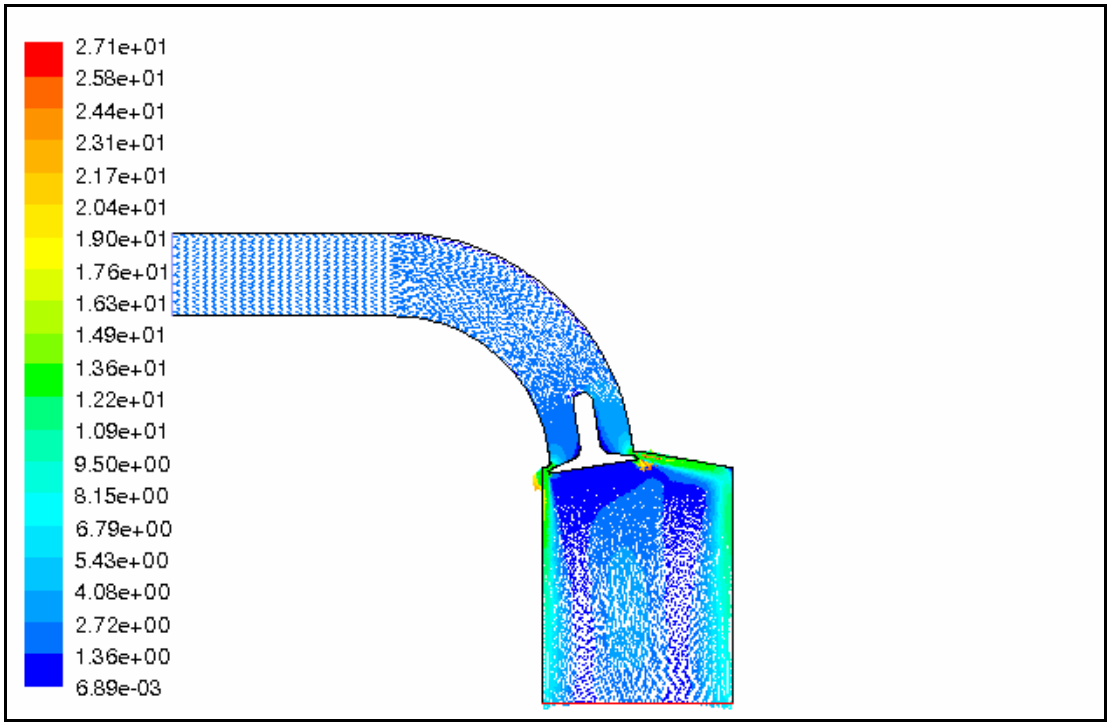


a)

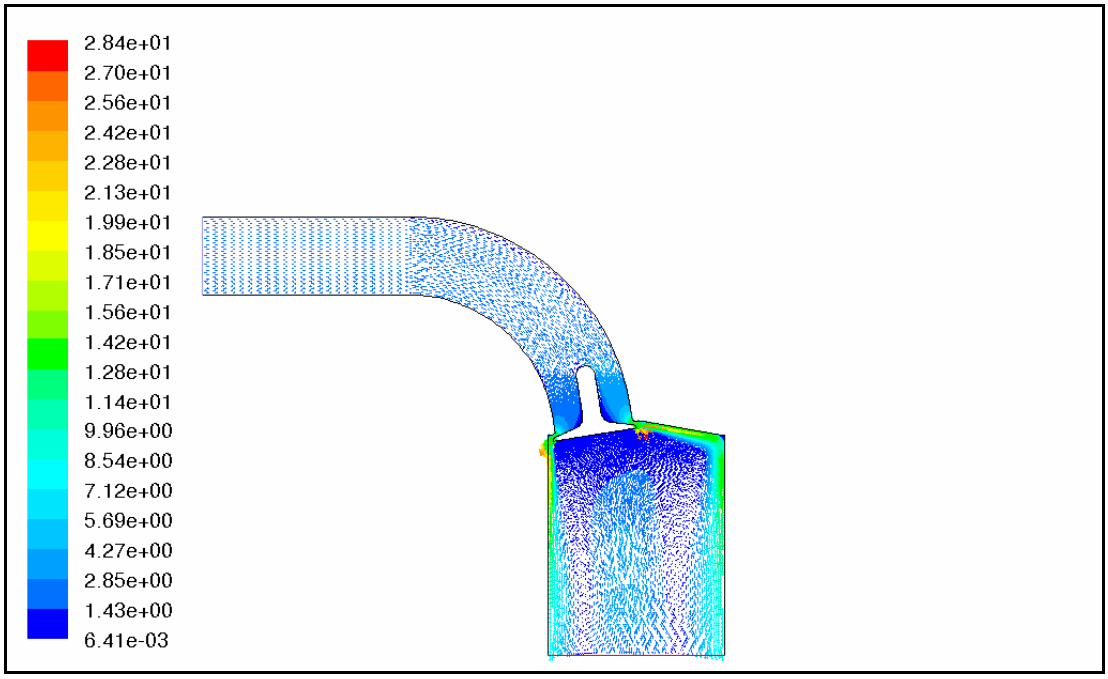


b)

Figure 4.15 Velocity vectors colored by velocity magnitude a) 9 mm valve lift standard turbulence method, b) 9 mm valve lift RNG turbulence method

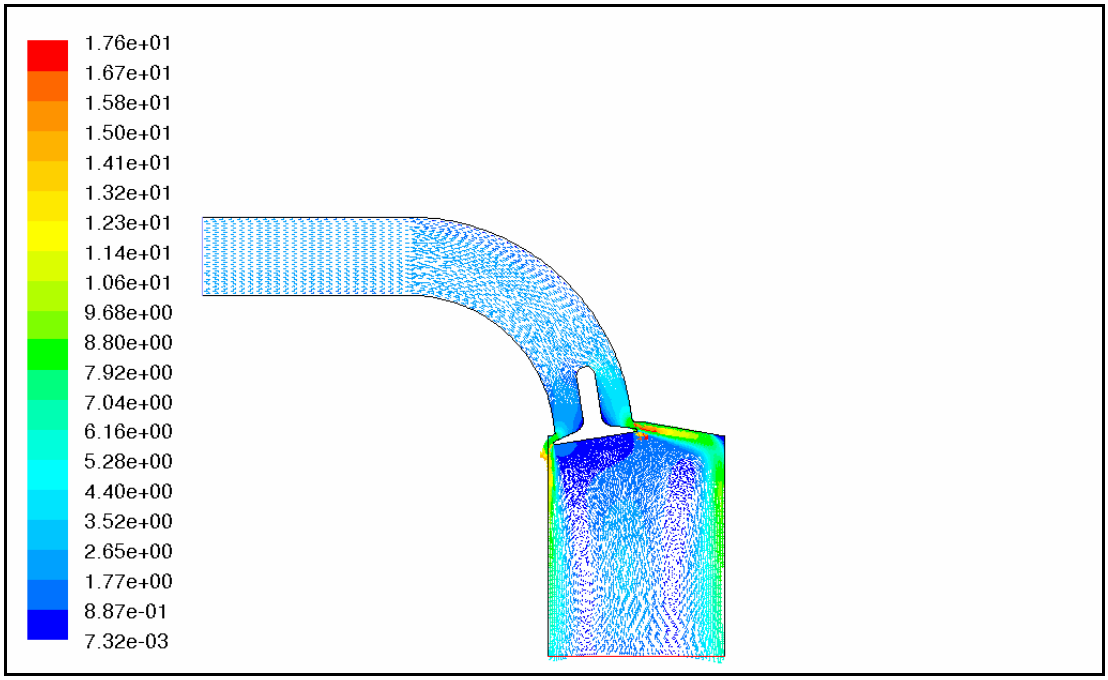


a)

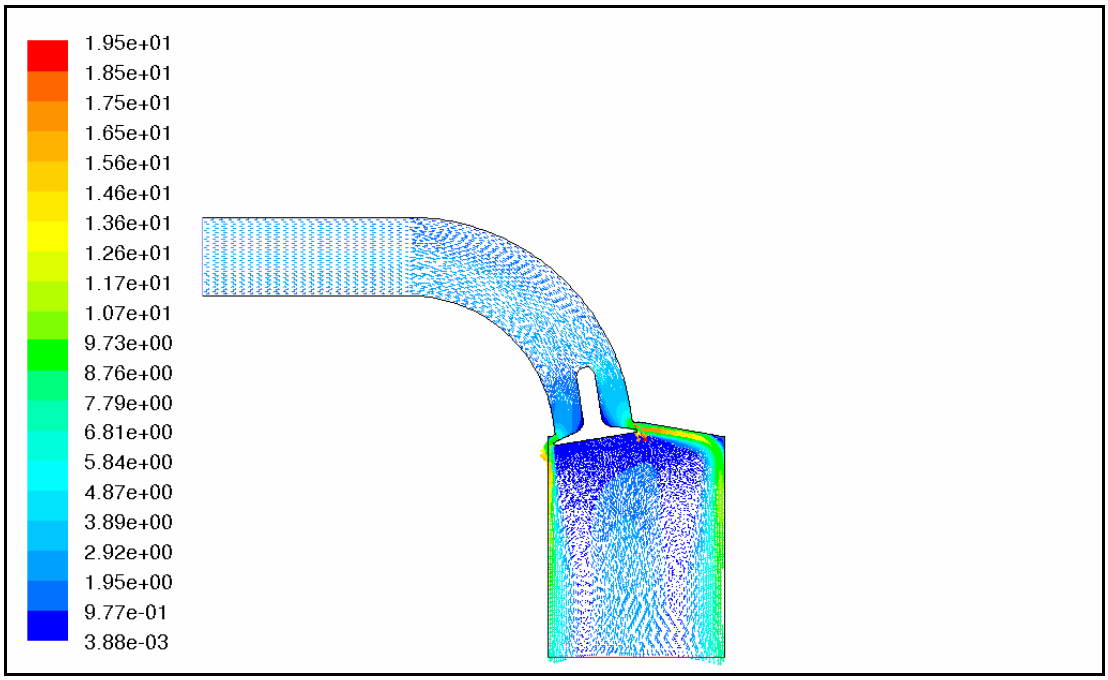


b)

Figure 4.16 Velocity vectors colored by velocity magnitude a) 3 mm valve lift standard turbulence method, b) 3 mm valve lift RNG turbulence method

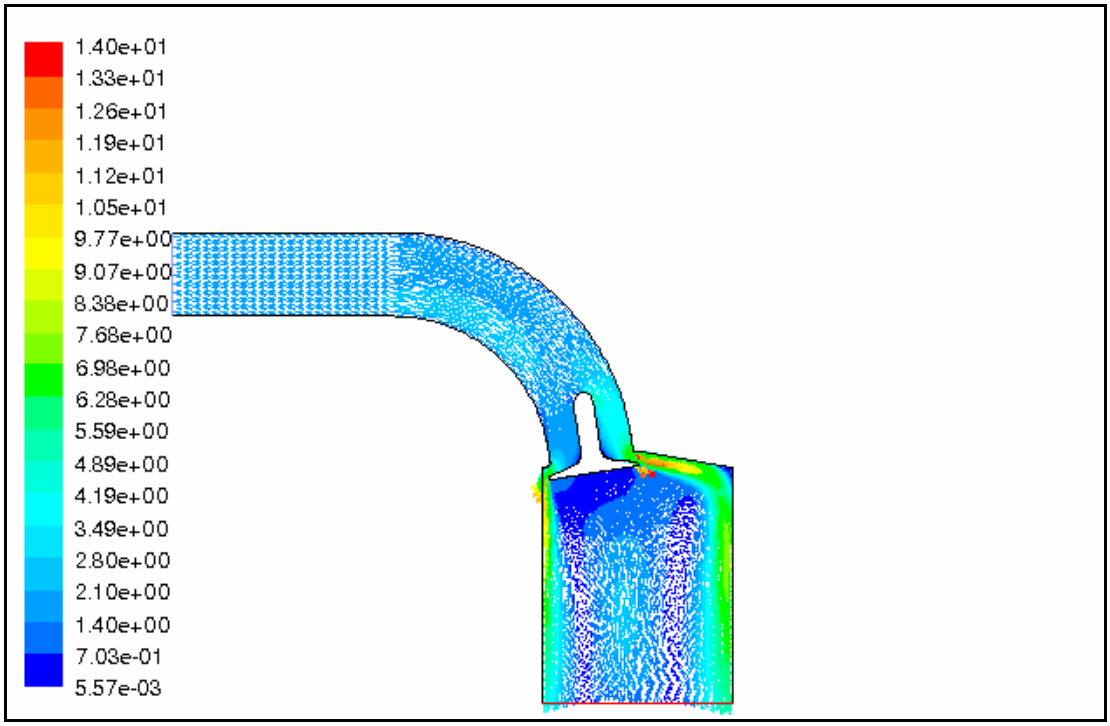


a)

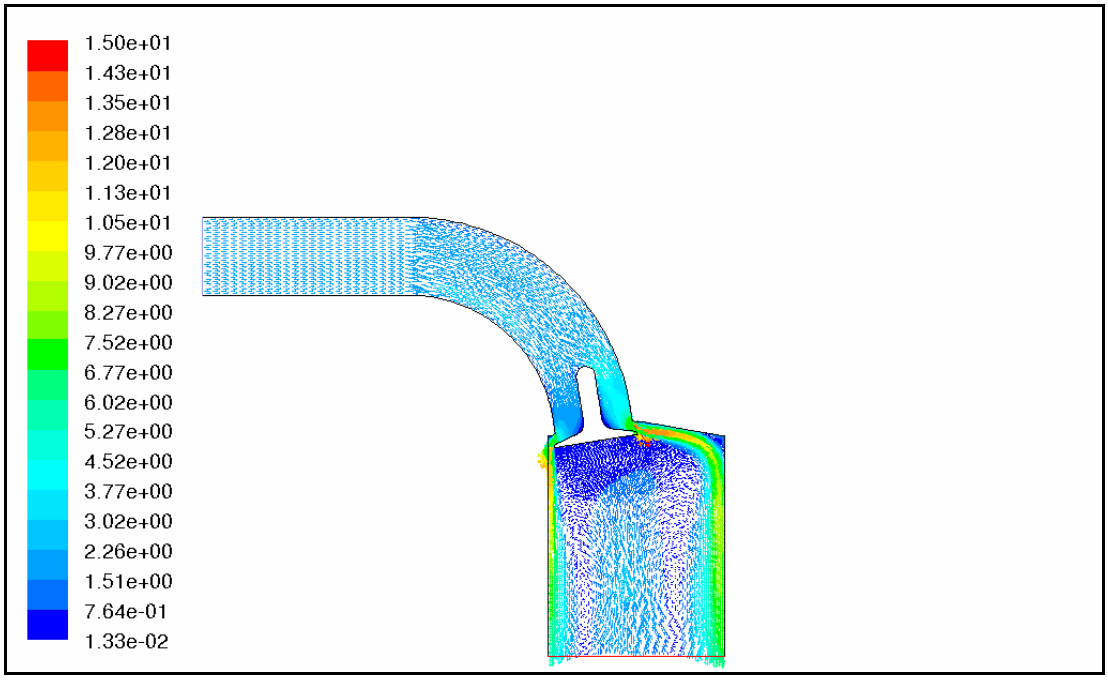


b)

Figure 4.17 Velocity vectors colored by velocity magnitude a) 5 mm valve lift standard turbulence method, b) 5 mm valve lift RNG turbulence method

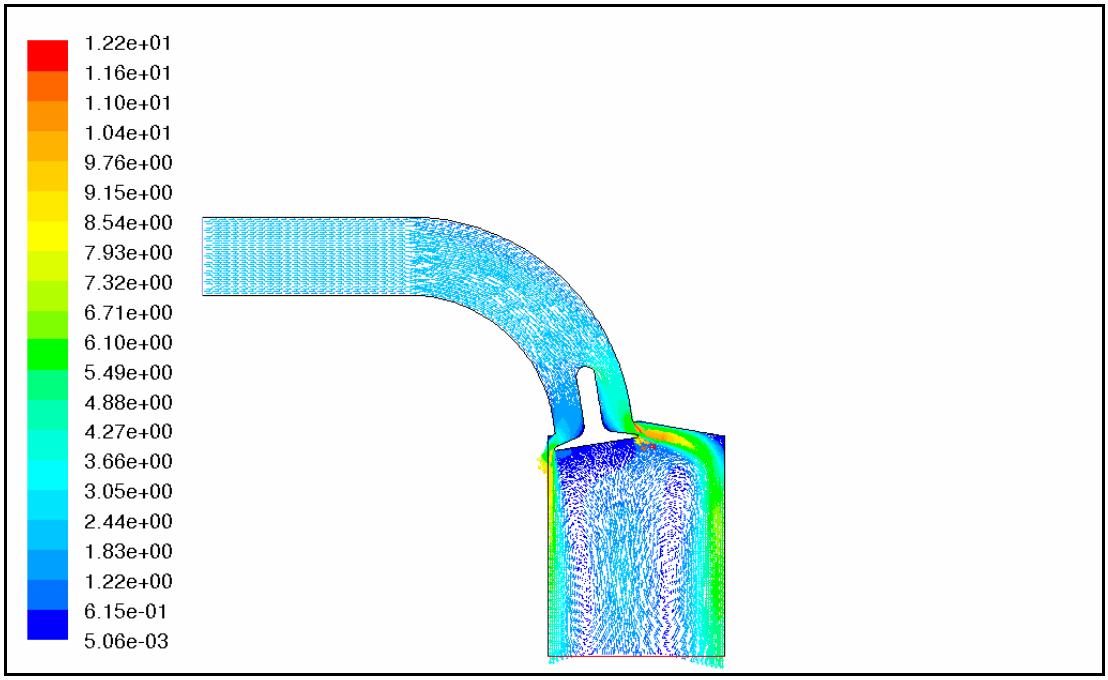


a)

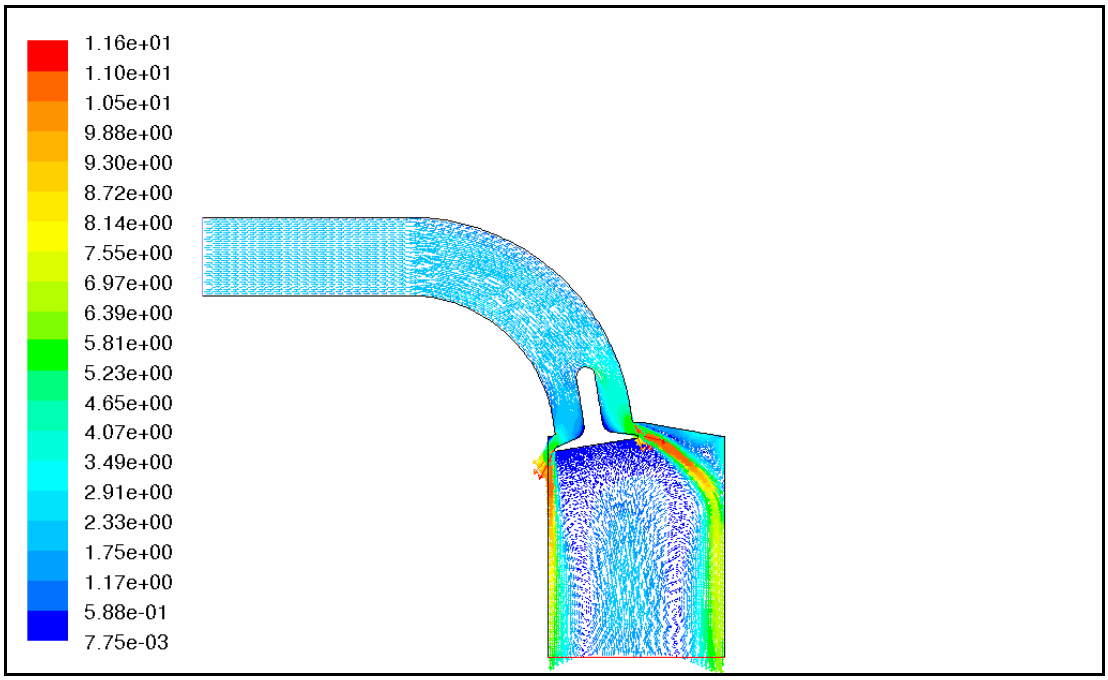


b)

Figure 4.18 Velocity vectors colored by velocity magnitude a) 7 mm valve lift standard turbulence method, b) 7 mm valve lift RNG turbulence method

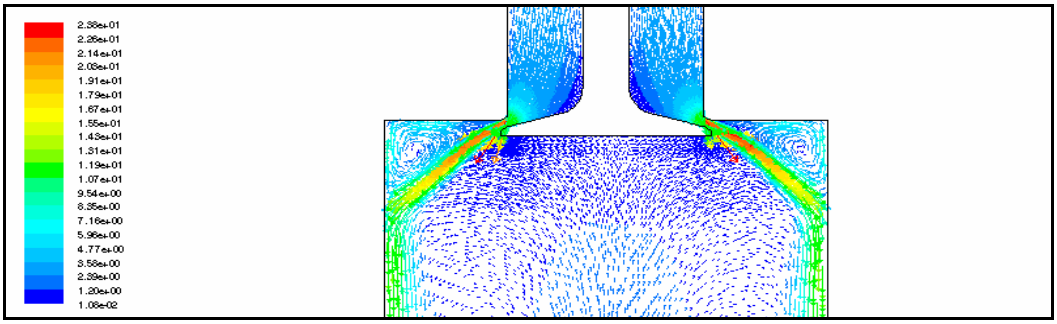


a)

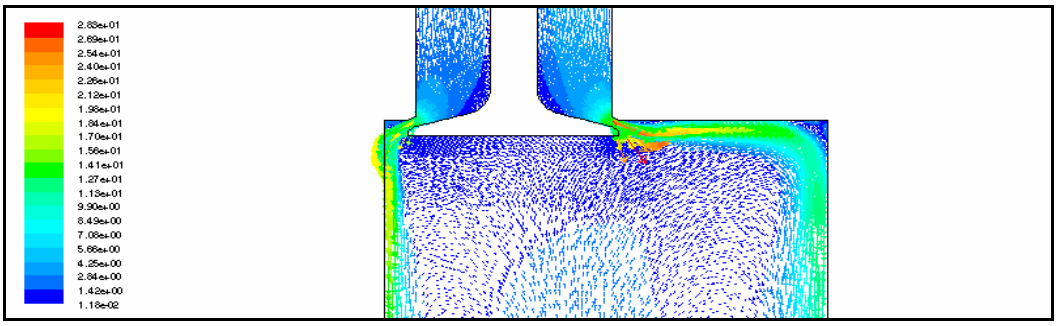


b)

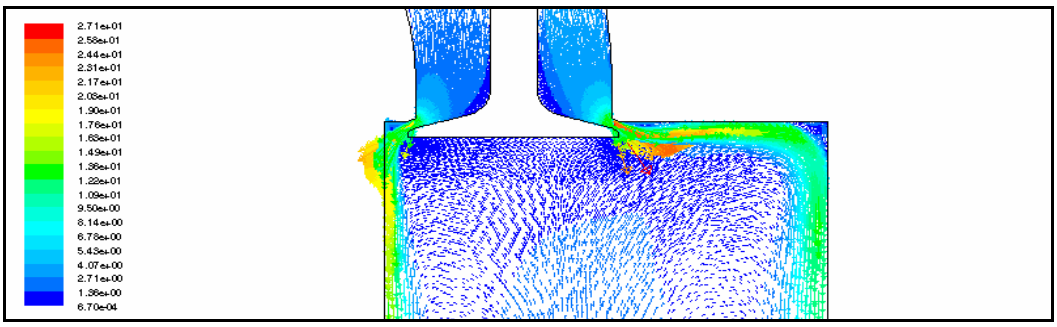
Figure 4.19 Velocity vectors colored by velocity magnitude a) 9 mm valve lift standard turbulence method, b) 9 mm valve lift RNG turbulence method



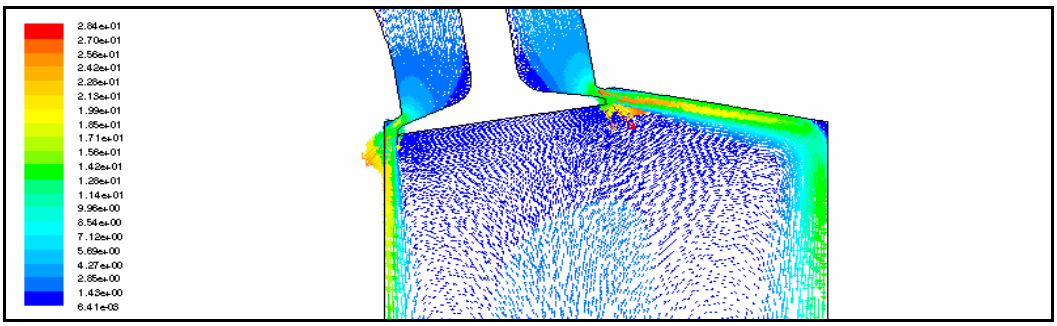
a)



b)

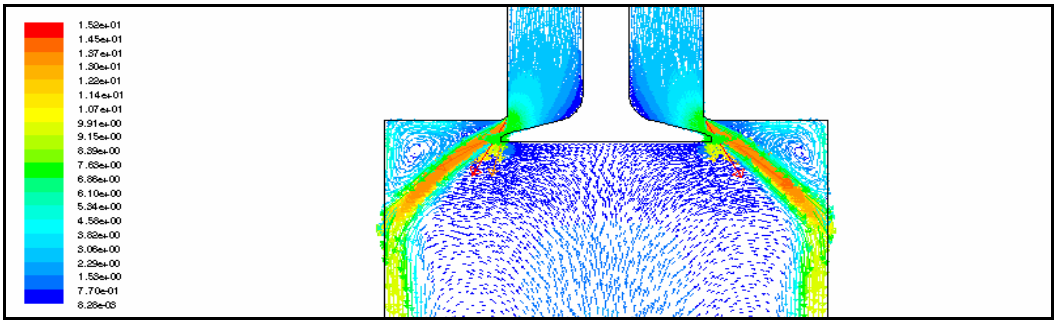


c)

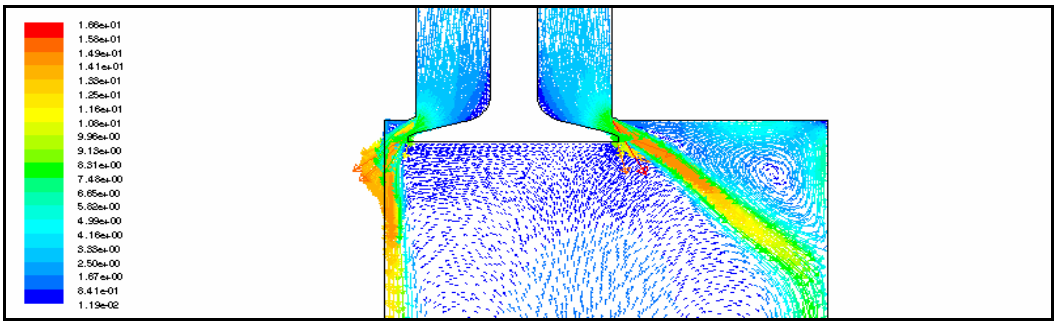


d)

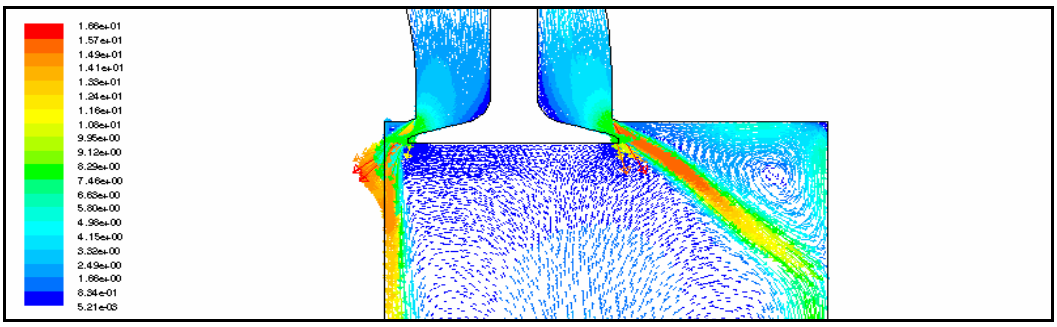
Figure 4.20 Velocity vectors colored by velocity magnitude near valve region for 3mm valve gap a) first model b) second model c) third model d) fourth model



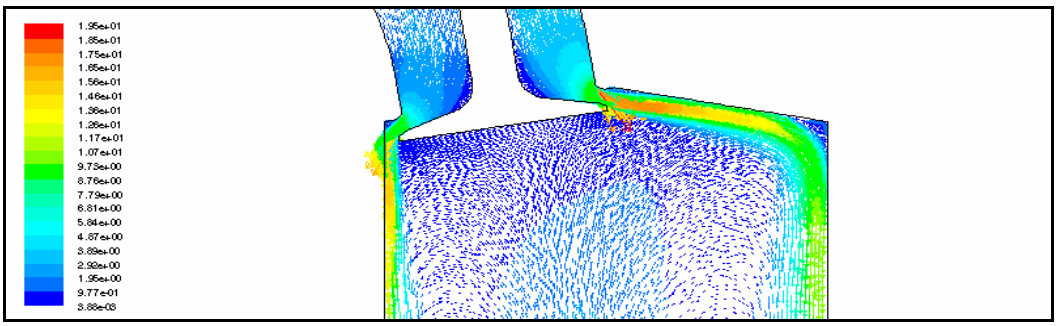
a)



b)

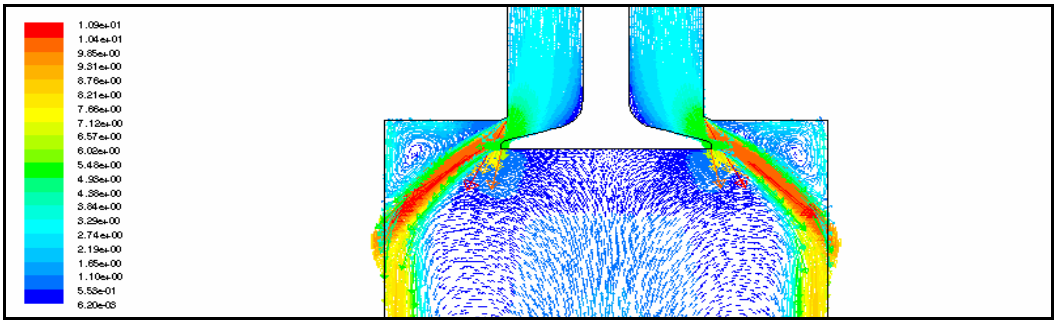


c)

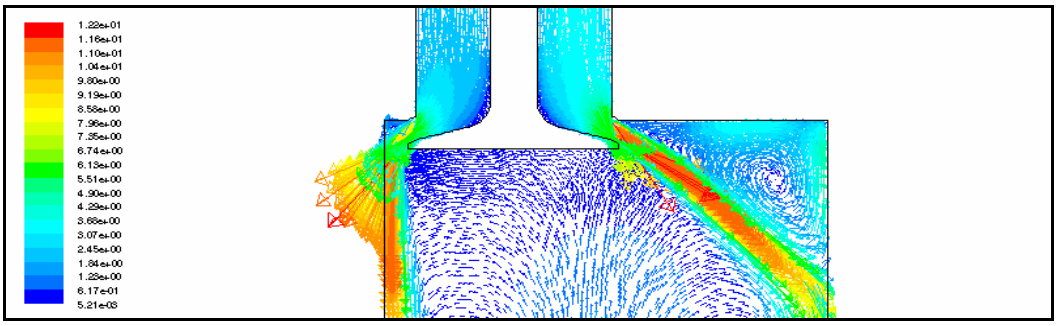


d)

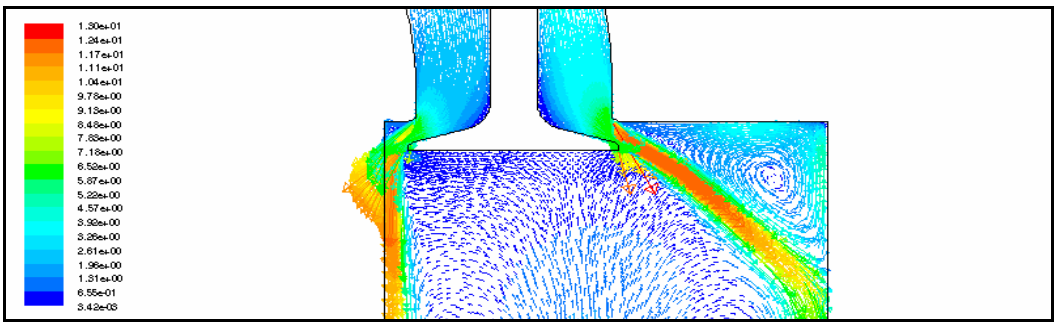
Figure 4.21 Velocity vectors colored by velocity magnitude near valve region for 5mm valve gap a) first model b) second model c) third model d) fourth model



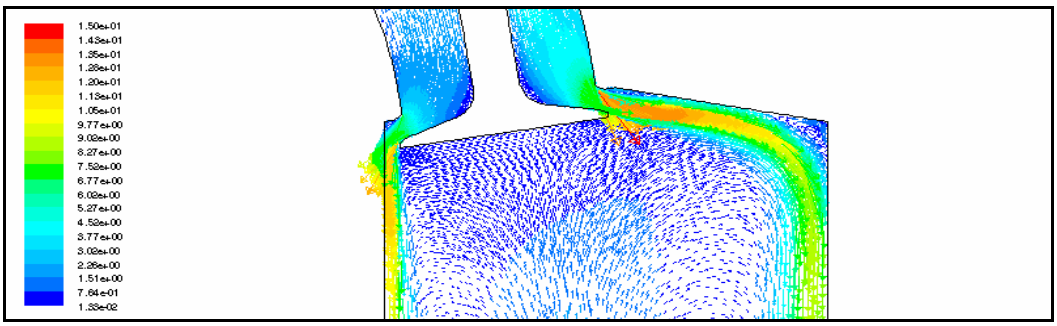
a)



b)

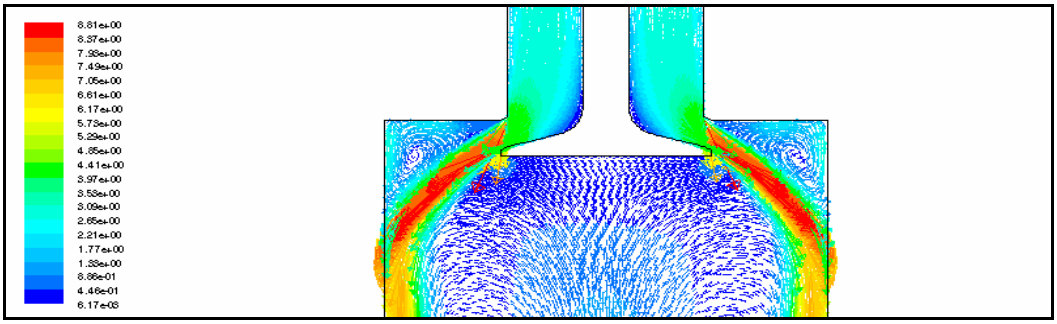


c)

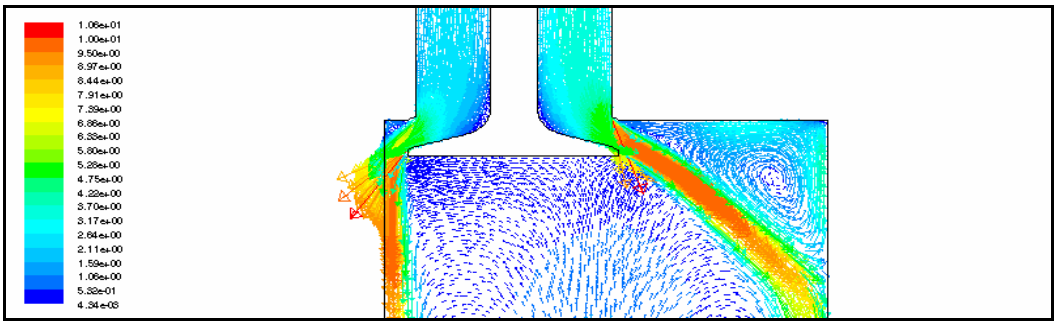


d)

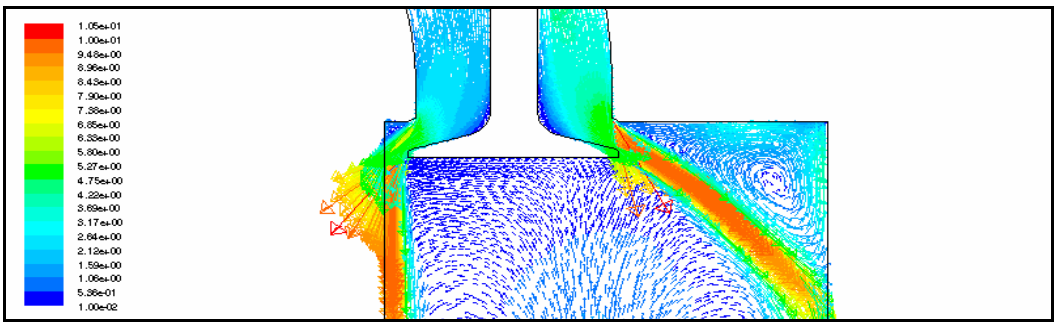
Figure 4.22 Velocity vectors colored by velocity magnitude near valve region for 7mm valve gap a) first model b) second model c) third model d) fourth model



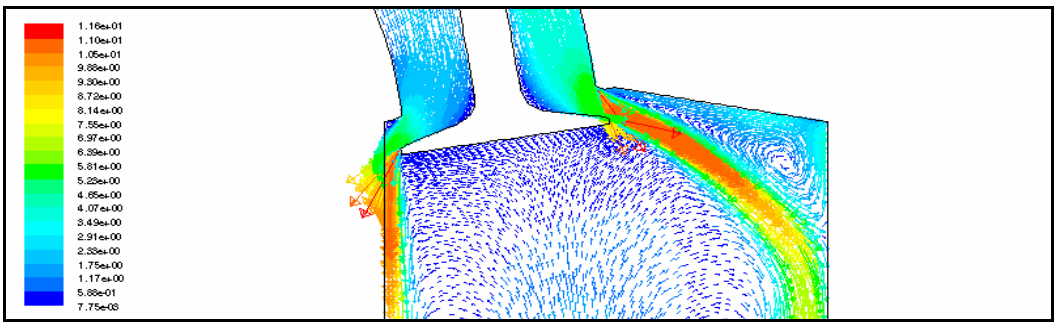
a)



b)



c)



d)

Figure 4.23 Velocity vectors colored by velocity magnitude near valve region for 9mm valve gap a) first model b) second model c) third model d) fourth model

4.2 Three-Dimensional Calculations

In this section of thesis, two 3d models are considered as they were illustrated in Chapter 3. These two models are also investigated for different valve gaps and different turbulence models like 2d model calculations. First model has one straight intake pipe that is concentric with cylinder. Second model has two intake pipes with radius as commonly used in modern engines. Geometric features of these models and the reason why they were chosen and other details can be found in Material Method section (Chapter 3). Figures will begin with straight pipe model results and than continue with second model.

As visualization view, velocity contours and turbulence intensity is considered since vector option is not suitable for 3d model.

The quality of the grid plays a significant role in the accuracy and stability of the numerical computation as it is mentioned in Chapter 3. In addition to quality, grid independency is an important issue to have accurate results and reduce computational time. Therefore, grid independency studies were carried out in this manner. Figure 4.24 shows a grid independency example which was performed for straight intake pipe model. As it is seen from figure, GAMBIT grid generator does not fit very well when it is compared with TGrid program. There are similar characteristics when GAMBIT uses approximately 1,200,000 elements and TGrid uses 230,000 elements. The results are acceptable in both situation but GAMBIT results needs more computational time and better computer hardware requirements than Tgrid. This shows another reason why TGrid program was used in this study in order to generate volume grid.

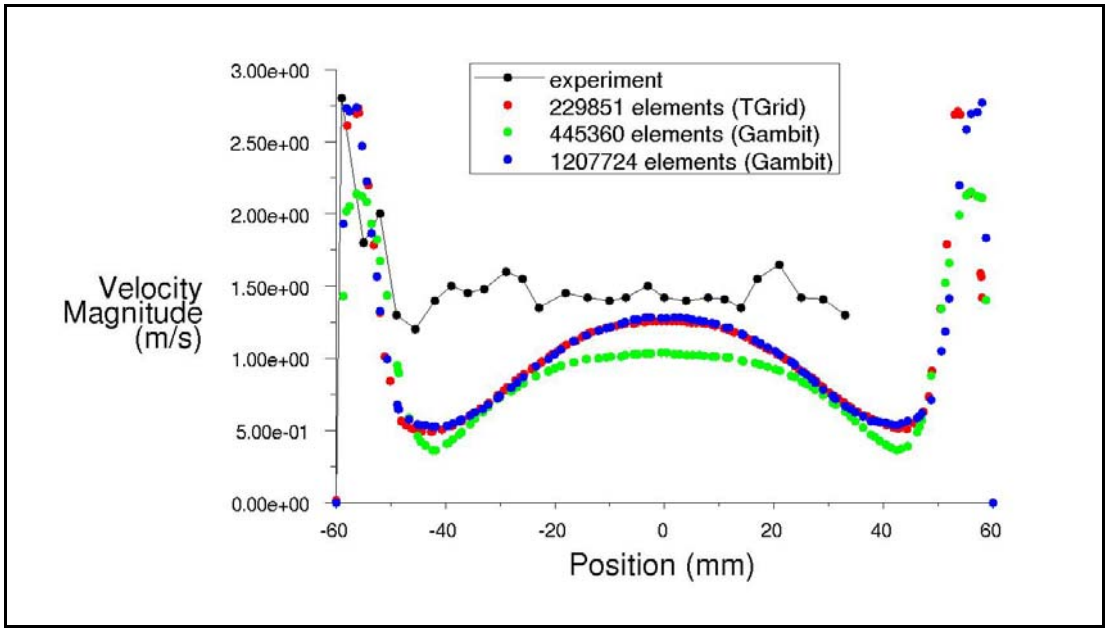


Figure 4.24 An example of grid independency study

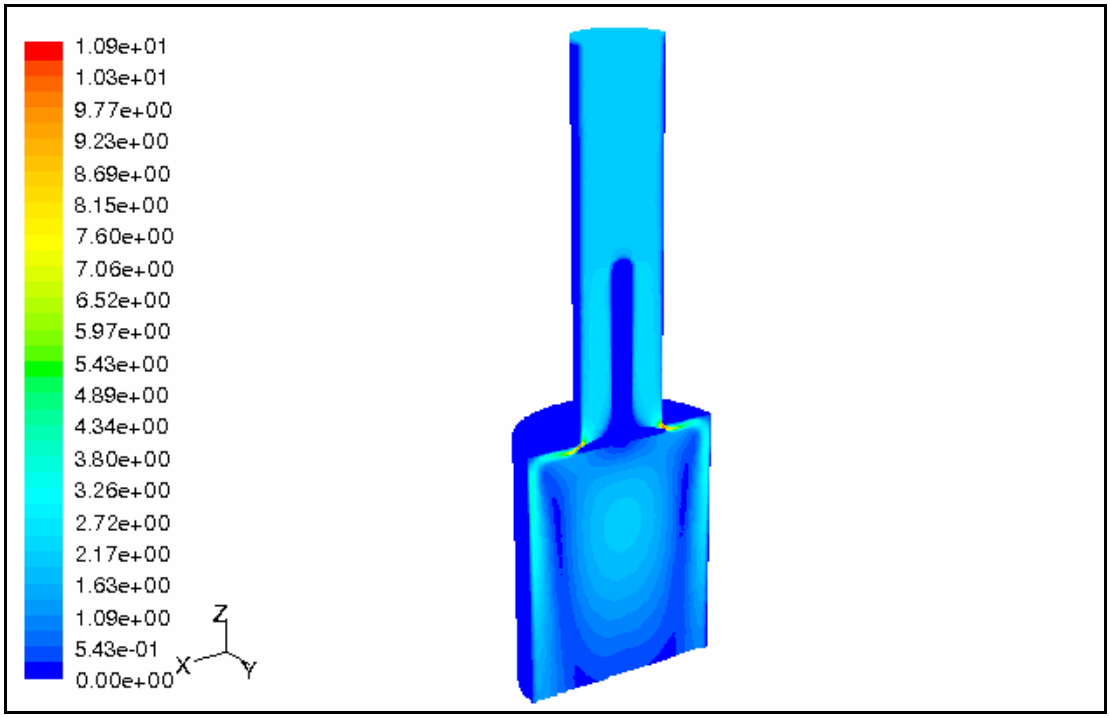
There have been some convergence problems during the 3d calculations. Some of them were solved by changing the solution procedure; the others were solved by increasing a number of discretization points in the volume. But only one case has not been solved. This is the 3d two intake model calculation for 3mm valve gap. At the beginning of the problem, it was assumed that, solution parameters caused this problem, but changing of the solution parametes did not effect the problem. Later, it was decided that insufficient grid numbers caused the problem. However, increasing and decreasing the grid number did not change solution convergence as well. As a result, this case is not shown in this thesis because of reasons mentioned above.

When following figures are investigated, it is seen that, they are perspective view of 3d model with one intake port. Figure 4.25 shows velocity contours and turbulence intensity for 3 mm valve gap. As it is seen from figure, valve jet does not directly collide with lateral walls. When jet enters the combustion chamber, it turns towards cylinder head. Since there is a developed swirl effect inside of cylinder, it has jet effect forced towards cylinder head. Another detail from figure is that walls of

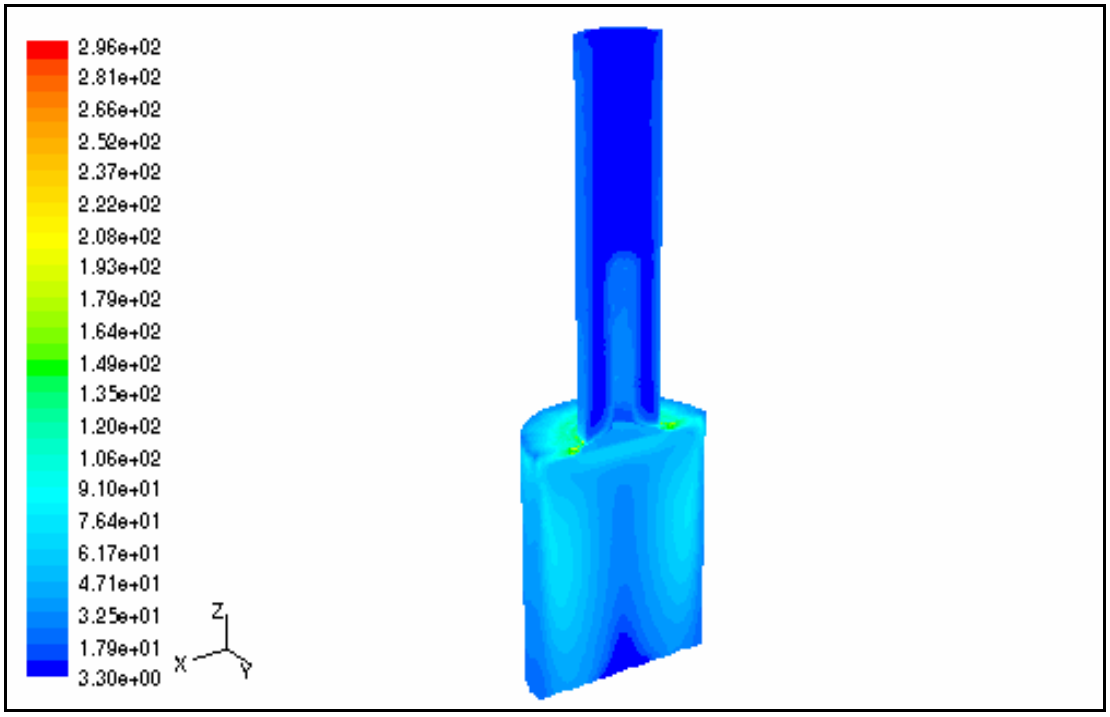
model have zero velocity value as it must be naturally. This detail is difficult to be seen when vector illustration option is selected. When looking at carefully, it is easy to see that maximum velocity value occur in valve jet area. Turbulence intensity figure shows where turbulence is more and where it is less. Moreover figure makes a sense in a way of turbulence generation. As it is expected, turbulence intensity is more in near valve region than other regions inside of cylinder because of highly strong jet effect. Once Figure 4.26 is investigated, it is easy to see jet collision to the cylinder walls. In this case, developed in-cylinder swirl effect does not force to the jet to turn towards cylinder head as it is done previous figure. Jet effect reaches cylinder walls and collides with them. As a result of this action, one clockwise and one anticlockwise small swirl near up cylinder corner are generated and velocity values near cylinder wall decrease getting to down. Turbulence intensity is seen very high level near valve jet area as it is expected. Figure 4.27 illustrates velocity contours and turbulence intensity for 7 mm valve gap. There are no big differences from 5 mm results in point of view. But when looking at figures carefully, it is noticed that velocity magnitude is getting to decrease since valve continues to open. Figure 4.28 also shows similar characteristics for 9 mm valve gap. In other words, there are no changes in small swirls near cylinder head or turbulence intensity regions. The only difference is that velocity value and turbulence intensity continue to calm down since valve is getting to open. Velocity vectors and their magnitudes are shown from Figure 4.29 through Figure 4.30 for measurement lines that were illustrated in Figure 4.3. Everything is clear and there is no need for explanation for these figures. These figures are only fixed to show comparison between numerical and experimental results later. Because there will be a conflict between two results. This conflict can be seen from Figure 4.31 through Figure 4.34. In these figures, vertical axis indicates velocity values and horizontal axis indicates coordinates of measurement points through the cylinder diameter. In position axis, zero point corresponds to cylinder axis.

When investigating most of the figures, there is a problem nearly between -50 mm and -30 coordinates. This is the mentioned conflict that has been explained above lines. The reason why most of the figures have this problem will be explained

in Conclusion section (Chapter 5) in detail. Except this problem, it is seen that numerical and experimental results have a good agreement in most of the measurement point. All of the figures contain three different turbulence model comparisons and experimental result. Experimental results are carried out to measure until 30 mm coordinate point, since there are difficulties for measurement in experiment place because of diameter of 5 holes pitot tube. As it is seen from all of the figures, -60 mm and 60 mm correspond to lateral walls of cylinder and velocity value is seen zero in these coordinates as it is expected normally. As a result of these figures, it is realized that standard $k-\varepsilon$ turbulence model is not sufficient to predict velocity values especially near jet region. RNG and realizable $k-\varepsilon$ turbulence models have similar characteristics in most of the figures. Therefore, RNG and realizable $k-\varepsilon$ turbulence methods are suitable for this type of engine applications from this point of view.

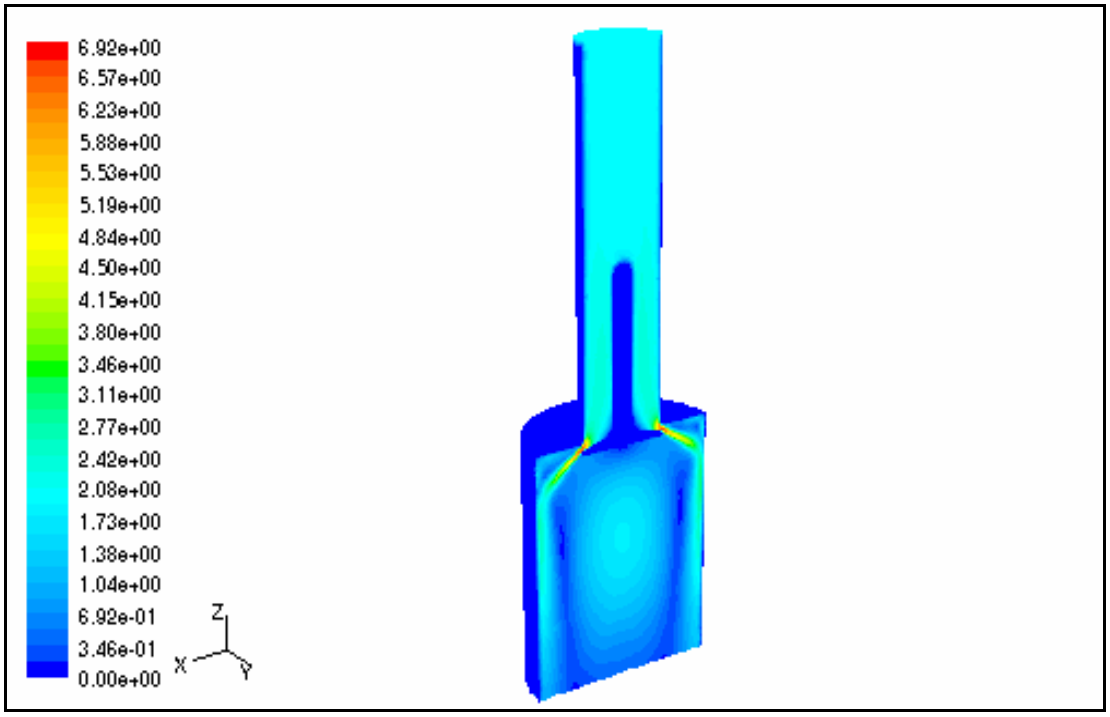


a)

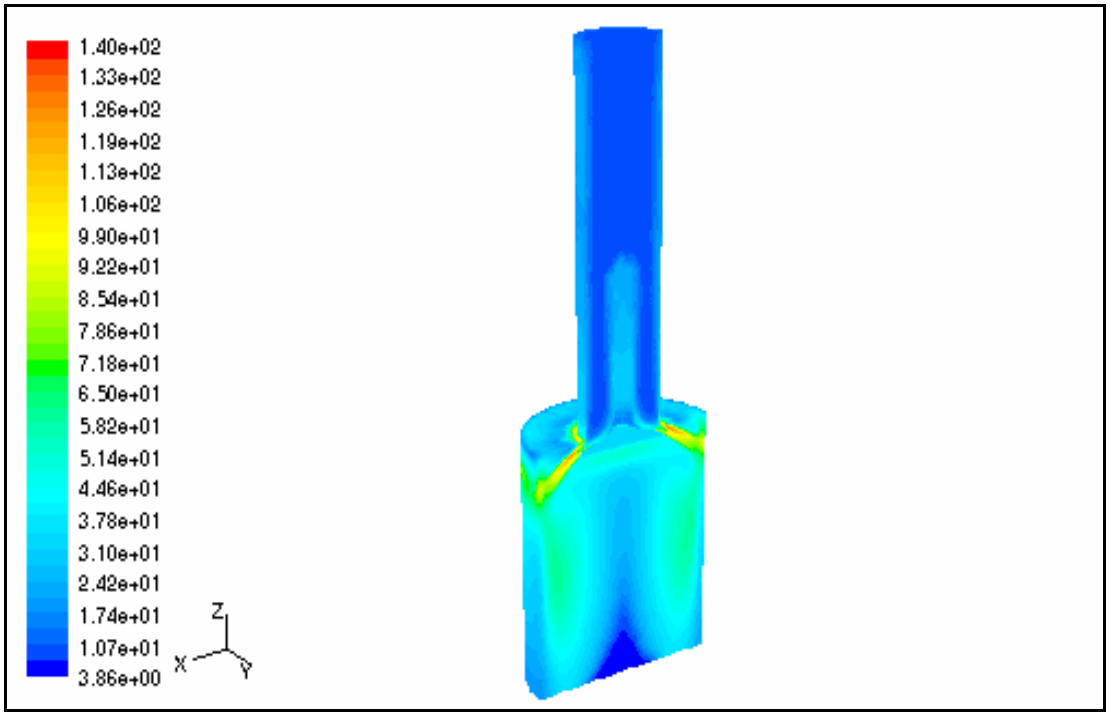


b)

Figure 4.25 a) Contours of velocity magnitude (m/s) b) contours of turbulence intensity (%) for 3 mm valve gap.

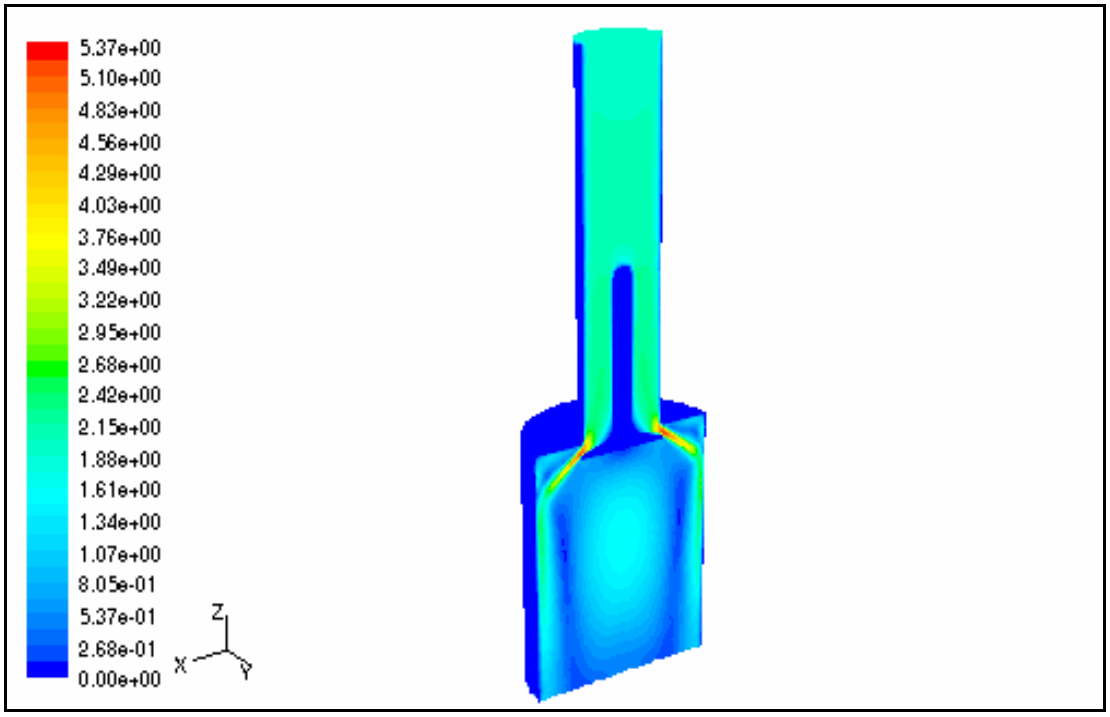


a)

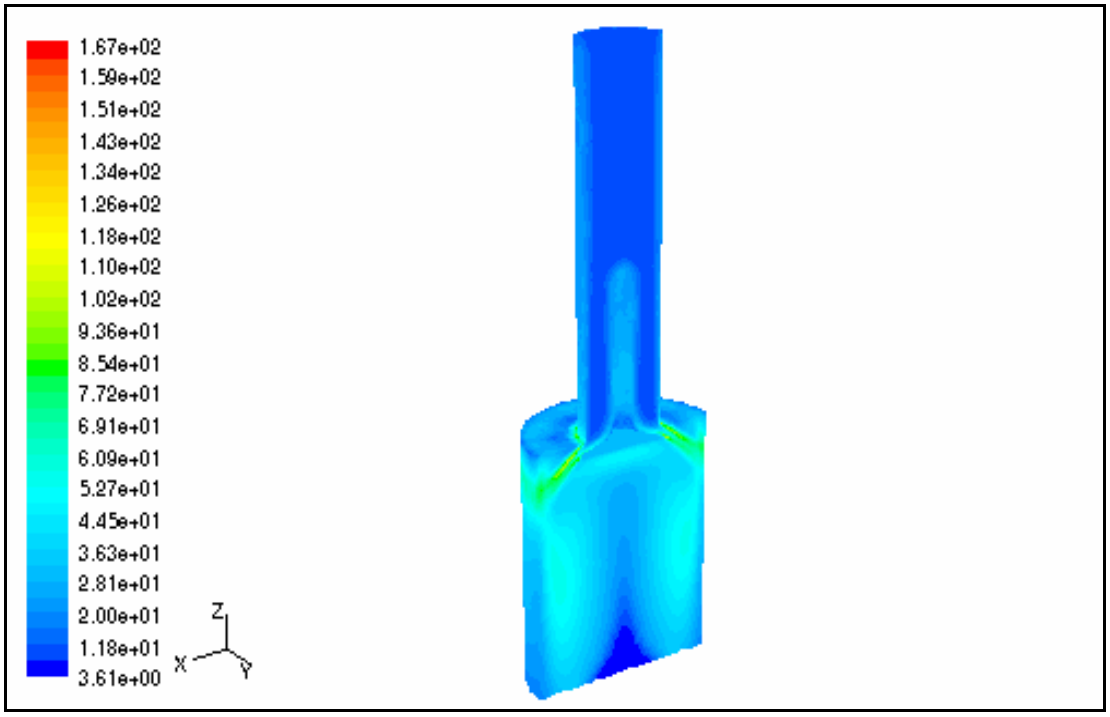


b)

Figure 4.26 a) Contours of velocity magnitude (m/s) b) contours of turbulence intensity (%) for 5 mm valve gap.

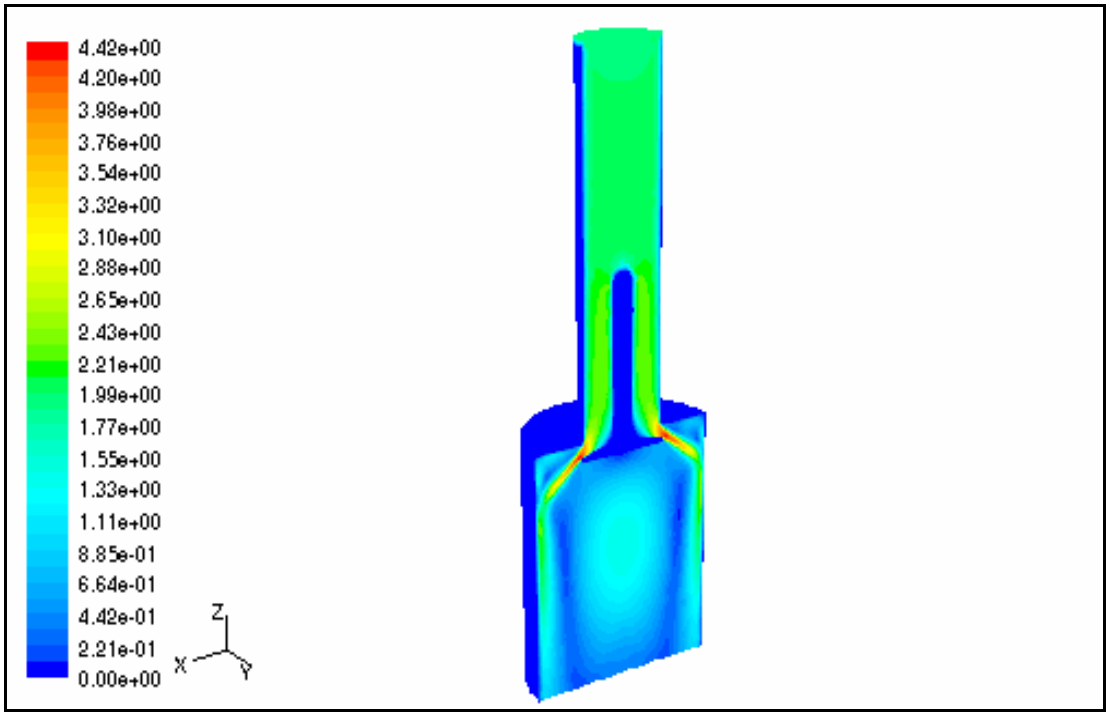


a)

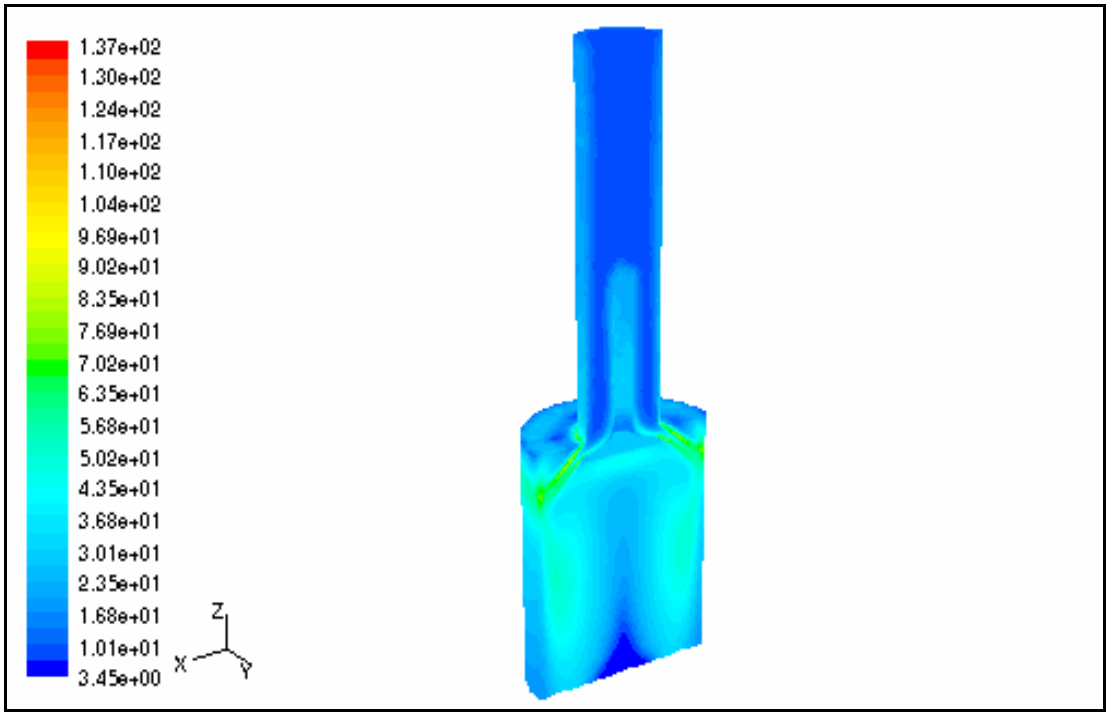


b)

Figure 4.27 a) Contours of velocity magnitude (m/s) b) contours of turbulence intensity (%) for 7 mm valve gap.

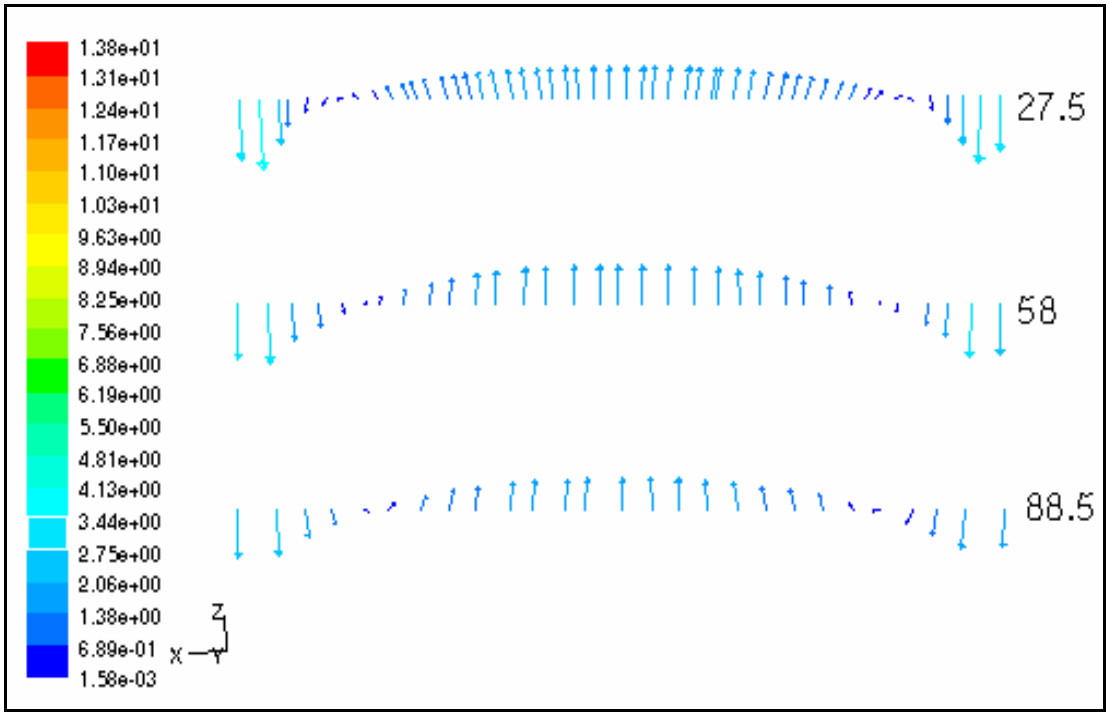


a)

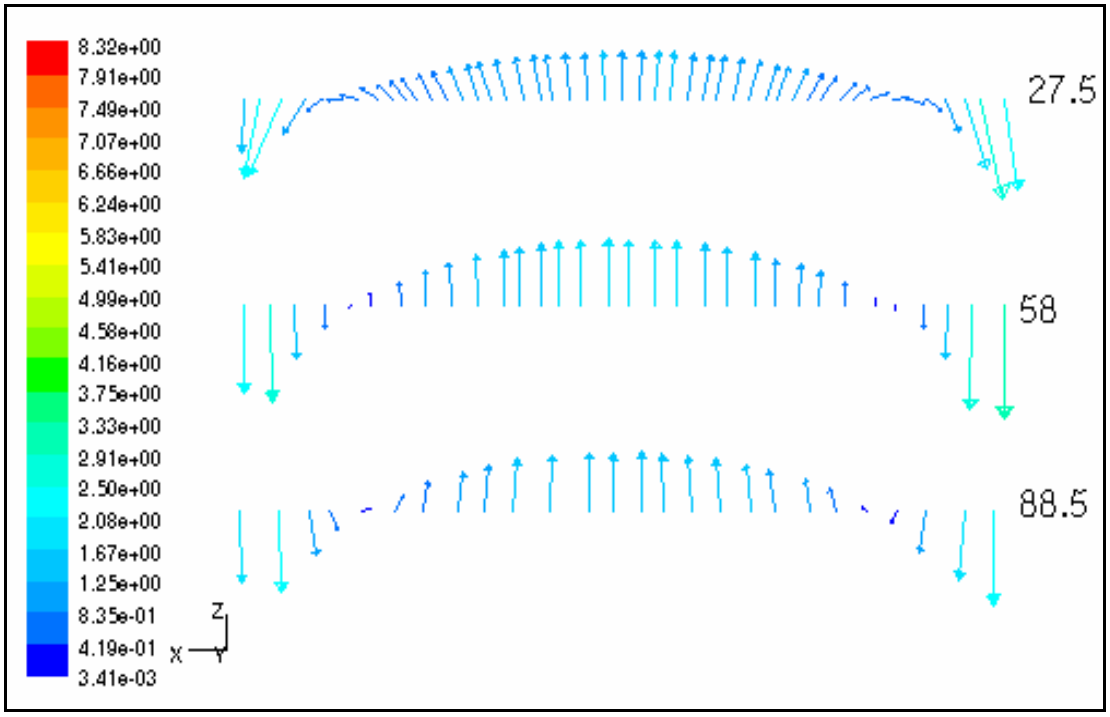


b)

Figure 4.28 a) Contours of velocity magnitude (m/s) b) contours of turbulence intensity (%) for 9 mm valve gap.

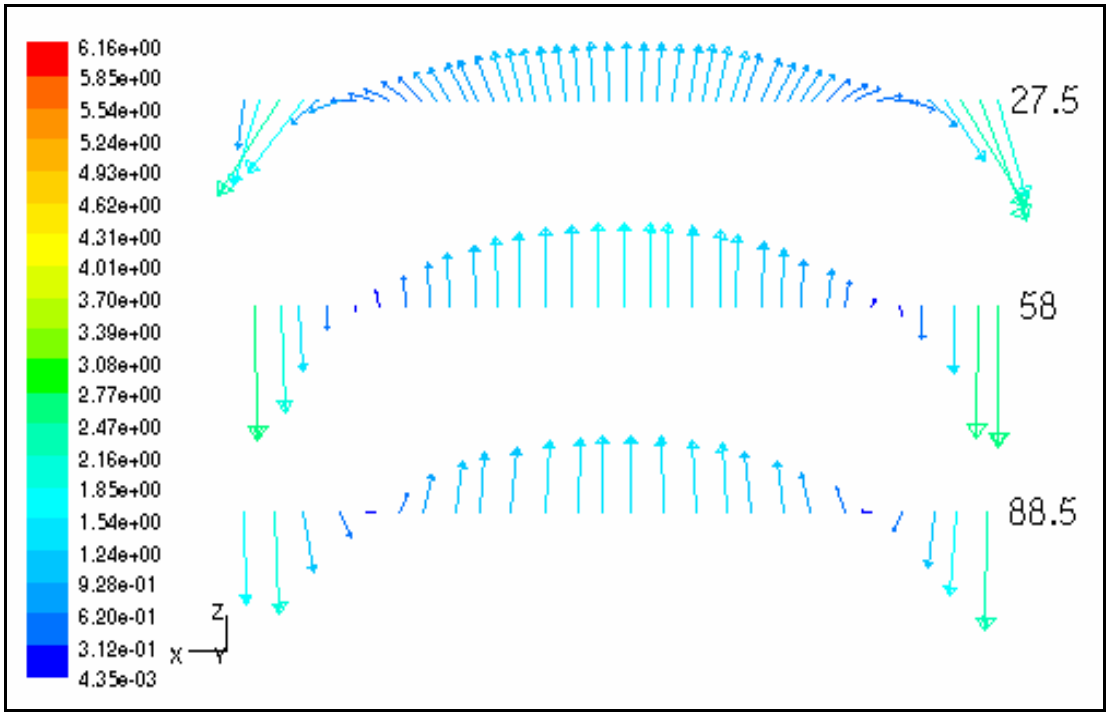


a)

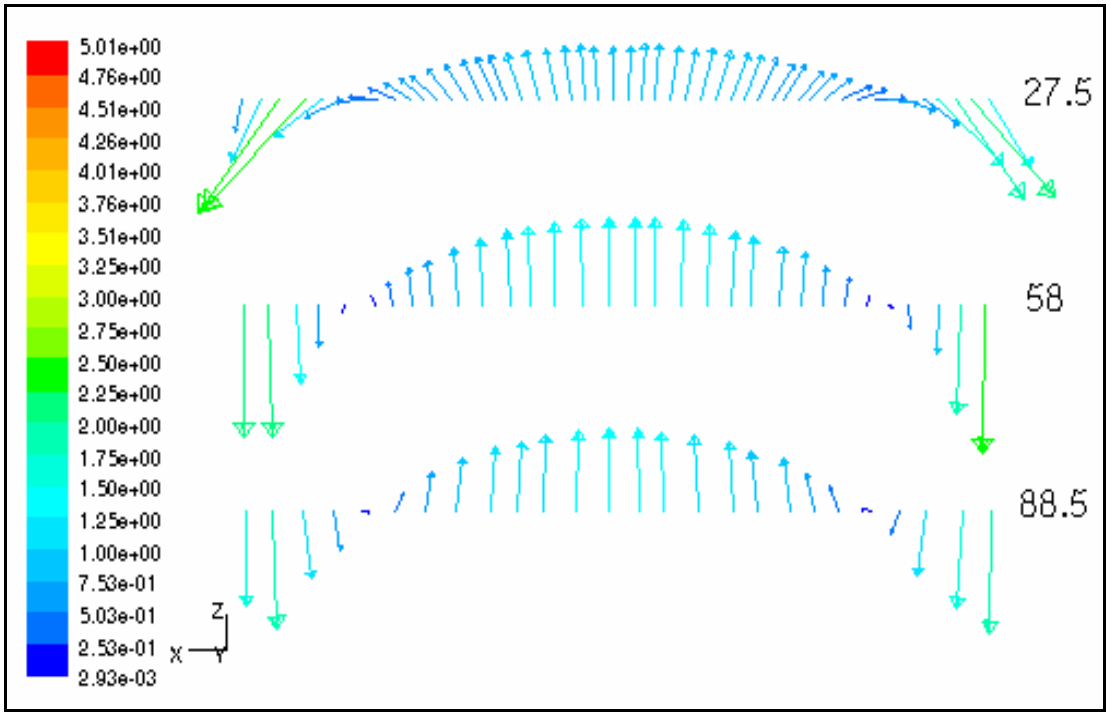


b)

Figure 4.29 Velocity vectors colored by velocity magnitude (m/s) for measurement points a) 3 mm valve gap b) 5 mm valve gap.

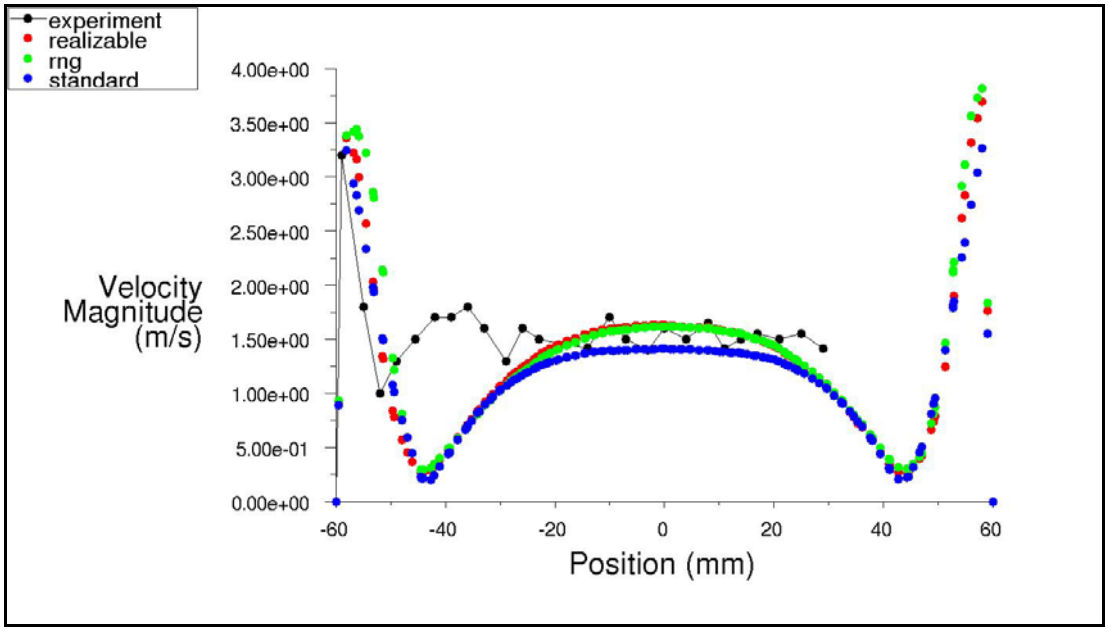


a)

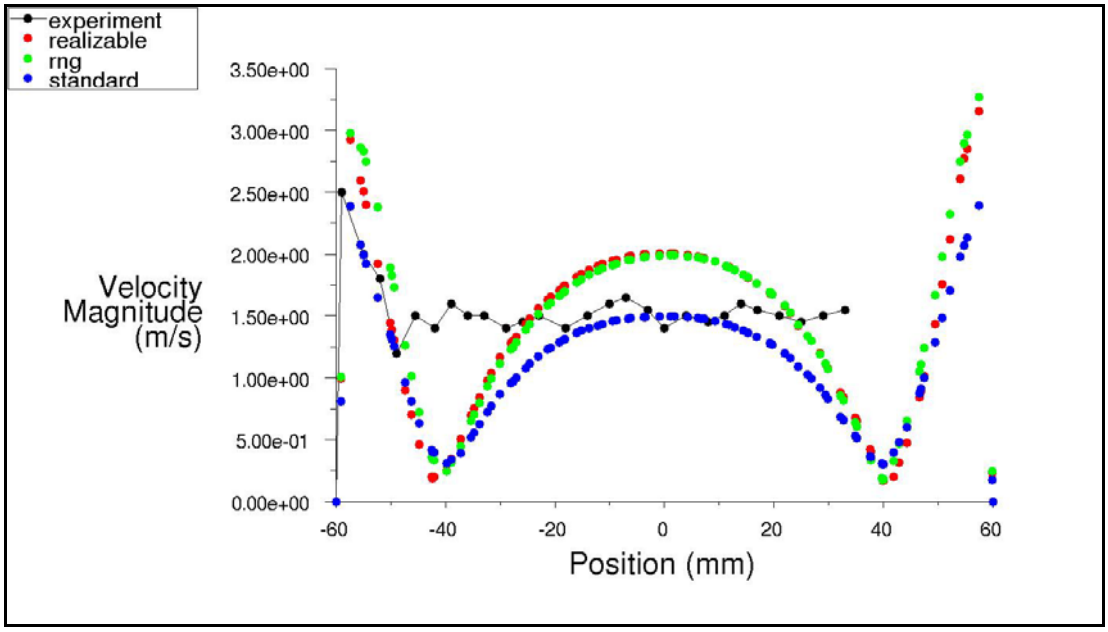


b)

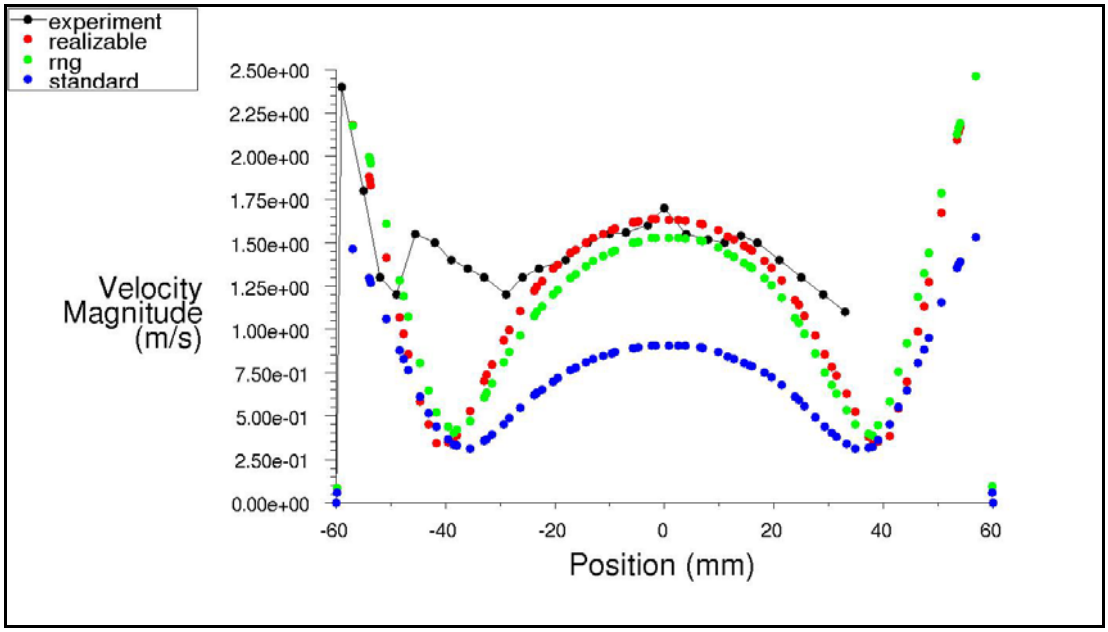
Figure 4.30 Velocity vectors colored by velocity magnitude (m/s) for measurement points a) 7 mm valve gap b) 9 mm valve gap.


experiment
realizable
rng
standard
Velocity Magnitude (m/s)
4.00e+00
3.50e+00
3.00e+00
2.50e+00
2.00e+00
1.50e+00
1.00e+00
5.00e-01
0.00e+00
-60
-40
-20
0
20
40
60
Position (mm)

a)

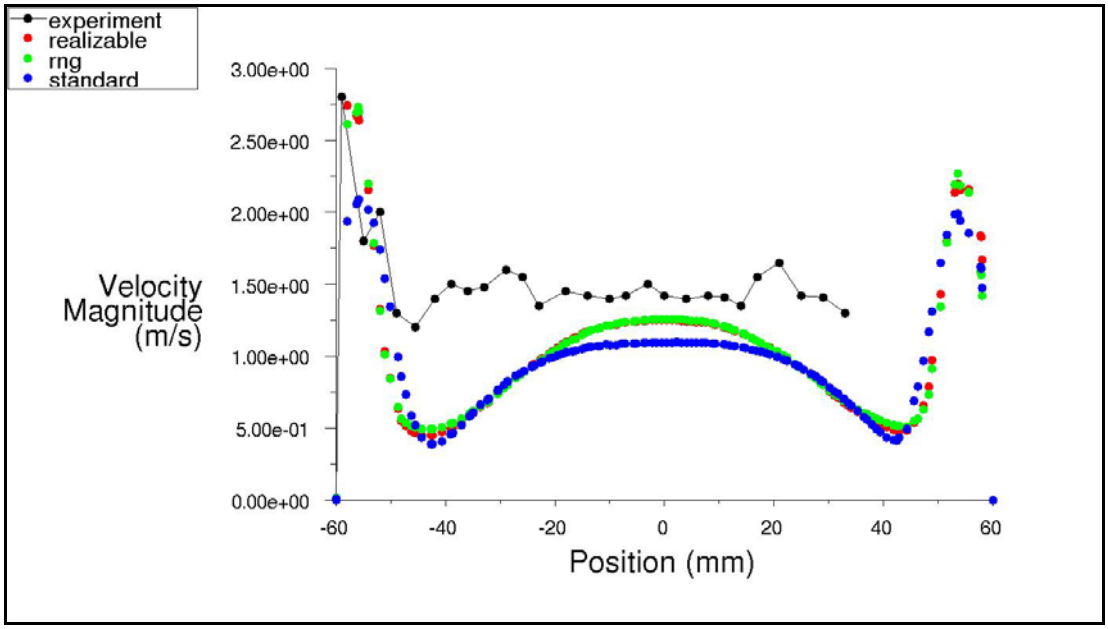

experiment
realizable
rng
standard
Velocity Magnitude (m/s)
3.50e+00
3.00e+00
2.50e+00
2.00e+00
1.50e+00
1.00e+00
5.00e-01
0.00e+00
-60
-40
-20
0
20
40
60
Position (mm)

b)

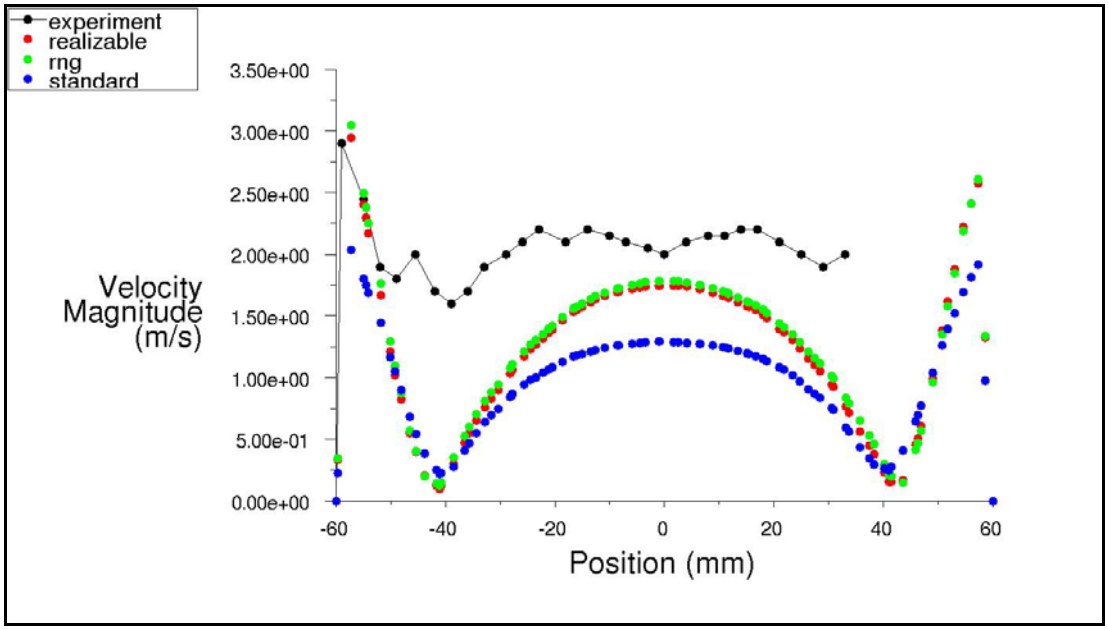


c)

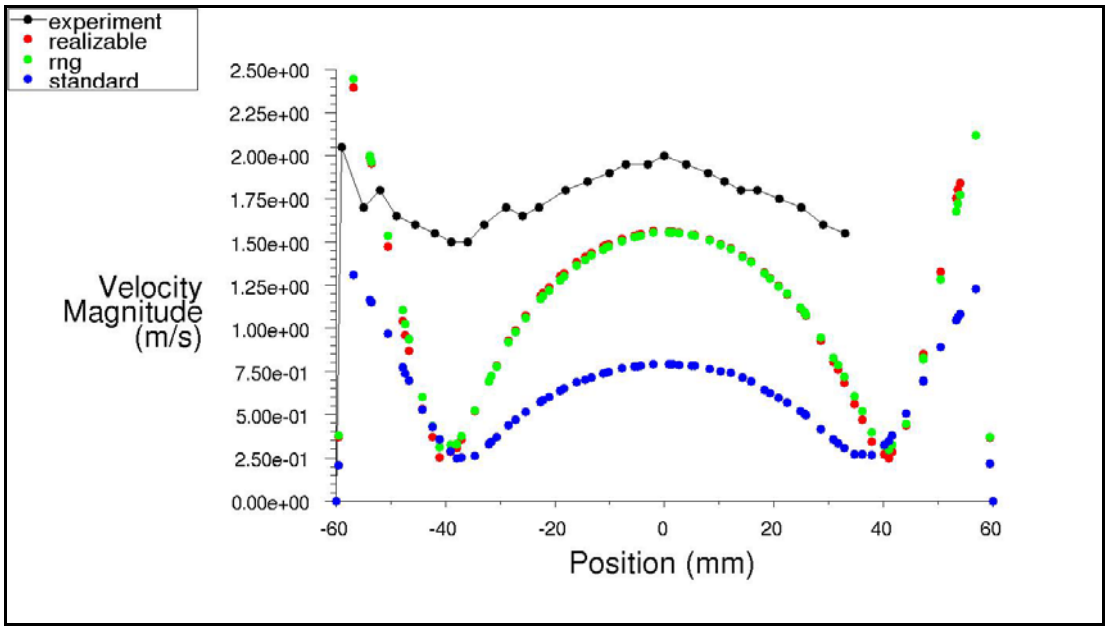
Figure 4.31 Velocity magnitude comparison between experimental results and turbulence models for 3 mm valve gap a) z = 27.5 mm b) z = 58 mm c) z = 88.5 mm



a)

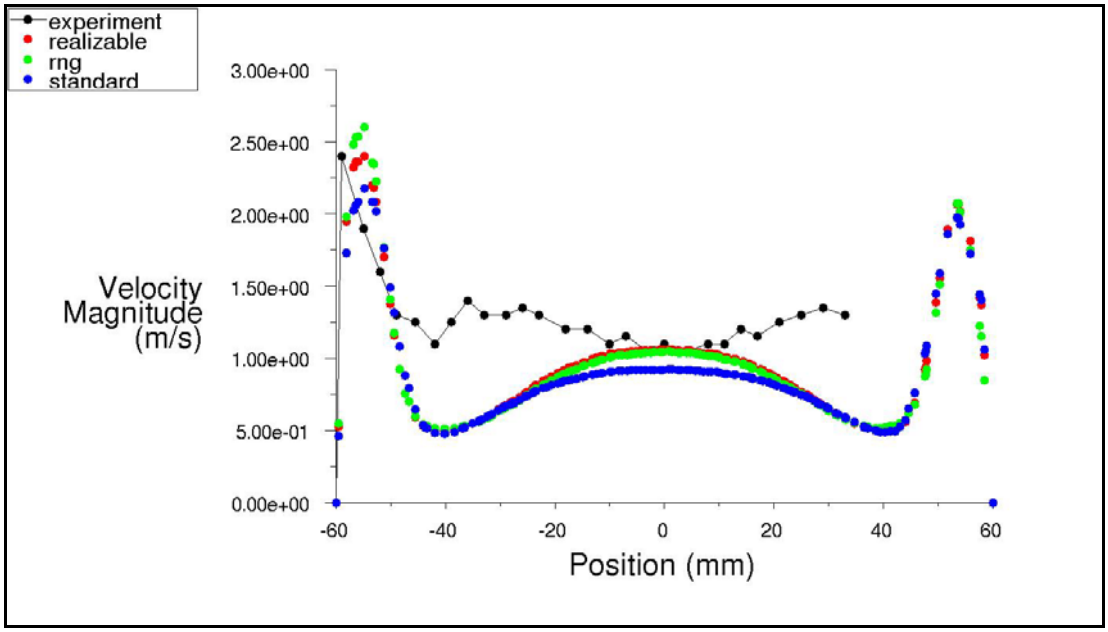


b)

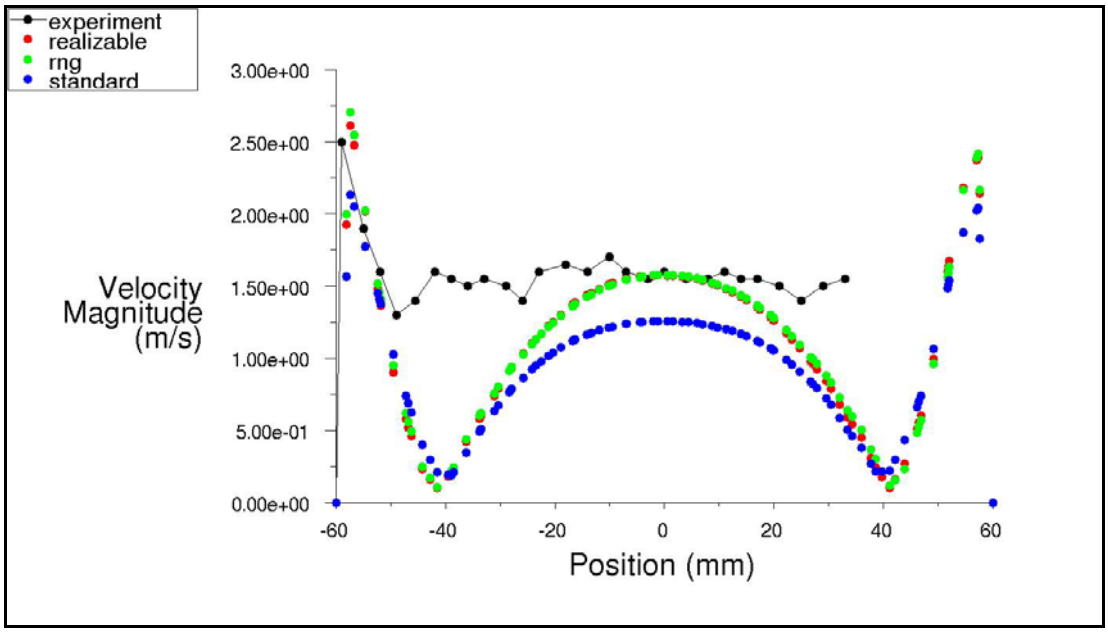


c)

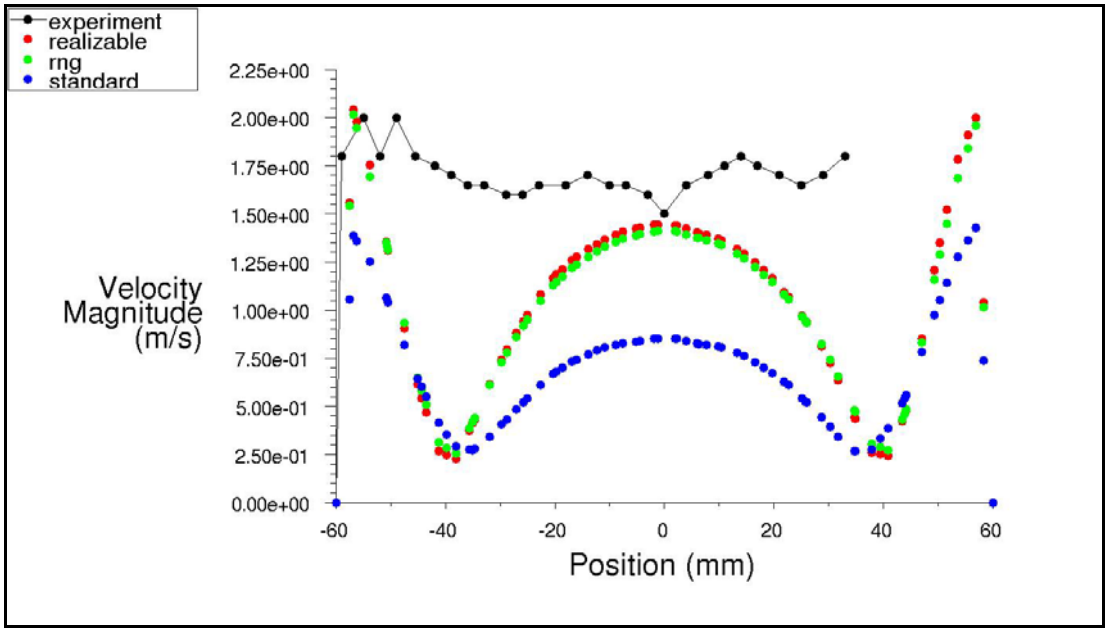
Figure 4.32 Velocity magnitude comparison between experimental result and turbulence models for 5 mm valve gap a) z = 27.5 mm b) z = 58 mm c) z = 88.5 mm


experiment
realizable
rng
standard
Velocity Magnitude (m/s)
3.00e+00
2.50e+00
2.00e+00
1.50e+00
1.00e+00
5.00e-01
0.00e+00
-60
-40
-20
0
20
40
60
Position (mm)

a)

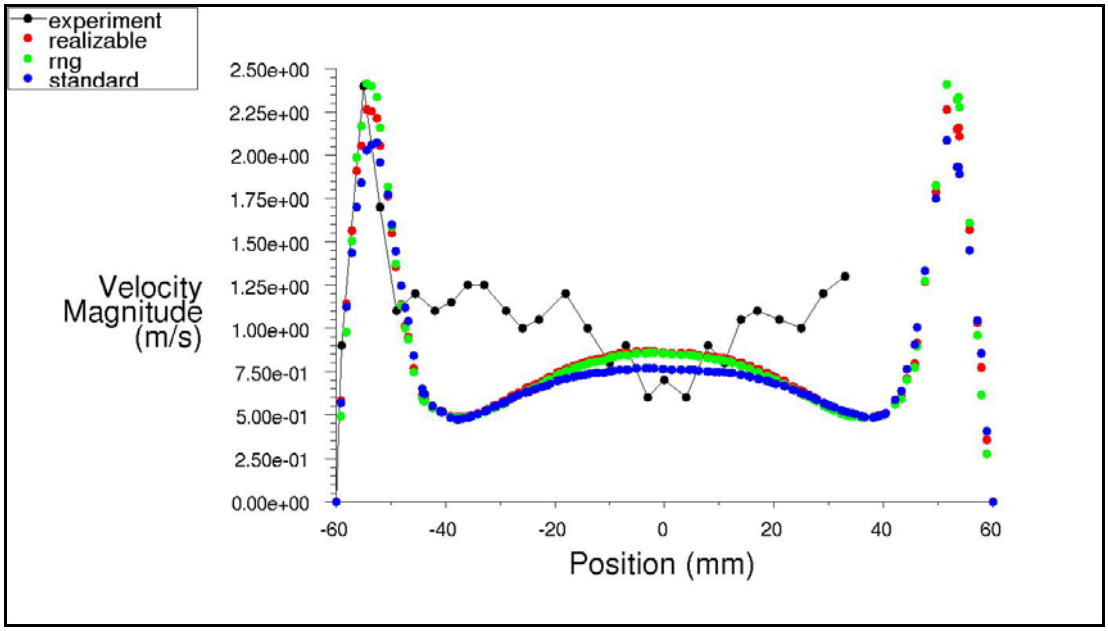

experiment
realizable
rng
standard
Velocity Magnitude (m/s)
3.00e+00
2.50e+00
2.00e+00
1.50e+00
1.00e+00
5.00e-01
0.00e+00
-60
-40
-20
0
20
40
60
Position (mm)

b)

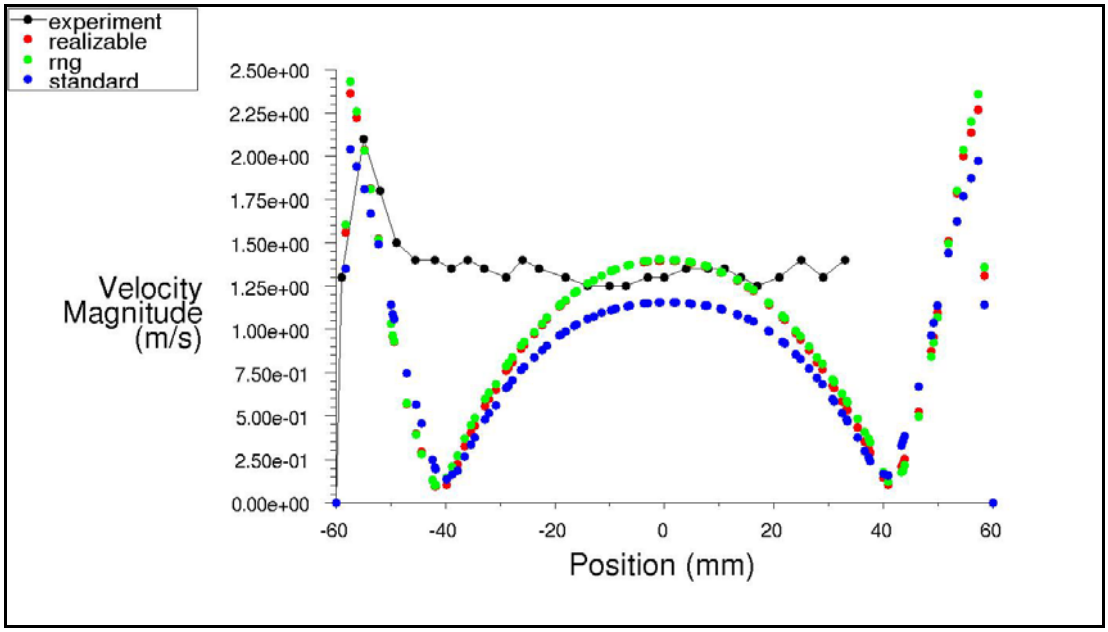


c)

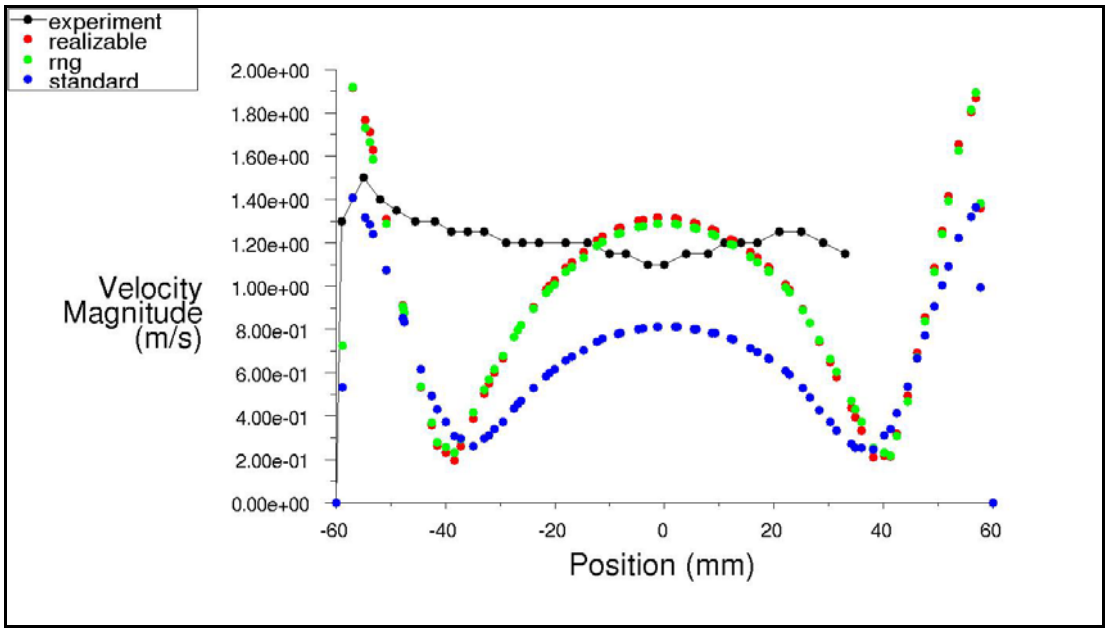
Figure 4.33 Velocity magnitude comparison between experimental result and turbulence models for 7 mm valve gap a) z = 27.5 mm b) z = 58 mm c) z = 88.5 mm



a)



b)



c)

Figure 4.34 Velocity magnitude comparison between experimental result and turbulence models for 9 mm valve gap a) z = 27.5 mm b) z = 58 mm c) z = 88.5 mm

During the 3d model that has two intake port calculations; different visualization technique was carried out. First of all, model was cut with a plane from center of intake ports and with a second plane 20 mm from cylinder head as they are shown in Figure 4.35.

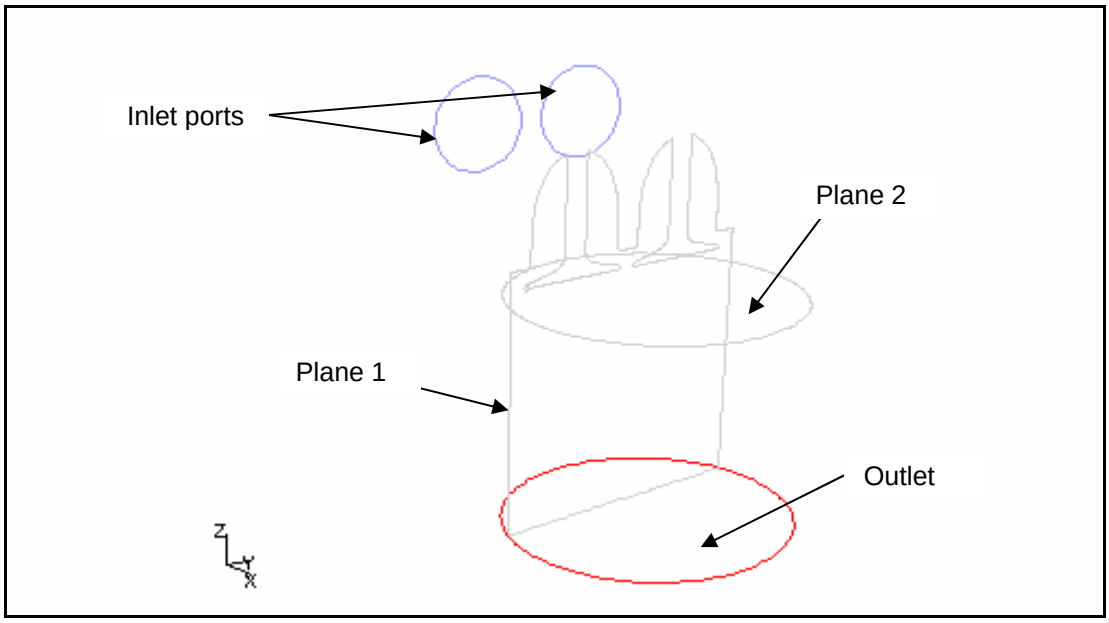


Figure 4.35 Visualization planes

Flow characteristic and movement for model will be shown by using these planes. Firstly, plane 1 results will be shown by comparing two different turbulence models and secondly results from plane 2 will be shown in similar way. 3d model is only shown in order to imagine flow domain in Figure 4.36. It is not illustrated for all valve gaps because of the space problem in thesis. As seen from Figure 4.36, vector illustration is not suitable for 3d models. Therefore, plane 1 and plane 2 were created.

Figure 4.37 shows velocity vectors in plane 1 for 5mm valve gap with different turbulence model. As it is indicated in two figures, there are no big differences between two turbulence models. But when looking at velocity color map, it can be seen that RNG method predicts maximum velocity value more than realizable method near valve jet area. Moreover, velocity vector curves in center of

figure tend to turn anticlockwise direction as it is not expected. Since there is a symmetric condition and no unbalancing condition, flow pattern must be similar as it is shown in realizable model. It is difficult to see velocity vectors near bottom of cylinder region in both figures and most of the plane 1 figures, since this region contains normal velocity vectors to the paper plane. Figure 4.38 shows a view from plane 2 for two different turbulence models. Like Figure 4.37, bottom region of cylinder, it is also difficult to see velocity vectors standing below valve here, since they are normal vectors. The important thing in these figures is that both of the figures generate small swirl motions after colliding with wall. Although they are small and their intensities are not too much, they affect all of the in-cylinder flow movement.

Figure 4.39 shows same planes and parameters for 7 mm valve gap. Here, it is noticed that velocity magnitude is getting to decrease, since valve continues to open and jet effect calms down. When these figures are investigated carefully, two small clockwise and anticlockwise swirls below each valve can be seen. These swirls are generated similar principles as they are seen in one intake port model. They are generated because there is a low pressure area in down stream namely, below valves. Therefore, flow tends to generate these swirls. Figure 4.40 illustrates that there are no important differences between these two turbulence models. Finally, two anticlockwise swirl effects in center of the cylinder for 9 mm valve gap are shown in Figure 4.41 for both turbulence models. As seen from this figure and all of the figures, there are some backflow movements in outlet boundary as it is expected. This backflow effect could have been decreased by extending cylinder length but this did not make since there would have been more time consumption and more hardware requirements for calculation.

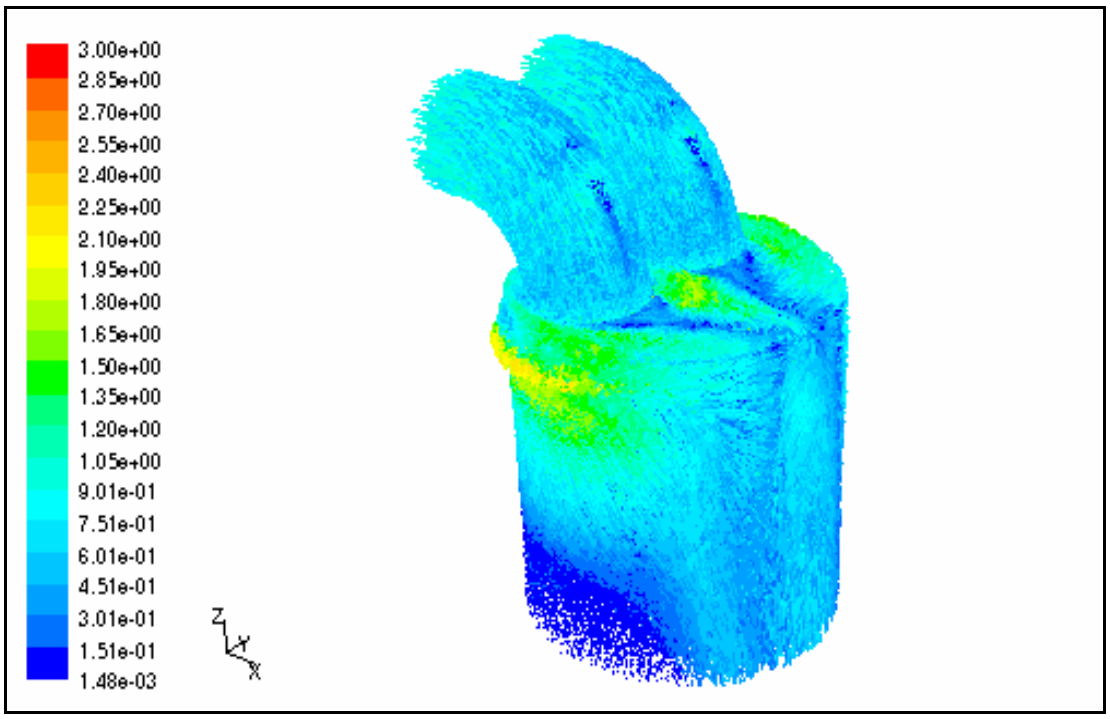
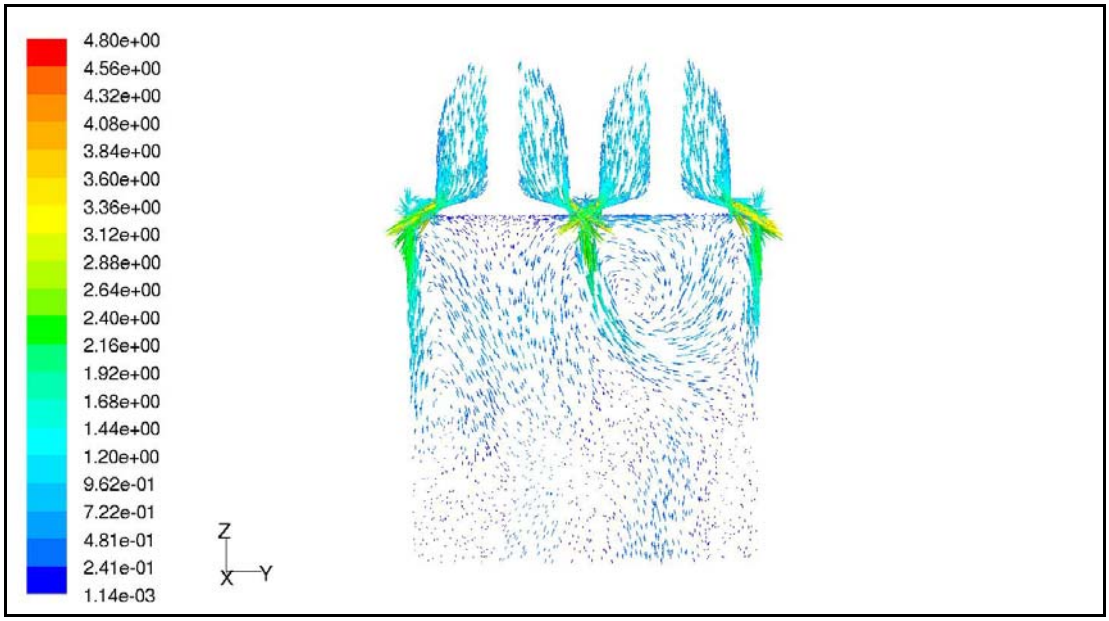
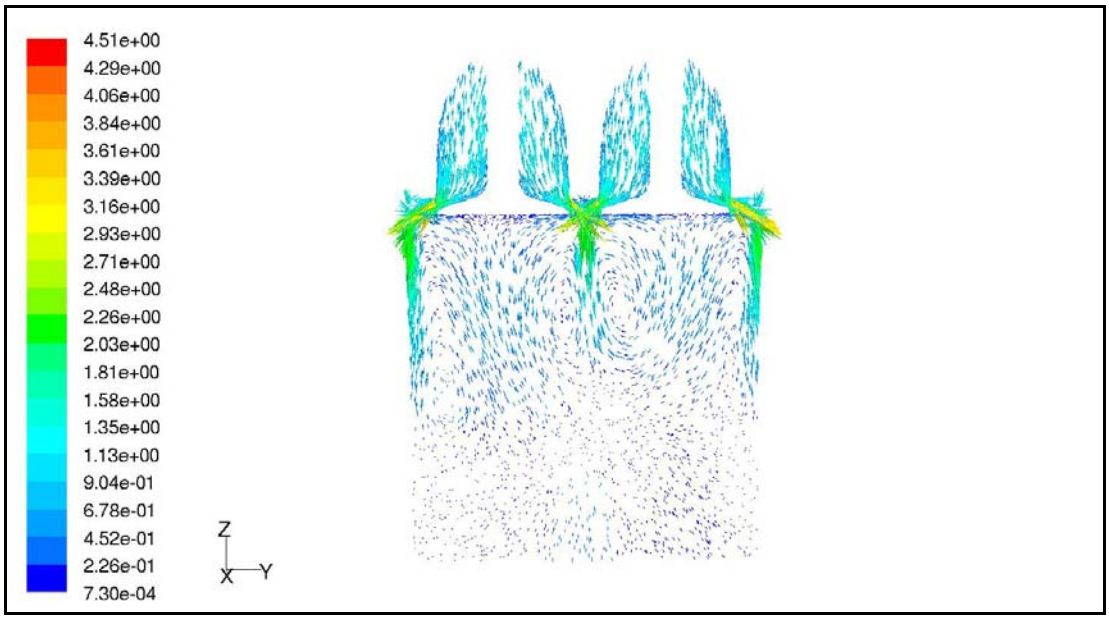


Figure 4.36 An example of 3d model with two intake pipes

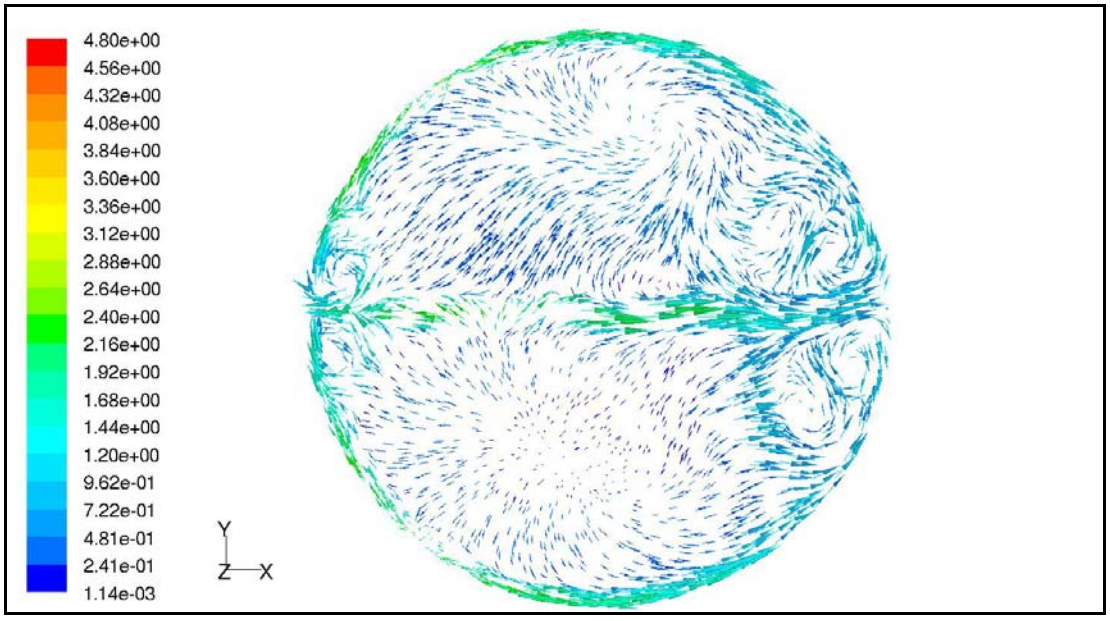


a)

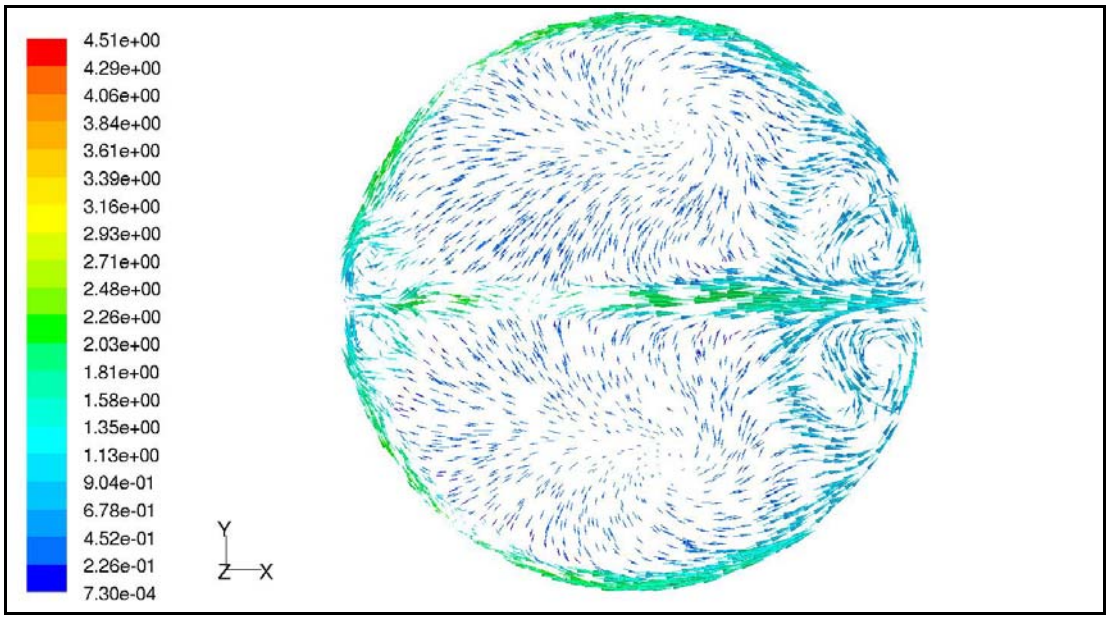


b)

Figure 4.37 A view from plane 1 for a) RNG $k-\varepsilon$ turbulence model b) realizable $k-\varepsilon$ turbulence model (valve gap = 5 mm)

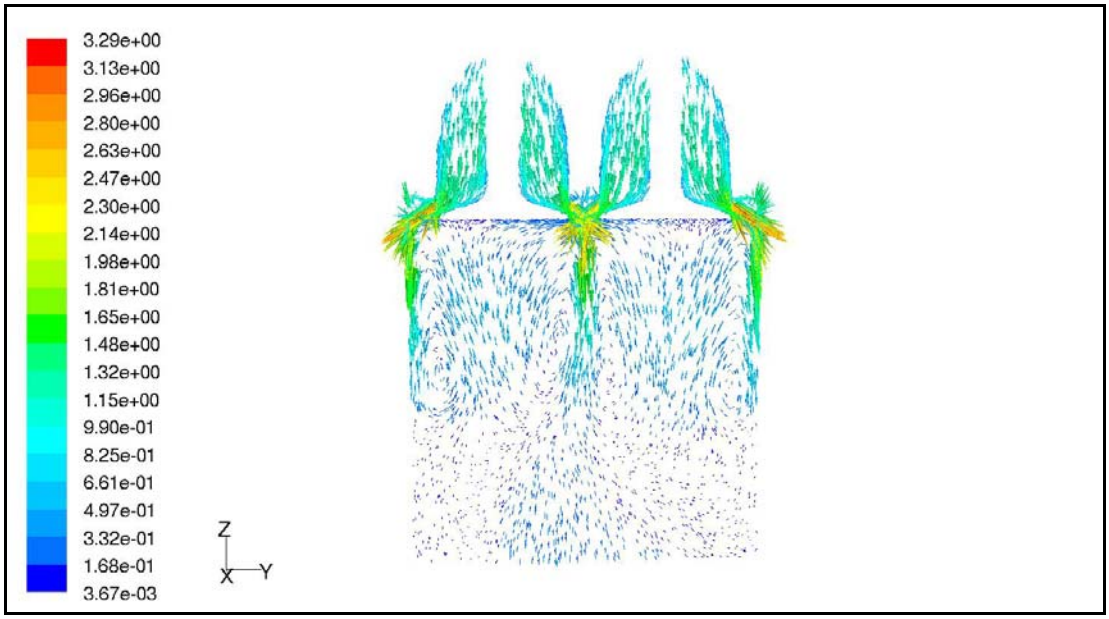


a)

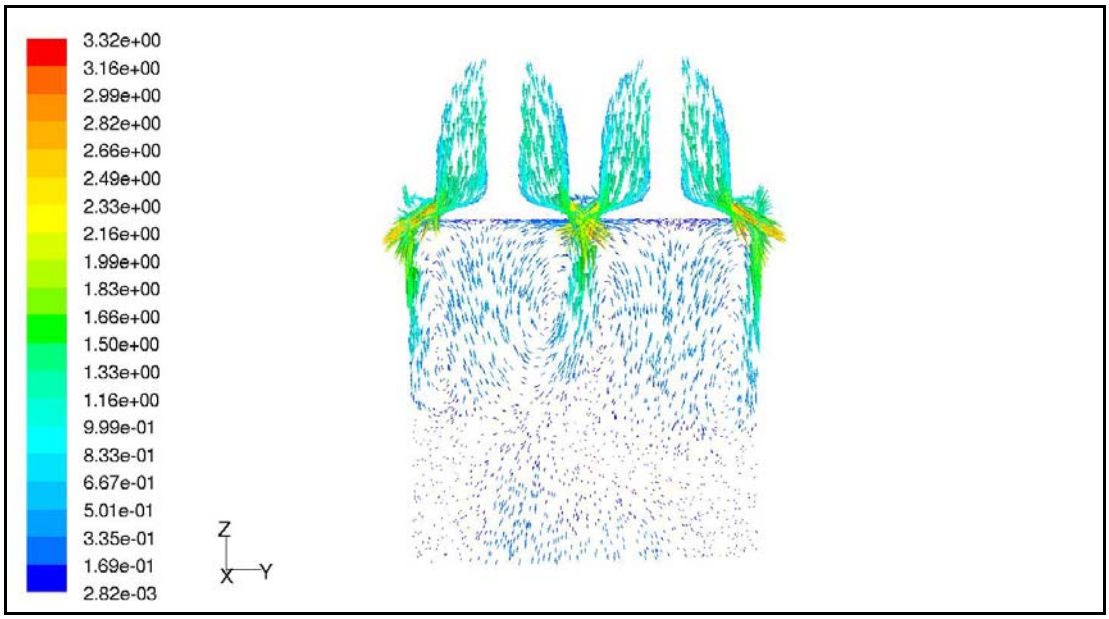


b)

Figure 4.38 A view from plane 2 for a) RNG $k-\varepsilon$ turbulence model b) realizable $k-\varepsilon$ turbulence model (valve gap = 5 mm)

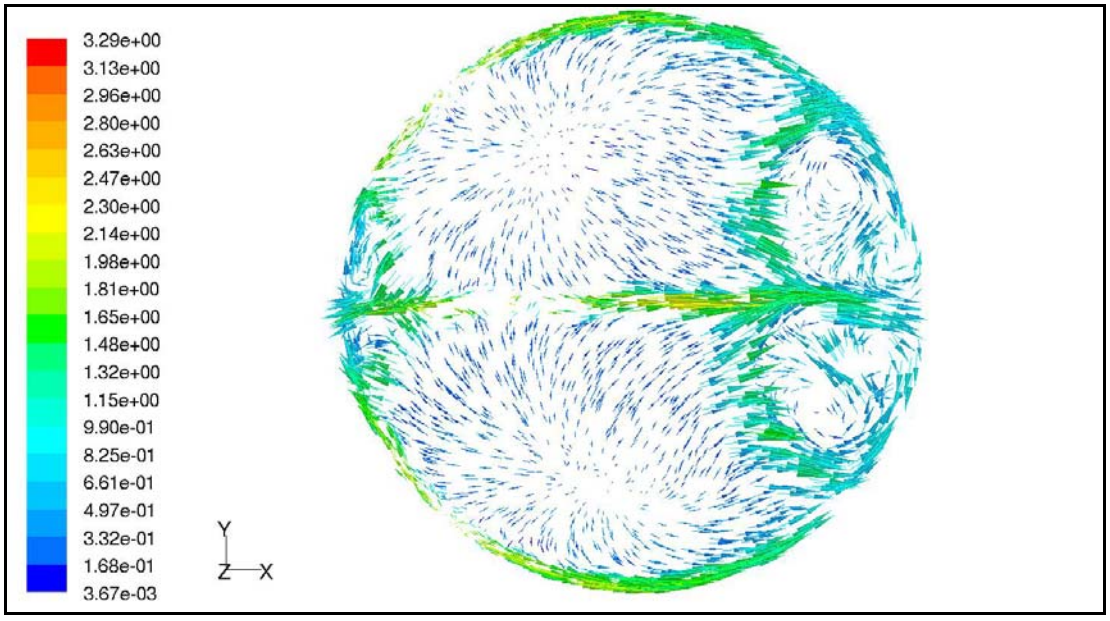


a)

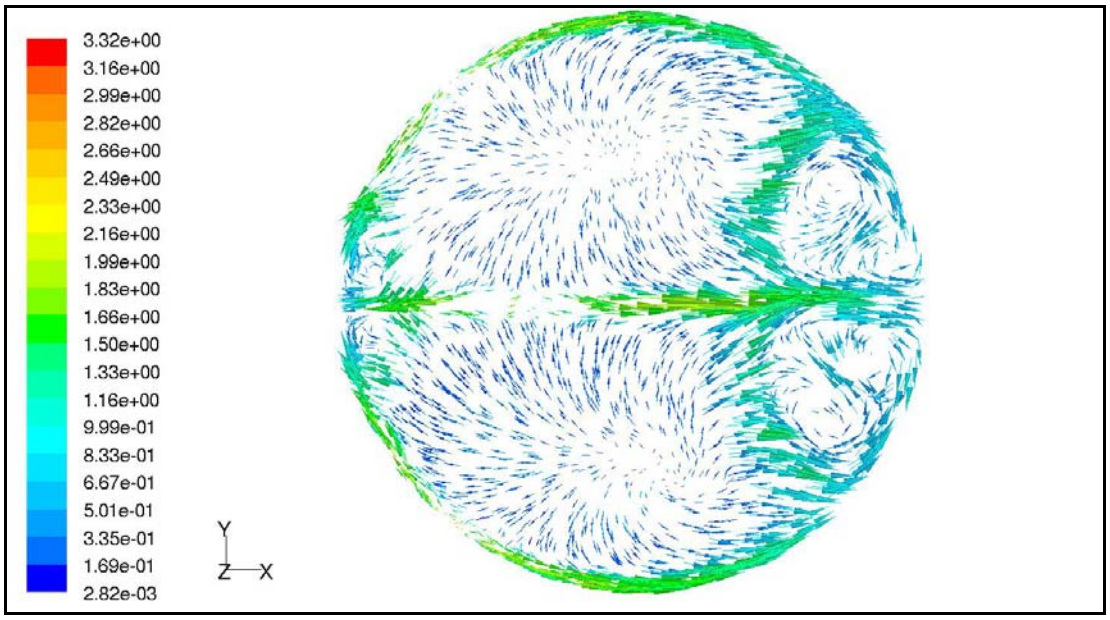


b)

Figure 4.39 A view from plane 1 for a) RNG $k-\varepsilon$ turbulence model b) realizable $k-\varepsilon$ turbulence model (valve gap = 7 mm)

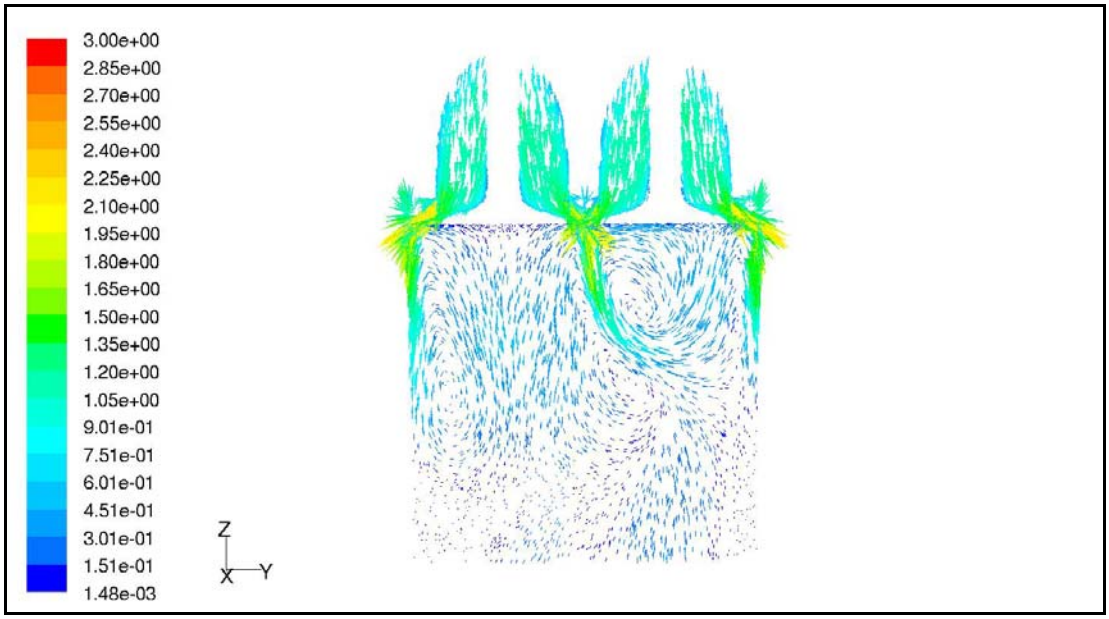


a)

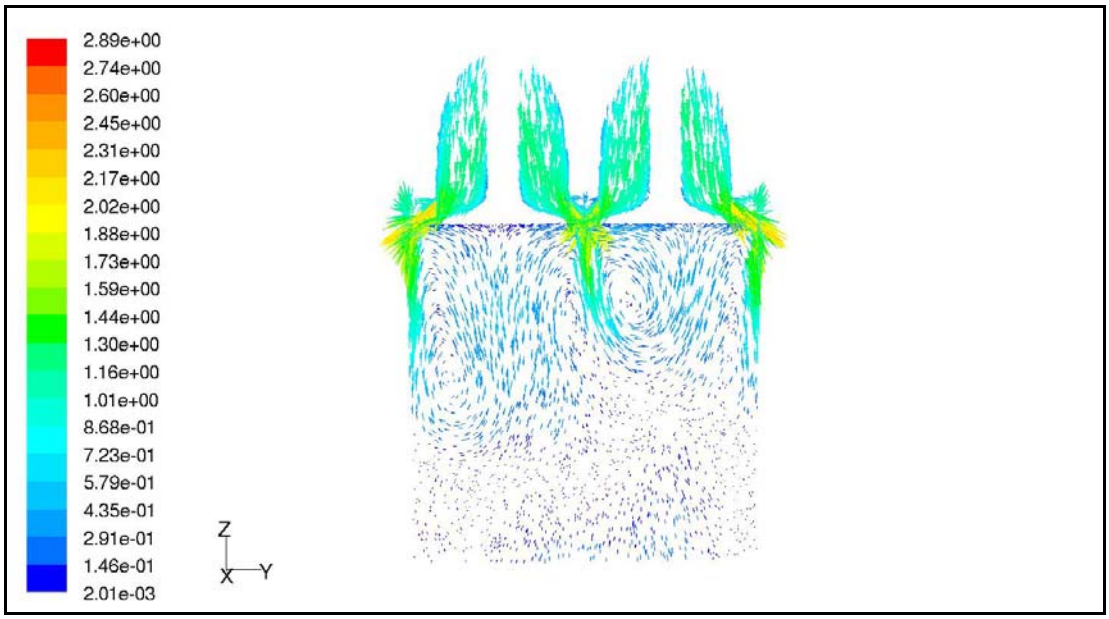


b)

Figure 4.40 A view from plane 2 for a) RNG $k-\varepsilon$ turbulence model b) realizable $k-\varepsilon$ turbulence model (valve gap = 7 mm)

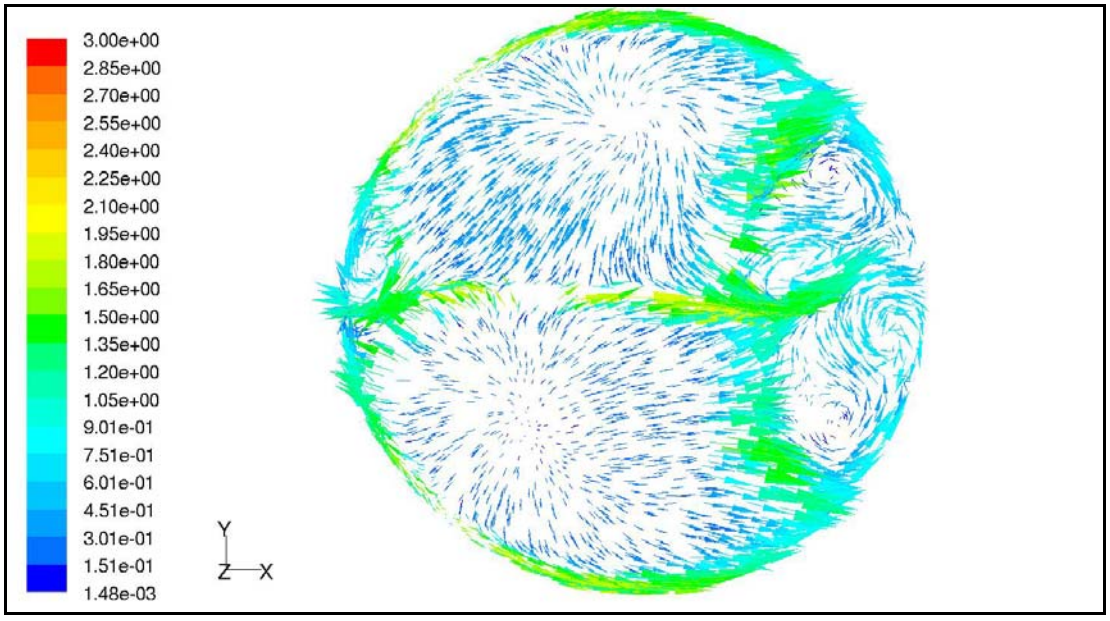


a)

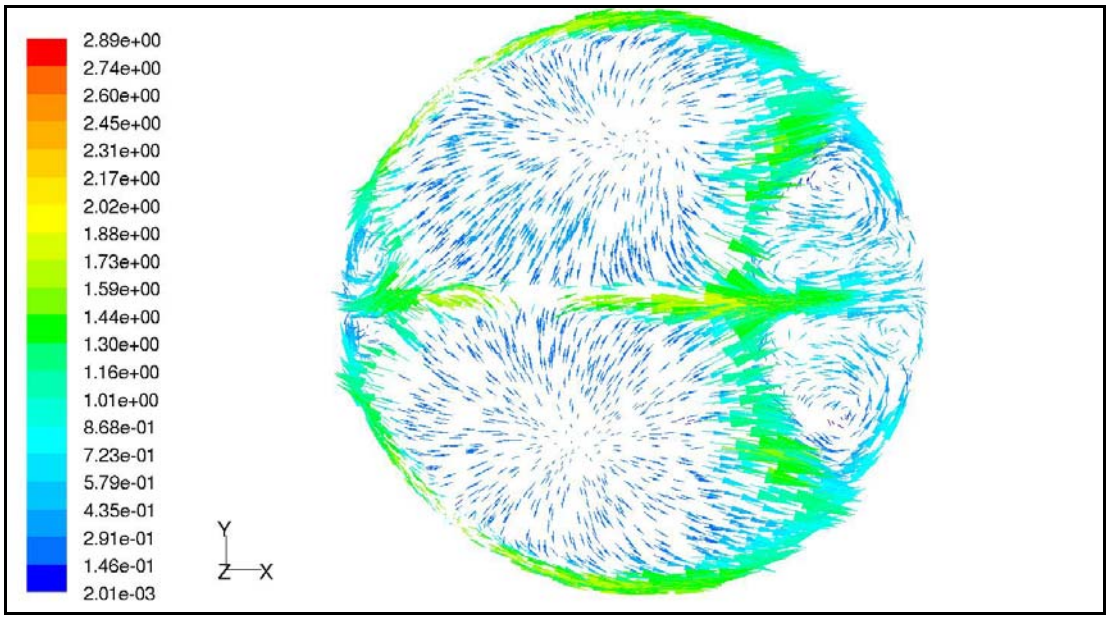


b)

Figure 4.41 A view from plane 1 for a) RNG $k-\varepsilon$ turbulence model b) realizable $k-\varepsilon$ turbulence model (valve gap = 9 mm)



a)



b)

Figure 4.42 A view from plane 2 for a) RNG $k-\varepsilon$ turbulence model b) realizable $k-\varepsilon$ turbulence model (valve gap = 9 mm)

4.3 Dynamic Grid Calculations

In this section of thesis, dynamic model results will be shown. The target of dynamic model is to show how real flow movement occurs inside of an engine. As model, 2d pent roof type cylinder model is selected because of some benefits that were explained in Material and Method section (Chapter 3) before. Dynamic model calculation starts 345° CA just before inlet valve opens and continues one entire cycle. Unlike 2d steady model results, some additional features will be investigated in following lines such as temperature and pressure values inside of cylinder. Since one cycle takes 720° CA degrees, it is difficult to show all of cycle one by one crank angle step. Therefore, some critical degrees were randomly selected, and these results will be shown in following figures. First of all, velocity vectors will be shown and than temperature and pressure variations will be illustrated in motored condition. It is understood from last sentence, study for dynamic model has been designed for cold flow calculation.

Figure 4.43 a shows velocity vectors in 390° CA degrees while piston goes down its BDC position and intake valve starts to open. As seen from figure, there are one clockwise and one anticlockwise small tumble that are created by the flow motion. In this stage, the jet in the right side does not create so big effect that it can totally sweep out rest of the area. It is also possible to see two small swirl inside of the exhaust port since exhaust valve is a little bit open in time when calculation has been just started and a small number of air particles have released to this area and generated this small swirls. In Figure 4.43 b, piston is near its BDC position but has not reached there yet. A big tumble motion dominates inside of cylinder caused by jet motion in right side of valve. As it is seen from figure, this jet has strong effect but it does not still sufficient to sweep out entire area and reach right lateral wall. Unlike this tumble, another anticlockwise tumble effect can be seen at the bottom of the figure, near the piston. This tumble is sustained by left side jet effect. Another important thing is that right side jet effect is stronger than left side as it is noticed from figure. This is because of the elbow that is fixed in intake system.

Figure 4.43 c shows near intake valve region. In this figure, piston has finished its intake period and turned its way to TDC position. Crack angle is 570° here. As seen from figure, inlet valve is such a position as if it is close. In this period some air release to the intake port although it is not wished. Another crucial thing in this figure is velocity vectors turning clockwise way in combustion chamber. As it is remembered from previous figure, there is a big clockwise tumble inside of cylinder and it is thought that its effect still continues in this period. Velocity magnitude in this figure reaches nearly 100 m/s because of the small section area in valve jet region.

Figure 4.43 d is captured in 705° CA, just before piston reaches its TDC position. Here, clockwise tumble effect in cylinder still continue as it has been explained why it is in this direction previous lines. Another important thing in this figure is small swirls inside of intake port caused by released gases during the closing period of intake valve. From Figure 4.43 e through Figure 4.43 h reflect exhaust period. Figure 4.43 e is taken from 907° CA just after BDC position. Some of the exhaust gases tend to enter combustion chamber in this figure. This is thought that there is a sudden pressure drop whilst piston goes to its BDC position and this pressure drop causes exhaust gases to enter combustion domain. In addition to this, small swirls can be seen near over valve region because of the flow movement.

Finally, exhaust process begin in Figure 4.43 f and continue in very high velocity. As it is indicated in figure, there are two jet effects like intake period but this time towards outside. In this case, jets collide with valve pivot walls and this creates small eddies inside of exhaust port. It is clearer to see how much velocity level exhaust process reaches in Figure 4.43 g. Here, exhaust process continue and piston is getting nearer its TDC position. Small eddies in exhaust port can also be seen from this figure and finally the last captured figure (Figure 4.43 h) is from 1080° CA, piston is exactly in its TDC position. It is seen that intake valve has just start to open and two valves are a little bit open in this period interestingly. This period is also called “valve overlap” period. Should the manufacturer uses turbocharger, this period can help to sweep out entire combustion chamber effectively. In our case also, had turbocharger used, there would not have been

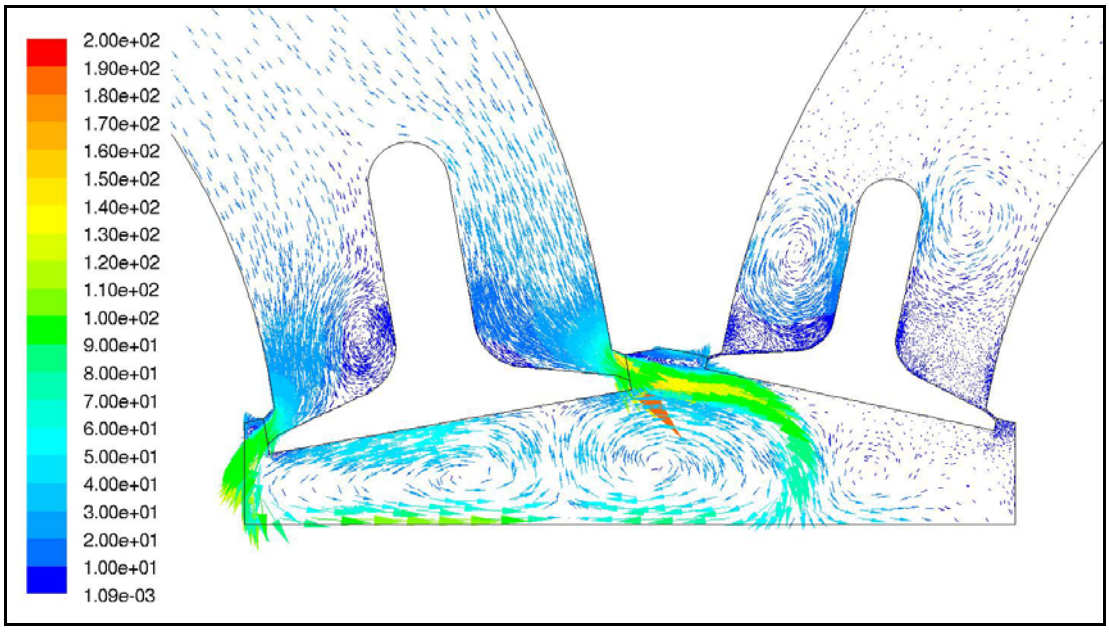
backflow in intake port; in contrast there would have been more pressure than combustion chamber and this pressure would have helped sweeping event.

Figure 4.44 shows contours of static pressure and temperature near TDC position (705° CA) respectively. Both of the figures are in expected range if reversible and adiabatic compression rules are applied to the model. These values are sufficient for an Otto engine to initiate a spark. Following figures after Figure 4.44 show two convergence histories; one of them belongs to mass fraction of burned gases inside of cylinder and the other one shows static pressure history on combustion chamber. As it is explained in Material Method section, burned and unburned gases assumption is made for dynamic model. As a result of this assumption, Figure 4.45 is created during the calculation. As it is seen from figure, burned gases level 100% at the beginning. After advancing a few time steps, it starts to go down since intake valve opens. It reduces approximately 10% levels and continues this level until exhaust valve starts to open near 2200 time steps. Detailed mixture process figures can be seen from Figure 4.47 a) through 4.47 g). As it is seen from these figures, combustion chamber and exhaust port are shown in red color as if there are burned gasses and intake port is shown in blue color that indicates burned gas level is zero namely, fresh air.

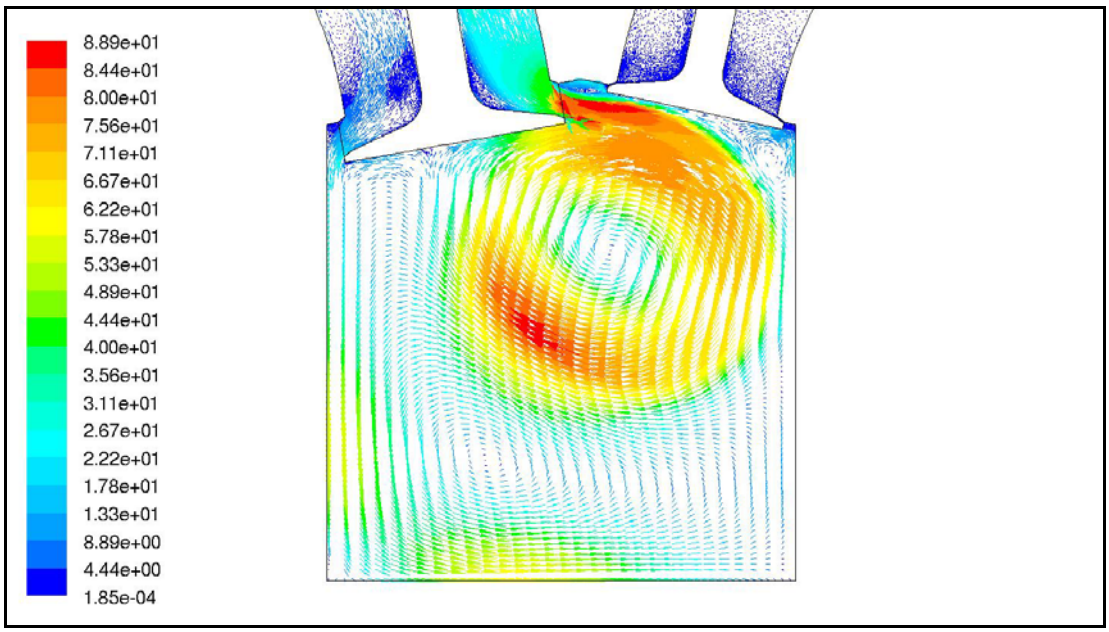
Time step definition is used along the calculation and one time step corresponds to 0.25° CA degrees. Therefore, calculation requires 2880 time steps as it is seen from Figure 4.45 and 4.46 in order to complete one revolution of crank shaft. After 2200 time steps, exhaust valve starts to open and some exhaust gases start to enter combustion domain as it is mentioned in Figure 4.43 e. This action increases burned gases level in combustion chamber. This event explains why burned gases level increase a little bit after 2200 time steps.

Figure 4.46 is about static pressure history in combustion chamber. In this figure, pressure rising in cylinder without combustion can be seen. Pressure starts to go up after 1000 time steps since this level corresponds to beginning of compression stroke and it reaches its maximum level after 1500 time steps namely, in TDC position. When looking at maximum pressure, the level is seen 4 MPa. This is also expected value for this compression ratio. Anyway, maximum pressure for Otto

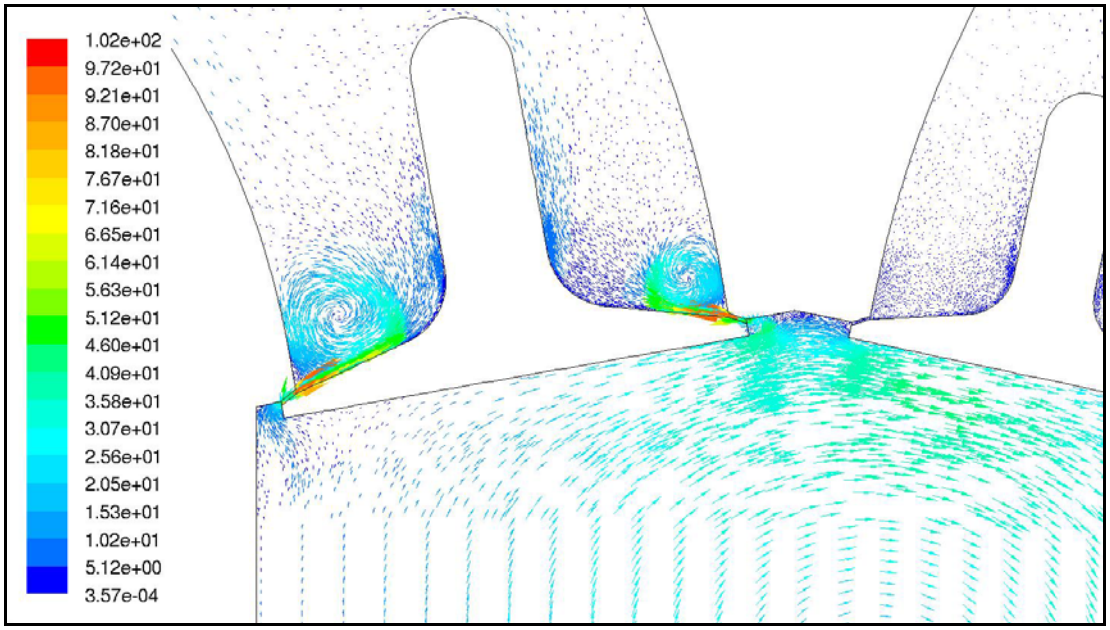
engines without combustion generally differs between 3.5 and 4.5 Mpa. These last two figures show that dynamic grid application is in good agreements with real world engines and it is thought that this type of applications will provide good innovations for automotive industry near future.



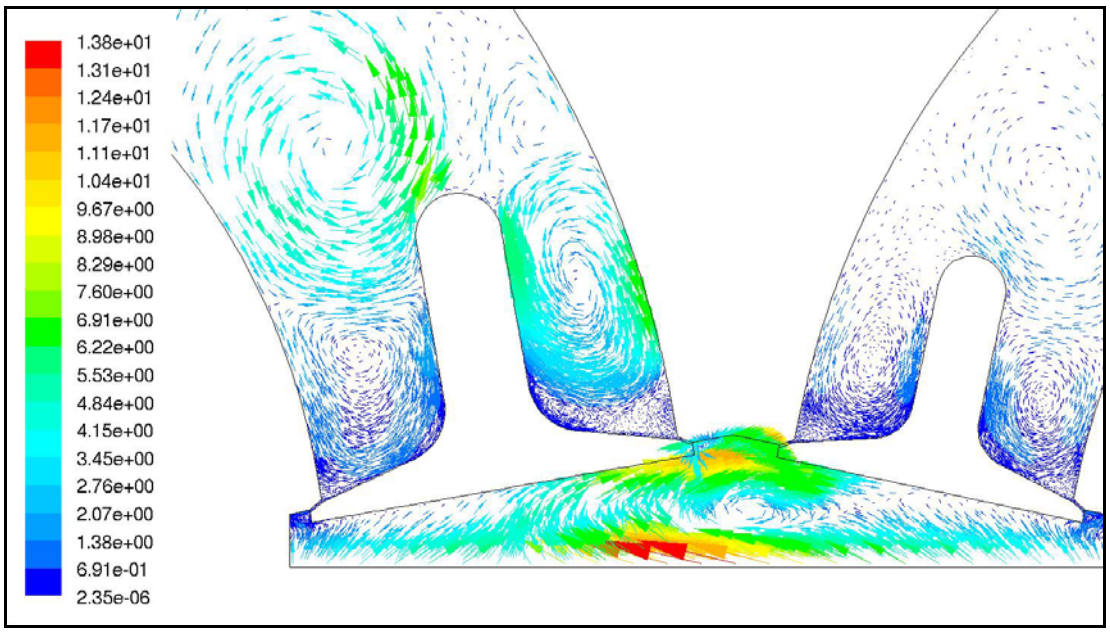
a)



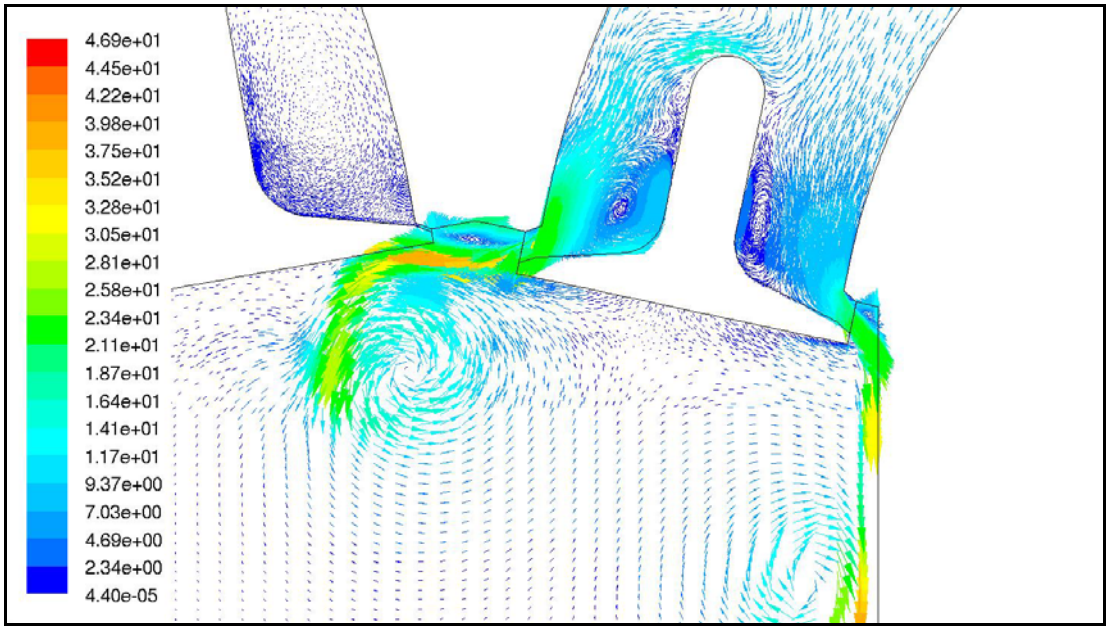
b)


1.02e+02
9.72e+01
9.21e+01
8.70e+01
8.18e+01
7.67e+01
7.16e+01
6.65e+01
6.14e+01
5.63e+01
5.12e+01
4.60e+01
4.09e+01
3.58e+01
3.07e+01
2.56e+01
2.05e+01
1.53e+01
1.02e+01
5.12e+00
3.57e-04

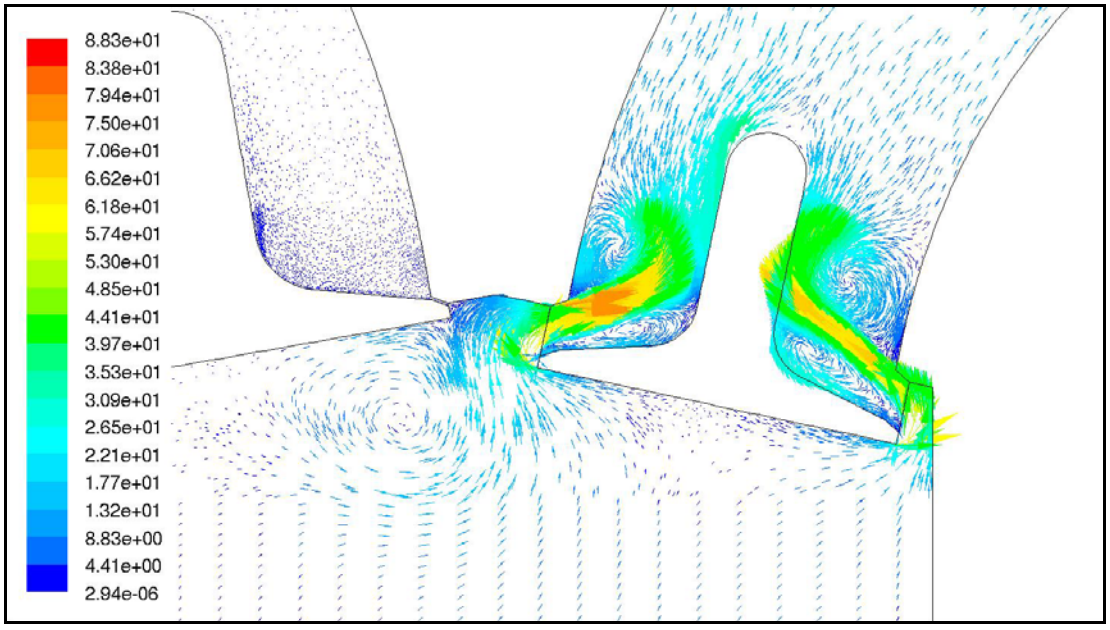
c)


1.38e+01
1.31e+01
1.24e+01
1.17e+01
1.11e+01
1.04e+01
9.67e+00
8.98e+00
8.29e+00
7.60e+00
6.91e+00
6.22e+00
5.53e+00
4.84e+00
4.15e+00
3.45e+00
2.76e+00
2.07e+00
1.38e+00
6.91e-01
2.35e-06

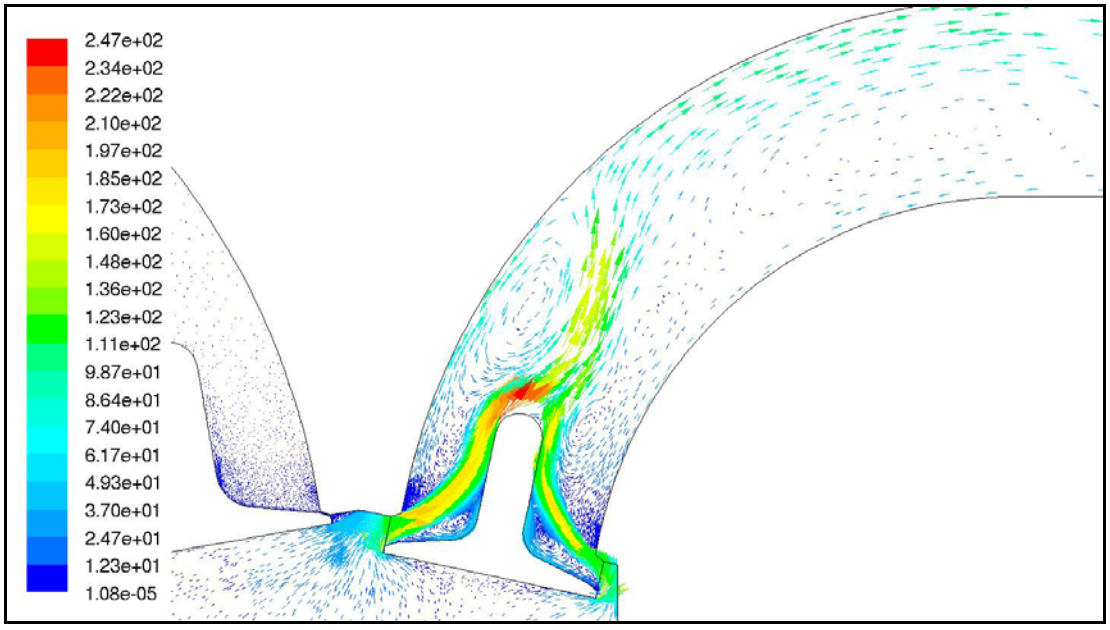
d)


4.69e+01
4.45e+01
4.22e+01
3.98e+01
3.75e+01
3.52e+01
3.28e+01
3.05e+01
2.81e+01
2.58e+01
2.34e+01
2.11e+01
1.87e+01
1.64e+01
1.41e+01
1.17e+01
9.37e+00
7.03e+00
4.69e+00
2.34e+00
4.40e-05

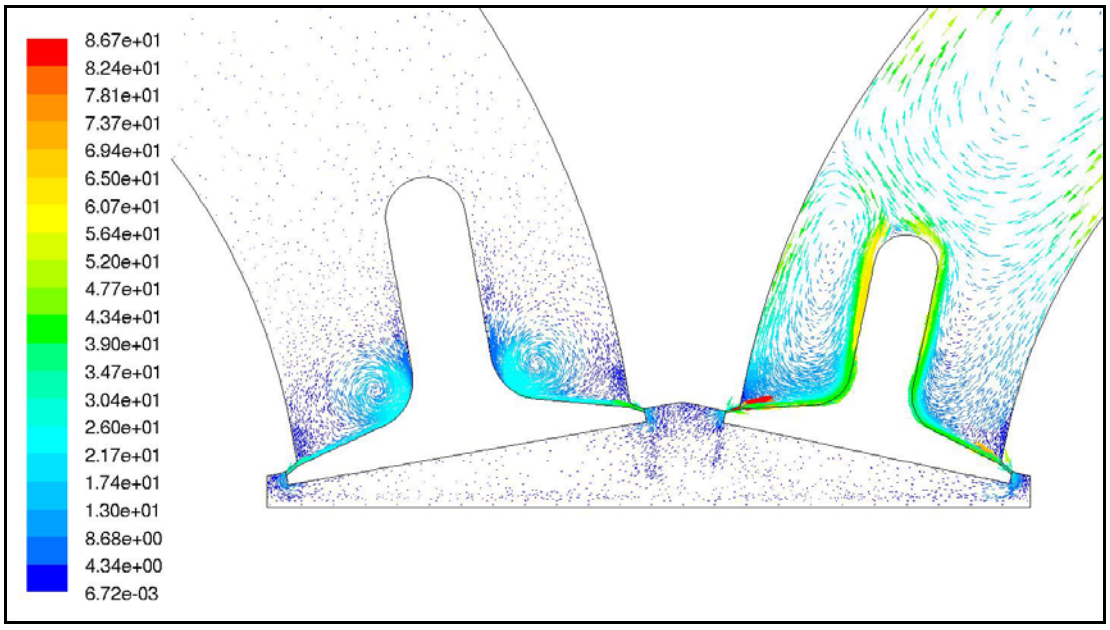
e)


8.83e+01
8.38e+01
7.94e+01
7.50e+01
7.06e+01
6.62e+01
6.18e+01
5.74e+01
5.30e+01
4.85e+01
4.41e+01
3.97e+01
3.53e+01
3.09e+01
2.65e+01
2.21e+01
1.77e+01
1.32e+01
8.83e+00
4.41e+00
2.94e-06

f)

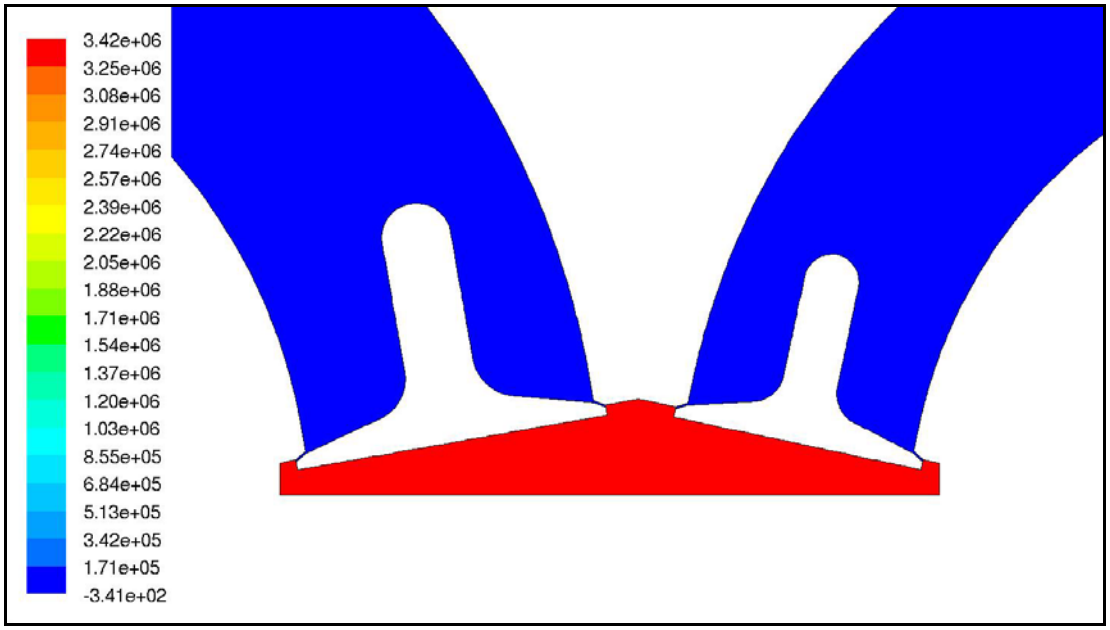


g)

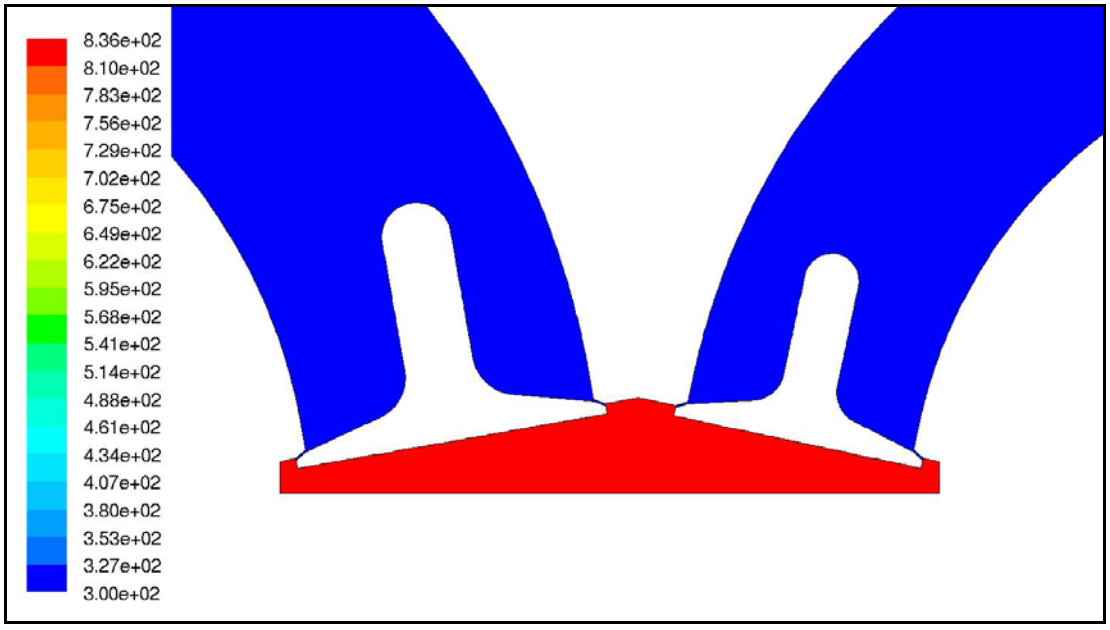


h)

Figure 4.43 Velocity vectors in different CA a) 390° b) 502° c) 570° d) 705° e) 907° f) 930° g) 1020° h) 1080°



a)



b)

Figure 4.44 a) Contours of Static pressure (Pa) b) Contours of temperature (K) near the TDC position

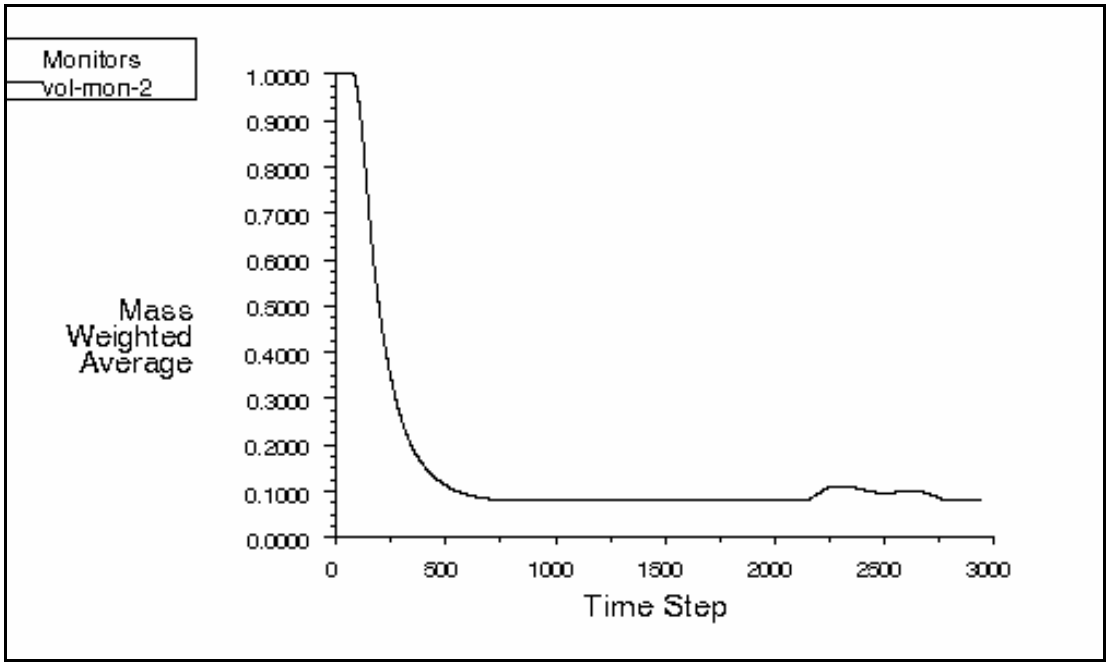


Figure 4.45 Convergence history of mass fraction of burned gases on combustion chamber

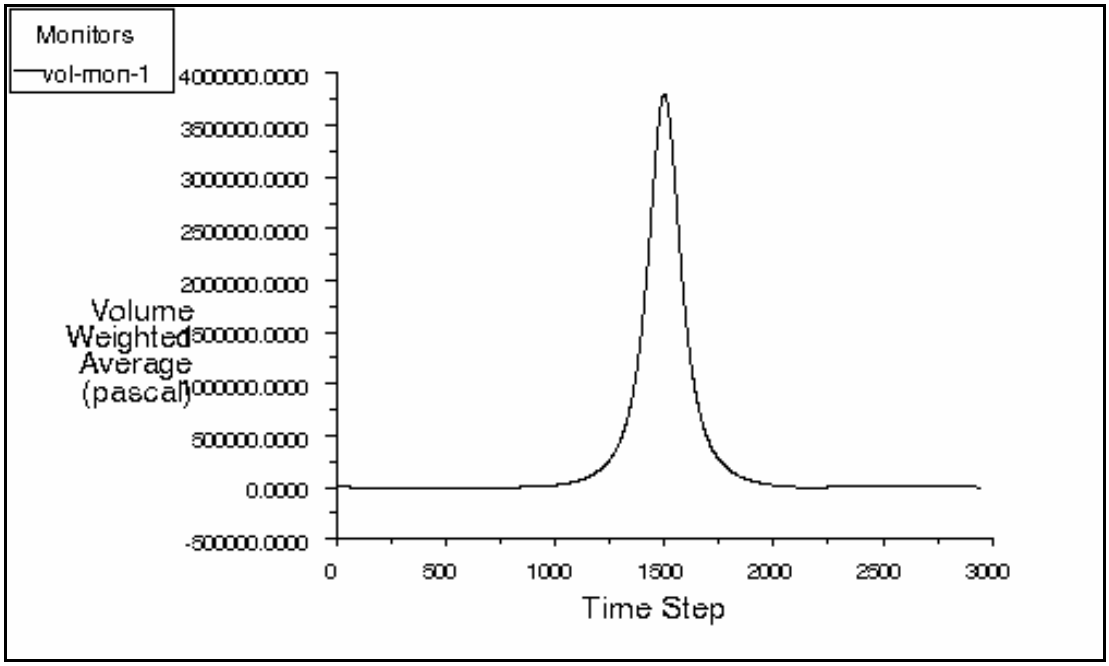
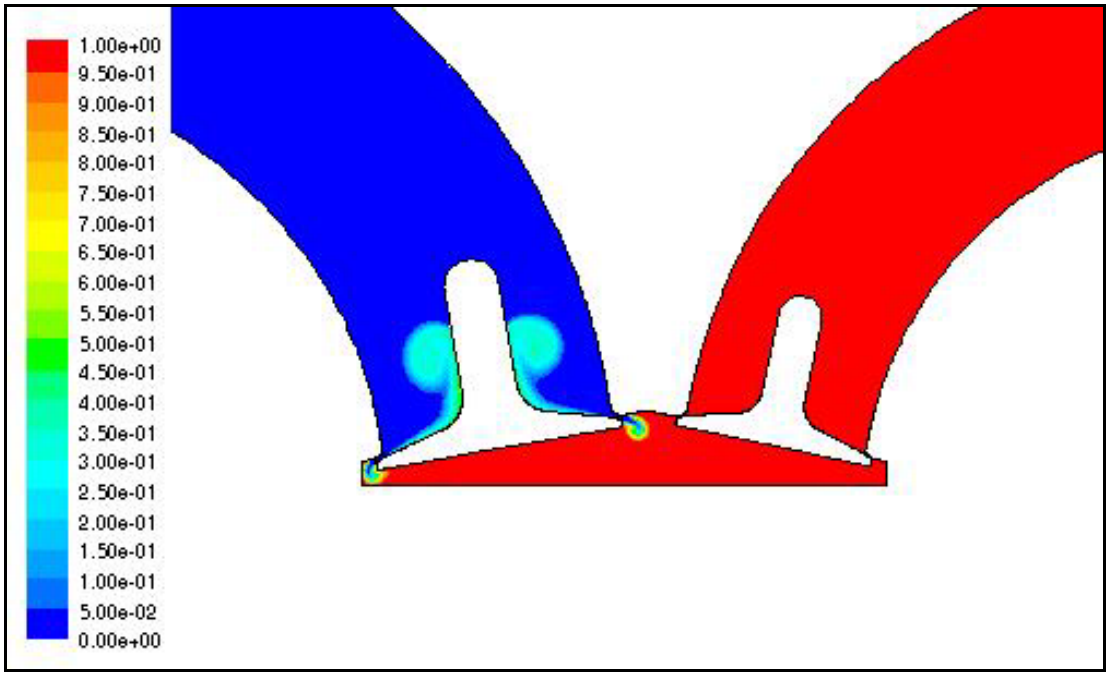
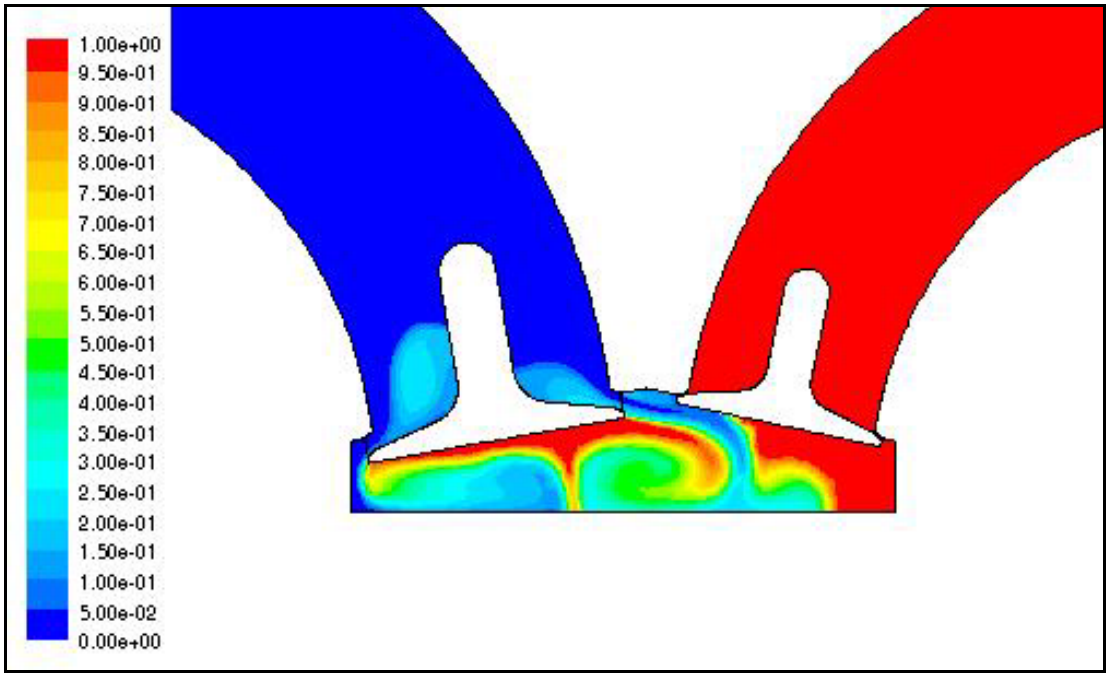


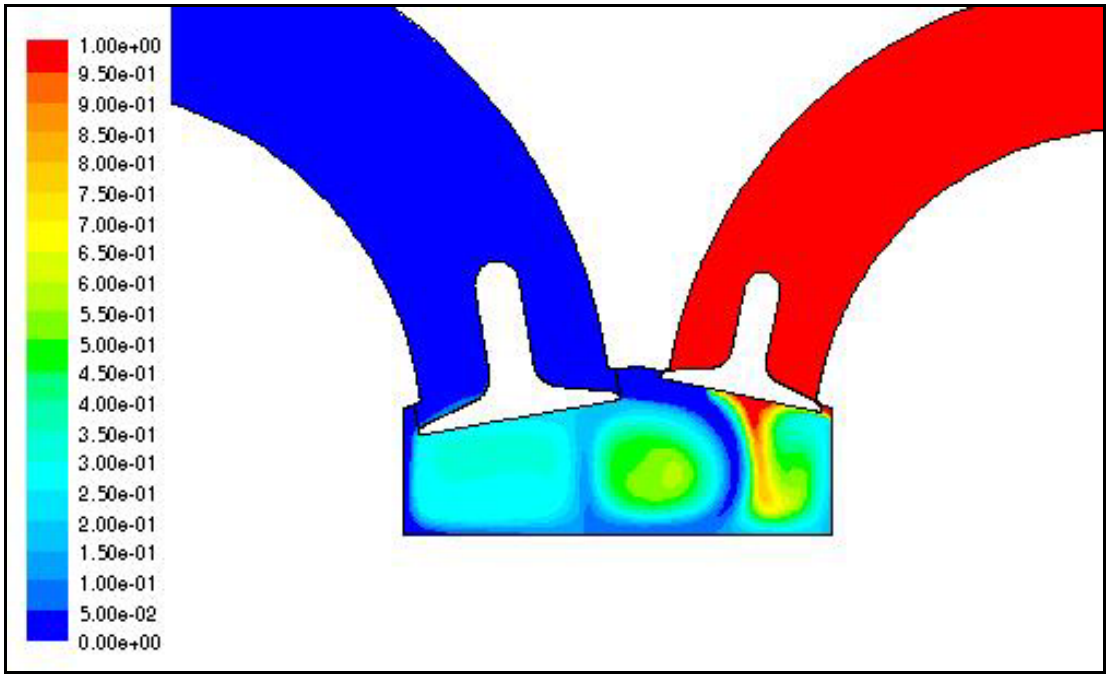
Figure 4.46 Convergence history of static pressure on combustion chamber without combustion


1.00e+00
9.50e-01
9.00e-01
8.50e-01
8.00e-01
7.50e-01
7.00e-01
6.50e-01
6.00e-01
5.50e-01
5.00e-01
4.50e-01
4.00e-01
3.50e-01
3.00e-01
2.50e-01
2.00e-01
1.50e-01
1.00e-01
5.00e-02
0.00e+00

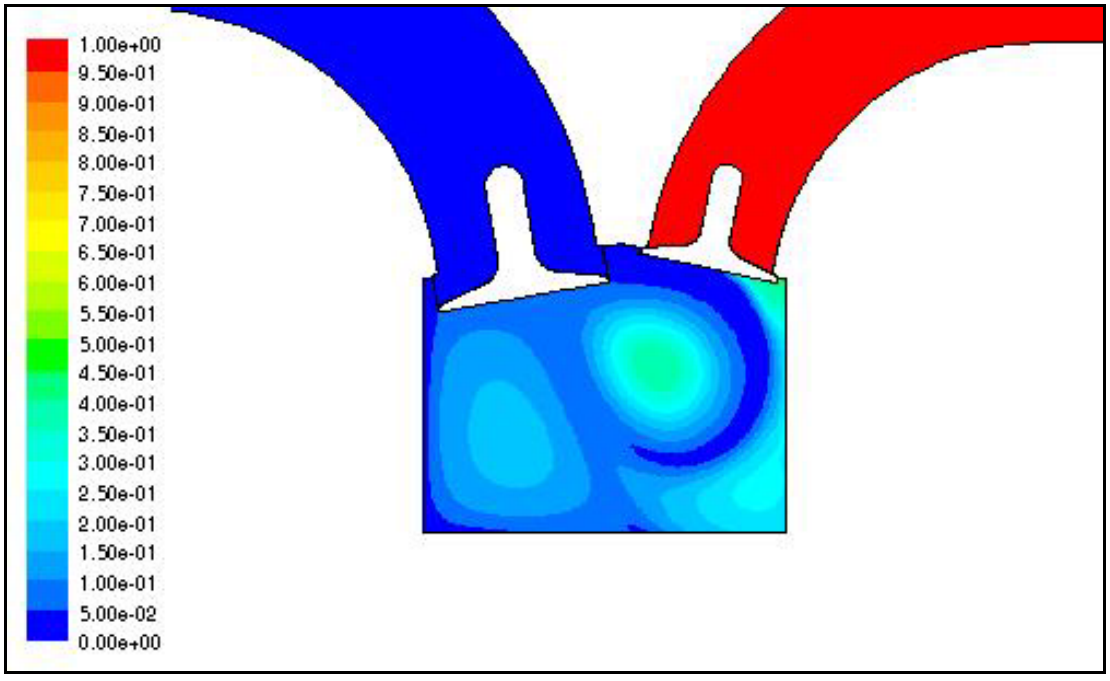
a)


1.00e+00
9.50e-01
9.00e-01
8.50e-01
8.00e-01
7.50e-01
7.00e-01
6.50e-01
6.00e-01
5.50e-01
5.00e-01
4.50e-01
4.00e-01
3.50e-01
3.00e-01
2.50e-01
2.00e-01
1.50e-01
1.00e-01
5.00e-02
0.00e+00

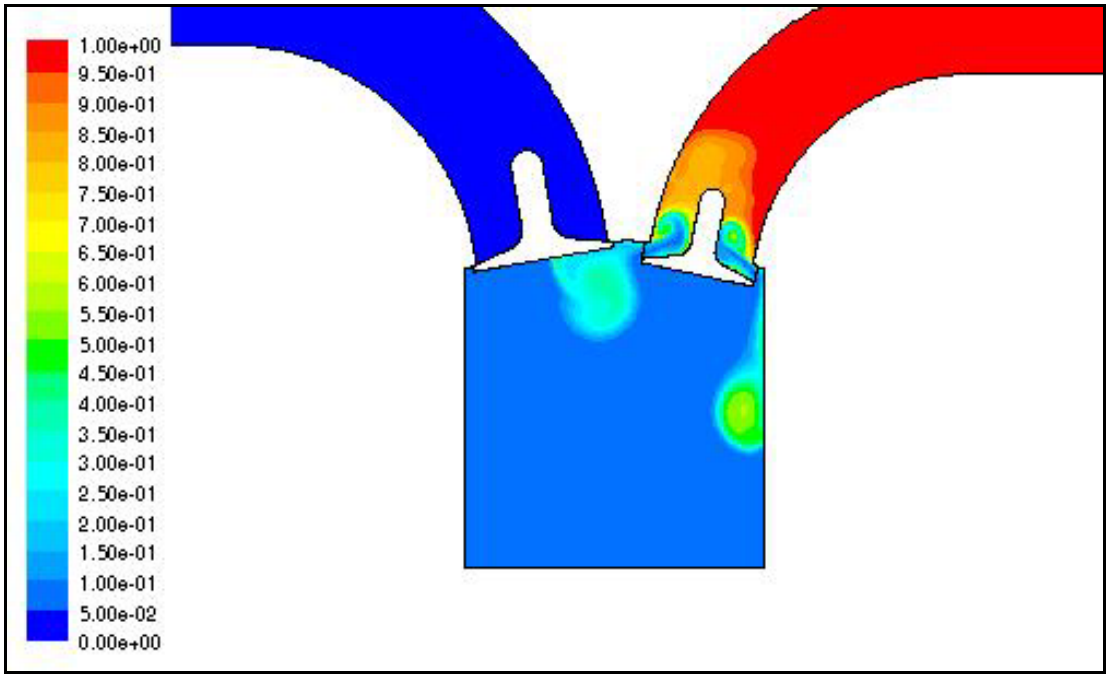
b)


1.00e+00
9.50e-01
9.00e-01
8.50e-01
8.00e-01
7.50e-01
7.00e-01
6.50e-01
6.00e-01
5.50e-01
5.00e-01
4.50e-01
4.00e-01
3.50e-01
3.00e-01
2.50e-01
2.00e-01
1.50e-01
1.00e-01
5.00e-02
0.00e+00

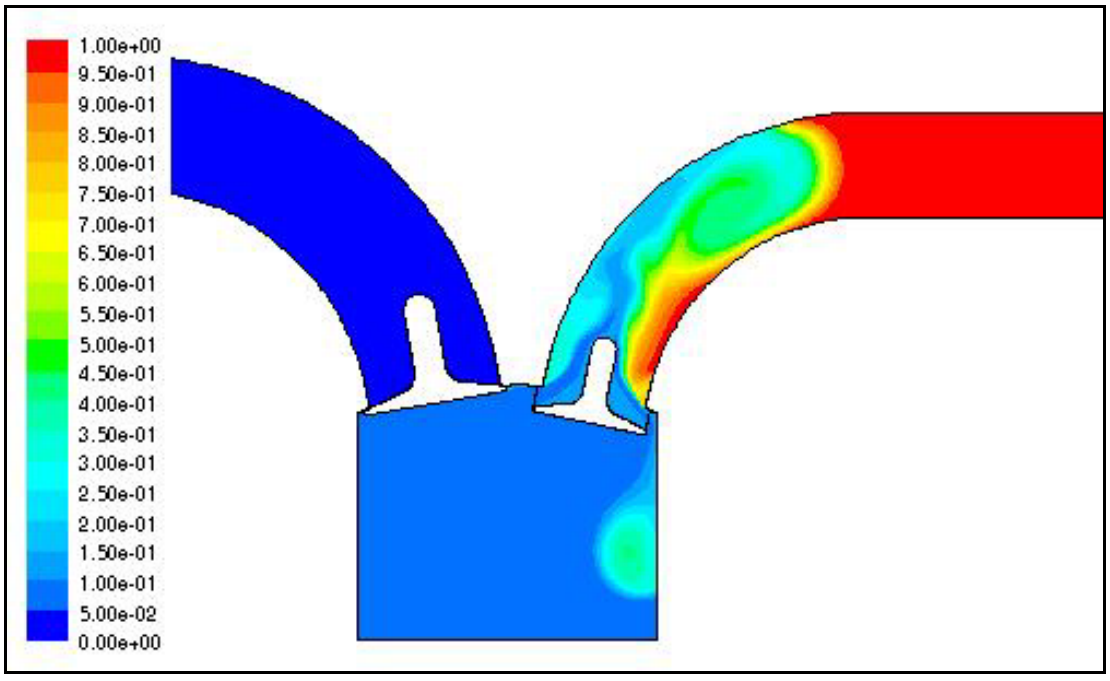
c)


1.00e+00
9.50e-01
9.00e-01
8.50e-01
8.00e-01
7.50e-01
7.00e-01
6.50e-01
6.00e-01
5.50e-01
5.00e-01
4.50e-01
4.00e-01
3.50e-01
3.00e-01
2.50e-01
2.00e-01
1.50e-01
1.00e-01
5.00e-02
0.00e+00

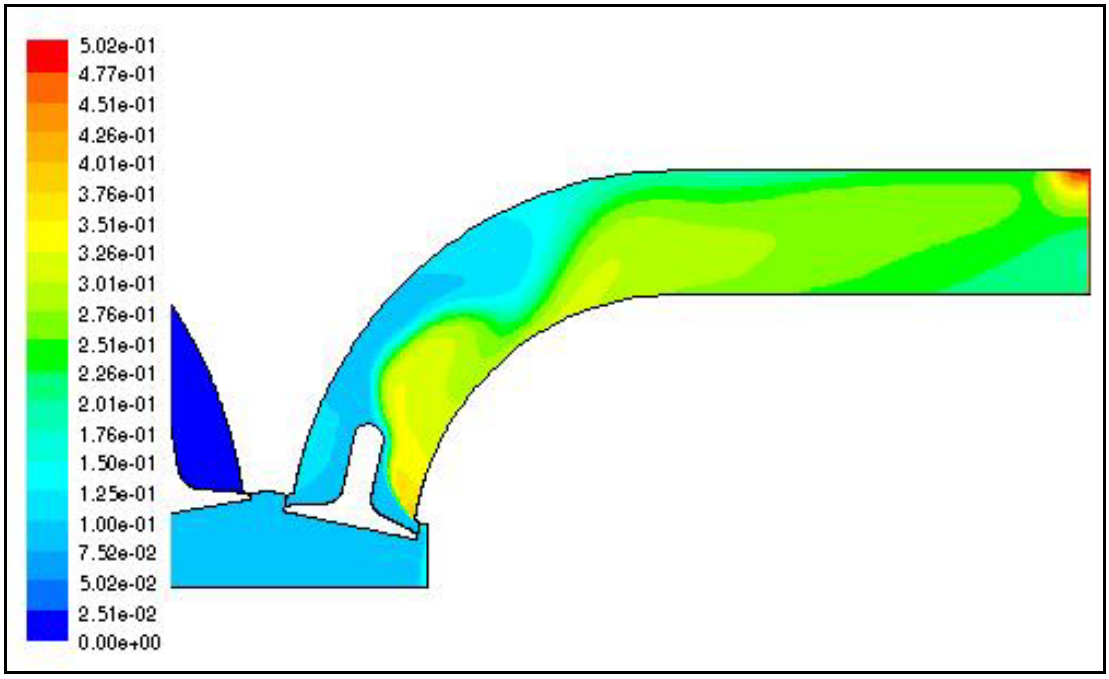
d)


1.00e+00
9.50e-01
9.00e-01
8.50e-01
8.00e-01
7.50e-01
7.00e-01
6.50e-01
6.00e-01
5.50e-01
5.00e-01
4.50e-01
4.00e-01
3.50e-01
3.00e-01
2.50e-01
2.00e-01
1.50e-01
1.00e-01
5.00e-02
0.00e+00

e)


1.00e+00
9.50e-01
9.00e-01
8.50e-01
8.00e-01
7.50e-01
7.00e-01
6.50e-01
6.00e-01
5.50e-01
5.00e-01
4.50e-01
4.00e-01
3.50e-01
3.00e-01
2.50e-01
2.00e-01
1.50e-01
1.00e-01
5.00e-02
0.00e+00

f)



g)

Figure 4.47 Contours of mass fraction of burned gasses in different CA a) 367° b) 390° c) 412° d) 457° e) 930° f) 975° g) 1042°

5. CONCLUSIONS

Computational Fluid Dynamics, commonly referred to by the acronym CFD, is generally accepted as describing the broad topic encompassing the numerical solution, by computational methods, of the governing equations which describe fluid flow - the set of the Navier-Stokes equations, continuity and additional conservation equations. Computational Fluid Dynamics is attractive for two reasons. Firstly, the desire to be able to model physical fluid phenomena that cannot be easily simulated or measured with a physical experiment, for example weather systems or hypersonic aerospace vehicles. Secondly, the desire to be able to investigate physical fluid systems low cost effectively and more rapidly than with experimental methods.

The ultimate goal of this work was to show the effect of different valve gaps and how flow acts inside of an engine cylinder on the 2d, 3d and dynamic models by means of CFD. Also, the present work intended to show how the flow characteristics change by using different turbulence models.

CFD analysis was conducted with the commercial software, called FLUENT. The present numerical analysis was conducted for incompressible, compressible, turbulent, mixture, steady and unsteady flow. In this study, fluid was assumed to be air as it is normally used in engines.

From the numerical results and discussions, the following conclusions can be summarized as follows;

- 2d models must be firstly created to make an idea for engine models, before real models are generated.
- 2d models should be considered as pre-design applications, they are not thought to find numerical results.
- During the 2d model calculation, it was noticed that pent-roof model had better performance and flow characteristics than other 2d models.
- Using of pent-roof design, the area of valves can be increased that is result of more boost and good volumetric efficiency.
- Two types 3d model was used. First model had same geometrical features with the model that was used for experimental study. Second model had 2

intake ports and it reflects real engine situation. Obtaining results from first model help to solve parameters of second model.

- Velocity vectors were showed in measurement lines. They were seen to be meaningful condition.
- In order to reduce time and hardware requirements, some features were used, such as symmetry boundary condition.
- Parametric studies were carried out for all 2d and 3d models. Therefore, exact dimensions for all engine part were not needed. But during calculation period, it was seen that CFD world had not been ready for parametric studies yet. Because changing of the model dimension, in other words, creating model totally again requires more time and more hardware for calculation.
- Different turbulence models show that there can be some differences between results. Especially it was seen during the 3d one intake port calculations. Results from this model show that standard $k-\varepsilon$ turbulence model is not sufficient to predict flow domain regardless of different valve gap. But RNG and realizable method have a good agreement with experimental results except a small conflict. This conflict mentioned in Results and Discussion section but this reason has not been discussed yet. First of all, one reason is thought that cylinder length is small and this cause more backflow. This can be recovered by extending cylinder stroke. But this time, calculation needs more time and hardware requirements, since total elements number would increase. Another and most crucial reason is that experimental results did not predict correct results in some measurement distances.
- Dynamic model was only used for 2d model. It could have been used for 3d model but this event requires much more time and hardware requirements.
- From dynamic model calculations, it is noticed that valve overlap period has little effect in sweeping out combustion chamber, since used valve profile does not let it happen. Therefore it should be investigated more by chancing valve timing.

- Revolution of crankshaft was chosen 0.25 CA degrees per one time step. In order to visualize and investigate combustion process for future studies this value should be reduced.
- Modeling of dynamic model provides crucial importance during design process. There are a lot of parameters affecting design period and all of these parameters can be changed using dynamic model in order to obtain optimum conditions.
- Cold flow characteristics were investigated using dynamic model. Combustion process can be also carried out with same model for future studies.

REFERENCES

ANDERSON, J., 1995. Computational Fluid Dynamics. McGRAW-HILL, Singapore, 547s.

BAYRAKTAR, H. and DURGUN, O., 2004. "Development of an Empirical Correlation for Combustion Durations in Spark Ignition Engines" Journal of Energy Conversion and Management, Vol. 45, pp. 1419-1431.

BENSON, R., WHITEHOUSE, N.D., 1979. Internal Combustion Engines. Pergamon Press Ltd, England, 170s.

CHAN, V.S.S. and TURNER, J.T., 2000. "Velocity Measurement Inside a Motored Internal Combustion Engine Using Three-Component Laser Doppler Anemometry" Journal of Optics and Laser Technology, Vol. 32, pp. 557-566.

CHIAVOLA, O., 2002. "Multi Dimensional CFD Transmission Matrix Modelling of IC Engine Intake and Exhaust Systems" Journal of Sound and Vibration, Vol. 256, pp. 835-848.

FANG, D. and MAJDALANI, J., 2003. "Simulation of the Cold-Wall Swirl Driven Combustion Chamber" The 39th AIAA/ASME/SAE/ASEE Joint Propulsion Conference and Exhibit, AIAA 2003-5055.

FERZIGER, J.H., PERIC, M., 2002. Computational Methods for Fluid Dynamics. Springer-Verlag, Germany, 423s.

FLUENT User's Guide, 2002.

FUJIMOTO, M., IWAI, K., KATAOKA, M. and TABATA, M., 2002. "Effect of Combustion Chamber Shape on Tumble Flow, Squish-Generated Flow and Burn Rate" Journal of JSAE Review, Vol. 23, pp. 291-296.

HEYWOOD, J.B., 1998. Internal Combustion Engine Fundamentals, McGraw-Hill, New York.

HONG, C.W. and TARNG, S.D., 1998. "Direct Measurement and Computational Analysis of Turbulence Length Scales of a Motored Engine" Journal of Experimental Thermal and Fluid Science, Vol. 16, pp. 277-285.

HUANG, R.F., HUANG, C.W., CHANG, S.B., YANG, H.S., LIN, T.W. and HSU, W.Y., 2005. "Topological Flow Evolutions in Cylinder of a Motored Engine

During Intake and Compression Strokes" Journal of Fluids and Structures, Vol. 20, pp. 105-127.

JOHAN, Z., MORAES, A., BUELL, J.C. and FERENCZ, R.M., 2001. "In-Cylinder Cold Flow Simulation Using a Finite Element Method" Journal of Computational Methods Applications, Vol. 190, pp. 3069-3080.

KANG, K.Y. and BAEK, H., 1998. "Turbulence Characteristics of Tumble Flow in a Four-Valve Engine" Journal of Experimental Thermal and Fluid Science, Vol. 18, pp. 231-243.

KIM, Y.J., LEE, S.H. and CHO, N., 1999. "Effect of Air Motion on Fuel Spray Characteristics in a Gasoline Direct Injection Engine" SAE 010177.

LARAMEE, R.S., HAUSER, H., DOLEISCH, H., POST, F.H., 2004. "The State of the Art in Flow Visualization: Dense and Texture-Based Techniques" Computer Graphics Forum, Vol. 23, pp. 203-221.

LARAMEE, R.S., SCHNEIDER, J. and HAUSER, H., 2004. "Texture-Based Flow Visualization on Isosurfaces from Computational Fluid Dynamics" The Joint Eurographics-IEEE TVCG Symposium on Visualization, Eurographics Association, pp. 85-90, 342.

LAUNDER, B.E. and SPALDING, D.B., 1972. Lectures in Mathematical Models of Turbulence, Academic Press, London, England.

MANTEL, T., 1992. "Three Dimensional Study of Flame Kernel Formation around a Spark Plug" SAE International Congress and Exposition, 920587.

MILTON, B.E., BEHNIA, M. and ELLERMAN, D.M., 2001. "Fuel Deposition and Re-Atomization from Fuel/Air Flows Through Engine Inlet Valves" International Journal of Heat and Fluid Flow, Vol. 22, pp. 350-357.

MOUREAU, V. and ANGELBERGER, C., 2004. "Towards Large Eddy Simulation in Internal Combustion Engines: Simulation of a Compressed Tumble Flow" SAE 011995.

NKONGA, B., 2000. "On the Conservative and Accurate CFD Approximations for Moving Meshes and Moving Boundaries" Journal of Computational Methods Applications, Vol. 190, pp. 1801-1825.

PAYRI, F., BENAJES, J., MARGOT, X. and GIL, A., 2004. “CFD Modeling of the In-Cylinder Flow in Direct-Injection Diesel Engines” Journal of Computers and Fluids, Vol. 33, pp. 995-1021.

REEVES, M., TOWERS, D.P., TAVENDER, B. and BUCKBERRY, C.H., 1999. “A High-Speed All-Digital Technique for Cycle-Resolved 2-D Flow Measurement and Flow Visualization within SI Engine Cylinders” Journal of Optics and Laser in Engineering, Vol. 31, pp. 247-261.

STONE, R., 1992. Introduction to Internal Combustion Engines, Second Edition, MacMillan Press Ltd, Hong Kong, 574s.

SUKEGAWA, Y., NOGI, T. and KIHARA, Y., 2003. “In-Cylinder Airflow of Automotive Engine by Quasi-Direct Numerical Simulation” Journal of JSAE Review, Vol. 24, pp.123-126.

VERSTEEG, H.K. and MALALASEKERA, W., 1995. “An Introduction to Computational Fluid Dynamics” Longman Scientific and Technical, Essex.

WILCOX, D.C., 2000. Turbulence Modeling for CFD, Second Edition, DCW Industries Inc., USA, 540s.

WU, H.W. and PERNG, S.W., 2002. “LES Analysis of Turbulent Flow and Heat Transfer in Motored Engines with Various SGS Models” International Journal of Heat and Mass Transfer, Vol. 45, pp. 2315-2328

YANG, S.L., SIOW, Y.K. and TEO, C.Y., 2005. “A Kiva Code with Reynolds-Stress Model for Engine Flow Simulation” Journal of Energy Conversion, Vol. 30, pp. 427-445.

YASAR, A., 2002, “Determination of the Cylinder Flow Characteristics in Internal Combustion Engine”, Phd thesis, Çukurova University, Instıtute of Natural and Applied Sciences, Adana.

ZELLAT, M., 2002 “Recent Advances in CFD Modelling of Internal Combustion Engine” Network Newsletter, Vol. 1, No. 3, pp. 12-16.

ZHENG, Q.P., ZHANG, H.M. and ZHANG, D.F., 2005. “A Computational Study of Combustion in Compression Ignition Natural Gas Engine with Separated Chamber” Journal of Fuel, pp. 1-9.

CURRICULUM VITAE

Personal details

Name	: Ramazan AKAR
Date Place of Bird	: 13 April 1980, Adana, TURKEY
Nationality	: Turkish
Marital Status	: Unmarried
Telephone	: +90-322-225 34 93
GSM	: +90-536-566 72 95
E-mail	: ramazan_akar@yahoo.com

Educational Background

1986	: Emine Sapmaz Primary School, Adana, TURKEY
1991	: Sıtkı Kulak High School, Adana, TURKEY
1994	: Baraj High School, Adana, TURKEY
1998	:Bsc, Department of Mechanical Engineering, Cukurova University, Adana, TURKEY
2002	:Msc, Department of Mechanical Engineering, Cukurova University, Adana, TURKEY

Research Activity

Fluid dynamics, production of any kind of mechanical part, computer programs, automotive.

Ongoing Researches

A new generation model excavator design, go cart design, model formula 1 car design, and elevator design for conveying grain.

Membership of Institutions

- Union of Chambers of Turkish Engineers and Architects Chamber of Mechanical Engineers (TMMOB)
- The Turkish Foundation for Combating Soil Erosion, for Reforestation and the Protection of Natural Habitats (TEMA)